UNIVERSITY OF SOUTHAMPTON

Faculty of Engineering and Physical Sciences
Optoelectronics Research Centre

Dispersion Engineering of Silicon Waveguides for Enhanced Nonlinearities

by

Shiyu Sun

[MEng in Huazhong University of Science and Technology]

ORCiD: 0000-0002-8308-2077

A thesis for the degree of
Doctor of Philosophy

May 2024

University of Southampton

Abstract

Faculty of Engineering and Physical Sciences
Optoelectronics Research Centre

Doctor of Philosophy

Dispersion Engineering of Silicon Waveguides for Enhanced Nonlinearities

by Shiyu Sun

Silicon photonics has gained popularity due to its mature fabrication process and outstanding integration potential, serving as a bridge between photonics and electronics. However, the material's inherent characteristics pose limitations for light amplification. Nonlinear silicon photonics, particularly through processes such as Raman scattering and four-wave mixing, offers an effective strategy for realising light amplification. Nonetheless, the challenge lies in the relatively small gain associated with each individual nonlinearity. Raman scattering attracted attention as a possible solution to enhance the four-wave mixing effect, offering the prospect of improving gain at Stokes wavelengths. This study delves into the numerical investigation of nonlinear processes in silicon waveguides and silicon core fibres utilising a generalised nonlinear Schrödinger equation. The exploration encompasses Raman scattering, four-wave mixing and Raman-enhanced four-wave mixing in silicon core fibres, with a focus on the telecom band and mid-infrared band. While successful enhancements of conversion efficiency and Stokes output power are achieved, the gains in silicon core fibres are modest due to phase mismatch issues. To address fabrication inaccuracy in silicon core fibres, planar silicon waveguides are employed, advancing in dispersion engineering by precise control of fabricated structure. Coherent Stokes Raman scattering is successfully observed, and the conversion efficiency reaches -30 dB with pump powers of 20 mW and 40 mW in the telecom band and mid-infrared band, respectively. Inspired by the request for wavelength extension via the generation of higher-order Stokes waves, slotted waveguides are investigated as a new promising method for constructing light sources or amplifiers. Slotted waveguides, owning a flat and low dispersion profile, open up avenues for further exploration nonlinear effects in the realm of silicon photonics.

Contents

List of Figures **ix**

List of Tables **xix**

Listings **xxi**

Declaration of Authorship **xxi**

Acknowledgements **xxiii**

Definitions and Abbreviations **xxv**

1 Introduction **1**
1.1 Significance of nonlinear silicon photonics . . . 1
1.1.1 Study on the Raman scattering . . . 3
1.1.2 Study on the FWM, supercontinuum generation and optical frequency comb . . . 4
1.1.3 Study on the interaction between FWM and Raman scattering . . . 7
1.2 Motivation . . . 10
1.3 Overview . . . 10

2 Background **13**
2.1 Waveguide structures . . . 13
2.2 Subwavelength grating structures . . . 14
2.3 Dispersion . . . 15
2.4 Nonlinear optics in silicon . . . 18
2.5 Linear and nonlinear losses . . . 19
2.6 Raman scattering . . . 20
2.7 Inverse Raman scattering . . . 22
2.8 Four-wave mixing . . . 23
2.9 Raman-enhanced four-wave mixing . . . 26
2.9.1 Coherent anti-Stokes Raman scattering . . . 26
2.9.2 Coherent Stokes Raman scattering . . . 27
2.10 Pulse propagation in nonlinear medium . . . 28
2.10.1 Nonlinear phenomena presented by the mathematical equation . . . 28
2.10.2 Validation of the Raman response model . . . 30

3 Raman scattering and coherent anti-Stokes Raman scattering in SCFs **37**
3.1 Structures and characteristics of SCFs . . . 37

3.2 Raman scattering in SCFs . . . 39
3.2.1 Raman scattering in the telecom band . . . 40
3.2.1.1 Pumped with CW light source . . . 40
3.2.1.2 Pumped with pulse light sources . . . 43
3.2.2 Raman scattering in the mid-infrared band . . . 47
3.2.2.1 Spontaneous Raman scattering and On-off gain . . . 47
3.2.2.2 Cascaded Raman scattering . . . 49
3.3 FWM and CARS in SCFs in the mid-infrared band . . . 52

4 Coherent Stokes Raman scattering in SCFs 57
4.1 Demonstration of the principle . . . 57
4.2 CSRS in the telecom band . . . 58
4.2.1 Dispersion properties and simulations for CSRS . . . 58
4.2.2 Experimental setup . . . 62
4.2.3 Experimental verification . . . 62
4.3 CSRS in the mid-infrared band . . . 68
4.3.1 Dispersion properties and simulations for CSRS . . . 69
4.3.2 Experimental setup . . . 71
4.3.3 Experimental verification . . . 72

5 Coherent Stokes Raman scattering in silicon planar waveguides 79
5.1 Comparison between SCFs and planar silicon waveguides . . . 80
5.2 CSRS in the telecom band . . . 82
5.2.1 Structural design and simulations for CSRS . . . 82
5.2.2 Experimental verification . . . 86
5.2.2.1 Characterisation of rib waveguide . . . 86
5.2.2.2 CSRS measurement . . . 88
5.3 CSRS in the mid-infrared band . . . 91
5.3.1 Structural design and CSRS simulation . . . 91
5.3.2 Experimental verification . . . 94
5.4 Exploration of the influencing factors for CSRS . . . 96

6 Slotted waveguides with flattened dispersion curve 105
6.1 Subwavelength grating design in slotted waveguides . . . 105
6.2 Nonlinear performances for different structures . . . 107
6.3 Effects of structure parameters on the dispersion curve . . . 110
6.4 Higher-order Stokes generation and supercontinuum generation . . . 114
6.5 Slotted waveguide testing . . . 116

7 Waveguide fabrication 119
7.1 Fabrication and fixing method of SCFs . . . 119
7.1.1 Fabrication of SCFs . . . 119
7.1.2 Fixing method of SCFs . . . 123
7.2 Fabrication of planar silicon waveguides . . . 125
7.2.1 Fabrication of rib waveguides . . . 125
7.2.2 Fabrication of slot waveguides . . . 128

8 Conclusions 133

8.1 Summary 133
8.2 Future development 136

Appendix A List of samples and the relating parameters **139**

Appendix B MATLAB code for NLSE **141**

Appendix C Parameters for characterizing rib waveguide **147**

References **149**

List of publications **163**
C.1 Journal 163
C.2 Conference Papers 164

List of Figures

1.1 (a) Measured spectral characteristic of SRS in silicon waveguide; (b) Spontaneous Raman Spectra of the same waveguide with the same pump power as in (a) [1]. (c) Schematic layout of the silicon waveguide laser cavity with optical coatings applied to the facets and a p-i-n structure along the waveguide; (d) the pump wavelength is 1550 nm and the laser wavelength is 1686 nm. [2]. 3

1.2 The plot of on-off Raman gain as a function of effective pump intensity interacting with the Stokes input. [3] 4

1.3 Experimental observation of IRS in silicon. [4] 5

1.4 (a) Measured on/off signal gain as a function of signal wavelength for several waveguide cross-sectional areas and lengths. [5] (b) Measured FWM conversion efficiency (normalized) as a function of signal-idler wavelength separation for different tapered SCFs at selected pump wavelengths. [6] (c) Series of FWM spectra taken at the output of the 4-mm-long waveguide. [7] (d) Measured four-wave mixing spectrum across a range of 241 nm. [8] 6

1.5 Theoretical (curve) and measured (dots) conversion efficiencies as functions of idler wavelength. The inset shows the measured FWM spectra. [9] 6

1.6 (a) Supercontinuum created in a 3-mm-long SOI waveguide. [10] (b) SC generation in a 1 cm long $500 \times 220\,nm^2$ a-Si-H waveguide. [11] (c) Measured spectra for the powers. [12] (d) Broadband frequency comb generation from 2.1 to 3.5 μm in the etchless silicon micro-resonator. [13] . . . 7

1.7 (a) Measured spectra with two different waveguide widths (W) of 6 and 8 μm. The input pumping powers were set to be over 25 mW. [14] (b) Individual spectra generated with 3.25 and 2.4 μm wide waveguides. [15] 8

1.8 Variation of normalized powers versus propagation coordinate in the presence of Raman effects. [16] 8

1.9 Maximum amount of a-Stokes signal obtained, at 1328.8 nm. [17] 9

1.10 (a) Primary comb lines generated by a 60-μm-radius AlN chip. [18] (b) Raman-assisted broadband comb spectrum from an AlN microring at TE mode input. Inset shows the TE mode profile at 1.55 μm wavelength. [19] 10

2.1 Waveguide structures: (a) slab waveguide, (b) strip waveguide, (c) rib waveguide, (d) fibre. 14

2.2 Modes in a strip waveguide, silicon (Si) in the rectangular is surrounded by silicon dioxide (SiO_2): (a) propagation mode,$n_{eff} \sim n_{core}$; (b) propagation mode, $n_{clad} < n_{eff} < n_{core}$; (c) leaky mode, $n_{eff} \sim n_{clad}$. 14

2.3 The SWG structure and its equivalent structure in the simulation. 15

2.4 (a) Standard microring resonator where three parameters are available for dispersion engineering, ring radius (RR), ring width (RW) and material thickness (H). (b) Variation of second-order dispersion (D_2), power in the dispersive waves (DW), and separation between the two potential DW locations (in units of mode number) as a function of ring width. (c) The frequency splittings modify dispersion, resulting in a higher dispersion branch and a lower dispersion branch (shown in green). (d) The resulting ring resonator has a ring width modulation profile. [20] 17
2.5 (a) Effective index for bulk Si_3N_4 (dashed line) and that predicted for a 730×2580 nm Si_3N_4 waveguide with oxide cladding (solid green). (b) Corresponding β_2 of bulk Si_3N_4 (dashed red) and waveguide (solid red) and dispersion function (D) (solid blue). Spectra produced via SCG in the 5-cm-long waveguide (c) and via Kerr-comb generation (KCG) in a micro-resonator (d), both with waveguide cross-sections as in (a). [21] . 17
2.6 The nonlinear refractive index values of the considered materials in near- and mid-infrared bands. [22] 18
2.7 The energy level diagram of TPA and FCA. 20
2.8 The values of β_{TPA} in silicon. [23] 20
2.9 Energy level diagrams of Raman scattering. (a) The Stokes-shifted Raman scattering. (b) The anti-Stokes-shifted Raman scattering. (c) The stimulated Raman scattering. The angular frequencies ω_p, ω_s, ω_a and ω_v correspond to the pump, Stokes waves, anti-Stokes waves and Raman shift, respectively. 21
2.10 The Raman response function for silicon in time (a) and frequency domain (b). 22
2.11 The differences of the energy diagrams (above) and spectra (below) between the Raman scattering (a) and the inverse Raman scattering (b). The angular frequencies ω_p, ω_s and ω_a correspond to the pump, Stokes waves and anti-Stokes waves. 23
2.12 FWM process. (a) Sum frequency generation. (b) Third-harmonic generation. (c) Four-photon parametric interaction. The angular frequencies ω_1, ω_2, ω_3 and ω_4 correspond to different waves. 24
2.13 Evolution of the relative phase, idler power (P_4) and the pump power (P_1) along the propagation length when $\kappa = 0$, $\theta = -2/\pi$, $P_1 = P_2 = 70\,W$, $P_3(0) = P_4(0) = 0.1\,\mu$W (solid line), $P_3(0) = 6$ mW, $P_4(0) = 0.1\,\mu$W (dash line) . [24] 25
2.14 Energy diagrams for CARS process. The angular frequencies ω_p, ω_s, ω_a and $\Delta\omega_{nu}$ correspond the pump, Stokes waves, anti-Stokes waves and Raman shift. 27
2.15 CSRS process. (1) Degenerate FWM. (2) Stimulated Raman scattering (SRS). (3) Inverse Raman scattering (IRS). 28
2.16 The simulation results under different dominant effects. (a) Dispersion effect on the 100 fs-pulse propagation without losses and nonlinear effects. (b) Third-order nonlinear effects on the 100 fs-pulse propagation without losses and Raman scattering. (c) Third-order nonlinear effects without Raman scattering and linear loss on the 100 fs-pulse propagation accompanying with FCA and TPA. (d) Raman scattering effect on the 10 ps-pulse propagation without losses. 29
2.17 The flow chart of the code. 30

2.18 The calculation results and calculation time as a function of the distance segment at propagation lengths of 1 cm (a) and 10 cm (b). 34
2.19 The pulse propagation comparison between (a) the simulation results by using our own MATLAB code and (b) the simulation results in the literature. [10] 34
2.20 Silicon waveguide used and the resulting TM mode.[25] 35
2.21 The CW light propagation comparison between (a) the simulation results by using our own MATLAB code and (b) the experiment results from [25] 35

3.1 The schematic of SCF structure consisting of a down taper, a waist region and an up taper. D_w denotes the core diameter and L_w represents the length of the waist region. 38
3.2 Experimental setup for loss measurement. BS, beam splitter; OL, optical lens. 39
3.3 The relation between the pump power and the output power, with stars and circles representing the experimental and simulation results, respectively. The dash line is the fitting curve for the points with low pump power. 40
3.4 Comparison of the Raman output power between the experimental data and the simulation results of fibre A at different pump wavelengths of 1432nm (a) and 1500nm (b). The dash lines denote the simulation results, and the solid lines denote the experimental results. 41
3.5 The Stokes output power as functions of length and pump power with the pump wavelength of 1.432 μm for Fibre A. 42
3.6 (a) The experimental on-off gain of Fibre B for the 1432 nm pump with the power of 48 mW compared with the simulation results. (b) The prediction of the on-off gain as functions of the pump power and the propagation lengths. 43
3.7 (a) The Stokes output power of Fibre B changing with the varying pulse duration. The pump peak power is fixed at 5 W. (b) The trend of the Stokes output Power as functions of propagation length and average pulse pump power. (c) The output power of 1^{st}-order anti-Stokes wave, 1^{st}- and 2^{nd}-order Stokes waves at the propagation length of 10 cm. The pump wavelength is 1432 nm and the repetition rate of the pulse pump is 100 MHz. 45
3.8 (a) 1^{st}, 2^{nd}, 3^{rd} and 4^{th}-order Stokes output power as function of the propagation length. (b) Evolution of the pulse spectrum along the propagation length. The average pump power in this simulation is 40 mW. . . . 46
3.9 (a) The experimental Stokes output power under different pump powers as labeled in the legend compared with the simulation results. (b) The average Raman output power as functions of propagation length and average pump power. 48
3.10 (a) The experimental on-off gain compared with the simulation results with the pump power of 12.4 mW. (b) On-off gain as functions of propagation length and average pump power. 49
3.11 Higher-order Stokes output power varying with the core diameter (a) and the pulse duration(b). The pump wavelength is 1992 nm with the peak pump power of 10 W, and the propagation length is 6 cm. 50

3.12 (a) The variation of the pulse spectrum along the propagation length. (b) Different higher-order Stokes output power as a function of the propagation length, as labeled in the legend. The pump is 1992 nm with the peak power of 20 W and the pulse duration is 40 ps. 51
3.13 (a) The evolution of the pulse spectrum within the propagation length of 20 cm. (b) The variation of different order Stokes waves along the propagation length, as labeled in the legend. The pump wavelength is 2200 nm with a peak power of 20 W and a pulse duration is 125 ps. . . . 52
3.14 (a) The second-order dispersion parameter (β_2) of SCFs with three different core diameters, as labeled in the legend. (b) The conversion efficiency as functions of signal wavelength and core diameter with the propagation length of 4 cm. (c) Conversion efficiency as functions of propagation length and signal wavelength with the core diameter of 1600 nm. The pump is fixed at 1992 nm with the average pump power of 4 mW and the power of the CW signal is 4 mW. 54
3.15 Output spectra of Fibre G with the signal wavelength switching from 2000 nm to 2400 nm while pumping at 1992 nm. Both the coupled-in pump power and signal power are fixed at 4 mW. 55
3.16 (a) The conversion efficiency for Fibre G with the core diameter of 1590 nm extracted from Figure 3.14 (b). (b) The comparison of the conversion efficiencies varying with the signal wavelength between the experimental data (red dots) and the simulation results (blue line). 56

4.1 (a) Pump output power, (b) signal output power and (c) idler output power changing along the propagation length for different nonlinear process under no loss conditions, as labeled in the legend. The pump is 1545 nm with the power of 100 mW, the signal is 1432 nm with the power of 2 mW and the propagation length is 2 cm. 59
4.2 (a) Variation of β_2 as a function of core diameter at the wavelength of 1545 nm. (b) The dispersion profiles for SCFs with core diameters of 860 nm and 750 nm. 59
4.3 (a) Conversion efficiency as functions of core diameter and λ_s. (b) shows the conversion efficiencies of the CSRS processes, marked with black dash box in (a), where signal is tuned to the anti-Stokes wavelength of 1430 nm. In all cases the pump wavelength is 1545 nm with a power of 100 mW, the signal power is 5 mW and the propagation length is 1 cm. . 60
4.4 (a) Conversion efficiency and (b) Stokes output power as functions of pump power and propagation length for the SCF with the core diameter of 920 nm when pumping at 1545 nm with a 5 mW signal beam positioned at 1430 nm. 61
4.5 Experimental setup for CSRS in the telecom band. PC, polarization controller; WDM, wavelength-division multiplexing; PM, power meter; OC, optical coupler; TLF, taper lens fibre; OSA, optical spectrum analyzer. . . 62
4.6 Comparison between two approaches: moving pump wavelength (blue solid line) and moving signal wavelength (red dashed line) under different pump powers, (a) 15 mW and (b) 35 mW. 63

4.7 (a) Conversion efficiency as λ_i is tuned across Γ_R for Fibre A under different pump powers, 12 mW and 25 mW, as labeled in the legend. The experimental results are compared with simulations of CSRS and FWM only. (b) Conversion efficiency at the Raman peak with the increasing pump power under different conditions: FWM ($f_R = 0$) and CSRS ($f_R = 0.043$). (c) Enhancement of the conversion efficiency compared between CSRS and FWM. 64
4.8 Conversion efficiency as λ_i is tuned across Γ_R for Fibre A (orange), Fibre B (yellow) and Fibre C (blue). The experimental results are compared with simulations of CSRS and FWM, as labeled in the legend. 65
4.9 (a) Comparison of the conversion efficiency as λ_i is tuned across Λ_R for Fibre A (orange) and Fibre E (gray). Experiments are compared with simulations of CSRS and FWM, as labeled in the legend. (b) Simulated conversion efficiencies as a function of tapered waist length conducted both with (solid) and without Raman (dashed). The vertical lines mark the waist lengths for the SCFs in (a). 66
4.10 Simulated conversion efficiency as functions of the tapered SCF core diameter and pump wavelength, for a fixed length of 1 cm. The input pump intensity is set as 8.6×10^{11} W/m^2, with a signal power of 2 mW. . 67
4.11 (a) Comparison of the normalized idler output power with the increasing pump power under different conditions: FWM, Raman scattering and CSRS for fibre A with pump at 1545nm. (b) Enhancement of the Stokes output power as a function of pump power, which is the difference between the output power of CSRS and FWM in (a). 68
4.12 (a) Variation of β_2 as a function of core diameter at the wavelength of 2710 nm. (b) The dispersion profiles for SCFs with core diameters of 1976 nm and 1984 nm. 69
4.13 (a) Conversion efficiency as functions of diameter and λ_s. (b) shows the conversion efficiencies of the CSRS processes, marked with black dash box in (a), where signal is tuned to the anti-Stokes wavelength of 1950 nm. In all cases the pump wavelength is 2170 nm with a power of 100 mW, the signal power is 5 mW and the propagation length is 1 cm. . 70
4.14 (a) Conversion efficiency and (b) Stokes output power as functions of pump power and propagation length for a SCF with a core diameter of 1890 nm when pumping at 2170 nm with a 5 mW signal beam positioned at 1950 nm. 71
4.15 Experimental setup for CSRS in the mid-infrared band. BS, beam splitter; OL, optical lens; MMF, muti-mode fibre; OSA, optical spectrum analyzer. 72
4.16 (a) Variation of pump output power and (b) signal output power with changing the pump wavelength around 2170 nm; (c) variation of pump output power and (d) signal power with changing the pump wavelength around 2140 nm, maintaining a fixed pump power of 300 mW for Fibre H. 73
4.17 (a) Conversion efficiency as λ_i is tuned across Γ_R for Fibre H under different coupled-in pump power, 40 mW and 70 mW, as labeled in the legend. The experimental results are compared with simulations. (b) Conversion efficiency at the Raman peak with the increasing pump power under different conditions: FWM ($f_R = 0$) and CSRS ($f_R = 0.043$). (c) Enhancement of the conversion efficiency compared between CSRS and FWM. 74

4.18 (a) Simulated and experimental results of conversion efficiency for Fibre H and Fibre I with the coupled-in pump power of 70 mW and the pump wavelength of 2170 nm. (b) Variation of conversion efficiency as functions of core diameter and propagation length, the pump is fixed at 2170 nm with the power of 70 mW, the signal is fixed at 1950 nm and the linear loss is 1 dB/cm. 75
4.19 (a) Conversion efficiency as λ_i is tuned across Γ_R for Fibre H under different coupled-in pump power, 40 mW and 70 mW, as labeled in the legend. The experimental results are compared with simulations. (b) Conversion efficiency at the Raman peak with the increasing pump power under different conditions: FWM ($f_R = 0$) and CSRS ($f_R = 0.043$). (c) Enhancement of the conversion efficiency compared between CSRS and FWM. 76
4.20 (a) Comparison of the normalized idler output power with the increasing pump power under different conditions: FWM, Raman scattering and CSRS for fibre A with pump at 2170 nm. (b) Enhancement of the Stokes output power as a function of pump power, which is the difference between the output power of CSRS and FWM in (a). 77

5.1 (a) Diagram of the SCF structure, cross section of the waist region was depicted at left-up corner with the mode distribution example, A_{eff} varying with the change of the core diameter is shown at the right-up corner. (b) Diagram of planar waveguide, cross section of the waveguide was depicted at left-up corner with the mode distribution example, A_{eff} varying with the change of the etch depth (h) and width (W) is shown at the right-up corner. Blue represents the silicon and gray represents silica as the legend shows. 80
5.2 (a) β_2 denoted by the solid lines and β_4 denoted by the dash lines. (b) Conversion efficiencies as functions of the signal wavelength (λ_s) when pumping at 1545 nm, the signal power is 5 mW and the propagation length is 1 cm. Results are presented for the SCF and planar platforms, as labelled in the legends. 82
5.3 (a) β_2, (b) Scattering loss and (c) A_{eff} varying with etch depth and width. The black dash line represents β_2 is equal to zero. (d) Plot of conversion efficiency as a function of λ_s for waveguide designs with different combinations of h and W that have a GVD equal to zero at the 1545 nm pump wavelength (i.e., the dimensions are selected from the black dash line in (a). The simulations are conducted with a pump power of 100 mW, a signal power of 5 mW and a propagation length of 1 cm. 84
5.4 (a) Conversion efficiency as functions of h and λ_s. (b) Conversion efficiency as functions of W and λ_s. (c) and (d) show the conversion efficiencies of the CSRS processes, marked with black dash boxes in (a) and (b), respectively, where signal is tuned to the anti-Stokes wavelength of 1430 nm. In all cases the pump wavelength is 1545 nm with a power of 100 mW, the signal power is 5 mW and the propagation length is 1 cm. . 85
5.5 (a) Conversion efficiency and (b) Stokes output power as functions of the pump power and waveguide length when pumping at 1545 nm with a 5 mW signal beam positioned at 1430 nm. The waveguide width is 790 nm and the etch depth is 350 nm. 85

5.6 (a) Comparison of the output pump power between experimental data and simulation results under various conditions labeled in the legend corresponding to Table C.1 (details provided in Appendix C), where the average input power ranges from several hundred micro-watts to tens of milli-watts. (b)-(d) Spectrum of SPM for Rib A under different linear loss and β_{TPA} conditions labeled in the legend corresponding to Table C.1, Table C.2 and Table C.3, respectively with the average pump power of 60 mW. The pump wavelength is 1.54 μm with a pulse duration of 720 fs, and a repetition rate of 47 MHz. 1, 2,3, 4 and 5 correspond to the serial numbers in various tables. 87
5.7 Spectrum of SPM for Rib A under different linear loss and coupling loss conditions labeled in the legend corresponding to Table C.4 with the average pump power of 60 mW. The pump wavelength is 1.54 μm with a pulse duration of 720 fs, and a repetition rate of 47 MHz. 1, 2, 3 and 4 correspond to the serial number in the table. 88
5.8 Comparison of the output pump power between experimental data and simulation results for Rib B (linear (a) and log (b) format of y axis) and Rib C (linear (c) and log (d) format of y axis), where the average input power ranges from several hundred micro-watts to tens of milli-watts. The pump wavelength is 1.54 μm with a pulse duration of 720 fs, and a repetition rate of 47 MHz. 89
5.9 Conversion efficiency as λ_i is tuned across Γ_R for Rib A (a) and Rib D (b). The experimental results are compared with simulations of CSRS and FWM, as labeled in the legend. The pump wavelength is tuned around 1545 nm with a coupled-in power of 12 mW, while the signal is fixed at 1432 nm with a coupled-in power of 70 μW. 90
5.10 Trends of idler output power (a) and conversion efficiency (b) for CSRS and FWM for Rib A, as labeled in the legend, as a function of pump power. Enhancement of idler output power (c) and conversion efficiency (d), which is the difference between those of CSRS and FWM in (a) and (b), respectively. The pump wavelength is fixed at 1545 nm, the signal is fixed at 1432 nm with the coupled-in power of 70 μW. 91
5.11 (a) β_2, (b) Scattering loss and (c) A_{eff} varying with etch depth and width at a wavelength of 2170 nm. The black dash line represents β_2 is equal to zero. 92
5.12 (a) Conversion efficiency as functions of h and λ_s. (b) Conversion efficiency as functions of W and λ_s. (c) and (d) show the conversion efficiencies of the CSRS processes, marked with black dash boxes in (a) and (b), respectively, where signal is tuned to the anti-Stokes wavelength of 1950 nm. In all cases the pump wavelength is 2170 nm with a power of 100 mW, the signal power is 5 mW and the propagation length is 1 cm. . 93
5.13 (a) Conversion efficiency and (b) Stokes output power as functions of the pump power and waveguide length when pumping at 2170 nm with a 5 mW signal beam positioned at 1950 nm. The waveguide width is 1540 nm and the etch depth is 250 nm. 94

5.14 Conversion efficiency as λ_i is tuned across Γ_R for Rib E. The experimental results are compared with simulations of CSRS and FWM, as labeled in the legend. The pump wavelength is tuned around 2171 nm with a coupled-in power of 40 mW, while the signal is fixed at 1950 nm with a coupled-in power of 350 μW. 95
5.15 (a) Conversion efficiency and (c) Stokes output power for CSRS and FWM for Rib E, as labeled in the legend, as a function of pump power. Enhancement of conversion efficiency (b) and Stokes output power (d), which is the difference between those of CSRS and FWM in (a) and (c), respectively. The pump wavelength is fixed at 2171 nm, the signal is fixed at 1950 nm with the coupled-in power of 350 μW. 96
5.16 The influence of β_2 (a), β_3 (b) and β_4 (c) on CEE and PE, as labeled in the legend. In this simulation, $A_{eff} = 0.3\,\mu\text{m}^2$, $n_2 = 6 \times 10^{-18}\text{m}^2/\text{W}$, $f_R = 0.043$, $\beta_{TPA} = 10 \times 10^{-12}\text{m/W}$, the pump is 1545 nm with power of 1 W, the signal is 1432 nm with power of 2 mW, the free carrier life time is 7.5 ns, and the propagation length is 1 cm. 98
5.17 The influence of P_p (a) and A_{eff} (b) on CEE and PE, as labeled in the legend. In this simulation, $\beta_2 = 9.3 \times 10^{-4}\,\text{ps}^2/\text{m}$, $\beta_3 = 6.4 \times 10^{-4}\,\text{ps}^3/\text{m}$, $\beta_4 = -6.2 \times 10^{-7}\text{ps}^4/\text{m}$, $n_2 = 6 \times 10^{-18}\text{m}^2/\text{W}$, $f_R = 0.043$, $\beta_{TPA} = 10 \times 10^{-12}\text{m/W}$, the pump is 1545 nm, the signal is 1432 nm with power of 2 mW, the free carrier life time is 7.5 ns, and the propagation length is 1 cm. 99
5.18 The influence of n_2 (a) and P_s (b) on CEE and PE, as labeled in the legend. In this simulation, $A_{eff} = 0.3\mu\text{m}^2$, $\beta_2 = 9.3 \times 10^{-4}\,\text{ps}^2/\text{m}$, $\beta_3 = 6.4 \times 10^{-4}\,\text{ps}^3/\text{m}$, $\beta_4 = -6.2 \times 10^{-7}\text{ps}^4/\text{m}$, $f_R = 0.043$, $\beta_{TPA} = 10 \times 10^{-12}\text{m/W}$, the pump is 1545 nm with the power of 1 W, the signal is 1432 nm, the free carrier life time is 7.5 ns, and the propagation length is 1 cm. 100
5.19 The influence of f_R (a) and β_{TPA} (b) on CEE and PE, as labeled in the legend. In this simulation, $A_{eff} = 0.3\mu\text{m}^2$, $\beta_2 = 9.3 \times 10^{-4}\,\text{ps}^2/\text{m}$, $\beta_3 = 6.4 \times 10^{-4}\,\text{ps}^3/\text{m}$, $\beta_4 = -6.2 \times 10^{-7}\text{ps}^4/\text{m}$, $n_2 = 6 \times 10^{-18}\text{m}^2/\text{W}$, the pump is 1545 nm with the power of 1 W, the signal is 1432 nm with the power of 2 mW, the free carrier life time is 7.5 ns, and the propagation length is 1 cm. 101
5.20 The influence of τ (a) and L (b) on CEE and PE, as labeled in the legend. In this simulation, $A_{eff} = 0.3\mu\text{m}^2$, $\beta_2 = 9.3 \times 10^{-4}\,\text{ps}^2/\text{m}$, $\beta_3 = 6.4 \times 10^{-4}\,\text{ps}^3/\text{m}$, $\beta_4 = -6.2 \times 10^{-7}\text{ps}^4/\text{m}$, $n_2 = 6 \times 10^{-18}\text{m}^2/\text{W}$, $f_R = 0.043$, $\beta_{TPA} = 10 \times 10^{-12}\text{m/W}$, the pump is 1545 nm with the power of 1 W, the signal is 1432 nm with the power of 2 mW. 102
5.21 The influence of LL on CEE and PE, as labeled in the legend. In this simulation, $A_{eff} = 0.3\mu\text{m}^2$, $\beta_2 = 9.3 \times 10^{-4}\,\text{ps}^2/\text{m}$, $\beta_3 = 6.4 \times 10^{-4}\,\text{ps}^3/\text{m}$, $\beta_4 = -6.2 \times 10^{-7}\text{ps}^4/\text{m}$, $n_2 = 6 \times 10^{-18}\text{m}^2/\text{W}$, $f_R = 0.043$, $\beta_{TPA} = 10 \times 10^{-12}\text{m/W}$, the pump is 1545 nm with the power is 1 W, the signal is 1432 nm with the power of 2 mW, the free carrier life time is 7.5 ns. . . 102

6.1 Structure diagram (a) and the cross-section diagram (b) of the slotted waveguide which is consist of a side waveguide and a core waveguide separated by the SWG. 106

6.2 (a) Fundamental mode in the core waveguide at 1.3 μm, $n_{eff} = 3.29$; (b) Fundamental mode in the side waveguide at 1.3 μm, $n_{eff} = 3.23$; (c) higher mode in the core waveguide at 1.3 μm, $n_{eff} = 3.14$; (d) fundamental mode in the core waveguide at 2.5 μm, $n_{eff} = 2.88$; (e) fundamental mode in the side waveguide at 2.5 μm, $n_{eff} = 2.67$; (f) slot mode in the slotted waveguide at 3.8 μm, $n_{eff} = 2.47$. 107
6.3 Cross sections of different slotted waveguide designs. Structure 1: slotted waveguide without a silicon slab beneath the waveguide and the preserved silicon in the slot; (b) Structure 2: slotted waveguide without a silicon slab beneath the waveguide but the preserved silicon in the slot; (c) Structure 3: slotted waveguide with a silicon slab beneath the waveguide and the preserved silicon in the slot. 108
6.4 (a) Second-order (denoted by solid lines) and fourth-order (denoted by dash lines) dispersion parameters, β_2 and β_4, comparison. (b) Linear phase mismatch among structure 1, structure 2 and structure 3, when pumping at the ZDWs with negative β_2. 109
6.5 The conversion efficiency with and without the Raman scattering of (a) structure1; (b) structure 2; (c) structure 3, when pumping near ZDWs with negative β_2. The pump power is 100 mW the signal power is 1 mW and the propagation length is 1 cm 109
6.6 Comparison of the dispersion profiles with the changing (a) waveguide height, H; (b) core width, $core_w$; (c) slot width, $slot_w$; (d) side width, $side_w$; (e) slab height, $slab_h$; (f) preserved silicon step height, h. 111
6.7 Comparison of β_2 with the variation of H and $core_w$ at the pump wavelength of 2.17 μm (a) and 3 mum. The dash lines represent β_2=0. 112
6.8 Comparison of β_3 as functions of $slot_w$ and $side_w$ (a) and as functions of $slab_h$ and h (b) at the wavelength of 3 μm. The dash lines represent β_3=0. 113
6.9 (a) Output power of various higher-order stokes along the propagation length, as labeled in the legend (b) Evolution of pulse spectrum. The pulse pump source is 2.17 μm with the time duration of 40 ps and the fixed peak power of 20 W, the CW signal is 1.95 μm with the power of 5 mW, the linear loss is assumed to be 0.2 dB/cm. 115
6.10 (a) Spectrum output power at a propagation length of 10 cm. (b) Evolution of pulse spectrum. The pulse pump source is 2.1 μm with the time duration of 5 ps and the fixed peak power of 20 W, the CW signal is 1.95 μm with the power of 5 mW, the linear loss is assumed to be 0.2 dB/cm. 116

7.1 (a) Molten core drawing method of SCFs; (b) Tapering process of the drawing fibres; (c) facet of as-drawn fibres; (d) magnified view of the area, tapering section, indicated by arrows; (e) facet of tapering fibres. [6] 120
7.2 Instrument diagram of vytranGPX300 121
7.3 (a) Fibres after the first tapering step; (b) fibres after the second tapering step; (i) photograph of the vacuum section; (ii) trend near the end of the tapering section. 121
7.4 An typical example for tension variation as a function of time, T_0 to T_5 represents different situation during tapering. [26] 122

7.5 (a) Top view of the fibre fixed with the capillary on the right side; facet of the fibre in the capillary (b) Top view of the fibre fixed with the chip holder, facet of the fibre in the chip holder. 125
7.6 Tapering waveguides at the input and output port. 126
7.7 (a) Layout examples for rib waveguides; (b) second etch steps for the deep etch to improve coupling efficiency, photographs at two sides showing the real exposure position after the lithography. 127
7.8 Layout examples for slot waveguides. 129
7.9 (a) Coupling waveguides before slot waveguides. (b) Cross-section of the slot waveguide which is consist of a side waveguide and a core waveguide separated by the SWG. 130
7.10 Mode coupling between the rib waveguide and the slot waveguide, x axis centered on the midpoint of w_c and y represents the electric field distribution, (a) mode mismatch condition when the width of the rib waveguide is the same as the slot waveguide; (b) mode match condition when the width of the rib waveguide is optimised. 130

List of Tables

3.1 The corresponding parameters of SCFs used in the nonlinear experiments. 38

5.1 The corresponding parameters of rib waveguide used in the nonlinear experiments. 97

6.1 The suitable structure parameters for the slotted waveguide. 114
6.2 The linear loss of slotted waveguides with the DC of 0.36. 117
6.3 The linear loss of slotted waveguides with the DC of 0.34. 117

7.1 Various tension combinations of 1^{st} and 2^{nd} step and the corresponding measured linear loss 124
7.2 Waveguide width values for different operation wavelengths 126
7.3 Optimised w_c for different structural parameters of slot waveguides. . . 131

Appendix A.1 The corresponding parameters of rib waveguide used in the nonlinear experiments. 139
Appendix A.2 Linear and nonlinear parameters for silicon at different wavelength. [22] 139

Appendix B.1 MATLAB code for NLSE. 145
Appendix B.2 Fourier transform code 145
Appendix B.3 FWHM calculation code 146

Appendix C.1 Parameters for choosing the proper β_{TPA} with the linear loss of 2 dB/cm. 147
Appendix C.2 Parameters for choosing the proper β_{TPA} with the linear loss of 3 dB/cm. 147
Appendix C.3 Parameters for choosing the proper β_{TPA} with the linear loss of 4 dB/cm. 147
Appendix C.4 Parameters for choosing the proper $\beta_T PA$ and linear loss. . . 148

Declaration of Authorship

I declare that this thesis and the work presented in it is my own and has been generated by me as the result of my own original research.

I confirm that:

1. This work was done wholly or mainly while in candidature for a research degree at this University;
2. Where any part of this thesis has previously been submitted for a degree or any other qualification at this University or any other institution, this has been clearly stated;
3. Where I have consulted the published work of others, this is always clearly attributed;
4. Where I have quoted from the work of others, the source is always given. With the exception of such quotations, this thesis is entirely my own work;
5. I have acknowledged all main sources of help;
6. Where the thesis is based on work done by myself jointly with others, I have made clear exactly what was done by others and what I have contributed myself;
7. Parts of this work have been published as: See List of Publications.

Signed:..... Date:.....

Acknowledgements

The past four years of research experience in ORC have been the most significant chapter of my life so far. I am deeply grateful for the opportunity provided by the Chinese Scholarship Council, which sponsored my project throughout these four years.

This transformative journey began with the first email I sent to Prof. Anna C. Peacock. You guided me on practical research and introduced me to a new scientific realm—silicon nonlinear photonics. Every time I faced challenges or overlooked possible problems, you stood by me, offering invaluable suggestions. Although my English writing skills may have troubled you on numerous occasions, I appreciate your patience and concern. Your sense of responsibility has left a lasting impression on me. Thank you, once again! I wish to express this gratitude multiple times in this acknowledgment because I find it hard to convey it face to face, feeling a bit embarrassed.

I extend my thanks to my other supervisor, Prof. Goran Z. Mashanovich—an interesting and approachable teacher. My entrance into your group was coincidental, but I experienced a friendly and warm research environment. Despite not meeting on campus frequently, every time I sought your help online, you responded promptly and efficiently. Your unwavering support for my new research ideas without hesitation is something every student hopes for in a supervisor, especially for those with a research direction but no clear path to realization. Thank you very much for your steadfast support in my research. By the way, your skills as a photographer are commendable—thanks for sharing those beautiful photos.

I also express gratitude to my colleagues, Dr. Meng Huang, Dr. Callum Sirling, Dr. Amar Nath Ghosh, Dr. Colin Mitchell, Dr. Dave Rowe, Dr. Milos Nedeljkovic, Dr. Haonan Ren, Dr. Li Shen, Dr. Weiwei Zhang, Dr. Wei Cao, and Dr. Yangbo Wu. Your assistance in the lab has been invaluable in advancing my project, with my inquiries and questions consistently answered promptly. My Chinese colleagues have enriched my life with various activities such as dinner parties, short journeys, and live CS, always filled with joy and fun.

During this journey, I made a new and cherished friend, Huijun. Living together, we engaged in intense discussions over trivial matters from time to time. Thank you for enduring my impatience and occasional bad temper.

I eagerly anticipate our graduation trip. To my old friend Renwen, who appeared in the acknowledgment of my master's degree thesis, thank you for your weekly calls and for sharing the happiness in your life.

This four-year adventure has come to an end, and it is time to say goodbye. Due to the worldwide pandemic, I have been separated from my family for over four years. Mom and Dad, your unconditional love has been my anchor. Love you!

Definitions and Abbreviations

HNLF	Highly nonlinear fibre
SOI	Silicon on insulator
TPA	Two-photon absorption
SRS	Stimulated Raman scattering
FCA	Free carrier absorption
3PA	Three-photon absorption
IRS	Inverse Raman scattering
FWM	Four-wave mixing
CW	Continuous wave
SCG	Supercontinuum generation
OFC	Optical frequency comb
Ge	Germanium
SiO_2	Silicon dioxide
CSRS	Coherent Stokes Raman scattering
CARS	Coherent anti-Stokes Raman scattering
NLSE	Nonlinear Schrödinger equation
SCF	Silicon-core fibre
SPM	Self-phase modulation
n_{core}	Refractive index of core material
n_{clad}	Refractive index of cladding material
n_{eff}	Effective refractive index
SWG	Subwavelength grating
Λ	Grating pitch
L	Length
DC	Duty cycle
$n_{\parallel}$	Equivalent refractive index when the electric field is parallel to periodic structure
$n_{\perp}$	Equivalent refractive index when the electric field is perpendicular to periodic structure
n_{Si}	Refractive index of silicon
n_{air}	Refractive index of air
n_B	Effective refractive index of Bloch-Floquet mode

λ	Wavelength
$n(\omega)$	Frequency-dependent refractive index
β	Propagation constant
ω_0	Central wavelength
n_g	Group index
v_g	Group velocity
β_m	m-order dispersion parameter
D	Group velocity dispersion parameter
ZDW	Zero-dispersion wavelength (ZDW)
TE	Transverse electric field
TM	Transverse magnetic field
$P(t)$	Polarization
$E(t)$	Electric field
$\chi^{(j)}$	jth-order susceptibility
XPM	cross-phase modulation
n_2	Nonlinear refractive index
I_0	Output intensity
I_i	Input intensity
α	Linear propagation loss
β_{TPA}	Two-photon absorption parameter
$N_c(t)$	Free carrier density
$\hbar$	Planck's constant
A_{eff}	Effective mode area
τ	Free carrier lifetime
ω_s	Frequency of Stokes wave
ω_a	Frequency of anti-Stokes wave
$R(t)$	Nonlinear response function
f_R	Fractional contribution of the delayed Raman response
g_R	Raman gain
Γ_R	Raman gain bandwidth
Ω_R	Raman frequency shift
$h_R(t)$	Raman response function
G	Gain coefficient
R	Reflectivity of mirrors
$\omega(\nu)$	Raman frequency shift
SFG	Sum frequency generation
THG	third-harmonic generation
Δk	Phase mismatch factor
Ω_s	Frequency shift between two waves
κ	Effective phase mismatch
θ	Phase

A	Pulse amplitude
σ	FCA cross section
μ	Free carrier dispersion
γ	Nonlinearity
$F(x,y)$	Field transverse field distribution
Z	Calculation distance
dz	Distance segment

Chapter 1

Introduction

1.1 Significance of nonlinear silicon photonics

The increasing costs and energy requirements of information technologies are driving the search for new platforms that can improve the capacity and efficiency of networks. A potential solution that has gained a lot of attention over past decades is silicon photonics as it offers the possibility to seamlessly link optical and electronic components in a best of both worlds' scenario due to its mature fabrication and compatibility with CMOS. Nowadays, silicon photonics has grown as a research field so much that it is also being applied over a wide range of areas such as communications, computing, medicine, biological or chemical sensing, and imaging.

Silicon photonics has been researched as the key technology in communication systems since the 1980s [27][28][29]. During the development stages of silicon photonics, it was established that some of the material characteristics of silicon can cause various challenges such as the lack of Pockels effect, owing to its centrosymmetric crystal structure, low absorption at the telecom wavelength range, or the indirect bandgap, but researchers have still made a significant progress, such as the breakthrough on modulators [30][31][32], photodetectors [33], amplifiers [34] etc. Nonlinear silicon photonics plays an important role in these significant leaps forward, especially in light amplification, wavelength conversion and so on, owing to the large third-order nonlinearity of silicon. The nature of nonlinear phenomena involves generating new frequency waves, which has been applied in signal processing in communication systems [35][36]. Compared with the traditional optical and electronic signal processing [37], passive device designs based on nonlinear effects are environmentally friendly, and their instantaneous response also conserves time. Additionally, its ability to produce multiple frequency outputs during laser buildup is noteworthy [38][2], which is in contrast to the typical semiconductor-based silicon laser [39].

Besides silicon, other classical materials for realizing nonlinearity include highly nonlinear fibres (HNLF) and III-V materials which has been widely applied in optical frequency generation (OFC) [40][41][42][43], computing [44], sensing [45][46], imaging [47][48] and more. HNLFs are known for their extremely low linear loss, approximately 0.1 dB/km [49], and mature fabrication techniques, enabling efficient nonlinear processes over propagation lengths of hundreds of meters, despite their low nonlinear refractive index of around $10^{-20}\,m^2/W$ [50]. On the other hand, III-V materials, with their high nonlinear refractive index of around $10^{-17}\,m^2/W$ [51] and large $\chi^{(2)}$ or $\chi^{(3)}$, has successfully demonstrated second harmonic generation (SHG) [52][53] and FWM [54][55][56]. However, the manufacturing process for devices based on III-V materials is typically multi-steps and complex [51]. Compared with conventional nonlinear platforms such as HNLF and III-V materials, silicon platforms possess distinct advantages in dispersion engineering. Advanced and compact manufacturing techniques ensure highly precise structural control, enabling efficient adjustment of dispersion profiles through waveguide dispersion. The design of wavelength-scale structures also enables the achievement of a small effective mode area and footprint to minimize the device size. Additionally, the significant distinction between the refractive index of the cladding and core materials results in tight light confinement, leading to high light intensity in the waveguide core, a crucial factor for the occurrence of nonlinearities.

Initially, research on nonlinear silicon photonics focused on the telecom band. For example, wavelength conversion around 1550 nm was exploited in SOI waveguides in the early 2000s [57][58]. However, a common problem in these studies is that the two-photon absorption (TPA) in silicon [59][23] is significant in the telecom band, which weakens the nonlinear effects. Accordingly, a feasible method to achieve stronger nonlinearities is by switching the pump wavelength over 2.2 μm, where TPA vanishes. As the development of mid-infrared laser sources has matured, the wavelength range of the nonlinear applications has begun to transfer from the telecom band to the mid-infrared band to avoid the TPA, enhancing the nonlinearities.

Light amplification based on nonlinear effects has been studied for many years. Compared with the conventional method that is utilising III-V semiconductor materials placed on top of silicon circuits [60][61][62], the obvious advantage of nonlinear silicon photonics is that no special integration techniques are needed, which increase the complexity during the fabrication process. Light amplification based on nonlinear effects can be mainly classified as two types, Raman amplification and parametric amplification.

1.1.1 Study on the Raman scattering

In contrast to other Raman crystals, silicon exhibits wide transparent windows up to 8 μm and a high thermal conductivity range, as well as a high damage threshold [63].The first observation of the light amplification based on Raman scattering in silicon waveguides occurred in 2003 [1] in the telecom band, as shown in Figure 1.1 (a) and (b), followed by a rapid development. Raman gain, reaching up to about 6 dB with a pulse pump and 0.7 dB with a continuous-wave (CW) pump source, has been observed based on stimulated Raman scattering (SRS) [64][65][66]. The Stokes output power generated by SRS is typically only in the order of micro-watts. A Raman laser was successfully investigated based on a silicon planar waveguide via applying p-i-n diode to remove the influence of TPA and free-carrier absorption (FCA) [2] in the telecom band, as illustrated in Figure 1.1 (c) and (d). The maximum output power of around 9 mW can be obtained with a pump power of 600 mW and a bias voltage of 25 V. The cascaded Raman laser emerges as a prosperous development [67].

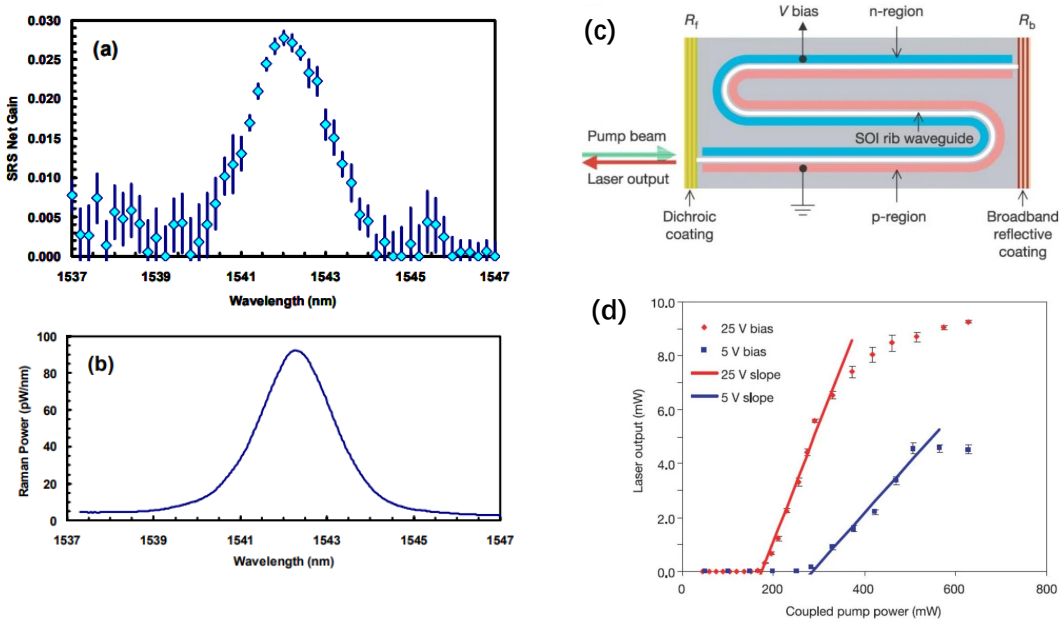

FIGURE 1.1: (a) Measured spectral characteristic of SRS in silicon waveguide; (b) Spontaneous Raman Spectra of the same waveguide with the same pump power as in (a) [1]. (c) Schematic layout of the silicon waveguide laser cavity with optical coatings applied to the facets and a p-i-n structure along the waveguide; (d) the pump wavelength is 1550 nm and the laser wavelength is 1686 nm. [2].

A light amplifier was reported in bulk silicon crystal with the gain reaching up to 12 dB at 3.39 μm [3], as depicted in Figure 1.2. while the feasibility of on-chip Raman laser has been theoretically validated [68][69][70], the fabrication of Raman laser in the mid-infrared band has not yet been successful in the experiments. Possible limitations for the Raman light source in the mid-infrared band include the three photon absorption (3PA) and induced FCA due to the high light intensity necessary for strong

Raman scattering [71]. The waveguide size increases with the operating wavelength, leading to the extension of the free carrier lifetime, resulting in surges of FCA. Moreover, the Raman gain is inversely proportional to λ^2, indicating that the Raman effect weakens compared to that in telecom band.

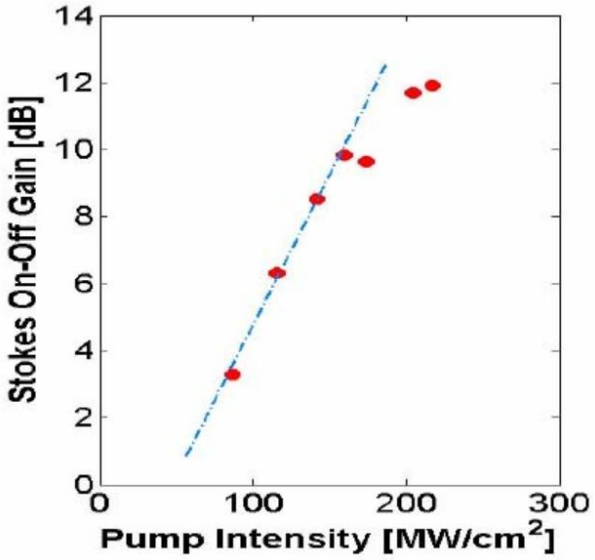

FIGURE 1.2: The plot of on-off Raman gain as a function of effective pump intensity interacting with the Stokes input. [3]

The novel Raman scattering, named inverse Raman scattering (IRS), is the optical loss induced by Raman scattering at the red-shifted (Stokes) wavelength and the blue-shifted (anti-Stokes) wavelength. Since first defined by W. J. Jones etc. in 1964 [72], this nonlinear phenomenon was observed with pulse pump at 1.55 μm [4], as shown in Figure 1.3, and applied to precisely estimate the Raman gain [73]. Apart from all-optical switches [74] and photonic differentiators [75] at 1.55 μm, the reported applications so far are still limited. To our knowledge, a significant characteristic of silicon-based Raman application is that the gain spectrum is narrow, $\sim$ 1.2 nm and the efficiency is relatively low. These features makes practical applications challenging.

1.1.2 Study on the FWM, supercontinuum generation and optical frequency comb

Unlike Raman amplification, parametric amplification based on four-wave mixing (FWM) has a broad and relatively flat gain spectrum when the phase-matching condition is satisfied. Successful parametric amplification has also been demonstrated in the telecom [5][6] (Figure 1.4 (a) and (b)) and mid-infrared bands [7][8] (Figure 1.4 (c) and (d)). However, the gain of the parametric amplification is determined by the FWM frequency conversion efficiency using CW laser source. Typically, the conversion efficiency is defined as the ration between the idler out put power and the

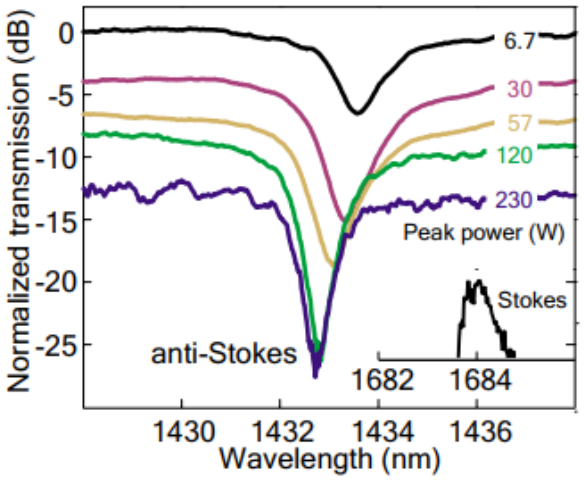

FIGURE 1.3: Experimental observation of IRS in silicon. [4]

signal input power, which evaluates the coupling efficiency between the signal and the generated idler. A conversion efficiency exceeding 0 dB indicates that more energy is transferred to the idler than to the signal, conversely, the FWM process is considered unsatisfactory. Without resorting to pulsed pump sources [76] or complex resonator geometries [77], the conversion efficiencies in these chip-based systems are typically very low (~ -30 dB), with the maximum value of ~ -10 dB [58] obtained for a waveguide with very precise dispersion engineering.

In the mid-infrared band, the conversion efficiency is up to ~ -18 dB, and the bandwidth exceeds 700 nm [9] via CW pump sources, as illustrated in Figure 1.5. By adopting femtosecond laser source, the peak conversion efficiency could be over 0 dB with the bandwidth over 260 nm both in the telecom and mid-infrared band. The performance of amplifiers based on nonlinear phenomena, especially the gain, is still limited, which needs more effort to be improved.

In addition, wavelength conversion can be exploited in a wide range of applications, such as supercontinuum generation (SCG), or optical frequency comb (OFC). The main nonlinear effects contributing to SCG (OFC) are self-phase modulation (SPM), cross-phase modulation (XPM), Raman scattering, FWM and modulation instability. Achieving sufficient and stable SCG or OFC relies on several key factors, including the phase-matching condition, dispersion profiles, nonlinear properties of the medium, and the power level of the incident waves. These factors collectively determine the parametric gain in sidebands, ultimately shaping the final spectrum of the SCG or OFC. In waveguide systems, the power level required to achieve similar parametric gain is conventionally much smaller than in bulk systems due to the tight mode confinement, resulting in higher nonlinear coefficients. Remarkable progress in SCG based on silicon waveguides is evident in the extension of the upper limit of the SCG/OFC wavelength from 2 μm [10][11] (Figure 1.6 (a) and (b)) to 4 μm [12][13]

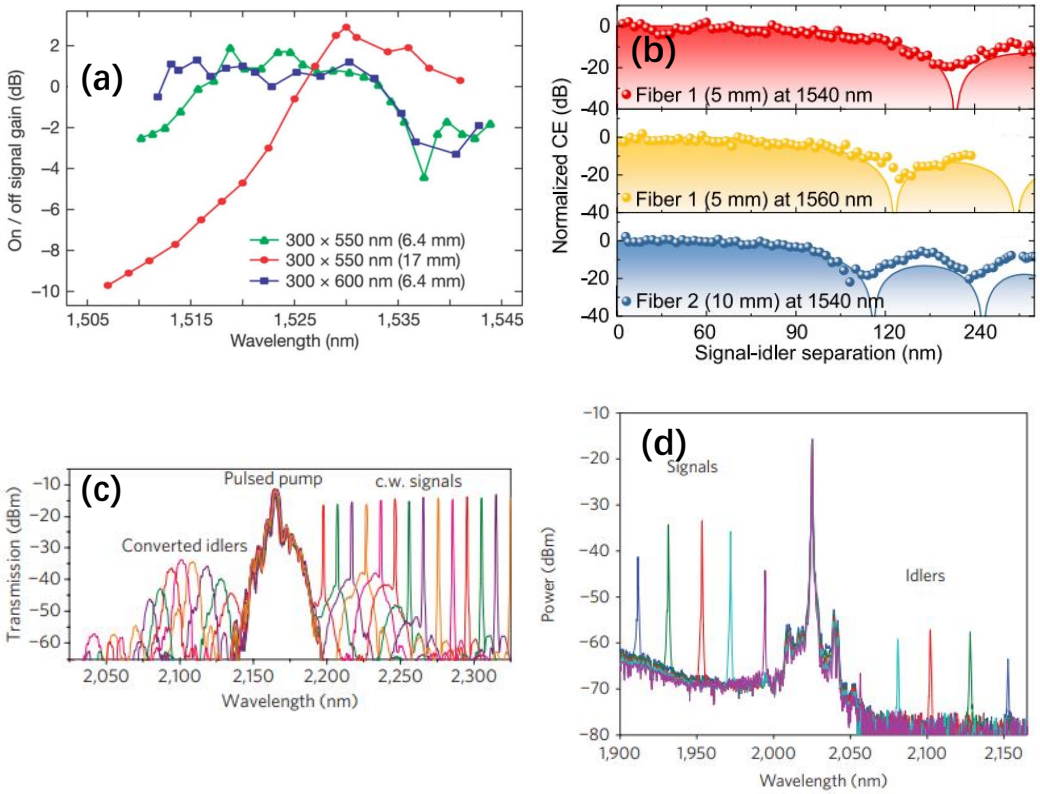

FIGURE 1.4: (a) Measured on/off signal gain as a function of signal wavelength for several waveguide cross-sectional areas and lengths. [5] (b) Measured FWM conversion efficiency (normalized) as a function of signal-idler wavelength separation for different tapered SCFs at selected pump wavelengths. [6] (c) Series of FWM spectra taken at the output of the 4-mm-long waveguide. [7] (d) Measured four-wave mixing spectrum across a range of 241 nm. [8]

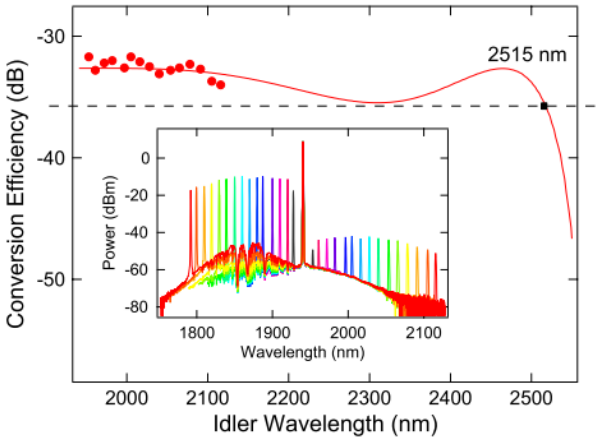

FIGURE 1.5: Theoretical (curve) and measured (dots) conversion efficiencies as functions of idler wavelength. The inset shows the measured FWM spectra. [9]

(Figure 1.6 (c) and (d)), showcasing the low nonlinear loss in the mid-infrared band. Furthermore, the remarkable oscillation threshold for boosting OFC is just around $\sim 3\,\mathrm{mW}$ with the implementation of a micro-resonator.

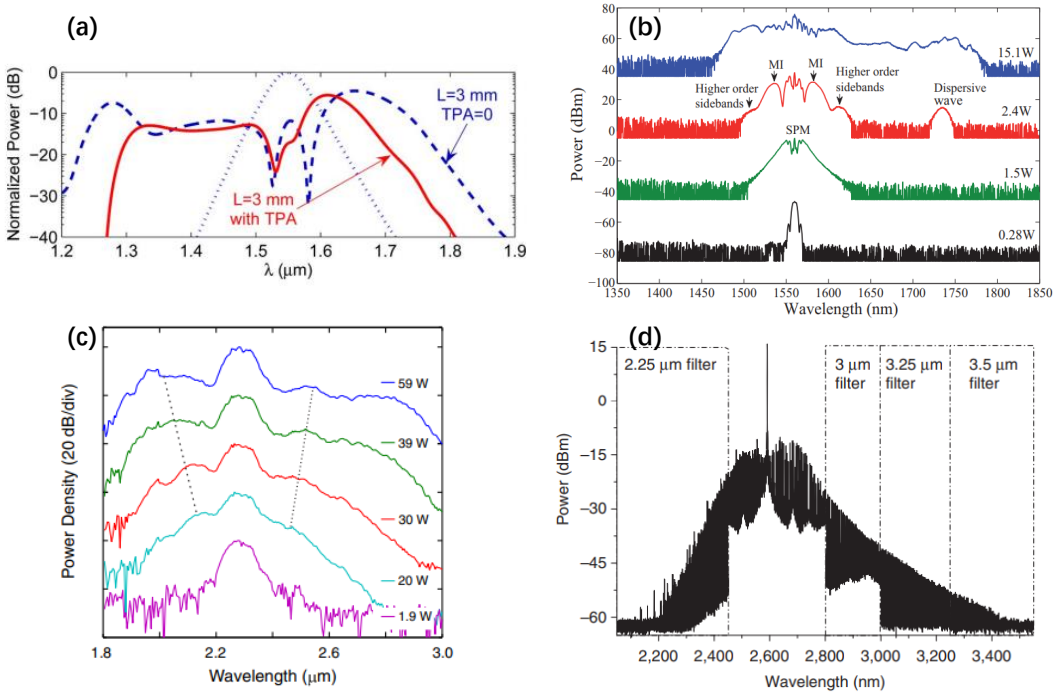

FIGURE 1.6: (a) Supercontinuum created in a 3-mm-long SOI waveguide. [10] (b) SC generation in a 1 cm long 500 × 220 nm^2 a-Si-H waveguide. [11] (c) Measured spectra for the powers. [12] (d) Broadband frequency comb generation from 2.1 to 3.5 μm in the etchless silicon micro-resonator. [13]

However, the absorption of silicon dioxide (SiO_2) above 4 μm limits the further extension of the SCG wavelength. The utilisation of suspended silicon waveguides [14] (Figure 1.7 (a)) and germanium (Ge) [15] (Figure 1.7 (b)) has extended the wavelength to 8 μm, overlapping the full transparent windows of silicon. Theoretical advancements in the application of suspended Ge has even broadened the wavelength to over 12 μm [78][79][80]. As the mid-infrared band covers large portions of molecules' absorption fingerprints, there is increasing interest in applications such as spectroscopy [81][82][83] based on nonlinear silicon photonics. Unfortunately, the average output power of SCG or OFC remains modest at the hundreds of micro-Watt level, primarily due to linear and nonlinear losses in the waveguides. Although the maximum output power to date has increased to 10 mW in SiGe waveguides [84], further exploration is needed for improvements in the silicon waveguide.

1.1.3 Study on the interaction between FWM and Raman scattering

Reviewing the development of nonlinear silicon photonics, Raman scattering and FWM play essential roles in applications such as light amplification and wavelength conversion. The limitations of Raman scattering include inherent low efficiency and a narrow gain band. Although a broad gain band could be obtained through FWM by dispersion engineering in silicon waveguides, idler gain, which is subject to the FWM

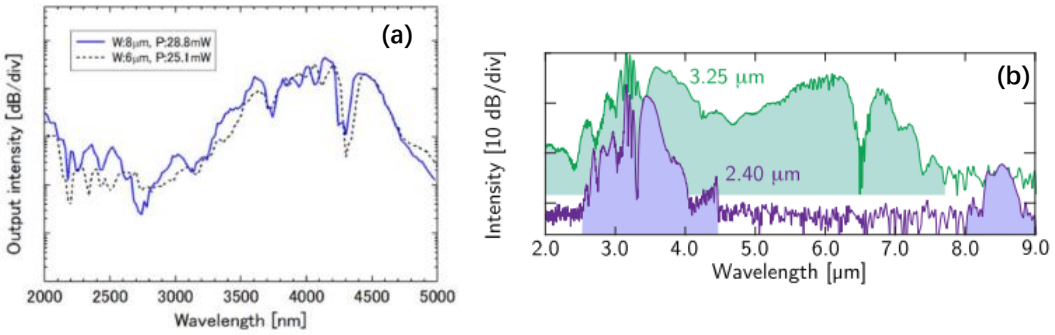

FIGURE 1.7: (a) Measured spectra with two different waveguide widths (W) of 6 and 8 μm. The input pumping powers were set to be over 25 mW. [14] (b) Individual spectra generated with 3.25 and 2.4 μm wide waveguides. [15]

conversion efficiency, remains modest. To realise the enhancement of the idler gain, previous studies on the interaction between Raman scattering and FWM has researched the gain variation under different light excitation modes and phase conditions. The detailed comparison among these results will be summarized in this section.

The research conducted by E. Lantz's team demonstrated the coherent Stokes Raman scattering (CSRS) [85] in a normally dispersive single-mode silica fibre under a special light excitation mode [16]. They verified that even in a non-phase-matched parametric frequency-conversion process, a relatively large gain enhancement of Stokes idler by mixing a strong pump with a weak anti-Stokes signal was possible. The Raman response induces an energy transfer from the signal to the pump, and the pump power required for the gain enhancement of the idler is minimised when the wavelength shift is equal to the Raman shift, as Figure 1.8 shows. The Stokes idler is firstly generated through the FWM and then continually amplified by the Raman gain. Their work, based on silica fibres, explored influences of Raman scattering on FWM in detail, nevertheless, relatively little investigations of the coupling between Raman scattering and FWM in silicon has been done.

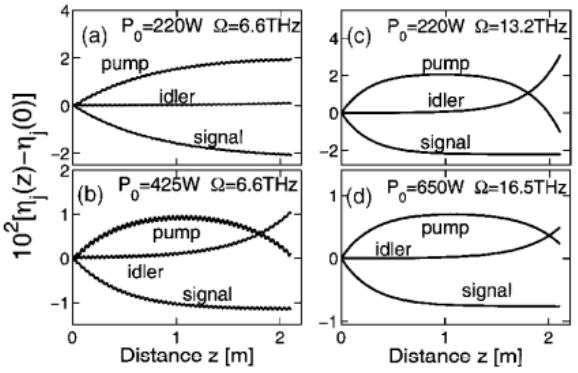

FIGURE 1.8: Variation of normalized powers versus propagation coordinate in the presence of Raman effects. [16]

Early studies on silicon were about the suppression of Raman scattering [86] due to the efficiency of the parametric process. The strong Stokes wave is generated from stimulated Raman scattering (SRS), and the anti-Stokes wave is absent when phase matching is poor between the pump wave, Stokes wave and anti-Stokes wave in the parametric process. Parametric suppression of the Raman gain occurs when the phase matching condition is satisfied among these three waves. The Stokes wave from SRS is weakened, and the anti-Stokes wave occurs due to parametric interaction, then disappears when SRS saturates. In this case, there is only pump wave, and the initial Stokes/anti-Stokes wave intensities are equivalent to the noise level. Furthermore, when a signal is seeded at the Stokes wavelength [87], the gain of Stokes wave experiences a decrease when the linear phase mismatch is close to zero due to parametric gain suppression. In this theoretical analysis, an appropriate linear phase mismatch could motivate the coherent anti-Stokes Raman scattering (CARS) which converts Stokes photons into anti-Stokes photons, resulting in the decrease in Stokes gain to a certain extent [88]. As of the present date, the conversion efficiencies obtained via this process using CW pump sources have been limited. For example, the largest reported conversion of ~ -50 dB required a pump of 700 mW due to the strong phase mismatch [17], as Figure 1.9 depicts. Nevertheless, when the inverse process of CARS occurs as a result of the phase mismatch induced by the pump depletion, converting anti-Stokes photons into Stokes photons, the Stokes gain increases and level out eventually.

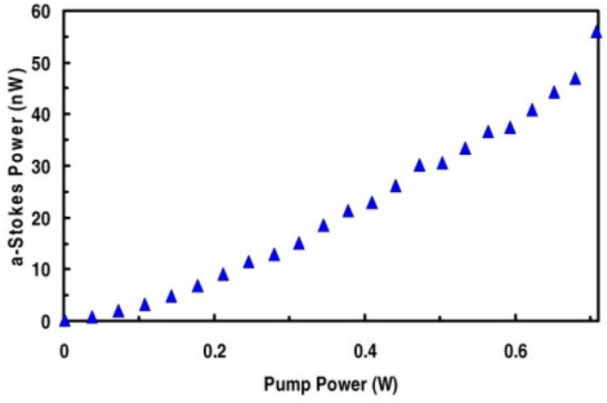

FIGURE 1.9: Maximum amount of a-Stokes signal obtained, at 1328.8 nm. [17]

The majority of existing research on the interaction between FWM and Raman scattering in silicon has been focused on CARS. The enhancement of the Stokes wave, CSRS, as a result of mixing these two nonlinear phenomena has not been studied in-depth, except for the early study based on silica fibres. Nevertheless, this phenomenon holds potential for applications which require strong Stokes wave, for example, Kerr and Raman frequency combs [18][19] as Figure 1.10 shows. The frequency comb band could be broadened by a sub-comb generated at longer wavelengths by the enhanced Stokes light, serving as a new light source. Higher-order

Stokes scattering supports sub-combs at an even longer wavelength region, which is a possible approach to generate a mid-infrared comb with an infrared input pump.

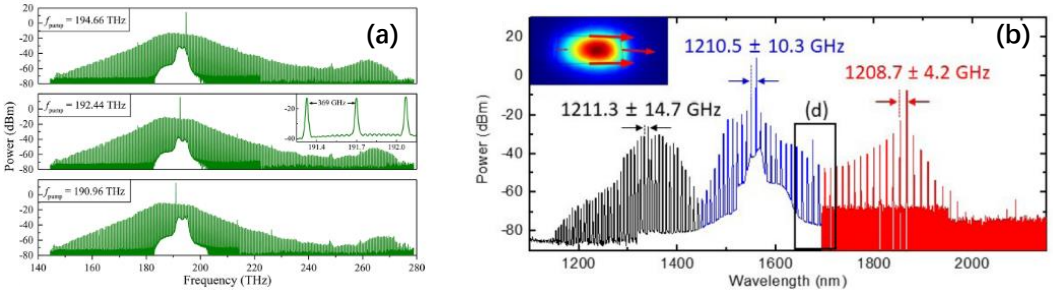

FIGURE 1.10: (a) Primary comb lines generated by a 60-μm-radius AlN chip. [18] (b) Raman-assisted broadband comb spectrum from an AlN microring at TE mode input. Inset shows the TE mode profile at 1.55 μm wavelength. [19]

1.2 Motivation

The low conversion efficiency of individual nonlinear effects, such as Raman scattering or FWM, has motivated researchers to study the interaction between these two nonlinear phenomena. Some research groups have investigated FWM with CARS in recent years, confirming that FWM can be excited by CARS under phase mismatch conditions. However, this research has focused on shorter wavelengths with low conversion efficiencies. Meanwhile, given that the gain efficiency of Raman scattering is higher at the Stokes wavelength compared to the anti-Stokes, higher gains should be possible using CSRS process. The enhancement of the Stokes wave supported by CSRS has had limited demonstrations in previous studies. According to the study based on silica fibres, the presence of Raman scattering can enhance the Stokes wave even in poor phase matching conditions. This indicates the possibility of strengthening the Stokes wave with CSRS, offering a meaningful direction for applications in light amplification and light sources. On the other hand, the high conversion efficiency produced by CSRS, which is beneficial for obtaining high-quality signal processing, could be achieved.

1.3 Overview

During my four-year PhD study, the COVID-19 pandemic had a significant impact on my research, especially in the first two years. The pandemic began six months after the start of my study, coinciding with a long-term lockdown in the UK. During this time, I was limited to literature reading and simulations as access to the laboratory was restricted. Even after the laboratory reopened, there were strict limitations on the number of people allowed inside at one time. Additionally, the maintenance cycles of

essential machines, such as the DUV scanner, E-Beam, and polishing machine, were unexpectedly extended, resulting in a considerable delay in sample production. While the worldwide pandemic initially slowed down the progress of my project, the granted extension of my study allowed me to complete my research within an acceptable timeframe.

This thesis focuses on nonlinear wavelength conversion and amplification in silicon, primarily through FWM and its enhancement via Raman effects. In Chapter 2, theories about waveguide structures, dispersion, loss and nonlinear optics in silicon are briefly described. The MATLAB code for the following simulations, based on the nonlinear Schrödinger equation (NLSE) including the delayed Raman response, is validated at the end of the chapter.

The collaborative work in Chapter 3 involves the exploration of Raman scattering in both the telecom and mid-infrared bands as well as the FWM and CARS in the mid-infrared band in silicon core fibres (SCF). In this work, I took responsibility for all simulation aspects, collaborating with Meng Huang and Dong Wu, who conducted the experiments. The experiments demonstrated considerable Raman gain, consistent with the simulation results. Simulations were also conducted to predict the possibility of cascaded Raman generation in the mid-infrared band. In the subsequent research on CSRS, I undertook all simulations and major experiments.

In Chapter 4, CSRS in SCFs is demonstrated in both the telecom and mid-infrared bands. The dispersion properties for SCFs with varying core diameters are studied. Experimental data are analysed and compared with the simulation results. Further simulations are conducted to predict the proper length and appropriate pump power of the SCF to achieve the highest nonlinear gain and output power.

In Chapter 5, the similarities and differences, advantages and disadvantages between SCF and planar waveguides are illustrated firstly. The structure design parameters are calculated for rib waveguides in both telecom and mid-infrared wavelength ranges to achieve optimised nonlinear performance. Experimental data are collected to validate the predictions of simulations. Finally, the stability of the Raman enhancement is researched to analyse the influence of various parameters on the nonlinear performance.

In Chapter 6, the dispersion properties of a slotted waveguide are compared between different structural parameters. The optimised structural parameters to achieve a flat and low dispersion profile are summarized. The higher-order Stokes Raman scattering obtained through the optimised structure is simulated. The measured loss of the fabricated slotted waveguides is concluded to discuss the design limitations.

In Chapter 7, waveguide fabrications are illustrated for both SCFs and planar waveguides. The tapering processes and fixing methods for SCFs are introduced in

detail. For planar waveguides, the coupling efficiency between different structures has been optimised and the layout design is explained in detail.

Chapter 8 provides a summary to conclude the main achievements in this thesis, and proposes promising directions for the future development based on the existing results.

Chapter 2

Background

This chapter outlines the basic theory of silicon photonics which is relevant to this work. It includes discussions on the waveguide type, dispersion in silicon waveguides, as well as loss and nonlinearities in silicon. The main nonlinear effects are introduced in detail, including Raman scattering, FWM, and the interaction between Raman scattering and FWM. Finally, the mathematical description of nonlinear propagation, nonlinear Schrödinger equation (NLSE), in silicon is presented with some typical examples such as dispersion and self-phase modulation (SPM). The validation of the code to slove NLSE is conducted by the comparison of simulation results with the existing results recorded in the literature.

2.1 Waveguide structures

There are two main types of waveguide structures investigated in this report: planar waveguides and optical fibres. Planar waveguides are usually classified into three main structures: slab, strip and rib waveguides. Details of each structure are depicted in Figure 2.1. Planar waveguides have a significant advantage in dispersion engineering through multi-dimensional structural changes, especially rib waveguides. Compared with the planar waveguides, fibres have advantages in optical fibre integration. Different waveguide types are selected according to the actual requirements.

The general property of a waveguide is that the material with a high refractive index (n_{core}) is surrounded by a material with a lower refractive index (n_{clad}) to produce strong light confinement. Strong optical confinement can dramatically decrease dimensions of the device. On the other hand, high refractive index cores result in coupling difficulties due to high Fresnel reflections and optical mode mismatch between optical fibres and waveguides. Some groups have adopted special coupling

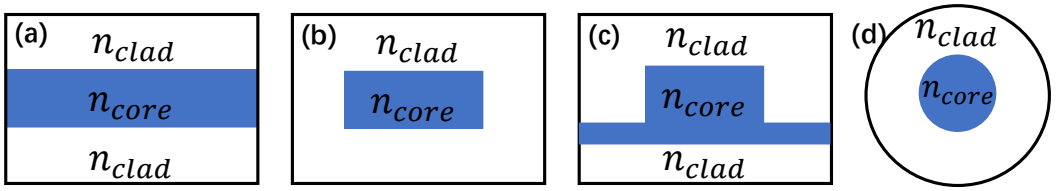

FIGURE 2.1: Waveguide structures: (a) slab waveguide, (b) strip waveguide, (c) rib waveguide, (d) fibre.

structures [15][89][90] such as grating couplers to increase the coupling efficiency. Most special couplers are designed for a specific working wavelength, which contradicts the nonlinear effects involving multiple frequencies, and bulk coupling is still the main method to achieve light coupling in this work.

Waveguide modes are a series of guided modes whose spatial field distribution does not change with propagation in the absence of loss. They can be characterised by the effective refractive index (n_{eff}), which is determined by the waveguide design. This parameter indicates the confinement of the mode. n_{eff} was calculated in COMSOL using mode analysis in the electromagnetic waves module. This module solves Maxwell's equations while setting the boundary condition of perfect magnetic conductors. For accuracy, a fine physics-controlled mesh was chosen. Taking the transverse electric (TE) mode in x-y plane calculated by COMSOL in a strip waveguide as an example, the difference between fundamental mode and higher-order modes are illustrated. When $n_{eff} \sim n_{core}$, this mode is tightly confined in the waveguide core as Figure 2.2 (a) shows. When $n_{clad} < n_{eff} < n_{core}$, this mode is also a guided mode, but its field is partially distributed in the cladding as Figure 2.2 (b) shows. When $n_{eff} \sim n_{clad}$, this mode is weakly guided in the waveguide as Figure 2.2 (c) shows.

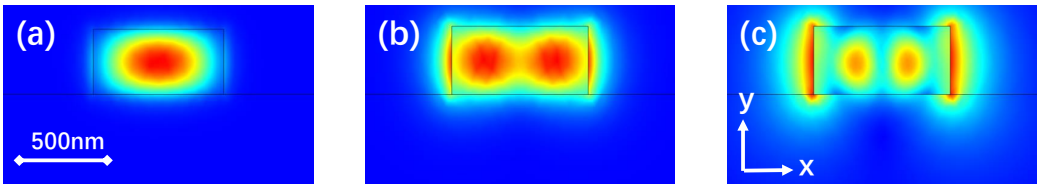

FIGURE 2.2: Modes in a strip waveguide, silicon (Si) in the rectangular is surrounded by silicon dioxide (SiO_2): (a) propagation mode,$n_{eff} \sim n_{core}$; (b) propagation mode, $n_{clad} < n_{eff} < n_{core}$; (c) leaky mode, $n_{eff} \sim n_{clad}$.

2.2 Subwavelength grating structures

Subwavelength grating (SWG) that can be applied as a material with the designed refractive index for dispersion engineering is the subwavelength periodic structures as Figure 2.3 illustrates. For example, it consists of rectangular silicon blocks spaced at a pitch Λ with the air top cladding and SiO_2 bottom cladding. This structure provides a

precise control of the refractive index of the equivalent material through adjusting the length of silicon blocks (L) and the duty cycle (DC=L/Λ). When the SWG is modeled as a homogeneous isotropic metamaterial, the equivalent refractive index (n) can be approximated by Rytov's formulas [91]:

$$n_{\parallel} \sim [DC \cdot n_{Si}^2 + (1 - DC) \cdot n_{air}^2]^{1/2}, n_{\perp} \sim [DC \cdot n_{si}^{-2} + (1 - DC) \cdot n_{air}^{-2}]^2, \tag{2.1}$$

Where $n_{\parallel}$ is the equivalent refractive index when the propagation is along y axis (electric field is parallel to the periodic structure); $n_{\perp}$ is the equivalent refractive index when the propagation is along x axis (electric field is perpendicular to the periodic structure). In this project, $n_{\parallel}$ is the necessary parameter which determines the proper DC value. This periodic structure operates in the subwavelength regimes when the ratio of the wavelength and the pitch is high enough. In other words, the effective index of the Bloch-Floquet mode (n_B) drops below the Bragg threshold [92]:

$$n_B < \frac{1}{2}\frac{\lambda}{\Lambda}. \tag{2.2}$$

Reflection and diffraction in the SWG is suppressed and there is no extra loss caused by SWG during the wave propagation. During the simulation of a waveguide containing SWGs, the SWG section could be treated as a strip waveguide with the equivalent refractive index to simplify the waveguide construction.

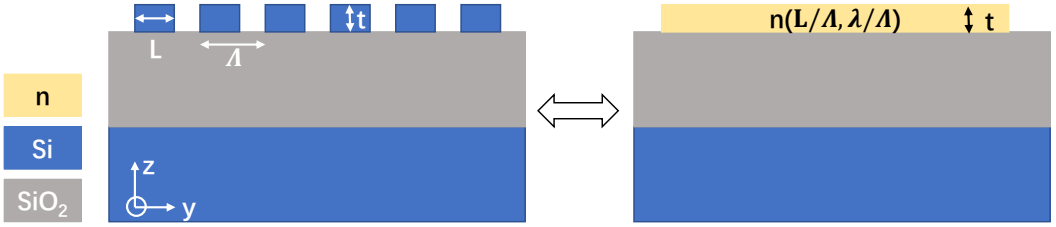

FIGURE 2.3: The SWG structure and its equivalent structure in the simulation.

2.3 Dispersion

Dispersion is a phenomenon that results from the frequency-dependent refractive index ($n(\omega)$). It is critical in the propagation of short optical pulses, which consist of a band of wavelengths, even in linear optics because it can cause pulse spreading. In nonlinear optics, the dispersion effects can be described by the mode-propagation constant β expanded in a Taylor series about the central frequency ω_0 of the incident pulse [24]:

$$\beta(\omega) = n(\omega)\frac{\omega}{c} = \beta_0 + \beta_1(\omega - \omega_0) + \frac{1}{2}\beta_2(\omega - \omega_0)^2 + \cdots, \tag{2.3}$$

where

$$\beta_m = (\frac{d^m\beta}{d\omega^m})_{\omega=\omega_0} \ (m = 0, 1, 2, \cdots). \tag{2.4}$$

The parameters β_1 and β_2 are related to the refractive index $n(\omega)$ and their derivatives through the following relations:

$$\beta_1 = \frac{1}{v_g} = \frac{n_g}{c} = \frac{1}{c}(n + \omega\frac{dn}{d\omega}), \ \beta_2 = \frac{1}{c}(2\frac{dn}{d\omega} + \omega\frac{d^2n}{d\omega^2}), \tag{2.5}$$

where n_g is the group index, and v_g is the group velocity. In a waveguide structure, when the incident wave is a short pulse, the pulse envelope propagates at the group velocity. β_2 represents the dispersion of the group velocity and is the main influencing factor of pulse broadening. The higher-order dispersive terms need to be considered in SCG for calculation precision because the wavelength range is very broad. The group velocity dispersion parameter (D) used in practice can be derived from β_2 as:

$$D = -\frac{2\pi c}{\lambda^2}\beta_2. \tag{2.6}$$

A noteworthy point is that D vanishes and changes sign at the zero-dispersion wavelength (ZDW), the position of which is controlled by a combination of the material and waveguide dispersion through changing the structure of the waveguide as shown in Figure 2.4 [20]. Figure 2.4 (a) and (b) shows that the dispersion curves especially the position of ZDW can be adjusted by changing the fundamental structural parameters such as the ring width. Additionally, Figure 2.4 (c) and (d) indicates that the re-shape of the waveguide even can precisely control the slope between ZDWs. The advantage of planar waveguides is that the dispersion curve can be controlled by the structure design in multi dimensions, and its fabrication process is easily controlled as well as the fabrication precision compared with SCFs, which will be demonstrated in the section of the waveguide fabrication. In parametric processes, achieving phase matching conditions is crucial for efficient wavelength conversion as shown in Figure 2.5 [21]. In Figure 2.5 (b), adjusting the dispersion profiles ensures that the ZDW aligns with the designed pump wavelength of 1.55 μm.

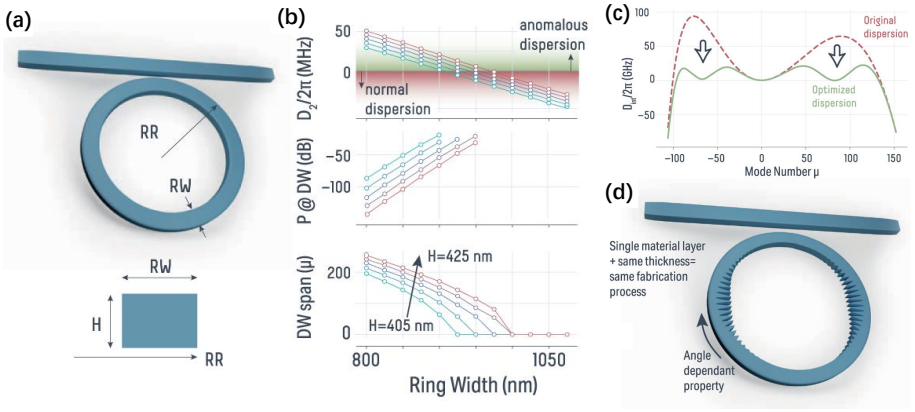

FIGURE 2.4: (a) Standard microring resonator where three parameters are available for dispersion engineering, ring radius (RR), ring width (RW) and material thickness (H). (b) Variation of second-order dispersion (D_2), power in the dispersive waves (DW), and separation between the two potential DW locations (in units of mode number) as a function of ring width. (c) The frequency splittings modify dispersion, resulting in a higher dispersion branch and a lower dispersion branch (shown in green). (d) The resulting ring resonator has a ring width modulation profile. [20]

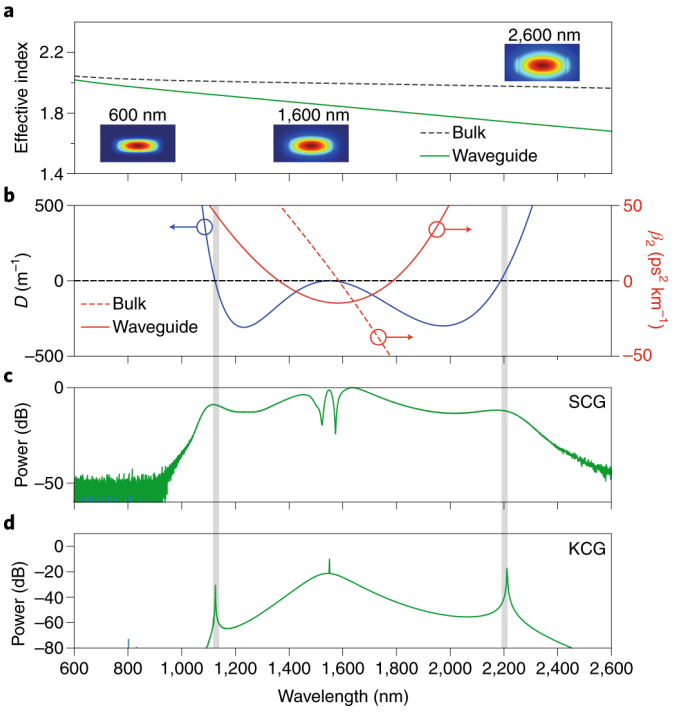

FIGURE 2.5: (a) Effective index for bulk Si_3N_4 (dashed line) and that predicted for a 730×2580 nm Si_3N_4 waveguide with oxide cladding (solid green). (b) Corresponding β_2 of bulk Si_3N_4 (dashed red) and waveguide (solid red) and dispersion function (D) (solid blue). Spectra produced via SCG in the 5-cm-long waveguide (c) and via Kerr-comb generation (KCG) in a micro-resonator (d), both with waveguide cross-sections as in (a). [21]

Moreover, maintaining a flat slope between ZDWs is beneficial for achieving broadband parametric conversion, as depicted in Figure 2.5 (c) and (d).

2.4 Nonlinear optics in silicon

The nonlinearity in silicon is the interaction of the optical field with electrons and photons in the material. It can be described by the relation between the induced polarization ($P(t)$) and the electric field ($E(t)$) in its simplest form [24]:

$$P(t) = \epsilon_0(\chi^{(1)}E(t) + \chi^{(2)}E(t)^2 + \chi^{(3)}E(t)^3 + \cdots), \tag{2.7}$$

where ϵ_0 is the vacuum permittivity and $\chi^{(j)}$ is the jth-order susceptibility. $\chi^{(1)}$ is the linear susceptibility which is the dominant factor to $P(t)$ when the incident wave power is low. With the incident wave power increasing, the nonlinear terms become competitive with the linear term and cannot be ignored. In centrosymmetric crystal structures such as silicon, the second-order susceptibility $\chi^{(2)}$ is absent. In silicon, the most important nonlinearity is the third-order nonlinearity. It generates various nonlinear phenomena such as SPM, cross-phase modulation (XPM), FWM, SRS and so on. Most of the nonlinear processes originate from nonlinear refraction, which is the intensity dependence of the refractive index. The refractive index can be given by [24]:

$$\tilde{n}(\omega, I) = n(\omega) + n_2 I, \;\; n_2 = \frac{3}{8n} Re(\chi^{(3)}), \tag{2.8}$$

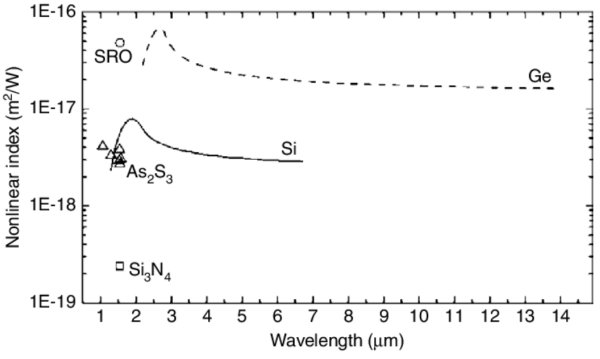

FIGURE 2.6: The nonlinear refractive index values of the considered materials in near- and mid-infrared bands. [22]

where $n(\omega)$ is the linear refractive index, n_2 is the nonlinear-index coefficient related to $\chi^{(3)}$ which changes with the wavelength as Figure 2.6 shows, I is the optical intensity. There is a maximum value of n_2 in silicon around 2 μm, which means that the choice of the nonlinear operation wavelength should be around this peak to ensure relatively larger nonlinear refractive index. Furthermore, the strength of the nonlinear effect depends on the nonlinear loss in addition to the linear refractive

index, which varies with wavelength. The nonlinear losses induced by high input powers will be explained in detail in the next section.

2.5 Linear and nonlinear losses

When the incident wave propagates through a waveguide, both linear and nonlinear losses need to be taken into consideration. The linear loss is also considered as the propagation loss and the main contributions to the linear loss include scattering, absorption and radiation. The linear loss can be evaluated by the cut-back method, using a transmission experiment with low input optical power. The output intensity (I_o) with a certain linear loss can be expressed in this simple form:

$$I_o = I_i \exp(-\alpha L), \tag{2.9}$$

where I_i is the input intensity, α is the loss coefficient, L is the propagation length. Under different lengths (L_1, L_2), α can be derived from the ratio of the corresponding output intensities (I_1, I_2):

$$\frac{I_1}{I_2} = \exp(-\alpha(L_1 - L_2)) \Longrightarrow \alpha = \frac{1}{L_1 - L_2} \ln \frac{I_1}{I_2}. \tag{2.10}$$

The nonlinear loss includes multiphoton absorption and FCA. The multiphoton absorption is the absorption of multiple photons in order to excite an atom/molecule from the ground state to an excited electric state. The energy difference between the involved lower and upper states of the molecule is less than or equal to the sum of the photon energies of the absorbed photons as Figure 2.7 illustrates. The multiphoton absorption coefficient, represented by the two-photon absorption (β_{TPA}), varies across different wavelength bands, as depicted in Figure 2.8. The multiphoton absorption can induce free carriers, which results in intraband absorption between different excited states that is simply depicted in Figure 2.7. When the wavelength is under 2.2 μm, TPA is obvious and can prohibit the development of FWM or other nonlinear effects. Above 2.2 μm, multi-photon absorption such as 3PA appears and this, as well as FCA, is the main nonlinear loss at longer wavelengths. The effective ways to minimize the nonlinear losses are changing the pump wavelength for reducing multiphoton absorption and reducing the free carrier lifetime for reducing FCA [93][94][95]. The operation wavelength in this work is focused on the telecom band and mid-infrared band below 2.2 μm, hence, here we just take the TPA coefficient

(β_{TPA}) into consideration. The free carrier density ($N_c(t)$) is governed by the following equation [93]:

$$\frac{\partial N_c(t)}{\partial t} = \frac{\beta_{TPA}}{2\hbar\omega_0}\frac{|E(t)|^4}{A_{eff}^2} - \frac{N_c(t)}{\tau}, \tag{2.11}$$

where $\hbar$ is Planck's constant, A_{eff} is the effective mode area, $E(t)$ is the electric field envelope, ω_0 is the central frequency of the incident wave, and τ is the free carrier lifetime.

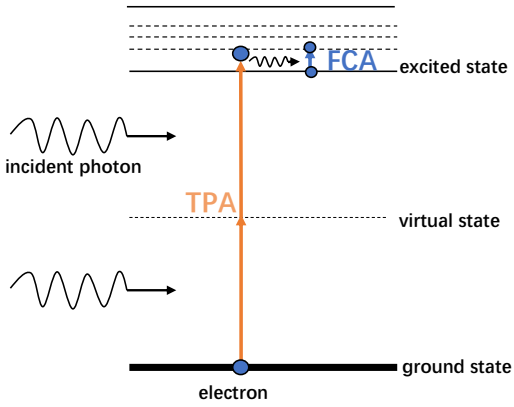

FIGURE 2.7: The energy level diagram of TPA and FCA.

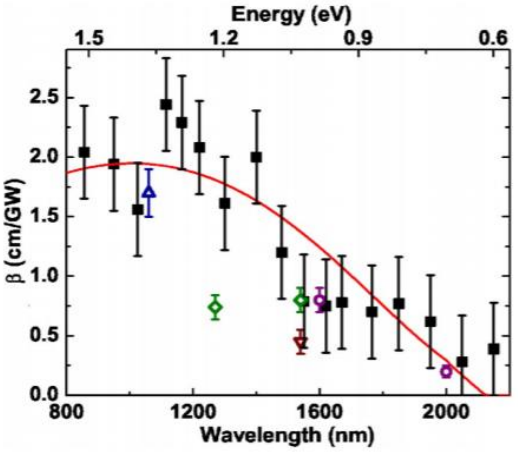

FIGURE 2.8: The values of β_{TPA} in silicon. [23]

2.6 Raman scattering

Raman scattering is the inelastic scattering of photons by matter, meaning that there is an exchange of energy and a change in the light direction. This involves vibrational energy being gained or consumed by a molecule as incident photons are shifted to lower or higher frequencies. Raman scattering is observed in all types of materials including solids, gases and liquids. The Raman frequency shift depends on the frequency of the intramolecular motion of the material. Thus, the Raman frequency shift can be considered as an intrinsic material property, and what the material is can be checked by testing the Raman frequency shift. This means that Raman scattering can be used in spectroscopy. The scattered wave with lower frequency (ω_s) is called the Stokes wave, while the scattered wave with higher frequency (ω_a) is named as the anti-Stokes wave. The energy level diagrams of Raman scattering are illustrated in Figure 2.9. An incident photon with frequency ω_p is annihilated and a photon with frequency ω_s (or ω_a) is created, leaving the molecule in an excited state (or ground state) with energy $\hbar\omega_v$.

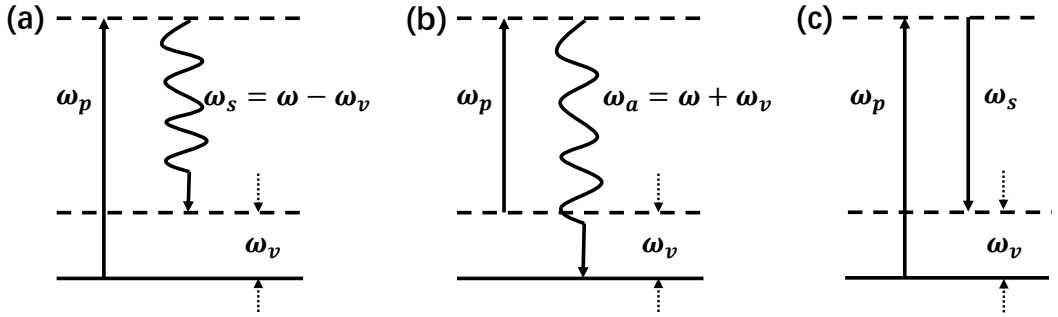

FIGURE 2.9: Energy level diagrams of Raman scattering. (a) The Stokes-shifted Raman scattering. (b) The anti-Stokes-shifted Raman scattering. (c) The stimulated Raman scattering. The angular frequencies ω_p, ω_s, ω_a and ω_v correspond to the pump, Stokes waves, anti-Stokes waves and Raman shift, respectively.

The delayed Raman response is governed by the nonlinear response function $R(t)$ [24] as:

$$R(t) = (1 - f_R)\delta(t) + f_R h_R(t), \tag{2.12}$$

where $f_R = g_R \Gamma_R / (n_2 k_0 \Omega_R)$ (for silicon, $f_R = 0.043$) represents the fractional contribution of the delayed Raman response to the nonlinear polarization in which g_R is the Raman gain, Γ_R / π is the gain bandwidth, $\Omega_R / 2\pi$ is the peak gain frequency shift; $h_R(t) = (\tau_1^{-2} + \tau_2^{-2})\tau_1 \exp(-t/\tau_2) \sin(t/\tau_1)$ is a good approximation to the Raman response function, where for silicon $\tau_1 \approx 10\ fs$, $\tau_2 \approx 3\ ps$, and h_R for silicon, represented in both time and frequency domains, is depicted in Figure 2.10. τ_1 and τ_2 are two adjustable parameters and are chosen to provide a good fit with the actual Raman gain spectrum.

The difference between spontaneous Raman scattering and SRS is similar to that between the spontaneous emission and the stimulated emission in a laser system. When the incident pump intensity is lower than a certain threshold, which means that the occupation number of the Stokes mode is much less than unity, only the weak spontaneous Raman scattering signal appears. However, when the input pump intensity increases over the threshold, which means that many photons are in the Stokes mode, a strong and directional coherent scattering signal can be observed, which is SRS. The threshold condition of stimulated scattering can be written as [85]:

$$e^{(G-\alpha)L} \cdot R \geq 1, \tag{2.13}$$

where G ($\propto I_0$, I_0 is the input light intensity) is the gain coefficient, α is the overall attenuation of the material, L is the gain length, and R is the reflectivity of the mirrors

in the cavity. R is neglected in a single-pass amplified stimulated scattering, the threshold requirement is transferred to:

$$e^{(G-\alpha)L} \gg 1. \tag{2.14}$$

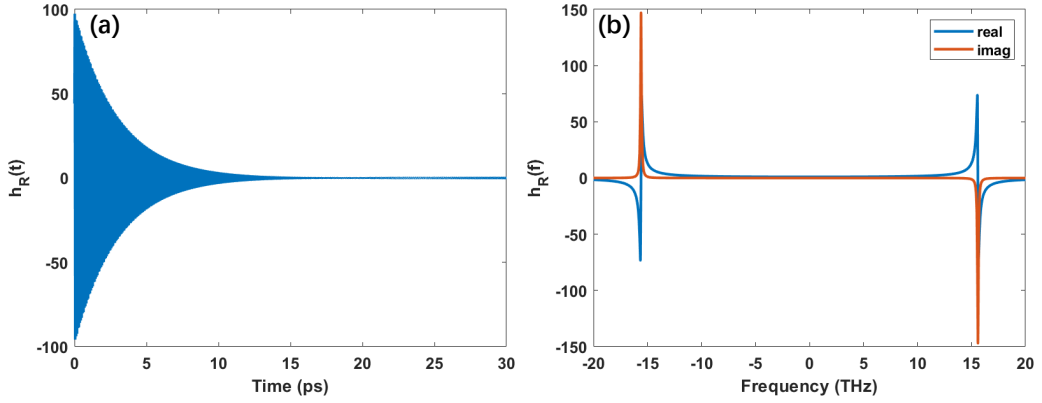

FIGURE 2.10: The Raman response function for silicon in time (a) and frequency domain (b).

The pump wave-induced change of the physical status of the material is essential to the stimulated process but can be neglected in the spontaneous process. The energy level diagram of the SRS is depicted in Figure 2.9 (c). The molecular vibration initially modulates the refractive index of the material to produce Stokes wave and anti-Stokes wave, then the Stokes wave beats with the pump wave to produce a modulation of the total intensity. This modulated intensity coherently excites the molecular oscillation at frequency ω_v. These two processes reinforce each other, which leads to a strong Stokes signal.

2.7 Inverse Raman scattering

Raman scattering discussed above produces optical gain at Stokes and anti-Stokes frequencies as shown in Figure 2.11, but it can also produce optical loss of the Stokes and anti-Stokes waves [72]. This phenomenon is named as the inverse Raman scattering (IRS). As Figure 2.11 (b) illustrates, the process of IRS is that a photon at the peak of the Raman frequency shift is consumed and a photon at the pump frequency is generated, which is opposite to the Raman gain that is depicted in Figure 2.11 (a). Normally the spontaneous Raman scattering happens with an intense pump, radiating a small amount of the Stokes wave and much weaker anti-Stokes wave. However, when adding weak input waves at the Stokes and anti-Stokes frequencies, the variations of the input waves are totally different. The input Stokes wave

experiences an amplification through SRS. The consumption rising from IRS could be ignored and is difficult to be observed in the experiments due to the high gain of the SRS. Instead, if the input is placed at the anti-Stokes position, it suffers depletion through IRS and the pump receives the supplement from the anti-Stokes waves. In experiments, IRS is difficult to be tracked due to CARS which realise the energy transfer between Stokes and anti-Stokes waves.

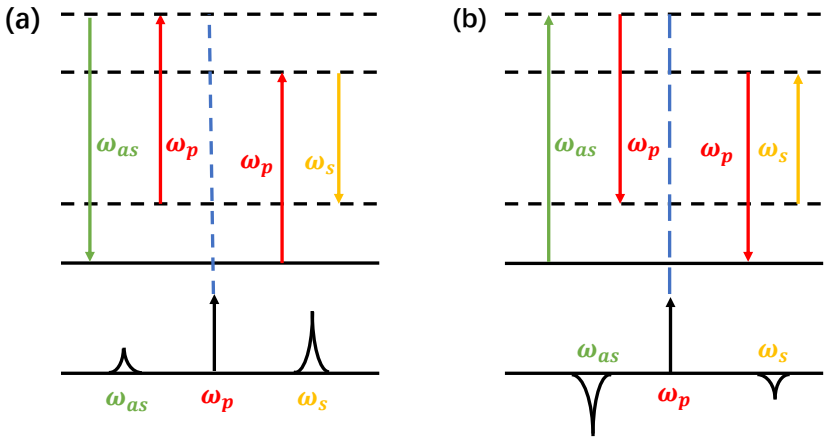

FIGURE 2.11: The differences of the energy diagrams (above) and spectra (below) between the Raman scattering (a) and the inverse Raman scattering (b). The angular frequencies ω_p, ω_s and ω_a correspond to the pump, Stokes waves and anti-Stokes waves.

2.8 Four-wave mixing

Four-wave mixing is a third-order nonlinear optical phenomenon, which includes processes such as sum frequency generation (SFG), third-harmonic generation (THG) and four-photon parametric interaction. The energy level diagrams of these three processes are depicted in Figure 2.12. Figure 2.12 (a) shows the SFG. Three electromagnetic waves of different frequencies, ω_1, ω_2, ω_3, interact with the nonlinear medium and generate a new signal at the sum frequency. The annihilation of the photons of frequencies ω_1, ω_2 and ω_3 induce the molecule excitation from the ground state to an intermediated state. Then the molecule returns to the ground state, meanwhile, a new photon with the sum-frequency ω_4 is generated. The time that the molecule spends in each intermediated state is extremely short, so these steps can be considered happening simultaneously. The other two processes can be understood in a similar way to SFG.

As the physical states of the molecule at the start and end of the FWM process are unchanged, conservation of energy and momentum should be obeyed between the annihilated photons and the created photon(s). The four-photon parametric interaction is considered here as a general circumstance, in which the degenerate

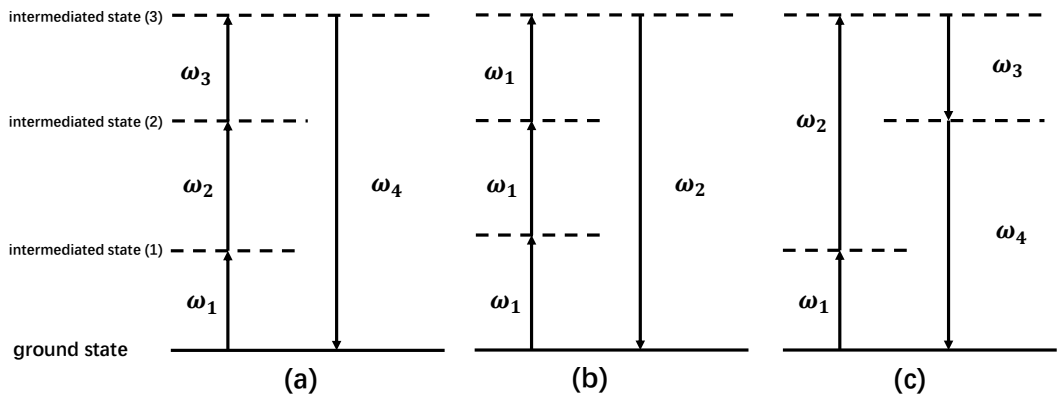

FIGURE 2.12: FWM process. (a) Sum frequency generation. (b) Third-harmonic generation. (c) Four-photon parametric interaction. The angular frequencies ω_1, ω_2, ω_3 and ω_4 correspond to different waves.

FWM is the special case ($\omega_1 = \omega_2$) applied in this work. Thus, the essential energy conservation and phase-matching conditions in FWM are:

$$\begin{aligned} \omega_3 + \omega_4 &= \omega_1 + \omega_2, \\ \boldsymbol{k_3} + \boldsymbol{k_4} &= \boldsymbol{k_1} + \boldsymbol{k_2}, \end{aligned} \tag{2.15}$$

where $\boldsymbol{k_i}$ is the wavevector of the wave with frequency ω_i. If $\boldsymbol{k_1}$, $\boldsymbol{k_2}$, $\boldsymbol{k_3}$, $\boldsymbol{k_4}$ are in the same direction (typical in a 1D waveguide), the second relation can be expressed in a scalar form. The linear phase mismatch factor Δk is given as:

$$\begin{aligned} \Delta k &= k_3 + k_4 - k_1 - k_2 \\ &= 2\pi[\frac{1}{\lambda_3 n(\omega_3)} + \frac{1}{\lambda_4 n(\omega_4)} - \frac{1}{\lambda_1 n(\omega_1)} - \frac{1}{\lambda_2 n(\omega_2)}]. \end{aligned} \tag{2.16}$$

if $\omega_1 = \omega_2$,

$$\Delta k \approx \beta_2 \Omega_s^2 + (\beta_4/12)\Omega_s^4, \tag{2.17}$$

where Ω_s is the frequency shift between ω_1 and ω_3 (or ω_4), β_2 and β_4 are the dispersion parameters at the pump frequency ω_1. It is obvious that Δk is inversely proportional to the refractive index, which is different at different pump frequencies. The linear phase mismatch could be reduced to dispersion-dependent formulation in degenerate FWM case ($\omega_1 = \omega_2$), which suggests that it could be canceled by β_2 and β_4 with opposite signs. Apart from the linear phase mismatch, the refractive index

variation depending on the intensity results in the nonlinear phase mismatch. The effective phase mismatch including linear and nonlinear phase mismatch is given by:

$$\kappa = \Delta k + \gamma(P_1 + P_2), \tag{2.18}$$

where $\gamma \approx \gamma_i$ is an average nonlinearity if the relatively small differences in optical frequency of these four waves are ignored; P_i is the pump power at a different frequency. The parametric gain is dependent on the pump power and is defined by [50]:

$$g = \sqrt{(\gamma P_0 r)^2 - (\kappa/2)^2}, \tag{2.19}$$

in which, $r = 2(P_1P_2)^{1/2}/P_0$, $P_0 = P_1 + P_2$. The maximum gain could be achieved at $\kappa = 0$. This shift of the gain peak from $\Delta k = 0$ is due to the influence of SPM and XPM. A typical means to minimize the phase mismatch is through the dispersion engineering of planar waveguides to ensure at least one term of the linear or nonlinear loss is negative.

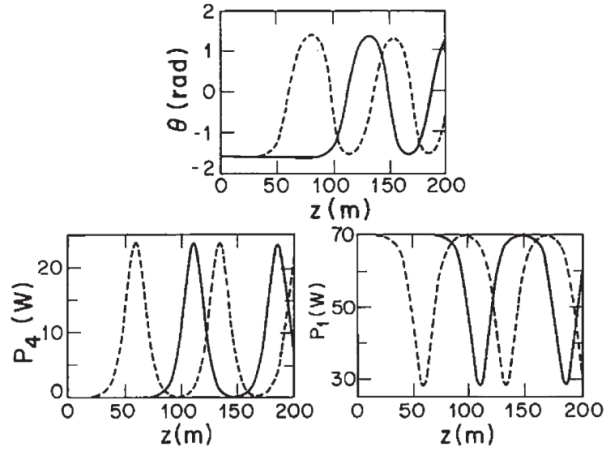

FIGURE 2.13: Evolution of the relative phase, idler power (P_4) and the pump power (P_1) along the propagation length when $\kappa = 0$, $\theta = -2/\pi$, $P_1 = P_2 = 70$ W, $P_3(0) = P_4(0) = 0.1\,\mu$W (solid line), $P_3(0) = 6$ mW, $P_4(0) = 0.1\,\mu$W (dash line) . [24]

When the phase matching condition is not perfect, the energy may transfer back to the pump waves. The energy conversion direction depends on the relative phase that is given by:

$$\theta = \phi_1 + \phi_2 - \phi_3 - \phi_4, \tag{2.20}$$

where ϕ_i is the phase at different frequencies. The variation of the relative phase obeys the following equations [24]:

$$\begin{aligned} \frac{dP_3}{dz} &= \frac{dP_4}{dz} = -4\gamma\sqrt{P_1P_2P_3P_4}\sin(\theta), \\ \frac{d\theta}{dz} &= \kappa + 2\gamma\sqrt{P_1P_2}\frac{P_3+P_4}{\sqrt{P_3P_4}}\cos(\theta). \end{aligned} \tag{2.21}$$

When accounting for pump depletion during propagation, the phase match κ varies along the propagation length, as shown in Figure 2.13 according to Eq.(2.21). In Figure 2.13, P_1 decreases along the propagation length, accompanied by a corresponding increase in relative phase from initial value to $\pi/2$, while P_4 increases simultaneously. This underscores the importance of careful length design, even under perfect phase matching conditions.

2.9 Raman-enhanced four-wave mixing

Raman scattering significantly influences the performance of FWM, when the frequency shift Ω_s moves within the Raman gain bandwidth. The interaction between Raman scattering and FWM (RE-FWM) realises the enhancement of the induced idler compared with the single nonlinear effect. When the signal is positioned at Stokes frequency, the enhancement of the anti-Stokes idler is named as coherent anti-Stokes Raman scattering (CARS); when the signal is positioned at anti-Stokes frequency, the enhancement of the Stokes idler is named as coherent Stokes Raman scattering (CSRS) [85].

2.9.1 Coherent anti-Stokes Raman scattering

When a pump laser beam assisted with a signal at Stokes frequency is applied to the Raman medium under near phase matching conditions, anti-Stokes wave is generated and enhanced by the interaction between Raman scattering and FWM, known as CARS. Raman scattering can be considered as down-conversion of a pump photon into a Stokes photon and a phonon associated with a vibrational mode of molecules. An up-conversion process in which a phonon combines with the pump photon to generate an anti-Stokes photon is also possible, but occurs rarely because it requires the presence of a phonon of the right energy and momentum. Because the energy conservation is inherently satisfied among pump, Stokes wave and anti-Stokes wave, FWM can occur provided the total momentum is conserved. The momentum-conservation requirement leads to the necessity of the near phase

matching condition, which must be satisfied for FWM to occur in CARS process. In the process of CARS, illustrated in Figure 2.14, under the near phase matching condition, the gain of SRS is suppressed as FWM transfers energy from Stokes waves (ω_s) to anti-Stokes waves (ω_a), in which one pump photon (ω_p) is annihilated to produce a Stokes photon and a phonon with the right energy and momentum to simultaneously induce the generation of an anti-Stokes photon.

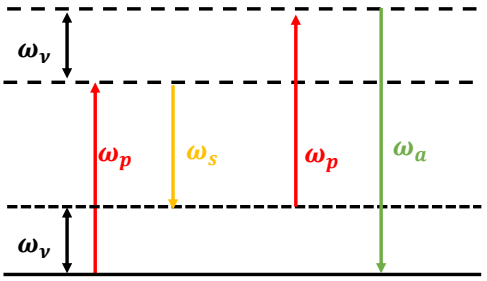

FIGURE 2.14: Energy diagrams for CARS process. The angular frequencies ω_p, ω_s, ω_a and $\Delta\omega_{nu}$ correspond the pump, Stokes waves, anti-Stokes waves and Raman shift.

2.9.2 Coherent Stokes Raman scattering

In contrast to CARS, which adds the signal at Stokes frequency, coherent Stokes Raman scattering (CSRS) injects the signal at anti-Stokes frequency to boost the Stokes wave, realising a high gain. The nonlinear processes that contribute to the gain at the Stokes wavelength include (1) degenerate FWM, (2) stimulated Raman scattering (SRS), and (3) inverse Raman scattering (IRS) as Figure 2.15 illustrates. FWM is the foundation of the process with two pump photons (ω_p) being consumed to generate a Stokes photon (ω_s) and an anti-Stokes photon (ω_a). Once the FWM induces photons at the Stokes wavelength, SRS can take place, which leads to enhancement of the conversion efficiency, defined here as the ratio of output idler power to output signal power. However, due to the presence of the anti-Stokes wavelength, IRS can also occur, resulting in a transfer of energy back to the pump. This compensation of the pump can thus further increase the conversion efficiency of the Stokes wavelength via the FWM and SRS processes. Meanwhile, pumping near ZDW enable the gain spectra of FWM and Raman scattering to overlap each other, which ensure the strong coupling between nonlinear effects. Hence, the gain at Stokes wavelength could be effectively enhanced with assistance of a weak anti-Stokes signal.

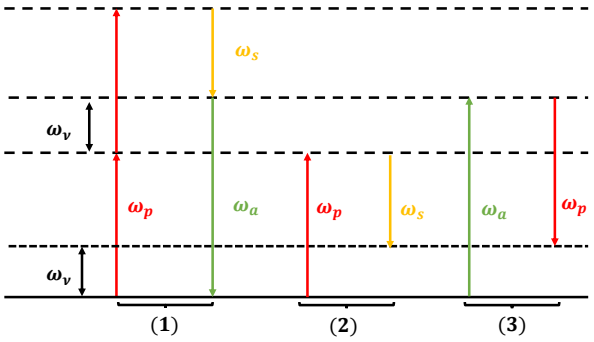

FIGURE 2.15: CSRS process. (1) Degenerate FWM. (2) Stimulated Raman scattering (SRS). (3) Inverse Raman scattering (IRS).

2.10 Pulse propagation in nonlinear medium

2.10.1 Nonlinear phenomena presented by the mathematical equation

Electromagnetic wave propagation in a dispersive nonlinear silicon waveguide can be described by the generalised nonlinear Schrödinger equation (NLSE) [24]:

$$\frac{\partial A}{\partial z} + \frac{\alpha}{2}A - i\sum_{n=1}^{\infty}\frac{i^n\beta_n}{n!}\frac{\partial^n A}{\partial t^n} - \frac{\sigma}{2}(1+i\mu)N_c A = i(\gamma(\omega_0) + i\gamma_1\frac{\partial}{\partial t})(A(z,t)\int_0^{\infty} R(t')|A(z,t-t')|^2 dt'). \tag{2.22}$$

In the left-hand formula describing the linear light propagation, A is the pulse amplitude; α is the linear propagation loss; β_n is the nth-order dispersive term; σ (1.45×10^{-21} m^2 for crystalline silicon) is the FCA cross section, μ ($\mu = 2k_c k_0/\sigma$, $k_c = 1.35\times10^{-27}$) and N_c are the free carrier dispersion and density, respectively. The right-hand formula describes the nonlinear propagation, where γ is the nonlinearity of the waveguide (including both the Kerr effects that represents the change in the refractive index of a material in response to an applied electric field and nonlinear loss), $\gamma_1 = (d\gamma/d\omega)_{\omega=\omega_0}$. γ is given in the form of $\gamma = (\omega n_2)/(cA_{eff}) + i\beta_{TPA}/(2A_{eff})$, in which n_2 is the nonlinear refractive index, β_{TPA} is the TPA coefficient, $A_{eff} = (\iint_{-\infty}^{\infty}|F(x,y)|^2dxdy)^2/\iint_{-\infty}^{\infty}|F(x,y)|^4dxdy$ is the effective mode area, $F(x,y)$ is the field transverse distribution.

To illustrate the roles played by the different terms in Eq.(2.22), simulation results obtained under different conditions are depicted in Figure 2.16. Figure 2.16 (a) shows the effects of dispersion on short pulse (100 fs, FWHM) propagation with second-order dispersion term, $\beta_2 = 3\,\text{ps}^2/\text{m}$, linear loss, $\alpha = 0\,\text{dB}$, $\beta_{TPA} = 0\,\text{m}^2/\text{W}$, and nonlinear refractive index, $n_2 = 0\,\text{m}^2/\text{W}$. It is clear that dispersion causes temporal pulse

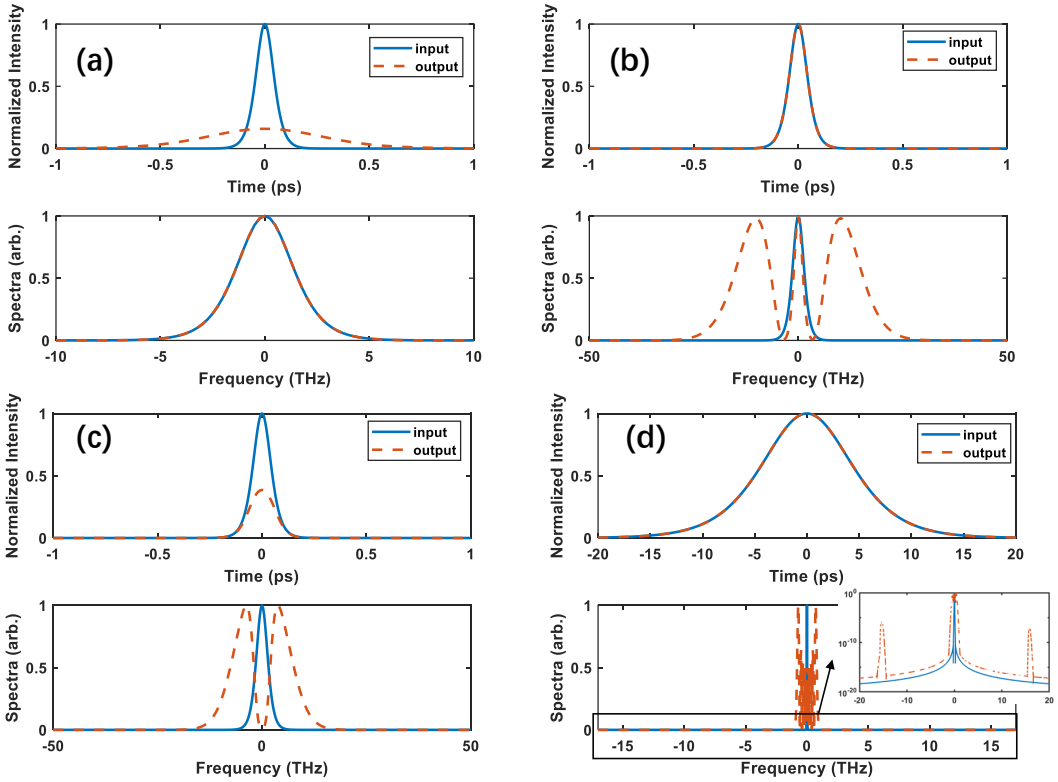

FIGURE 2.16: The simulation results under different dominant effects. (a) Dispersion effect on the 100 fs-pulse propagation without losses and nonlinear effects. (b) Third-order nonlinear effects on the 100 fs-pulse propagation without losses and Raman scattering. (c) Third-order nonlinear effects without Raman scattering and linear loss on the 100 fs-pulse propagation accompanying with FCA and TPA. (d) Raman scattering effect on the 10 ps-pulse propagation without losses.

broadening while maintaining the pulse characteristics in the frequency domain. In Figure 2.16 (b), this result only shows the effects of nonlinear propagation, calculated with second-order dispersion term, $\beta_2 = 0\,\mathrm{ps}^2/\mathrm{m}$, linear loss, $\alpha = 0\,\mathrm{dB}$, $\beta_{TPA} = 0\,\mathrm{m}^2/\mathrm{W}$, nonlinear effects, $n_2 = 6 \times 10^{-18}\,\mathrm{m}^2/\mathrm{W}$ and the Raman fractional contribution, $f_R = 0$. SPM, resulting in spectral broadening with three peaks in the frequency domain, is evident and symmetrical in this outcome due to the large nonlinearity. While under the same condition but considering $\beta_{TPA} = 5 \times 10^{-12}\,\mathrm{m/W}$, and FCA, as shown in Figure 2.16 (c), the output spectra in time domain and frequency domain significantly different. The intensity in the time domain become weaker, accompanied by spectra broadening, which is noticeable in a relatively narrow frequency range with two peaks. Figure 2.16 (d) show the pulse propagation (10 ps, FWHM) with the same condition as that of Figure 2.16 (b) except the Raman fractional contribution, $f_R = 0.043$. The obvious Raman scattering can be seen in addition to SPM at Raman frequency shift. These simulation results just simply show the basic nonlinear phenomena under the NLSE and helps to understand the different parts in the NLSE.

2.10.2 Validation of the Raman response model

Before validating the code, the basic structure is explained briefly in Figure 2.17 (more details can be found in the Appendix). Here, the split-step Fourier method was adopted to solve the NLSE. In practice, dispersion, nonlinear effects, and losses simultaneously work and interact with each other along the propagation path. The iteration loop of solving NLSE continues when the calculated length (Z) is smaller than the design propagation length (L). Within each step of this iteration, the dispersion, nonlinearity, free carrier and linear loss are separately solved in a distance segment. The values are then iterated based on the results from the previous step. The key point of this method is the assumption that during propagation of the optical field over a distance segment of dz, the dispersion, nonlinear effects and linear loss can act independently. The flow path of solving the NLSE are as follows.

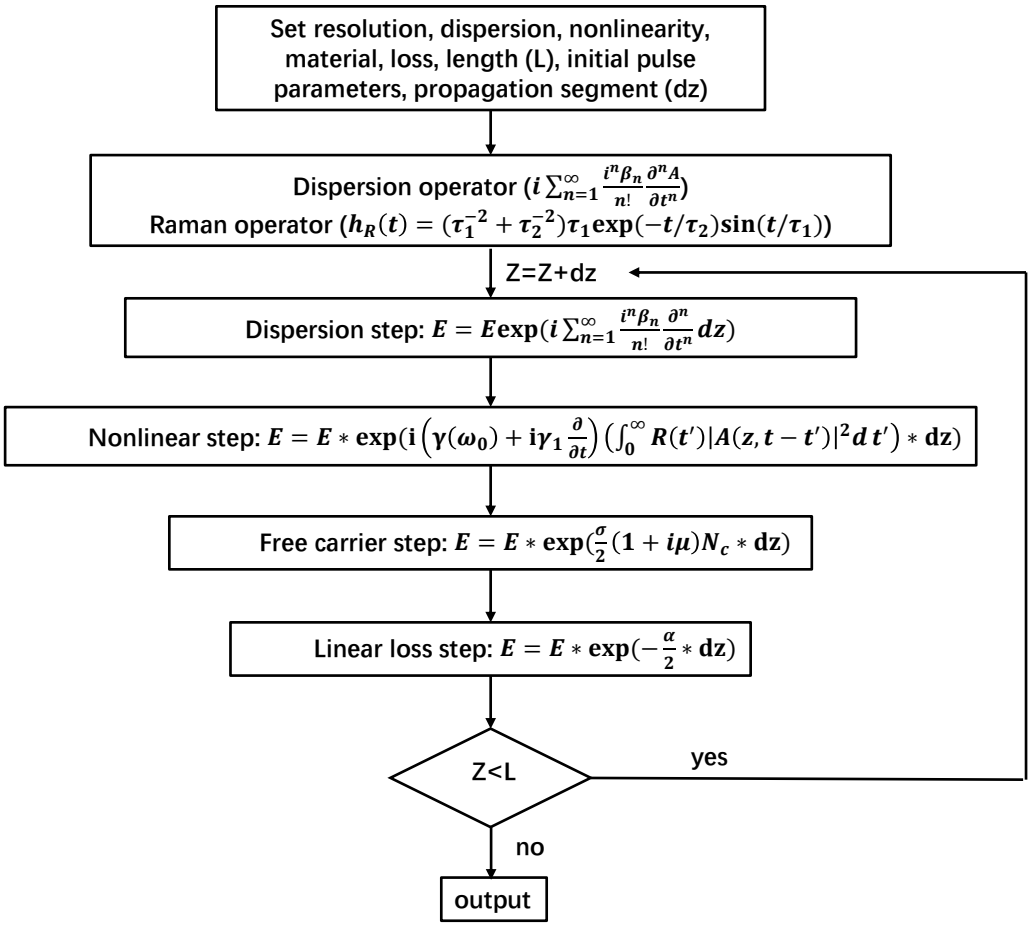

FIGURE 2.17: The flow chart of the code.

During the solve process, the fast Fourier transform (FFT) algorithm is utilized to expedite the speed of computing the discrete Fourier transform (DFT) of a sequence. This transformation, from the time domain to the frequency domain, is expressed in the main loop code as follows:

```
E1til = fftshift(ifft(fftshift(E1)));
```

The dispersion step in the code is expressed as follows:

```
GVD = exp((phi2+phi3+phi4)*dz);
E1til = E1til.*GVD;
E1 = fftshift(fft(fftshift(E1til)));
```

where phi2, phi3 and phi4 are second-, third- and fourth-order dispersion operator, GVD represents $exp(i\Sigma_{n=1}^{\infty}\frac{i^n\beta_n}{n!}\frac{\partial^n A}{\partial t^n}dz)$.

The nonlinear step is described by:

$$\frac{\partial A}{\partial z} = i(\gamma(\omega_0) + i\gamma_1\frac{\partial}{\partial t})(A(z,t)\int_0^{\infty} R(t^{'})|A(z,t-t^{'})|^2dt^{'}). \tag{2.23}$$

The time derivative is small over the integral $z_0 < z < z_0 + dz$, hence it is treated as perturbation. To simplify the deduction process, V(t,z) is introduced as a transition quantity:

$$\begin{aligned} V(t,z) &= A(t,z)\exp(-i(z-z_0)\gamma Int), \\ V_0 &= A_0 = A(t, z=z_0), \end{aligned} \tag{2.24}$$

where $Int = \int_0^{\infty} R(t^{'})|A(z,t-t^{'})|^2dt^{'}$, $Int0 = \int_0^{\infty} R(t^{'})|A_0(z,t-t^{'})|^2dt^{'}$. Then the derivation of V is given in:

$$\frac{\partial V}{\partial z} = i\gamma V(Int - Int0) - \gamma_1\frac{\partial}{\partial t}\{V\cdot Int\}. \tag{2.25}$$

The second-order Runge-Kutta scheme is utilised to solve Eq.(2.25).

$$V_1 = V_0 + \frac{dz}{2}\frac{\partial V_0}{\partial z} = V_0 - \frac{dz}{2}\gamma_1\frac{\partial}{\partial t}V_0\cdot Int0. \tag{2.26}$$

$$Int1 = \int_0^{\infty} R(t^{'})|V_1(z,t-t^{'})|^2dt^{'}). \tag{2.27}$$

$$V = V_0 + dz\frac{\partial V_1}{\partial z} = V_0 + i\gamma V_1(Int1 - Int0) - \gamma_1\frac{\partial}{\partial t}\{V_1\cdot Int1\}. \tag{2.28}$$

At last, the solution of A is:

$$A = V \exp(i \cdot dz \cdot Int0). \tag{2.29}$$

The corresponding code in the loop to solve the nonlinear step is as follows:

```
conv0 = (fft(fftshift(abs(E1).^2))).*fftshift(chi1111);
int0 = (1-fR)*abs(E1).^2 + fR*fftshift(ifft((conv0)));
v1 = E1-1/2*gamma/w0*dz*gradient(E1.*int0,TT);
conv1 = fft(fftshift(abs(v1).^2)).*fftshift(chi1111);
int1 = (1-fR)*abs(v1).^2+fR*fftshift(ifft((conv1)));
v = E1+i*gamma*dz*v1.*(int1-int0)-gamma/w0*dz*gradient(v1.*int1,TT);
E1 = v.*exp(i*dz*gamma*int0);
```

where chi1111 is the Raman response function $h(R)$ in Fourier domain, gamma is γ, w0 signifies pump wavelength, TT is the time sequence.

The free carrier step for the pulse pump in the loop is expressed by:

```
Nc = zeros(size(TT));
for ii = 1:length(TT)-2
Nc(ii+2) =(beta_TPA/(2*h*v0)*abs(E1(ii+1)).^4/Aeff^2*1e-24-Nc(ii+1)/tau)*2*dT + Nc(ii);
end
E1 = E1.*exp(-sigma/2*(1+i*mu).*Nc*dz);
```

where Nc is the free carrier density N_c, beta_TPA is β_{TPA}, h is the plank constant, v0 is the pump frequency, Aeff is the effective mode area A_{eff}, tau is the free carrier lifetime, dT is the time segment, sigma is σ and mu is μ. The zero of the free carrier density is crucial for accurately estimating the instantaneous carrier distribution as the pulse changes along the propagation path. During the pulse duration, changes in the free carrier density over time are calculated within a sub-loop. When the pump source switches to a continuous-wave (CW) source, the calculation for determining the time-independent free carrier density is switched to:

```
Nc = beta_TPA/(2*h*v0)*mean(abs(E1))^4/Aeff^2*1e-24*tau;
E1 = E1.*exp(-sigma/2*(1+i*mu).*Nc*dz);
```

The loss step in the loop is:

```
loss = exp(-0.5*alpha_l*dz);
E1 = E1.*loss;
```

where alpha_l is the linear loss.

Furthermore, the segment of the distance is a critical parameter in the Raman response model, which has a significant influence on the result and the calculation time. The choice of the distance segment should be smaller compared to both the dispersion length and the nonlinear length. The dispersion length (L_D) and nonlinear length (L_{NL}) are defined as [50]:

$$L_D = \frac{T_0^2}{|\beta_2|}, \tag{2.30}$$

$$L_{NL} = \frac{1}{\gamma P_0}, \tag{2.31}$$

where T_0 is the pulse width. L_D and L_{NL} serve as evaluation criteria for the influence of dispersion and nonlinear effects. Dispersion and nonlinearity begin to play significant roles when the propagation length exceeds these two length scales. Using a smaller distance segment ensures that both dispersion and nonlinear effects are properly accounted for in the simulation, leading to higher accuracy.

On the other hand, there is a trade-off between the accuracy and the calculation time, and a suitable selection of the segment could achieve the balance between them. When the propagation length is 1 cm, the variation of simulation results and the calculation time is shown in Figure 2.18 (a). It is obvious that, the simulation results become stable when the distance segment is smaller than 2×10^{-4} m and the calculation time dramatically decreases when the distance segment is larger than 2×10^{-5} m. When the distance segment is around 10^{-4} m, which is the zone marked by the dash-dot lines, the stability of the calculation results and the reduction of the calculation time could be obtained at the same time. As the simulated propagation length increases, the situation become complex, which is depicted in Figure 2.18 (b) with the propagation length of up to 10 cm. The stable simulation result requires the distance segment to be shorter than 2×10^{-4} m, while the calculation time substantially increases. The most proper choice of the distance segment is around 10^{-3} m to keep the relative stability of the calculation results and the compression of the calculation time, although the calculation accuracy is not the optimized but acceptable. In general, the distance segment should be two orders of magnitude shorter than the simulated propagation length. This practice helps maintain result stability and reduces calculation time, based on empirical observations. Another influence of the calculation time is the number of time points in the calculated time domain which has little effects on the calculation accuracy. The less the number of time points is, the narrower the frequency domain is while the less the calculation time is. Therefore, the selection of an appropriate number of time points depends on the desired frequency window and the minimum calculation time.

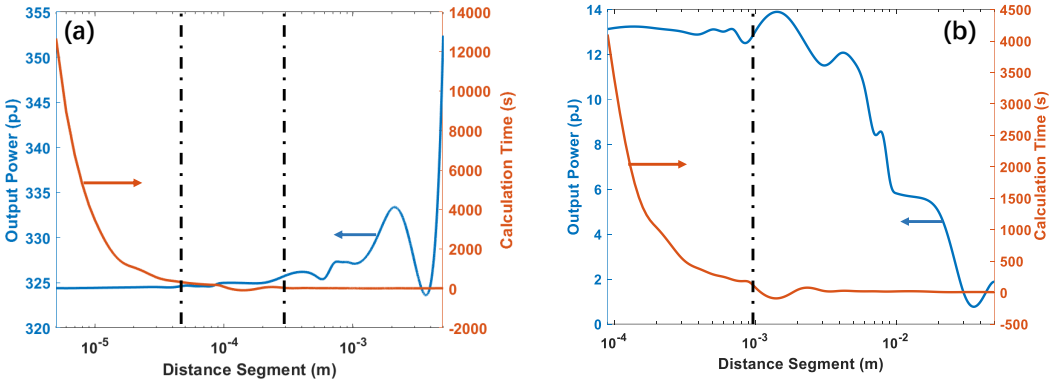

FIGURE 2.18: The calculation results and calculation time as a function of the distance segment at propagation lengths of 1 cm (a) and 10 cm (b).

Firstly, the code based on the NLSE needed to be checked and validated through a comparison between the simulation results and previous reports that have been published in literature. Two main references have been used for the validation, the first relates to SCG [10] and the second is for Raman scattering [25] in silicon waveguides. The comparison with the pulse propagation results obtained from [66] is shown in Figure 2.19. All the relating parameters come from reference [10]. The SCG results using our own MATLAB code are perfectly consistent with that in the literature.

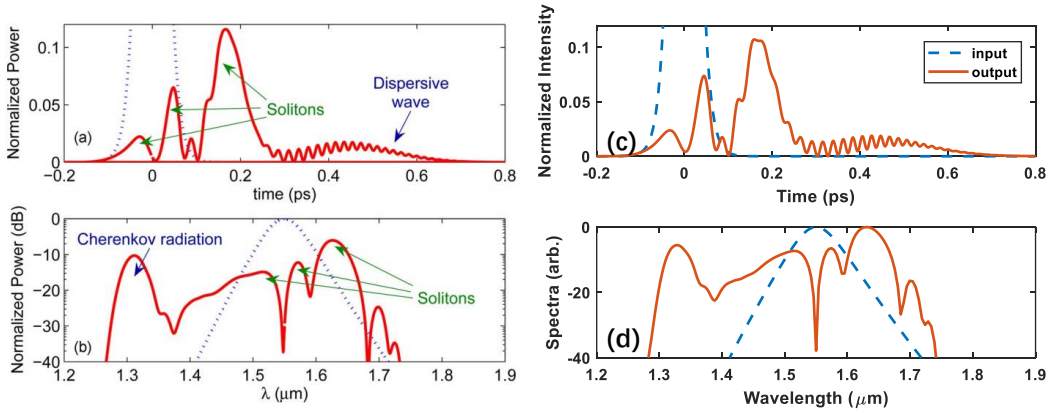

FIGURE 2.19: The pulse propagation comparison between (a) the simulation results by using our own MATLAB code and (b) the simulation results in the literature. [10]

The code was then compared with the Raman scattering results from [25], which was taken under a CW randomly polarized pump at 1427 nm, with a 2 nm linewidth. The rib waveguide used in this experiment was 2.4 cm long and the cross section is shown in Figure 2.20. Figure 2.21 shows excellent agreement between the experimental results and our simulations. In this simulation, the pump is a Gaussian pulse at 1427 nm with 100 ps FWHM, which can be considered as quasi-CW light in the calculation time domain. The effective mode area is 25 μm^2 and the propagation length is 2.4 cm. The small difference between the measured and simulated power

values may be the result of error of the Raman gain given in the reference. Meanwhile, the broader Raman spectrum of the literature's result is due to its pump linewidth being around 2 nm in the experiment, while the pump linewidth is narrower in the simulation process. The broad simulation output spectra could be obtained through the convolution of the Raman spectrum and pump spectrum. Here, the convolution was not applied due to the lack of the original pump pulse shape in this reference.

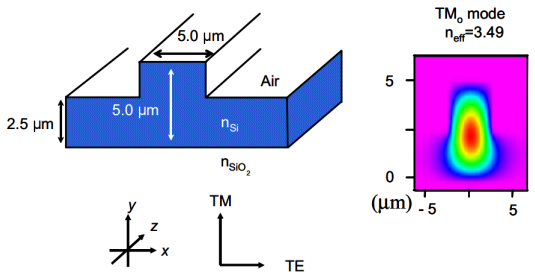

FIGURE 2.20: Silicon waveguide used and the resulting TM mode.[25]

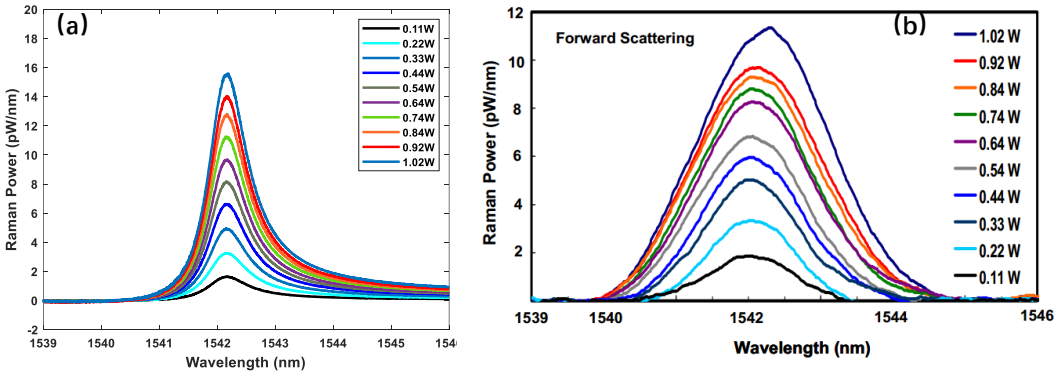

FIGURE 2.21: The CW light propagation comparison between (a) the simulation results by using our own MATLAB code and (b) the experiment results from [25]

Through this validation process, the MATLAB code can be directly used in the following study, predicting the nonlinear performance for different structures and conditions. It is important to note that the corresponding parameters such as β_{TPA} and n_2 need to be checked and estimated once the structure or pump wavelength changes in order to match the experimental data with the simulation.

Chapter 3

Raman scattering and coherent anti-Stokes Raman scattering in SCFs

Raman scattering and FWM are effective ways to generate wavelength tunable optical gain in highly nonlinear materials such as high nonlinear optical fibres (HNLFs) [96] and planar silicon waveguides [25]. This chapter begins with the first experimental demonstration of Raman scattering appearing in SCFs and uses numerical simulations to analyze the results in the telecom and mid-infrared bands. Then the first exploration of CARS, which involves the interaction between Raman scattering and FWM, using the SCFs is explained in detail in the mid infrared band. This chapter focuses on collaborative work with Meng Huang, Dong Wu, and others. I was responsible for all simulation sections and building the loss measurement setup.

3.1 Structures and characteristics of SCFs

The structure of SCFs is depicted in Figure 3.1 including the down taper, the waist region and the up taper. Dimensions of tapered submicron SCFs working in the telecom band vary precisely along the length from about 4.5μm to below 1 μm. The larger input and output core diameter is beneficial to improve the free space coupling efficiency, and the conventional length of the tapering section is about 3 mm. Short tapering sections minimize the impact on nonlinear propagation. These sections were excluded in the NLSE simulations due to the larger input core diameter, which hindered phase matching in the designed FWM and efficient Raman scattering with pump sources having pulse durations longer than picoseconds. Our investigation revealed that varying the core diameter and length of the tapering section had limited

influence on the desired nonlinear processes, compared to existing demonstrations of nonlinearity supported by silicon core fibre tapers [97]. In that study, significant effects on nonlinear propagation were observed when the core diameter was changed from 2.5 μm to 1 μm over a length of 2 mm, or from 640 nm to 850 nm over 10 mm using a femtosecond laser source. The parameters of SCFs used for Raman, FWM and Raman enhanced FWM are summarized in Table 3.1.

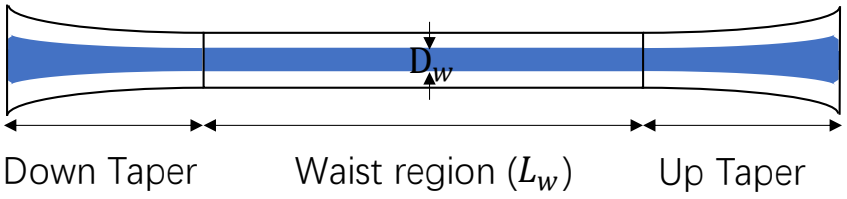

FIGURE 3.1: The schematic of SCF structure consisting of a down taper, a waist region and an up taper. D_w denotes the core diameter and L_w represents the length of the waist region.

Fibre No.	D_w **(nm)**	D_t **(μm)**	L_w **(mm)**	β_2 **(ps^2/m)**	A_{eff} **(μm^2)**	α_l **(dB/cm)**
Fibre A	$\sim$ 860	$\sim$ 4.5	10	0.17 (1432 nm) -0.16 (1545 nm)	0.38 (1432 nm) 0.4 (1545 nm)	2
Fibre B	$\sim$ 750	$\sim$ 4.5	15	0.22 (1432 nm) -0.11 (1545 nm)	0.31 (1432 nm) 0.33 (1545 nm)	1
Fibre C	$\sim$ 750	$\sim$ 4.5	10	-0.11 (1432 nm) -0.53 (1545 nm)	0.31 (1432 nm) 0.33 (1545 nm)	2
Fibre D	$\sim$ 760	$\sim$ 4.5	10	-0.08 (1432 nm) -0.49 (1545 nm)	0.32 (1432 nm) 0.33 (1545 nm)	2
Fibre E	$\sim$ 860	$\sim$ 4.5	15	0.17 (1432 nm) -0.16 (1545 nm)	0.38 (1432 nm) 0.4 (1545 nm)	2
Fibre F	$\sim$ 1590	$\sim$ 4.5	60	0.002 (1992 nm)	1.2 (1992 nm)	0.2
Fibre G	$\sim$ 1590	$\sim$ 4.5	40	0.002 (1992 nm)	1.2 (1992 nm)	0.5
Fibre H	$\sim$ 1976	$\sim$ 4.5	30	0.046 (2170 nm)	1.74 (2170 nm)	1
Fibre I	$\sim$ 1984	$\sim$ 4.5	10	0.051 (2170 nm)	1.75 (2170 nm)	1
Fibre J	$\sim$ 1816	$\sim$ 4.5	60	-0.063 (2170 nm)	1.5 (2170 nm)	0.2

TABLE 3.1: The corresponding parameters of SCFs used in the nonlinear experiments.

In the telecom band, the strong nonlinear losses, TPA and FCA, must be included in the Raman simulation. However, these can be neglected when pumping with some mid-infrared band sources. Thus, the relating key parameters, β_{TPA} and τ, need to be checked for the specific pump, which are estimated by n_2 given in Table A.2 in Appendix A in details for different pump wavelengths. In the telecom band, the CW pump induces an accumulation of free carriers which is dependent on τ, pump intensity, β_{TPA} and so on. The increase of the free carrier density leads to higher FCA, which can have a significant effect on the output power. The free carrier lifetime is estimated by fitting the relationship between the input and output CW pump powers.

The experimental setup for loss measurement, as illustrated in Figure 3.2, involves a CW laser at 1432 nm, serving as the pump source. To improve the coupling efficiency, two reflective mirrors were employed to adjust the light direction and angle. The injected pump power was fine-tuned using the attenuation. Two beam splitters (BS) with a 92% transmission rate were positioned at the input and output sides, reflecting light back to CCD cameras. CCD cameras at both ends monitored the beam profiles and determined core positions through collecting reflective light. Two 60× objective lenses (OL) facilitated light coupling into the fundamental mode, maximising coupling efficiency. Proper power meters were used to measure input and output light power.

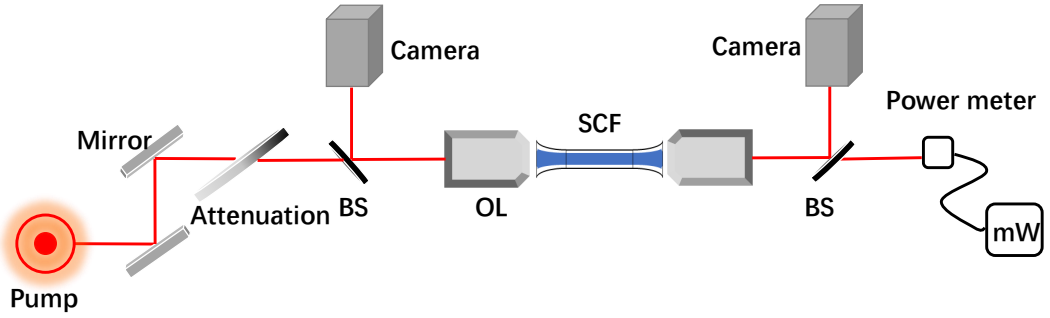

FIGURE 3.2: Experimental setup for loss measurement. BS, beam splitter; OL, optical lens.

The cutback method was utilized to estimated the linear loss of SCFs and the coupling loss of this set up. SCFs with similar core diameters were fabricated at different lengths using the same tapering recipe. The calculation of the linear loss is illustrated in Eq.(2.10). The coupling loss could be obtained by subtracting the linear loss from the total insertion loss, which was consistent for the measurement of different SCFs using the same setup. Figure 3.3 shows the simulation results of Fibre A, when pumping at 1432 nm, between the input and output pump powers, which are represented by circles. The slope of the fitting curve (dashed line) represents the total insertion loss, approximately 11,dB. The linear loss and the coupling loss in this simulation are 2 dB/cm and 9 dB respectively, which were measured in experiments. The bending trend observed under high pump power is due to the nonlinear loss, including TPA and FCA. With β_{TPA} fixed at 11.7×10^{-12} m/W, altering the value of the free carrier lifetime effectively changes the trend of the input and output power curve. It is consistent with the experimental results, which are represented by stars, under the condition $\tau = 7.5$ ns.

3.2 Raman scattering in SCFs

This part presents the first experimental observations of Raman scattering in SCFs in the telecom and mid-infrared band.The experiments using the SCFs were performed

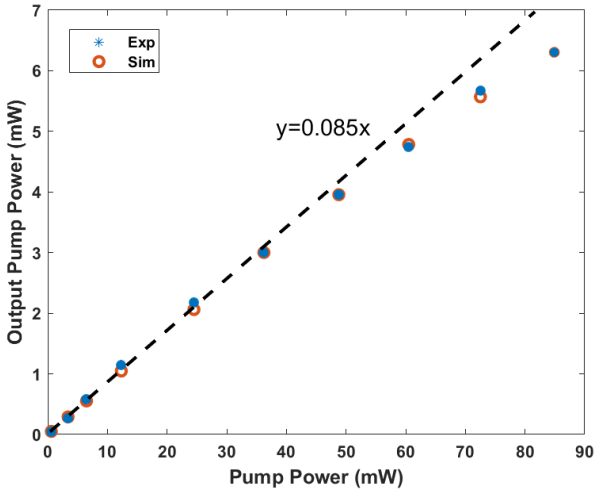

FIGURE 3.3: The relation between the pump power and the output power, with stars and circles representing the experimental and simulation results, respectively. The dash line is the fitting curve for the points with low pump power.

by Meng Huang to study the characteristic of Raman scattering in SCFs. I assisted by conducting the simulations of Raman scattering in SCFs. This part contains the related simulation results on Raman scattering in SCF. The simulations under corresponding working conditions such as the sample parameters and pump source are used to match the experimental results of Raman scattering. These results are then used to predict the performance of the fibres under higher pump powers and with longer length to further increase the measured gain. Based on the analysis of Raman scattering, the working conditions for generating cascaded Raman scattering are revisited. Suggested improvements, such as optimized length and dispersion engineering, for the SCF design in different working wavelength bands are also guided by these comparisons.

3.2.1 Raman scattering in the telecom band

3.2.1.1 Pumped with CW light source

During the FWM experiment in the telecom band using the tapered submicron SCF produced by Dong Wu and Haonan Ren, a small peak appeared at the Raman shift, distinct from FWM with a pump and a signal injected into Fibre A. By calculating the frequency generated through FWM, this small peak was confirmed to be induced by Raman scattering. This marked the first demonstration of Raman scattering in SCFs. The effective mode area of Fibre A is 0.372 μm^2 and the linear loss is approximately 2 dB/cm. Note, there had been no observation of Raman phenomenon in large-core fibres in previous experiments. Thus, we believe that it is the high intensity of light due to the small core size of the tapered section which leads to the appearance of the

Raman scattering in the experiment. The simulation results of the Raman output spectrum with pump wavelengths of 1.432μm and 1.5μm, convolved with approximation of the pump spectrum are shown in Figure 3.4 (a) and (b), in which the dash line represents the simulation results, and the solid line represents the experimental results. The Stokes output power increases with the pump power when the pump power maintains at a low level, and the results between the simulation and the experiment are in a good agreement. Thanks to this good agreement, the NLSE code including Raman scattering can be used to predict results roughly under any condition. In this Raman simulation, τ_1 in the Raman operator section should be altered to adjust the position of the Raman peak to match the experimental results and τ_2 is varied to adjust the width of the Raman peak, which is also influenced by the pump bandwidth in the spontaneous Raman scattering. τ_1 and τ_2 is calculated via the following equations:

$$\tau_1 \approx \frac{1}{\Omega_R}; \tau_2 \approx \frac{1}{\Gamma_R'}, \tag{3.1}$$

in which Γ/π is the gain bandwidth, and $\Omega/(2\pi)$ is the peak gain frequency shift. For Fibre A, τ_1 is 10.256 fs and τ_2 is 3.032 ps. The value of τ_1 and τ_2 are typically around these values as they are characteristic of this material, but may vary slightly due to the quality of silicon.

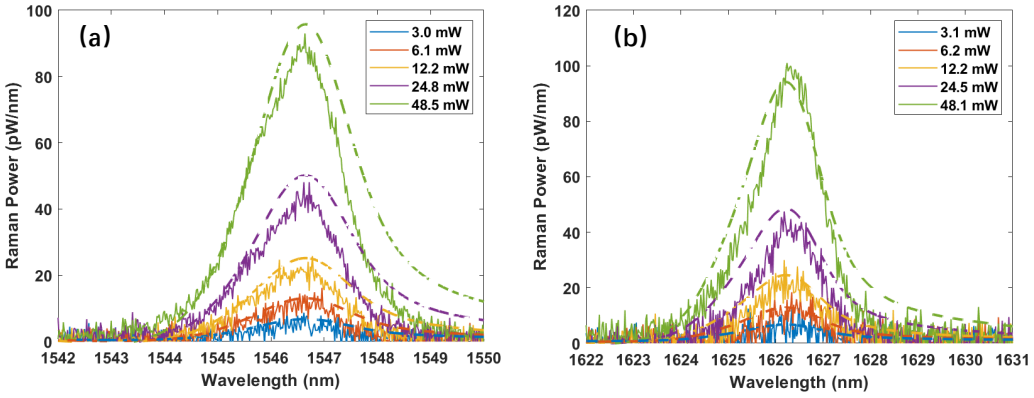

FIGURE 3.4: Comparison of the Raman output power between the experimental data and the simulation results of fibre A at different pump wavelengths of 1432nm (a) and 1500nm (b). The dash lines denote the simulation results, and the solid lines denote the experimental results.

The results of the Stokes output power under different pump powers and different fibre lengths at 1.432 μm are given in Figure 3.5. The value of the Stokes output power corresponds to the peak of the Raman spectrum. When the length is fixed, as the input power increases, the Stokes output power first increases, reaching the maximum value ($\sim$ 350 μW) with the pump power of $\sim$ 300 mW, before eventually declining. The

decrease in Stokes output power can be attributed to significant FCA and TPA resulting from the high pump power in the telecom band. Moreover, the Stokes output power drops when the length is longer for certain input powers as a result of increased linear loss. A suitable length determined from this result for spontaneous Raman scattering is about 17 mm. The linear and nonlinear losses are the main limitations to the Stokes wave power. The achievable Stokes output power is determined by the size of the Raman gain of the core and the transmission losses. When the total loss is higher than the Raman gain, the output power starts to decrease. The linear loss is determined by the material, the structure and the fabrication techniques. TPA is the dominant component of the nonlinear loss in this fibre when the pump is set in the telecom band. Meanwhile, high FCA under CW pumping is another reason for the limited Stokes power. Therefore, changing the pump wavelength to the mid-infrared band and using a pulsed pump are both effective methods to mitigate against the effects of TPA and FCA. For a pulse pump, the free carrier concentration would decrease due to the recombination of free carriers between two pulses, which can effectively reduce FCA.

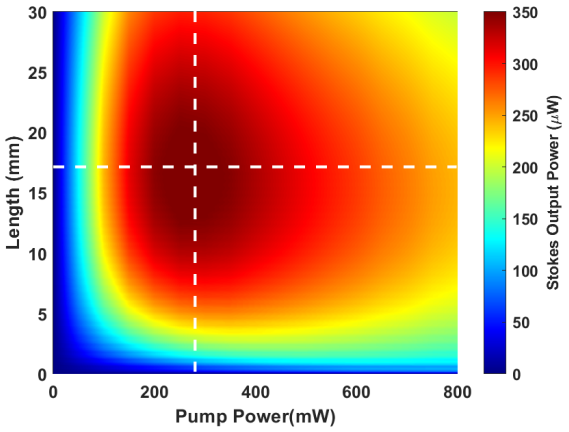

FIGURE 3.5: The Stokes output power as functions of length and pump power with the pump wavelength of 1.432 μm for Fibre A.

With the development of the tapering recipe and the maturity of the tapering process, Fibre B was fabricated with an estimated linear loss as low as 1 dB/cm. In the experiment, a tunable laser source which can be switched from 1542 nm to 1550 nm was added as a signal with the power of 0.1 mW to boost SRS. The on-off gain is defined as

$$G_{on-off} = 10 \times \log \frac{P_{s-on}}{P_{s-off}}, \tag{3.2}$$

where P_{s-on} is the signal power with the pump on and P_{s-off} is the signal power with the pump off. In the experiments, the signal power was monitored by an optical

spectrum analyzer (OSA, YOKOGAWA AQ6370D) with a pump of 48 mW on and off. The experimental results together with the simulation results are illustrated in Figure 3.6 (a). The maximum on-off gain for Fibre B is 1.1 dB which is consistent with the simulation results. Meanwhile, the peak and the linewidth of the on-off gain perfectly matches the spontaneous Raman shift which has been shown in Figure 3.4 (a). The coupling power into the fibre is limited in the experiment due to a relatively low melting point of the wax which is used to fix the fibre, thus the probe net gain under the higher CW pump power can only be predicted by simulations. Under the same conditions as the experiments, a map of the probe net gain verse SCF length and pump power is shown in Figure 3.6 (b). The maximum experimental on-off gain is marked as a white square in this figure, which excellently matches the simulation, and it could be slightly improved to 1.6 dB by increasing the pump power to 120 mW. However, strong TPA and its induced FCA leads to saturation of the gain and finally limits the further improvement. It is obvious that the maximum probe net gain can be obtained over 6 dB with the pump power larger than 120 mW and the propagation length longer than 10 cm. For comparison, when using a traditional highly nonlinear silica fibre, the equivalent gain would require a pump power on the order of kW instead of hundreds of mW, and the device length would be km rather than few cm [98].

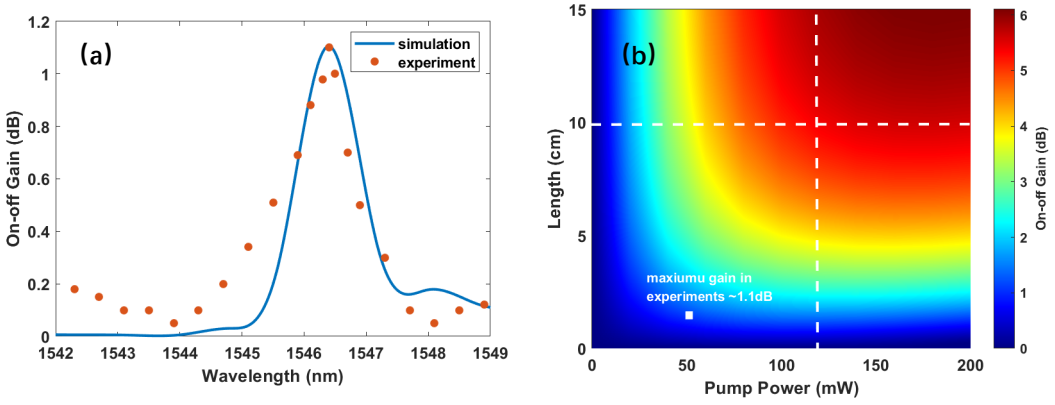

FIGURE 3.6: (a) The experimental on-off gain of Fibre B for the 1432 nm pump with the power of 48 mW compared with the simulation results. (b) The prediction of the on-off gain as functions of the pump power and the propagation lengths.

3.2.1.2 Pumped with pulse light sources

As mentioned in the discussion of the Stokes output power, one of the limitations in obtaining a large Raman gain is that the CW pump leads to the accumulation of free carriers, which could be reduced by using a pulsed pump. The following simulations and discussions focus on Fibre B. The pulse pump repetition rate is assumed to be 100 MHz to ensure the time between two pulse is larger than the free carrier lifetime, and the pump wavelength is still fixed at 1432 nm. The pulse duration should be

greater than 3 ps to ensure sufficient response time to stimulate the Raman scattering, but losses arising from TPA and FCA should increase with pulse duration. Therefore, the influence of pulse duration on Stokes output power is explored as shown in Figure 3.7 (a) to find out the optimal pulse duration to obtain maximum Stokes output power. In this simulation, the peak power is fixed at 5 W to maintain the same peak intensity at various pulse durations. It is clear that the maximum Stokes output power could be achieved with the pulse duration of 40 ps. SPM appears if the pulse duration is too short, while the nonlinear loss becomes large when the pulse duration is too long, both of which suppress the Raman scattering. After determining the appropriate pulse duration, the variation of the Stokes output power with propagation length and average pump power is shown in Figure 3.7 (b). The Stokes output power increases to the maximum and remains constant along the propagation length when the average pump power is weak, less than 5 mW. In this circumstance, the linear loss is comparable to the Raman gain which results in stable Stokes output power over longer propagation lengths. Upon applying a higher pump power, the Stokes output power initially increases with the propagation length, but starts to decrease as the length is further extended due to various losses, including linear and nonlinear losses. The red region depicted in Figure 3.7 (b) represents the optimal combinations of pump power and propagation length, resulting in the highest achievable Stokes output power. The sharp contraction of this area at higher pump powers is a result of the significant nonlinear absorption. Similarly, when the pump power exceeds 100 mW, another contributing factor to the reduction in Stokes output power at longer propagation lengths is the appearance of 1^{st} anti-Stokes wave and higher-order Stokes waves associate with cascaded Raman scattering as illustrated in Figure 3.7 (c). It is evident that the surges in the output power of the anti-Stokes waves are consistent with the decrease in the output power of the 1^{st}-order Stokes wave, represented by the light yellow curved area in Figure 3.7 (b). An indication of the occurrence of cascaded Raman is the subsequent increase in Stokes output power over a longer propagation length due to the energy transfer from higher-order Stokes waves back to 1^{st}-order Stokes wave. The maximum average 1^{st}-order Stokes output power is about 10 μW in relation to the peak power of 2.5 mW when the propagation length is 4.7 cm and the average pump power is 88 mW, corresponding to the peak power of 22 W . Compared with the Stokes wave generated under CW pump conditions, the saturation pump power reaches the watt level, leading to the occurrence of higher-order Stokes waves.

Cascaded Raman scattering typically serves as an efficient approach to generate longer wavelength Raman laser with multimode Raman laser [99] and supercontinuum generation [100] using standard telecom pump sources. Since cascaded Raman scattering was observed in previous simulations with pulsed pumps at high power levels, depicted in Figure 3.7, the performance of the higher-order Stokes will now be thoroughly discussed in the following section. The chosen pump wavelength was 1432 nm, with an average pump power of 600 mW, a pulse duration

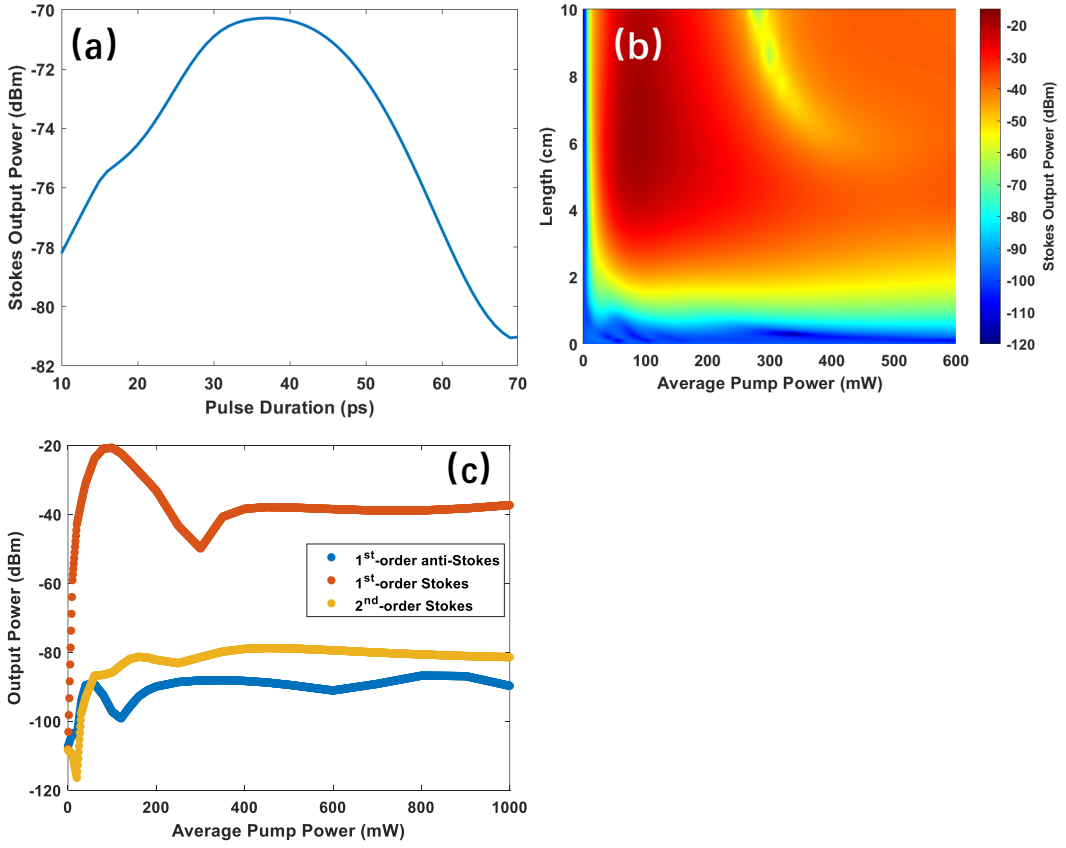

FIGURE 3.7: (a) The Stokes output power of Fibre B changing with the varying pulse duration. The pump peak power is fixed at 5 W. (b) The trend of the Stokes output Power as functions of propagation length and average pulse pump power. (c) The output power of 1^{st}-order anti-Stokes wave, 1^{st}- and 2^{nd}-order Stokes waves at the propagation length of 10 cm. The pump wavelength is 1432 nm and the repetition rate of the pulse pump is 100 MHz.

of 40 ps, and the propagation length was set to 10 cm in this simulation. The 1^{st}, 2^{nd}, 3^{rd} Stokes and 1^{st} anti-Stokes waves, corresponding to the wavelengths of 1547 nm, 1682 nm, 1844 nm and 1333 nm,respectively, are displayed in Figure 3.8 (a) to illustrate the variation of output powers along the propagation length. The 1^{st} Stokes wave sustainably increases to over -40 dBm within the propagation length of 4 cm, then begins to decrease within the propagation length of 4 cm to 6 cm, finally reaching stabilization in power after propagating over lengths greater than 6 cm. The 2^{nd} Stokes waves display a similar trend to the 1^{st} Stokes wave, but the output power starts to decreases at the propagation length of 4 cm. It is noticeable that the increase in 1^{st} anti-Stokes wave corresponds to the decline in 1^{st} and 2^{nd}-order Stokes waves, suggesting that the energy transfer to short wavelength due to the existing of parametric process. The 1^{st} anti-Stokes wave almost experiences synchronous growth with 1^{st} Stokes wave but encounters decrease at the propagation length of 2 cm. This is due to the energy transfer to 2^{nd} and 3^{rd} Stokes waves. The trends of various orders of Stokes waves suggest the optimal length for generating cascaded Raman is 4 cm, supporting maximum higher-order Stokes output power. Meanwhile, through

continually advancing the manufacturing techniques, in future it should be possible to taper the SCFs over lengths longer than 6 cm with relatively high quality, enabling the feasibility of cascaded Raman. The evolution of the spectrum for the pulse pump and the new generated wavelengths propagating along the length is shown in Figure 3.8 (b). The output power for the different orders of Stokes waves changes corresponding to the powers depicted in Figure 3.8 (a) along the propagation length. Moreover, a crucial observation is the slight broadening of the bandwidths of the higher-order Stokes waves, which expands with both the increasing order and length. This observation indicates that the higher-order Stokes waves are promising to serve as a seed for supercontinuum generation. Through the discussion of the variation of various Stokes and anti-Stokes waves concerning pump power and propagation length, it is evident that the primary limitation for generating higher-order Stokes waves in the telecom band is TPA. Additionally, higher-order Stokes waves is also constrained by the FWM process, which converts energy to shorter wavelengths. Therefore, a careful design is necessary to avoid the efficiency FWM in achieving cascaded Raman in the telecom band.

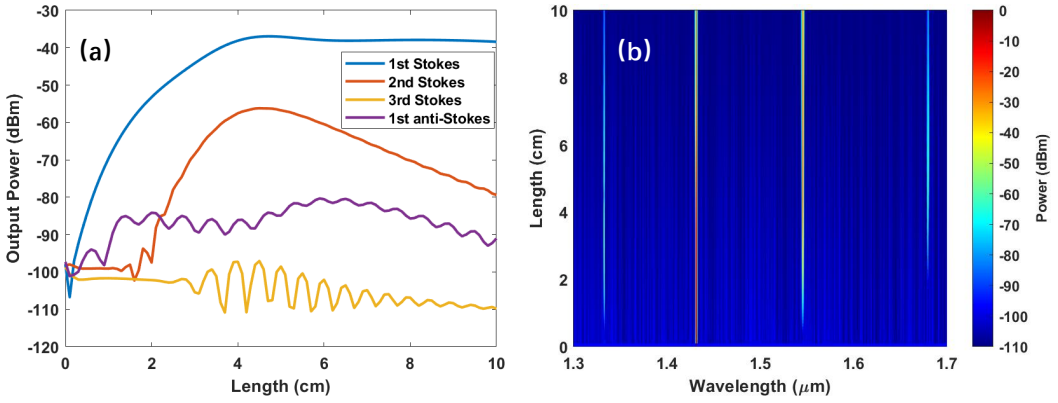

FIGURE 3.8: (a) 1^{st}, 2^{nd}, 3^{rd} and 4^{th}-order Stokes output power as function of the propagation length. (b) Evolution of the pulse spectrum along the propagation length. The average pump power in this simulation is 40 mW.

The simulation results for the pulsed pump show that a 1^{st}-order Stokes output power of several micro-watts could be obtained with a moderate average pump power of tens of milliwatts and a length of 3 cm. Furthermore, cascaded Raman scattering could be observed within a propagation length of 2 cm with an average pump power exceeding 25 mW, stabilizing after 6 cm. The exploration of the pulsed pump in the telecom band in SCFs provides a potential approach to construct a full-fibre integrated Raman laser through the use of the nano-spike coupling method [101].

3.2.2 Raman scattering in the mid-infrared band

3.2.2.1 Spontaneous Raman scattering and On-off gain

TPA and FCA are identified as the main limitations in achieving higher Raman gain in the telecom band, as previously discussed in the context of the Stokes output power under CW pumping. While employing a pulsed pump source instead of a CW pump source can effectively reduce the influence of FCA, it has no impact on TPA, which is inherent in silicon due to the characteristic of this material in the telecom band. Shifting the working wavelength from the telecom band to the mid-infrared band is an effective method to mitigate TPA. Mid-infrared Raman scattering in SCFs was initially observed in the experiments with Fibre F, which demonstrated an exceptional low linear loss of 0.2 dB/cm, consistent with the minimum recorded linear loss for SCFs [102]. In this experiment, a thulium-doped fibre laser supporting picosecond pulses ($\sim$ 125 ps) with a peak power of several watts at the wavelength of 1992 nm was utilized as a pump. The spontaneous Raman scattering with different average pump powers is displayed in Figure 3.9 (a), where the solid lines represent the simulation results, and the dash lines represent the experimental results. The simulation results of the Raman output spectrum, convolved with an approximation of the pump spectrum to ensure the consistency with the actual Raman spectra, are in good agreement with the experimental results. It clearly indicates an increase in the Stokes output power with the average pump power. To achieve higher Stokes output power, the variation of the average Stokes output power with respect to the average pump power and the propagation length is illustrated in Figure 3.9 (b). The maximum average Stokes output power exceeds 30 μW with an average pump power of 80 mW and a propagation length of 55 cm. The extended saturation propagation length is primarily attributable to the low linear loss, as well as the considerably higher saturation average pump power in comparison to that in the telecom band, stemming from the significantly lower TPA and FCA.

To study the capacity for efficient Raman amplification in the mid-infrared band, SRS was explored in the experiments with the coupled in pump power of 12.4 mW (corresponding to a peak power of 10 W), and an input signal power of 0.1 mW at a Stokes wavelength of 2.222 μm. The measured time-averaged on-off gain as the signal wavelength is tuned across the Raman gain curve is presented in Figure 3.10 (a), together with simulation results using parameters obtained from spontaneous Raman scattering measurement. The time-average pump-on signal power ($P_{av}^{pump-on}$) is calculated as follows to simulate the power measurement scenario in the experiments:

$$P_{av}^{pump-on} = (P_{p-time} - P^{pump-off}) \times Rep \times T + P^{pump-off}, \tag{3.3}$$

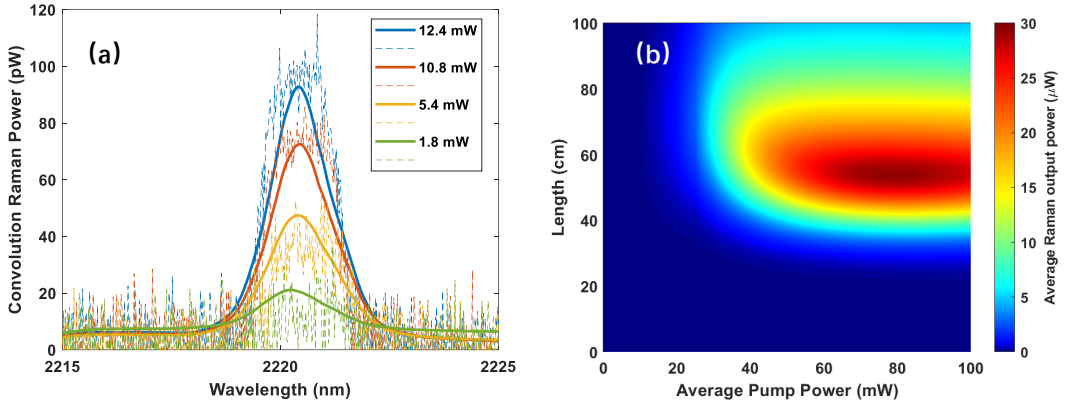

FIGURE 3.9: (a) The experimental Stokes output power under different pump powers as labeled in the legend compared with the simulation results. (b) The average Raman output power as functions of propagation length and average pump power.

where P_{p-time} represents the peak signal power in the time domain, $P^{pump-off}$ is the signal power with the pump off, Rep is the pulse repetition and T is the pulse duration. The maximum experimental time-average on-off gain is 3.7 dB, aligning with the simulation results, with a consistent bandwidth and peak position compared to the spontaneous Raman gain. Further simulations were conducted to investigate the role of the pump power and the fibre length in the Raman amplification performance of the SCFs. Figure 3.10 (b) describes the predicted time-averaged on-off gain, assuming the remaining SCF and pulse parameters are consistent with our experimental work. Notably, for pump power below $\sim$ 5 mW or propagation lengths shorter than $\sim$ 5 cm, the on-off gain is close to zero, highlighting the necessity of high pump power and adequate propagation length for Raman accumulation within a relatively small cross section. Increasing the SCF length while maintaining the same pump power leads to a substantial increase in the time-averaged on-off gain, reaching up to $\sim$ 20 dB (equivalent to a peak on-off gain of 49 dB) and yielding the average signal powers of up to 1 μW (peak power of 0.8 mW). The saturation length decreases with the pump power and stabilizes at $\sim$ 17 cm. When the propagation length is fixed, the on-off gain climbs with the average pump power, and the saturation pump power decreases as the length increases, stabilizing at 10 mW (peak power of 8 W). Interestingly, due to the non-negligible TPA parameter and linear loss at the 1.99 μm pump wavelength, increasing the pump power or propagation length beyond the saturation value offers little benefit to the on-off gain, primarily due to substantial FCA associated with the 125 ps pump pulse and attenuation as a result of the linear loss. The narrow rainbow transition region provides guidance on the optimal combination of propagation length and pump power. The 15 dB improvement in on-off gain, in comparison to that achieved in the telecom band, underscores the importance of system optimization to minimize the impact of nonlinear absorption processes in obtaining high gains.

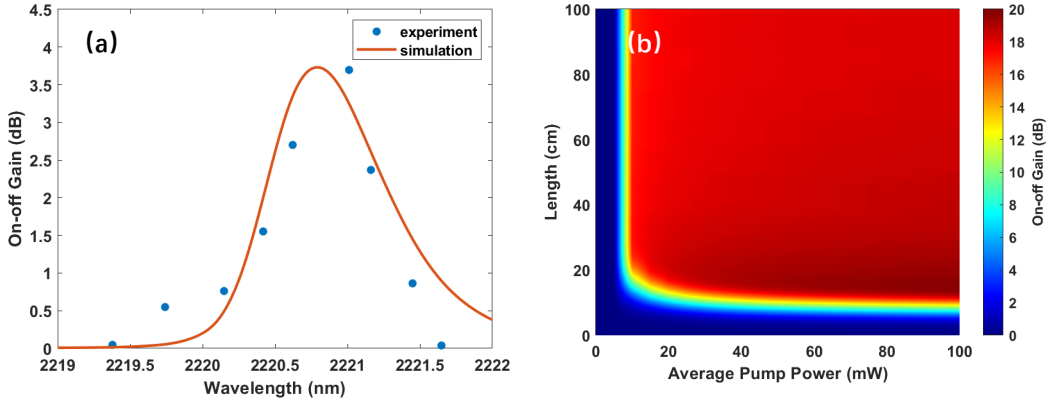

FIGURE 3.10: (a) The experimental on-off gain compared with the simulation results with the pump power of 12.4 mW. (b) On-off gain as functions of propagation length and average pump power.

3.2.2.2 Cascaded Raman scattering

To explore the potential for generating higher power and longer wavelength sources, additional simulations were conducted to investigate the conditions for efficient cascaded Raman scattering. The ZDW of Fibre F is close to the operating wavelength of the pump source. This introduces efficient FWM, transferring energy to the anti-Stokes wave and resulting in the weakness of 1^{st}-order Stokes, consequently suppressing the emission of the higher-order Stokes waves. Hence, determining the optimal core diameter is the first step to ensure that the ZDW is far from the working wavelength, prioritizing the Raman scattering as the dominant nonlinear effects while minimizing the influence of FWM. Figure 3.11 (a) depicts the change of the higher-order Stokes output power with increasing core diameter. The pump wavelength is fixed at 1992 nm with the peak pump power of 10 W and a pulse duration of 125 ps, and the propagation length is 6 cm. The output power of the 1^{st}-order Stokes wave surges and saturates when the core diameter changes from 1600 nm to 1700 nm, and then slightly decreases with further increases in the core diameter due to the decreasing light intensity. It confirms that the primary limitation for the 1^{st} Stokes generated via spontaneous Raman scattering is the influence of FWM. The optimized core diameter to achieve the maximum output power of the 2^{nd}, 3^{rd}, 4^{th} and 5^{th}-order Stokes waves is around 1700 nm due to the gradual diminishing influence of FWM. Further increases in the core diameter leads to a dramatic decrease in the higher-order Stokes waves as a result of the large effective mode area. Based on the analysis of the effect of core diameter on the generation of higher-order Stokes waves, the core diameter of 1700 nm is selected for the subsequent discussion of the cascaded Raman to maximize the possibility of higher-order Stokes waves generation.

In addition to the core diameter, the pulse duration, which introduces a non-negligible FCA, is another crucial factor that influences the higher-order Stokes output power.

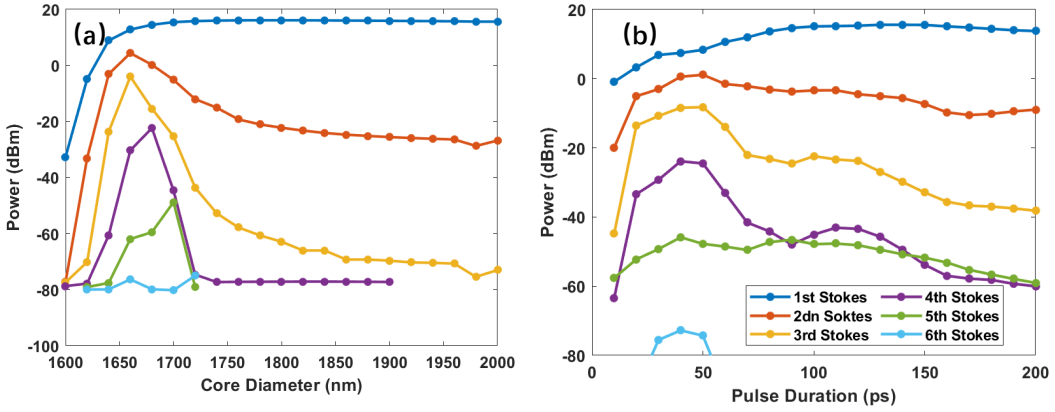

FIGURE 3.11: Higher-order Stokes output power varying with the core diameter (a) and the pulse duration(b). The pump wavelength is 1992 nm with the peak pump power of 10 W, and the propagation length is 6 cm.

Figure 3.11 (b) shows the variation in the higher-order Stokes output power with increasing pulse duration under the same calculation conditions as Figure 3.11 (a). For the 1^{st}-order Stokes wave, the decrease in output power with a pulse duration shorter than 100 ps is due to the energy transferring to the higher-order Stokes waves. According to the the variation in the 2^{nd}, 3^{rd}, 4^{th}, 5^{th} and 6^{th}-order Stokes waves, the optimal pulse duration is 40 ps, resulting in maximum output power of high-order Stokes waves. This specific pulse duration maximizes the energy transfer from the 1^{st}-order Stokes wave to the higher-order Stokes waves. The second peak of the output power of 3^{rd} and 4^{th}-order Stokes waves at the pulse duration of 120 ps arises from the competition between the nonlinear loss and the pump power. It is noteworthy that the optimized pulse duration for the mid-infrared band is consistent with that in the telecom band, suggesting that the optimal pulse duration remains the same even under distinct nonlinear loss parameters.

The evolution of the pulse spectrum within a propagation length of 20 cm is shown in Figure 3.12 (a). The pump peak power is 20 W and the pulse duration is 40 ps in this simulation. The 1^{st}, 2^{nd}, 3^{rd} and 4^{th}-order Stokes become significant over a propagation length of 3 cm, while the 5^{th}-order Stokes wave emerges a the propagation length of 15 cm. The linewidth of the higher-order Stokes waves remains narrow, and the energy is tightly confined within the Raman gain spectrum. To illustrate the variation of the different order Stokes waves along the propagation length clearly, the 1^{st} to 5^{th}-order Stokes output power is extracted from Figure 3.12 (a) and presented in Figure 3.12 (b). The 1^{st}-order Stokes wave reaches a maximum at a length of 2.5 cm, then decreases as the energy transfers to the 2^{nd}-order Stokes wave, which increases to its maximum at the same position, and eventually plateaus after 12 cm. The fluctuations in the output power are attributed to the existence of IRS [103]. The 3^{rd}-order Stokes wave increases to a maximum at the propagation length of 5 cm and then gradually decreases to a plateau. The 4^{th}-order Stokes wave peaks at a

slightly longer length of 10 cm and then maintains a level along the propagation length. The 5^{th}-order Stokes wave steadily increases along the propagation length before levelling off over the length of 20 cm. In this circumstance, the wavelength range of the energy conversion could cover from 1992 nm to 4100 nm.

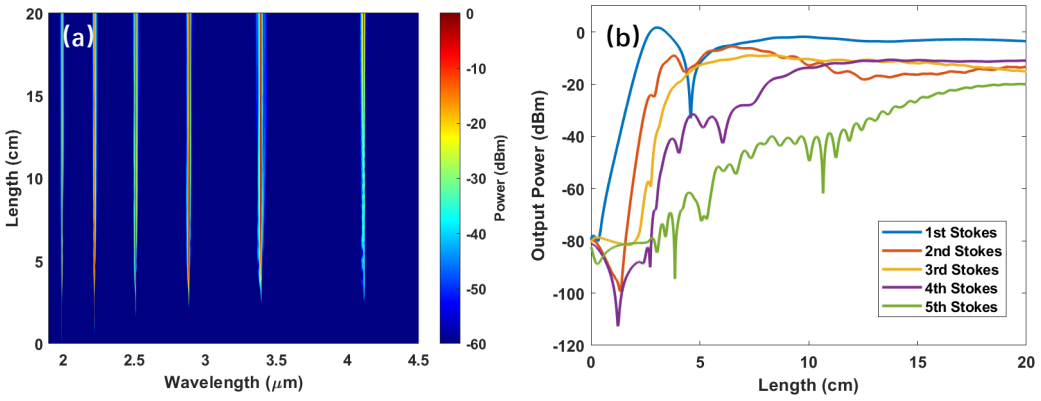

FIGURE 3.12: (a) The variation of the pulse spectrum along the propagation length. (b) Different higher-order Stokes output power as a function of the propagation length, as labeled in the legend. The pump is 1992 nm with the peak power of 20 W and the pulse duration is 40 ps.

Despite the pump wavelength being set at 1992,nm, which falls within the TPA absorption band, there is a limitation on further increasing the output power and generating higher-order Stokes waves. This limitation has inspired the consideration of moving to longer wavelengths that can be supported by similar fibre-based laser systems. Hence, the pump wavelength was tuned to a slightly longer value, 2.2 μm, which could be obtained through a holmium-doped fibre system. At this wavelength, the TPA could be negligible, enabling the use of longer pulse duration of 125 ps to be consistent with the previous experiments. Moreover, the simulations reveal that SPM becomes significant when the pulse duration is 40 ps, and using a longer pulse duration could effectively alleviate this issue. Theoretically, the three-photon absorption(3PA) and its inducing FCA should be taken into consideration at this wavelength. However, these effects are modest at the current pump intensity of $1.67 \times 10^4\,\mathrm{GW/m^2}$ and could be safely ignored, especially when compared with the typical threshold value of $10^5\,\mathrm{GW/m^2}$ at which 3PA start to exhibit significant influence [104]. The evolution of the pulse spectrum within the propagation length of 20 cm is shown in Figure 3.13 (a), where the pump peak power is 20 W. The 1^{st}, 2^{nd}, 3^{rd} and 4^{th}-order Stokes become prominent over a propagation length of 2 cm, while the 5^{th}-order Stokes wave emerges at the propagation length of 5 cm and the 6^{th}-order Stokes increases at the length of 10 cm. The increasing length of the occurrence of higher-order Stokes waves means that the Raman scattering is an accumulation effect along the propagation length. To clearly demonstrated the variation of different order Stokes waves along the propagation length, the 1^{st} to 6^{th}-order Stokes output power is extracted from Figure 3.13 (a) and presented in Figure 3.13 (b). The 1^{st}-order Stokes

wave achieves a maximum at a length of 2 cm, then fluctuates and slightly decreases as the energy transfers to the 2^{nd}-order Stokes wave, which peaks at a length of 4 cm, and finally stabilizes after 10 cm. The 3^{rd}-order Stokes wave reaches a maximum at a slightly longer length of 5.5 cm and then fluctuates up and down around the maximum value. The 4^{th}, 5^{th} and 6^{th}-order Stokes waves all increase along the propagation length, reaching maximum at lengths of 6.5 cm, 8 cm and 11.5 cm, respectively, and finally become stable over lengths of > 15 cm. It is significant that the wavelength range under these conditions could be extended to 7000 nm within the propagation length of 11.5 cm. Compared with the results obtained by pumping at 1992 nm, the absence of TPA and FCA leads to the significant appearance of SPM, XPM, and MI. This results in complex changes in the phase mismatch, leading to strong oscillations of the Stokes waves along the propagation length. This prospect provides a promising method to generate a mid-infrared light source via a robust SCF with shorter length compared to traditional fibre-based light sources [105], thereby offering the potential to minimize device size.

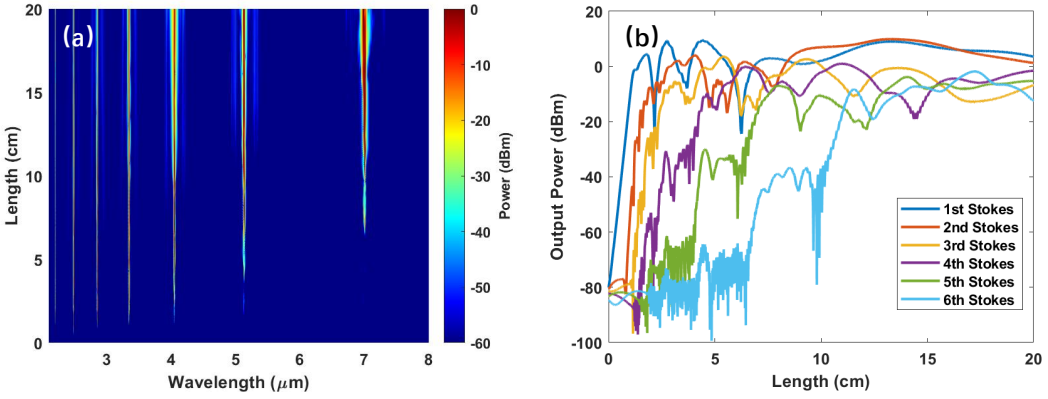

FIGURE 3.13: (a) The evolution of the pulse spectrum within the propagation length of 20 cm. (b) The variation of different order Stokes waves along the propagation length, as labeled in the legend. The pump wavelength is 2200 nm with a peak power of 20 W and a pulse duration is 125 ps.

3.3 FWM and CARS in SCFs in the mid-infrared band

Wavelength conversion in the mid-infrared band using fibre-based system is beneficial to the free-space communication [106]. However, achieving a stable and durable fibre system in the mid-infrared band is challenging. SCFs, known for the transparency in the mid-infrared band, is a standout platform due to the large nonlinearity and stability in this wavelength range. Successful demonstration of broadband FWM in the telecom band has been achieved in SCFs with a bandwidth of ~ 260 nm via a pulsed pump [6]. However, this achievement is limited by the strong TPA. The promotion of tunable wavelength conversion in the mid-infrared band aims to

develop efficient fibre laser sources using SCFs. In this project, I collaborated with Dong Wu et al. to refine the theoretical analysis in the simulation section. Here, FWM is the core mechanism for realizing wavelength conversion, which highly depends on the phase matching condition. To meet the phase matching condition, the ZDW of the targeted SCF should align with the experimental pump wavelength, 1992 nm, supported by the fibre laser that was used for the mid-infrared Raman scattering experiments. As mentioned previously, dispersion parameters are crucial for FWM to satisfy the phase matching conditions, and higher-order dispersion terms including third- and fourth-order need to be considered when the frequency range is large. In all simulations, the dispersion parameters are calculated by the software package COMSOL. Directly calculating the gradient of the propagation constant by using the gradient operator leads to invalid results due to the discontinuity of the propagation constant. Hence, the three-point numerical differential method is adopted [107]:

$$D = -\frac{1}{2\pi c}\frac{(\lambda_0 + \frac{d\lambda}{2})^2(\beta_{\lambda_0+d\lambda} - \beta_{\lambda_0}) - (\lambda_0 - \frac{d\lambda}{2})^2(\beta_{\lambda_0} - \beta_{\lambda_0-d\lambda})}{d\lambda^2} \tag{3.4}$$

where λ_0 is the central wavelength, $d\lambda$ is the frequency spacing, β_{λ_0} and $\beta_{\lambda_0+d\lambda}$ are the propagation constants at the corresponding wavelengths. Higher-order dispersion parameters can be calculated by using the same mathematical method. Through testing and verifying this method with references [6], the accuracy of the simulation dispersion parameters is ensured.

The dispersion profile for SCFs can be adjusted by controlling the core diameter, and β_2 as a function of wavelength for SCFs with different core diameter are shown in Figure 3.14 (a). The ZDW moves to the longer wavelength when the core diameter increases. The intended core diameter of the SCF designed for this work is 1600 nm according to the position of the ZDW. The actual tapered core diameter of the fabricated fibre, Fibre G, is 1590 nm, and its details are provided in Appendix A. The conversion efficiency (CE), traditionally adopted to evaluate the FWM performance, is defined as the power difference (in dB) between the induced idler (P_{idler}) and the input signal (P_{signal}):

$$CE = 10 \times log_{10}\frac{P_{idler}}{P_{signal}}. \tag{3.5}$$

The conversion efficiency as functions of core diameter and signal wavelength is demonstrated in Figure 3.14 (b). The average pump power is 4 mW, the signal is a CW laser with a fixed power of 4 mW, and the propagation length is 4 cm, consistent with the experimental conditions. The maximum conversion efficiency could be up to

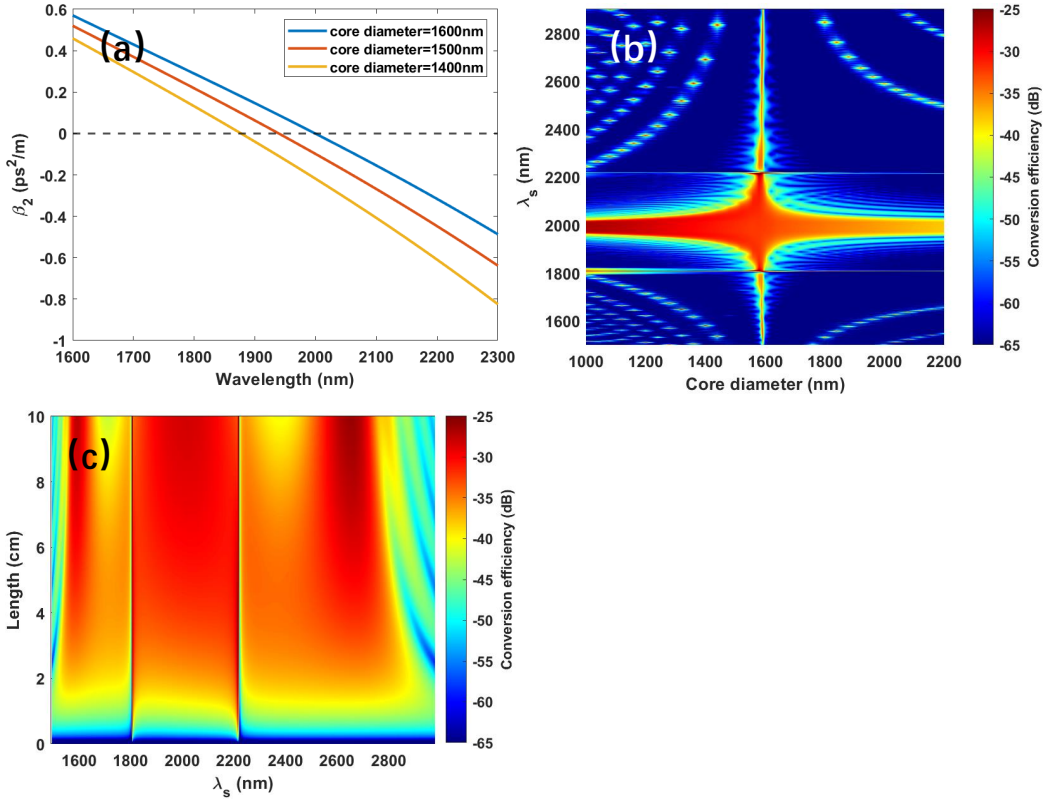

FIGURE 3.14: (a) The second-order dispersion parameter (β_2) of SCFs with three different core diameters, as labeled in the legend. (b) The conversion efficiency as functions of signal wavelength and core diameter with the propagation length of 4 cm. (c) Conversion efficiency as functions of propagation length and signal wavelength with the core diameter of 1600 nm. The pump is fixed at 1992 nm with the average pump power of 4 mW and the power of the CW signal is 4 mW.

-25 dB with a minimized core diameter of 1000 nm, which is attributed to the large light intensity as a result of the small effective mode area. However, the 3 dB bandwidth is only 48 nm for the large phase mismatch at this pump wavelength. The 3 dB bandwidth of the SCF with core diameter of 1590 nm reaches up to about 1255 nm and the conversion efficiency is -32 dB, which is suitable to realize the broadband tunable wavelength conversion. The conversion efficiency varying along the propagation length is investigated in Figure 3.14 (c). The wider 3 dB bandwidth can be achieved at the propagation length of 2 cm compared with that at the length of 4 cm but the CE is only -40 dB. The conversion efficiency could continue to increase to -25 dB with increasing propagation length, nevertheless, the 3 dB bandwidth also decrease dramatically over the propagation length of 8 cm. The experimental broadband wavelength conversion has been realized and reported in [108] with a bandwidth of 380 nm and a conversion efficiency of -30 dB, as illustrated in Figure 3.15.

The significant peak at the Raman wavelength shift, which is obvious in Figure 3.14 (b) and Figure 3.14 (c), can be attributed to CARS and CSRS. To further explore the

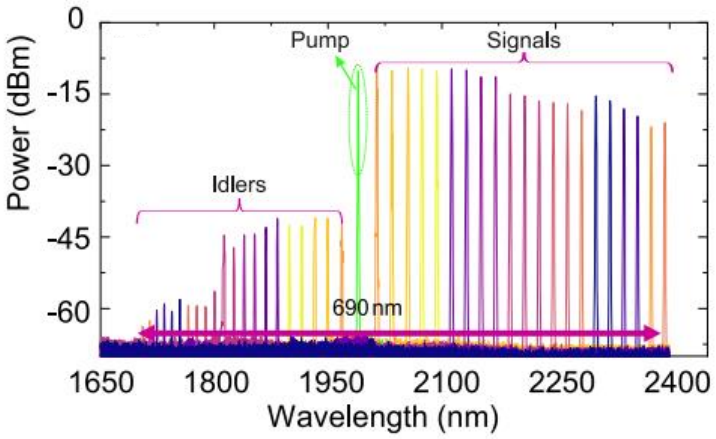

FIGURE 3.15: Output spectra of Fibre G with the signal wavelength switching from 2000 nm to 2400 nm while pumping at 1992 nm. Both the coupled-in pump power and signal power are fixed at 4 mW.

phenomenon at the Raman wavelength shift, the conversion efficiency of Fibre G with the core diameter of 1590 nm is extracted from Figure 3.14 (b) and depicted in Figure 3.16 (a). The two peaks appearing at the Raman shift are known as CSRS (left side) and CARS (right side), respectively. In the FWM experiment, CARS was observed which is displayed in Figure 3.16 (b). The red dots are the experimental results, which are perfectly consistent with the simulation results that are denoted by the blue line. The conversion efficiency maintains -32 dB from 2000 nm to 2200 nm and dramatically increases to -18 dB at the Stokes wavelength of 2217 nm, which is due to the interaction between the Raman scattering and FWM. This validates the enhancement of FWM through Raman scattering, which could be feasible in practice. The simulation, as shown in Figure 3.16 (a), suggests that CSRS could achieve a higher conversion efficiency, 3 dB larger than CARS, because the efficiency of generating the Stokes wave is higher than that of generating the anti-Stokes wave.

In this chapter, Raman scattering in both the telecom and mid-infrared bands were successfully demonstrated using SCFs with a CW and a pulsed pump,respectively. These validated that a remarkable gain can be achieved within an exceptionally short length when compared to traditional silica fibres. The exploration of tunable broadband FWM in the mid-infrared band, utilising a pulsed pump, reveals the potential for strong RE-FWM in SCFs to enhance the efficiency. Researches on the Raman scattering and FWM indicate that employing a CW pump source for a single nonlinear effect has limitations in terms of wavelength conversion efficiency. Consequently, RE-FWM became the main focus of the following study, with CSRS identified as the primary objective for further research due to its potential for superior efficiency.

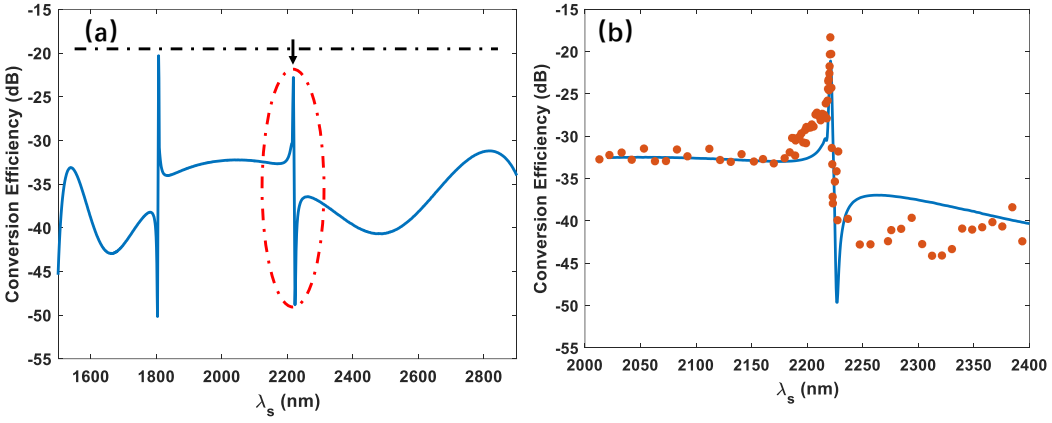

FIGURE 3.16: (a) The conversion efficiency for Fibre G with the core diameter of 1590 nm extracted from Figure 3.14 (b). (b) The comparison of the conversion efficiencies varying with the signal wavelength between the experimental data (red dots) and the simulation results (blue line).

Chapter 4

Coherent Stokes Raman scattering in SCFs

In recent years, advancements in SCF designs and increasingly mature tapering techniques have paved the way for dispersion engineering and low propagation losses [102], enabling the achievement of the net parametric gain. However, the efficiency of the wavelength conversion by FWM [109][108], even with pumping near the ZDW, or via Raman scattering [110][111] is still modest. The observation of Raman scattering and CARS in SCFs proves beneficial for realizing RE-FWM. Facilitated by Raman scattering, the FWM conversion efficiency experiences growth, and the power of the generated idler at the Stokes wavelength can be improved if the SCF is seeded by a weak signal at the anti-stokes wavelength. This phenomenon holds promise for applications such as amplifiers and light sources, that demand stronger Stokes output power when using SCFs. CSRS will be illustrated as the focus of this chapter. This part includes a demonstration of the CSRS implementation and observation principles, as well as a corresponding introduction to the experimental setup, experimental results and simulation analysis in the telecommunications and mid-infrared frequency bands. The results reveal the advantages and limitations of the different nonlinear phenomena. Comparison of the nonlinear performance at different wavelengths provides guidance for the design of SCF structures and working conditions. In this work, I was responsible for the simulations, partial fibre tapering, major fibre polishing, setup building, and nonlinear experiments.

4.1 Demonstration of the principle

As demonstrated in Figure 2.15, there are three nonlinear processes contributing to the Stokes wave. To qualitatively analyse the nonlinear processes during the light propagation, especially the influence of Raman scattering, the output power of the

pump, signal and idler for Fibre A are calculated as an example as shown in Figure 4.1. Linear and nonlinear losses are neglected in this analysis. In this simulation, the pump wavelength is set at 1545 nm with the power of 100 mW and the signal wavelength is 1432 nm with the power of 2 mW. The adjustment of f_R is intended to include or exclude Raman scattering, while the variation in β_2 is aimed at controlling the efficiency of FWM. The results of Raman scattering denoted by blue lines are calculated with $\beta_2 = 1\,\mathrm{ps}^2/\mathrm{m}$ and $f_R = 0.043$, that of FWM denoted by red lines are calculated with $\beta_2 = -0.16\,\mathrm{ps}^2/\mathrm{m}$ and $f_R = 0$, that of RE-FWM denoted by yellow lines are calculated with $\beta_2 = -0.16\,\mathrm{ps}^2/\mathrm{m}$ and $f_R = 0.043$. In Figure 4.1 (a), the pump power of Raman scattering almost linearly increases within the propagation length of 1 cm as a result of IRS that transfers energy from the anti-Stokes wave back to the pump. This behavior is consistent with the performance of the signal that linearly decreases along the propagation length, as depicted in Figure 4.1 (b). The growth starts to slow down as the energy of the pump transfers to the induced Stokes wave, which fluctuates and slightly increases as shown in Figure 4.1 (c). The oscillation and small increase slope of the idler generated by Raman scattering is attributed to the minimal noise in this simulation, which in turn leads to low efficiency of spontaneous Raman scattering. The pump power of the FWM decreases along the propagation length, as Figure 4.1 (a) shows, and the corresponding powers of signal and idler increase at the same time, as shown in Figure 4.1 (b)and (c). This indicates that the pump photons experience a continual consumption during FWM process. The pump power of CSRS displayed in Figure 4.1 (a) initially gains energy from the anti-Stokes signal which aligns with that for Raman scattering, and the consumption by FWM and Raman scattering is negligible. Meanwhile, the anti-Stokes signal wave shown in Figure 4.1 (b) firstly attenuates within the propagation range of 2 cm, which is consistent with the gain of the pump. As the propagation length increases, the gain of the anti-Stokes and Stokes waves due to FWM and Raman scattering start to dominate, leading to the decrease of the pump power and the growth of the signal and idler. Another interesting point is that the overall trend of idler power of CSRS is similar to that of FWM, which confirms that FWM is the foundation of CSRS. The variation of pump power validates the main processes contributing to CSRS, including IRS, SRS and FWM.

4.2 CSRS in the telecom band

4.2.1 Dispersion properties and simulations for CSRS

As mentioned in the background, the foundation of CSRS is FWM which heavily relies on the phase matching condition to achieve high conversion efficiency. Figure 4.2 (a) shows the variation of β_2 with the increasing core diameter at the wavelength of

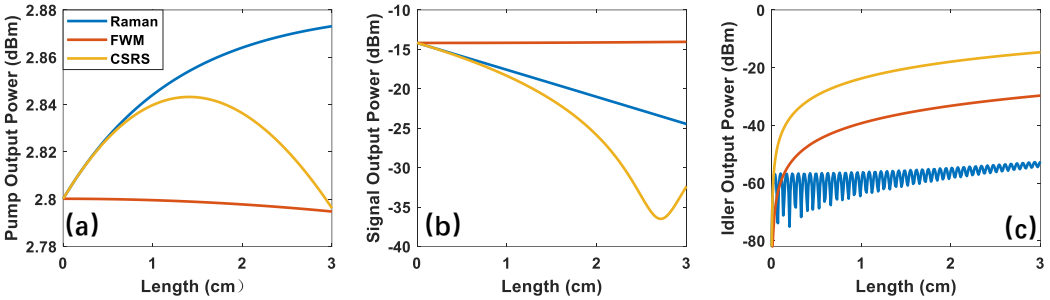

FIGURE 4.1: (a) Pump output power, (b) signal output power and (c) idler output power changing along the propagation length for different nonlinear process under no loss conditions, as labeled in the legend. The pump is 1545 nm with the power of 100 mW, the signal is 1432 nm with the power of 2 mW and the propagation length is 2 cm.

1545 nm. It is evident that the value of β_2 increases with the core diameter from negative to positive value and equals to zero when the core diameter is 930 nm. This suggests that the target size of tapered SCF should be around 920 nm. In practice, fabricated SCFs, Fibre A, Fibre C, Fibre D and Fibre E with core diameters of 750 nm and 860 nm are applied in this experiment. The dispersion profiles are depicted in Figure 4.2 (b), in which SCF with the core diameter of 860 nm has smaller phase mismatch than that of SCF with the core diameter of 750 nm at the specific pump wavelength of 1545 nm, which is denoted by red graded zone. The corresponding anti-Stokes and Stokes wavelength are denoted by green solid line and yellow graded zone, respectively.

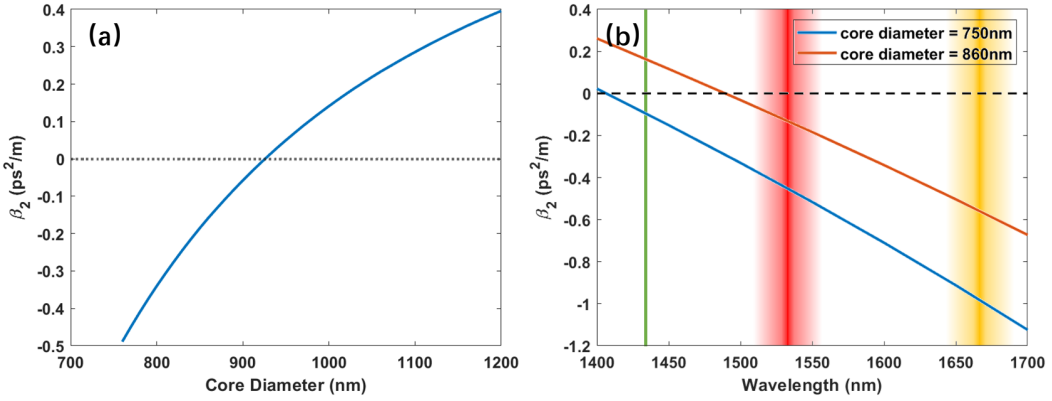

FIGURE 4.2: (a) Variation of β_2 as a function of core diameter at the wavelength of 1545 nm. (b) The dispersion profiles for SCFs with core diameters of 860 nm and 750 nm.

In order to investigate the impact of core size on the RE-FWM conversion efficiency in SCFs working at 1545 nm, the conversion efficiency is plotted as a function of λ_s as the core diameter is changed from 800 nm to 1000 nm as shown in Figure 4.2. This analysis aims to determine the optimised core dimension and validate this design for the existing tapering techniques. The pump power is 100 mW and the signal power is

5 mW. The propagation length is set to 1 cm to avoid the generation of higher-order Stokes and anti-Stokes waves due to the accumulation of Raman gain with increasing propagation length. The linear loss is assumed to be 1 dB/cm, based on average values from our fabrication of SCF. The bandwidth is at a maximum, ~ -30 dB, when the core diameter is equal to the optimum value of ~ 920 nm, while it shrinks rapidly when the core diameter increases or decreases from this value. This is consistent with the dispersion change in Figure 4.2 (a). Peaks at the anti-Stokes and Stokes wavelength representing CSRS and CARS, respectively, are strongly excited on both sides of the central band when the bandwidth of FWM overlaps with the Raman gain spectrum. The conversion efficiency of CSRS is displayed in Figure 4.3 (b), which has been extracted from the region marked by the black dash box in Figure 4.3 (a). The reference conversion efficiency is set as -15 dB, as denoted by the dashed line, which is around 4 dB less than the maximum conversion. Based on this reference value, we can determine the fabrication tolerance of SCF working at this wavelength to be 30 nm, which is outside the tolerance of existing tapering techniques, 100 nm. Therefore, it is challenging to achieve the SCF with the right core size, and the SCFs we tapered for this work are listed previously.

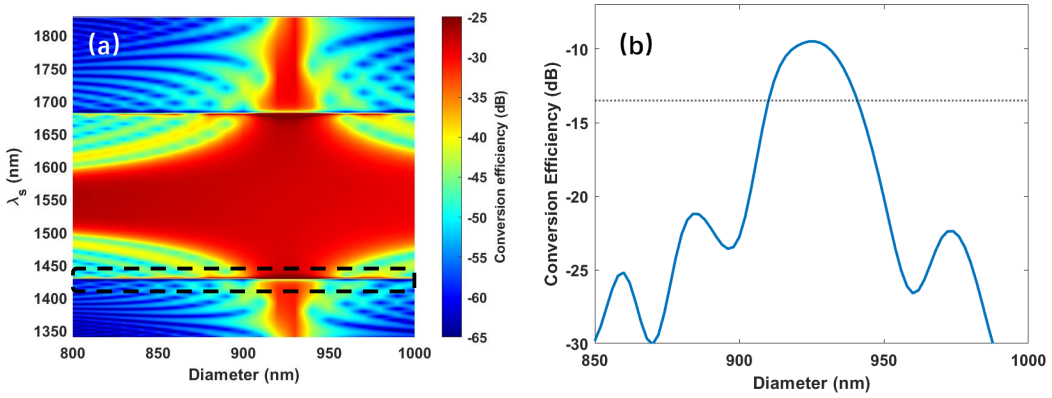

FIGURE 4.3: (a) Conversion efficiency as functions of core diameter and λ_s. (b) shows the conversion efficiencies of the CSRS processes, marked with black dash box in (a), where signal is tuned to the anti-Stokes wavelength of 1430 nm. In all cases the pump wavelength is 1545 nm with a power of 100 mW, the signal power is 5 mW and the propagation length is 1 cm.

To explore the conditions for obtaining the maximum conversion efficiency, the variation trends of conversion efficiency as functions of pump power and propagation length in the SCF with the core diameter of 920 nm are conducted and depicted in Figure 4.4 (a). The pump wavelength is 1545 nm and the signal is 1432 nm, with a power of 5 mW in this simulation. The maximum conversion efficiency of 45 dB could be obtained in SCF with the pump power of 190 mW and the propagation length of 3.6 cm. The saturation propagation length is consistently limited to 3 cm for any pump power, suggesting a promising approach to minimize the device size compared to traditional highly nonlinear glass fibres. For the pump power smaller than 120 mW, the conversion efficiency remains stable along the propagation length after achieving

the maximum. At the same time, for a fixed length shorter than 3.6 cm, the conversion efficiency also stabilizes with the pump power after reaching the maximum. The distribution of the dark red region, representing the maximum conversion efficiency suggests that high conversion efficiency could be obtained within the power of 110 mW to 210 mW within lengths between 6 cm and 3.2 cm. Further increasing the propagation length or the pump power leads to a decrease of conversion efficiency as a result of the occurrence of the higher-order Stokes and anti-Stokes waves. In addition to achieving high conversion efficiency, generating a large Stokes output power is another objective that can be applied to Raman amplification and light sources. The variation trend of the Stokes output power with changes in pump power and propagation length is analyzed under the same calculation conditions. The maximum Stokes output power, 562 μW, can be attained with a pump power of 190 mW and a propagation length of 3.2 cm in the SCF, as clearly shown in Figure 4.4 (b). The decrease in output power with increasing pump power over 190 mW is attributed to the nonlinear absorption, FCA and TPA, while the decline in output power along the propagation length over 3.2 cm is due to both the linear loss and the generation of higher-order Stokes and anti-Stokes waves.

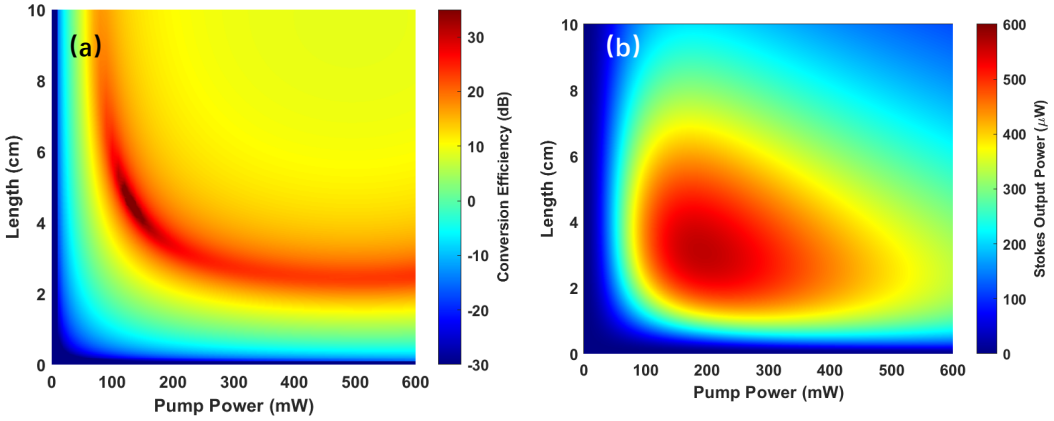

FIGURE 4.4: (a) Conversion efficiency and (b) Stokes output power as functions of pump power and propagation length for the SCF with the core diameter of 920 nm when pumping at 1545 nm with a 5 mW signal beam positioned at 1430 nm.

The conversion efficiency is 20 dB higher than that achieved in SCFs by pure FWM [6] with the same pump power level and propagation length. The Stokes output power is six orders of magnitude larger than that supported by the Raman scattering alone [110]. The simulation results suggest that CSRS could offer better performance in terms of high conversion efficiency and large Stokes output power. Furthermore, they provide guidance for the fabrication of the core size and length of SCFs, as well as for the experimental conditions.

4.2.2 Experimental setup

Figure 4.5 shows the experimental setup for CSRS experiments in the telecom band. A tunable CW laser covering from 1500 nm to 1680 nm was used as the pump source and a CW laser working at 1431 nm acted as a signal wave. Two polarization controllers were adopted to optimize the FWM conversion efficiency between pump and signal. Then a wavelength-division multiplexer was inserted to combine the two beams. Two optical couplers were used for the measurement of the input and output powers by power meters. The light coupling in/out of the SCF is through taper lens fibres. The output spectrum was monitored by an optical spectrum analyzer. Fibre A, Fibre C, Fibre D and Fibre E were tested to assess the potential relatively stronger Raman scattering and larger FWM conversion efficiency at the Stokes wavelength when operating individually. Moreover, these fibres have similar loss but different lengths and diameters, which may lead to different performance in gain enhancement that will be discussed later. To test Raman enhancement in the FWM experiments, the signal wavelength should ideally be tuned near the anti-Stokes wavelength. However, limitation of the existing light sources in the laboratory means that we instead had to fix the signal and tune the pump wavelength to confirm if there was any increase in the conversion efficiency due to coupling to Raman effects.

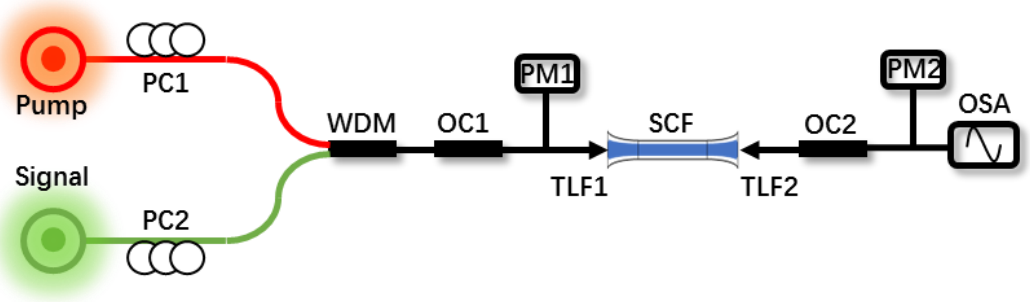

FIGURE 4.5: Experimental setup for CSRS in the telecom band. PC, polarization controller; WDM, wavelength-division multiplexing; PM, power meter; OC, optical coupler; TLF, taper lens fibre; OSA, optical spectrum analyzer.

4.2.3 Experimental verification

To assess the distinction between the two approaches, moving pump wavelength and moving signal wavelength, simulations of the conversion efficiency of CSRS based on Fibre A through the different methods, as labeled in the legend, are calculated and given in Figure 4.6. During the simulation process, only the frequency of the signal needs to be adjusted when a moving signal wavelength is adopted. On the other hand, the dispersion value, TPA coefficient and the pump wavelength need to be altered when the pump wavelength is moved. When the idler wavelength is shorter than Stokes wavelength, the red dashed line is slightly offset upward relative to the

blue line. Overall, these two curves approximately coincide with each other, especially when the idler wavelength is larger than Stokes wavelength. Meanwhile, the higher the pump power, the smaller the difference between the results of the two methods. Therefore, a narrow variation range of the pump wavelength would introduce a small change of the dispersion, but it has limited impact on the conversion efficiency. Thus, this experimental method is trustworthy.

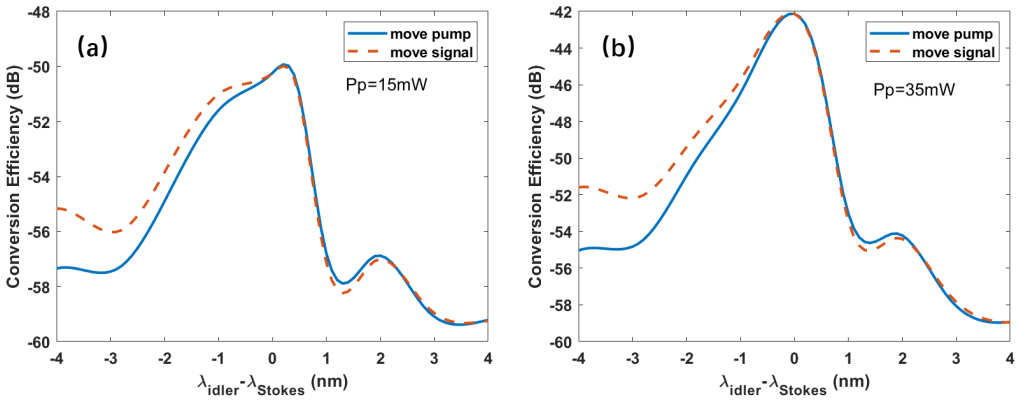

FIGURE 4.6: Comparison between two approaches: moving pump wavelength (blue solid line) and moving signal wavelength (red dashed line) under different pump powers, (a) 15 mW and (b) 35 mW.

The conversion efficiency comparisons between experimental data and simulation results for Fibre A under different pump powers are shown in Figure 4.7 (a). The signal power is fixed at 2 mW in the experiments. As the FWM generated idler wavelength (λ_i) moves closer to the peak Raman wavelength (Λ_R), the conversion efficiency increases by over an order of magnitude, from ~ -60 dB up to ~ -50 dB and ~ -57 dB up to ~ -44 dB for the pump powers of 12 mW and 25 mW, respectively, with a clear peak when the offset is zero. The peak at the Raman shift is due to CSRS and the experimental conversion efficiency is consistent with that of the simulations. To better understand the observed enhancement, the results were compared with simulations of the GNLSE conducted both with (solid curve) and without (dashed curve) the Raman term turned on. The conversion efficiency of CSRS and FWM grows with the increasing pump power. A significant feature is that the improvement of the conversion efficiency of Fibre A increases from about 11 dB to 15 dB when the pump power increases from 12 mW to 25 mW. Hence, the conversion efficiency increases with higher pump powers because higher pump powers introduce stronger nonlinear effects including FWM and Raman scattering. This observation indicates that the conversion efficiency could be further improved if the input power coupling in the fibre increases. To quantitatively analyze the influence of the pump power, the comparison of the conversion efficiency of FWM and CSRS, for Fibre A, when pumping at 1545 nm, are given in Figure 4.7 (b). The conversion efficiency of FWM linearly increases with pump power when the pump power is far from the

saturation point. The conversion efficiency of CSRS shows a similar trend to that of FWM but with a steeper slope. The two green dots on the plot represent the corresponding conversion efficiency in Figure 4.7 (a) observed in the experiments. The enhancement of the conversion efficiency, as depicted in Figure 4.7 (c), undergoes a surge with the increasing pump power, maintaining consistency with the variation of the conversion efficiencies of CSRS and FWM. The continual increase in simulations indicates that higher pump powers could achieve higher enhancement as well as higher conversion efficiency.

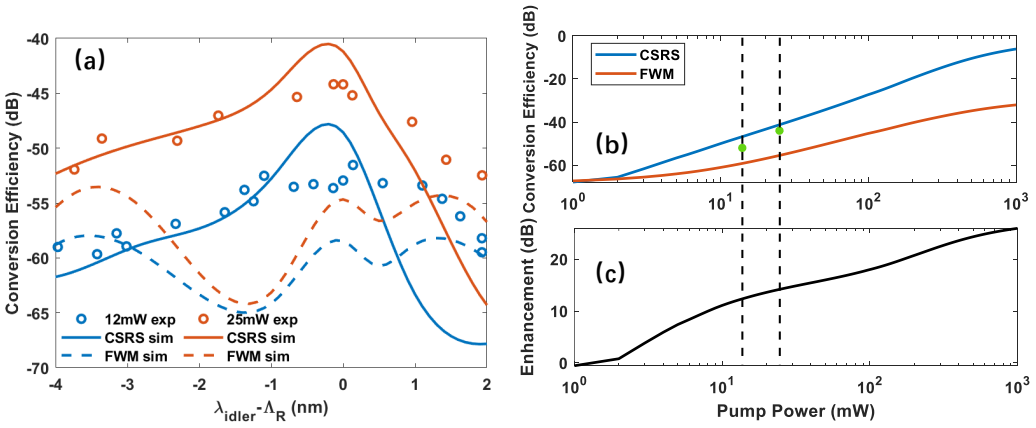

FIGURE 4.7: (a) Conversion efficiency as λ_i is tuned across Γ_R for Fibre A under different pump powers, 12 mW and 25 mW, as labeled in the legend. The experimental results are compared with simulations of CSRS and FWM only. (b) Conversion efficiency at the Raman peak with the increasing pump power under different conditions: FWM ($f_R = 0$) and CSRS ($f_R = 0.043$). (c) Enhancement of the conversion efficiency compared between CSRS and FWM.

To study the influence of the phase matching condition on CSRS, Fibre A, Fibre C and Fibre D, which have the same waist length of 1 cm but different waist diameters of 860 nm, 760 nm and 750 nm, respectively, are compared in experiments. Considering the variation of β_2 with the change in core diameter, as illustrated in Figure 4.2 (a), the absolute value of β_2 is close to zero for Fibre A, smaller than that for Fibre C and for Fibre D. The experiments were conducted with a pump power of $\sim$ 28 mW and a signal power of only 2 mW. The maximum conversion efficiency at the Raman peak decreases with the core diameter decrease, regardless of CSRS or FWM, as a result of the enlarging phase mismatch. The simulated results under these conditions are in good agreement with the experiments. The enhancement of the conversion efficiency under different phase matching conditions is $\sim$ 15 dB, $\sim$ 12 dB and $\sim$ 9 dB for the 860 nm, 760 nm and 750 nm diameters, respectively. Although, the enhancement decreases with the phase mismatch, it is still considerable with a low level of pump power.

Interestingly, when comparing the simulated FWM conversion efficiencies without Raman, we notice that these curves oscillate. We attribute this behavior to changes in the phase-matching conditions, and thus the energy transfer between the waves, as

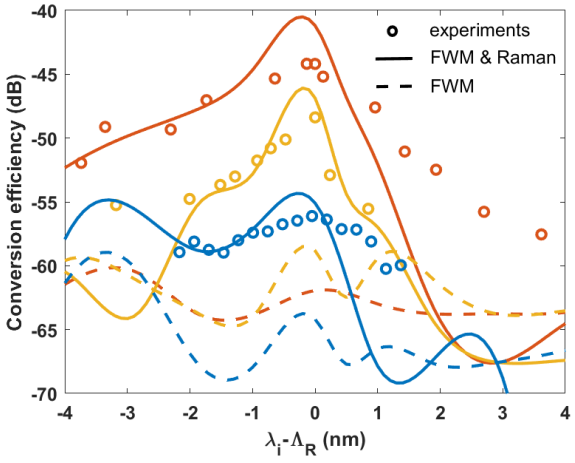

FIGURE 4.8: Conversion efficiency as λ_i is tuned across Γ_R for Fibre A (orange), Fibre B (yellow) and Fibre C (blue). The experimental results are compared with simulations of CSRS and FWM, as labeled in the legend.

the pump is tuned. Due to the phase mismatch, the energy transfer will also vary as the SCF length is changed, thus regarding to the previous simulation, the maximum FWM conversion will depend on propagation length. To better understand the length dependence of the conversion efficiency, Fibre E was fabricated with the same core waist diameter with Fibre A, but with a longer length of 1.54 cm. Figure 4.9 (a) plots the measured conversion efficiency as the pump is tuned to position the idler closer to the peak Raman shift for the two SCF lengths. For these experiments, the pump power was reduced slightly to 14 mW, but the signal power remained fixed at 2 mW, resulting in a reduced Raman enhancement of $\sim$ 4 dB for the 10 mm fibre (orange circles), as estimated from the simulation results. Although we might expect the Raman gain to increase for increasing fibre length, as the conversion process is initiated by FWM, we find that both the conversion efficiency and enhancement are reduced for the 1.54 cm SCF, by around 7 dB and 4 dB, respectively. This can be understood via plots of the simulated conversion efficiency as a function of length shown in Figure 4.9 (b), where it is clear that the FWM conversion efficiency varies greatly as the waves move in and out of phase, and that SRS only serves to amplify the conversion rather than alter the trend. From this plot it is clear that the shorter SCF length corresponds to a peak in the FWM conversion, whilst the longer SCF is positioned at a minimum. Importantly, this result also helps us to explain the relatively high conversion efficiency obtained for the 760 nm core diameter SCF compared with the 750 nm SCF in Figure 4.8, as the 1 cm length used in these investigations is closer to the optimal length for the larger core fibre.

Moreover, the conversion efficiency of FWM is inherently small due to the imperfect phase matching condition among pump, Stokes waves and anti-Stokes waves in the SCF used in experiments, which confirms that the limitation of CSRS is the mismatch

between the gain spectra of FWM and Raman scattering. One possible approach to improve the enhancement is careful dispersion engineering of SCFs which could expand the bandwidth of FWM to overlap with the Raman gain spectrum, as shown in Figure 4.3. According to our fabrication experience, obtaining the optimal core size is quite challenging because the manufacturing tolerance of $\sim 100\,\text{nm}$ is considerably larger than the calculated fabrication tolerance of 30 nm. Another possible method that is feasible in the laboratory is switching the operating pump wavelength and the corresponding signal wavelength.

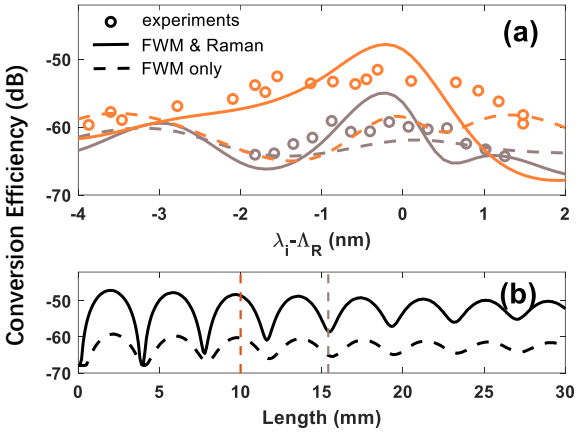

FIGURE 4.9: (a) Comparison of the conversion efficiency as λ_i is tuned across Λ_R for Fibre A (orange) and Fibre E (gray). Experiments are compared with simulations of CSRS and FWM, as labeled in the legend. (b) Simulated conversion efficiencies as a function of tapered waist length conducted both with (solid) and without Raman (dashed). The vertical lines mark the waist lengths for the SCFs in (a).

Although our results have shown that significant enhancements to the FWM conversion efficiency can be obtained with a phase-mismatch, much stronger enhancements should be attainable for a system that is perfectly phase-matched, i.e., correct SCF core diameter, pump and signal wavelengths, resulting in more practical output idler powers. Figure 4.10 plots simulation results of the conversion efficiency as functions of core diameter and pump wavelength. To compensate for the changing core diameter, the simulations were conducted with a fixed pump intensity of $8.6 \times 10^{11}\,\text{W/m}^2$, which corresponds to a peak power of 340 mW for a diameter of 860 nm, and signal power of 2 mW. It is notable that for these simulations higher pump powers were chosen such that they allowed for the maximum conversion efficiency to be achieved, even though TPA and TPA-induced FCA are no longer negligible. In all cases the tapered SCF length was fixed at 1 cm as increasing the length beyond this did not significantly increase the output efficiency. As can be seen, for each SCF core diameter there is an optimum pump wavelength that satisfies the phase-matching conditions, allowing for large conversion efficiencies of up to 2.3 dB, which equates to usable Stokes output powers of several μW for these pump/signal powers. Significantly, these results provide the first indication that FWM conversion

efficiencies exceeding 0 dB can be achieved in silicon waveguide systems when pumped in the telecom band with a CW source, without the need for complex p-i-n diode [112] or ring resonator structures [113]. Comparing Figure 4.10 with simulations conducted without the Raman term, the gain enhancement due to the nonlinear coupling can reach as high as 28 dB. Moreover, due to the strong coupling to the Raman term, the system is also fairly robust to changes in the pump wavelength and core size, with high conversion efficiencies being maintained over a wavelength band of ~ 20 nm and a ~ 25 nm variation in the diameter. The red shifting of the optimum pump wavelength to allow for phase-matching as the core diameter increases is consistent with the shift in the dispersion profiles seen in Figure 4.2 and highlights the convenience and flexibility of the tapered SCF platform to cover broad wavelength regions. Furthermore, by fabricating nano-spike couplers onto the SCF facets, these fibres can also be spliced directly into conventional fibre networks, allowing for the construction of robust systems.

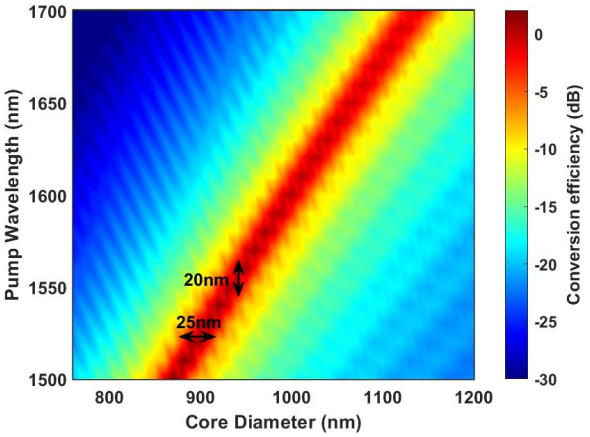

FIGURE 4.10: Simulated conversion efficiency as functions of the tapered SCF core diameter and pump wavelength, for a fixed length of 1 cm. The input pump intensity is set as 8.6×10^{11} W/m^2, with a signal power of 2 mW.

It is difficult to distinguish the differences in Stokes output power arising from CSRS, FWM and Raman scattering in the experiment. Hence, Figure 4.11 (a)provides a comparison of idler output power for propagation with FWM only, Raman only and the combined effects of CSRS using Fibre A with pump at 1545 nm under varying input power. When calculating FWM, $F_R = 0$, excluding the Raman response; when calculating Raman scattering, $Ps = 0$ mW , removing the FWM phenomenon; when calculating CSRS, $f_R = 0.043$ and $Ps = 2$ mW , containing both FWM and Raman scattering. For Raman scattering, the Stokes output power reaches a maximum with a pump power of 180 mW, and then gradually decreases due to nonlinear absorption. For FWM, the Stokes output power surges with the increasing pump power, reaching saturation when the pump power further increases to 250 mW. Due to the existence of nonlinear losses, the idler power slightly drops for high pump powers. The Stokes output power of CSRS has a similar trend as that of FWM, differing in the slope of the

initial surge, validating that FWM is the foundation of CSRS. The enhancement of the Stokes output power, as depicted in Figure 4.11 (b), could be increased further, up to $\sim$ 20 dB, by increasing the pump power and sustains such a high level even with presence of nonlinear loss. The saturation point is at few hundreds of milliwatts, while the coupling power in the SCFs in the experiments is limited, and it is hard to achieve values larger than 50 mW. Thus, the effect of the nonlinear loss could be ignored in experiments and the Stokes output power is weak.

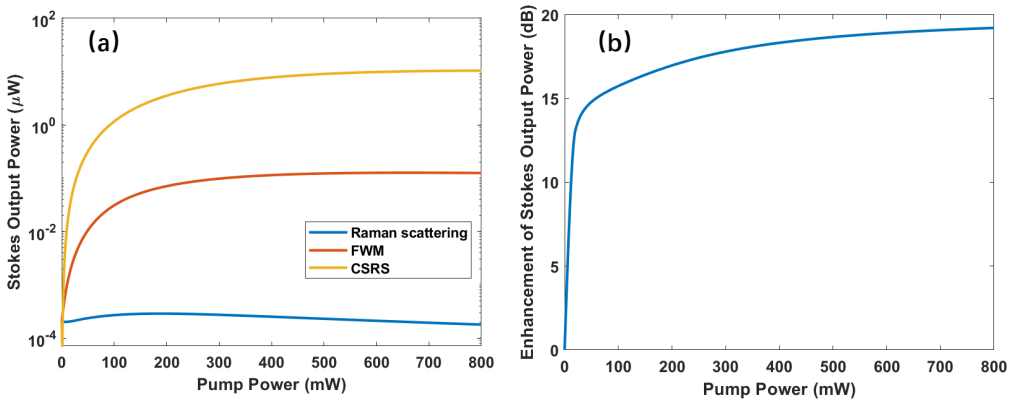

FIGURE 4.11: (a) Comparison of the normalized idler output power with the increasing pump power under different conditions: FWM, Raman scattering and CSRS for fibre A with pump at 1545nm. (b) Enhancement of the Stokes output power as a function of pump power, which is the difference between the output power of CSRS and FWM in (a).

In summary, this work has demonstrated that by coupling the FWM and Raman terms in low loss tapered SCFs it is possible to achieve a significant enhancement of the conversion efficiency and Stokes output power for CW pump beams with fairly modest power levels. Our experiments have shown that the maximum conversion efficiency depends on the phase-matching conditions and length of the tapered waist, but that substantial enhancements up to $\sim$ 15 dB can be obtained even under non-phase-matched conditions. By tailoring the core size to optimize the phase-matching, it should be possible to obtain large FWM conversion efficiencies of the order of a few dB without the need for complex carrier sweep-out schemes [112], or the use of pulsed pumps [5].

4.3 CSRS in the mid-infrared band

A critical limitation of the nonlinear performance in the telecom band is the nonlinear absorption, TPA and FCA. However, these effects can dramatically decrease when moving to longer wavelengths, even becoming negligible beyond 2.2 μm. CSRS will be explored in the mid-infrared band to achieve a higher conversion efficiency and a

larger Stokes output power, offering another promising method to realize the light amplifiers and light sources in the mid-infrared band in fibre systems.

4.3.1 Dispersion properties and simulations for CSRS

The first step in studying CSRS in the mid-infrared band involves analyzing the dispersion profiles for SCFs with various core sizes at a specific pump wavelength to determine the optimized core diameter. Figure 4.12 (a) shows the variation of β_2 with increasing core diameter at the wavelength of 2170 nm. The trend of β_2 with the core diameter is similar to that in the telecom band, transitioning from negative to positive and equaling zero when the core diameter is 1890 nm. This suggests that the target size of tapered SCF should be around 1890 nm. It is noteworthy that the effective mode area of SCFs working in the mid-infrared band is almost ~ 5 times larger that that working in the telecom band, leading to the need for higher injected pump power. In practice, fabricated SCFs, Fibre H and Fibre I with core diameters of 1976 nm and 1984 nm are applied in this experiment. The dispersion profiles are depicted in Figure 4.12 (b), where the SCF with the core diameter of 1976 nm remains positive, similar to that of SCF with the core diameter of 1984 nm, but with a smaller phase mismatch at the wavelength of 2170 nm.

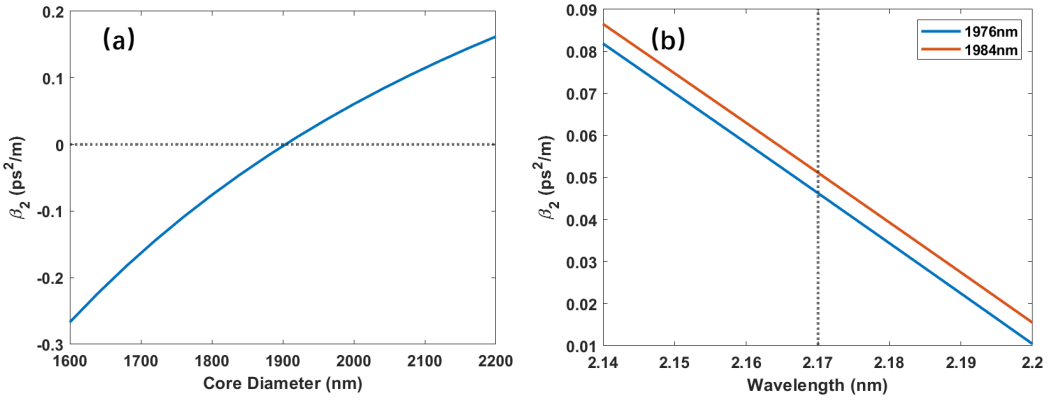

FIGURE 4.12: (a) Variation of β_2 as a function of core diameter at the wavelength of 2710 nm. (b) The dispersion profiles for SCFs with core diameters of 1976 nm and 1984 nm.

To explore the structural tolerance of SCFs working at 2170 nm, the conversion efficiency is plotted (a) as a function of λ_s as the core diameter is changed from 1800 nm to 2000 nm in Figure 4.13. The pump power and signal power were kept the same as was used in the telecom band, 100 mW and 5 mW, respectively. The propagation length is set to 1 cm and the linear loss is assumed to be 1 dB/cm. The bandwidth is at a maximum, ~ -40 dB, when the core diameter is equal to the optimum value of $\sim$ 1890 nm, while it gradually decreases when the core diameter increases or decreases from this value. The rate of the bandwidth change is less severe

than that in the telecom band as β_2 changes more slowly around this wavelength. The decrease of the maximum conversion efficiency is due to the large effective mode area. Peaks at anti-Stokes and Stokes wavelength representing CSRS and CARS, respectively, are still strongly excited on both sides of the central band. The conversion efficiency of CSRS marked by the black dash box is displayed in Figure 4.13 (b) in detail, which has been extracted from Figure 4.13 (a). The reference conversion efficiency is set at -29 dB, as denoted by the dashed lines, which is around 4 dB less than the maximum conversion. Based on this reference value, the fabrication tolerance of SCF working at this wavelength is determined to be 100 nm. The fabrication tolerance is larger than that in the telecom band, but the recipe for the tapering process still need to be investigated as so far suitable fibres for this work have not been made with the appropriate phase matching conditions.

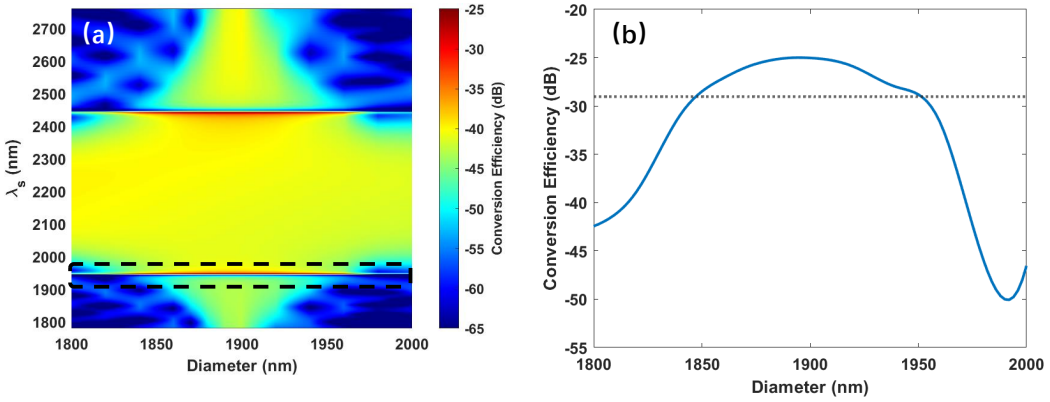

FIGURE 4.13: (a) Conversion efficiency as functions of diameter and λ_s. (b) shows the conversion efficiencies of the CSRS processes, marked with black dash box in (a), where signal is tuned to the anti-Stokes wavelength of 1950 nm. In all cases the pump wavelength is 2170 nm with a power of 100 mW, the signal power is 5 mW and the propagation length is 1 cm.

To investigate the nonlinear performance, the variation trends of conversion efficiency as functions of pump power and propagation length in the SCF with the optimized core diameter of 1890 nm are depicted in Figure 4.14 (a) . The pump wavelength is 2170 nm and the signal wavelength is 1950 nm with a power of 5 mW in this simulation. The maximum conversion efficiency of 30 dB could be obtained with a pump power of 1 W and a propagation length of 2.2 cm. The conversion efficiency could be further increased with the pump power, but in experiments, it is challenging to couple such power levels into SCFs with existing method of holding the fibres that involves the use of wax. Therefore, the pump power is limited to 1 W. The lower the power, the shorter the saturation propagation length. The conversion efficiency could be maintained during propagation when the length continues to increase. When the pump power increases over $\sim$ 700 mW, the conversion efficiency decreases as a result of the appearance of the higher-order Stokes and anti-Stokes waves, consistent with the variation in power evolution observed in the telecom band. The decrease in the

maximum of the conversion efficiency in the mid-infrared band compared to that in the telecom band is due to the reduced light intensity associated with the larger core diameters. Moving the pump wavelength to the mid-infrared allows for the highest possible Stokes output power, which is limited by the nonlinear absorption in the telecom band. The variation trends of the Stokes output power with the change of pump power and propagation length are conducted under the same structural parameter as Figure 4.14 (a) and depicted in Figure 4.14 (b). The maximum Stokes output power, over 1 mW, can be achieved with the pump power of 1 W and the propagation length of 2 cm. The reduction in the nonlinear losses results in a three-orders-of-magnitude increase in Stokes output power with 5 times larger pump power. The maximum Stokes output power could still be improved with pump power but 3PA should be taken into consideration with higher pump powers.

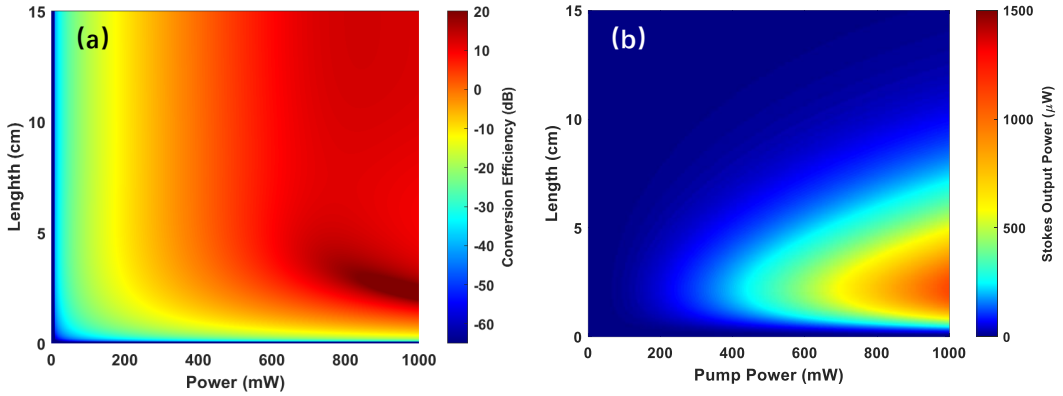

FIGURE 4.14: (a) Conversion efficiency and (b) Stokes output power as functions of pump power and propagation length for a SCF with a core diameter of 1890 nm when pumping at 2170 nm with a 5 mW signal beam positioned at 1950 nm.

4.3.2 Experimental setup

Figure 4.15 illustrates the experimental setup for the CSRS experiments in the mid-infrared band. A tunable ZnSe CW laser, covering a wavelength range from 2007 nm to 2500 nm, served as the pump source, while a CW laser working at 1950 nm functioned as the signal wave. The pump power around 2170 nm could reach up to 1 W, and the signal power was fixed at 8 mW. An attenuator was applied in front of the pump source to adjust the pump power during the measurement. Pump and signal waves were combined by a 45%/55% beam splitter (BS). Two beam splitters (BS) with a 92% transmission rate were positioned at the input and output sides, reflecting light back to CCD cameras. CCD cameras at both ends monitored the beam profiles and determined core positions through collecting reflective light. The light was coupled in and out of the SCF via two 60× optical lenses (OL). The output light was coupled into a multi-mode fibre (MMF), which has low loss in the mid-infrared band, using a 10× OL. The output spectra were recorded by an optical spectrum analyzer (YOKOGAWA

AQ6376). The coupling of the input facet was aligned according to the pump wavelength to ensure the highest possible coupled-in pump power. The output coupling efficiency was aligned with the idler wavelength to ensure the observation of the idler wave through the OSA. The coupling losses of the input and output facets are 7 dB and 3 dB, respectively. Fibre H and Fibre I were selected for the relatively stronger CSRS at Stokes wavelength compared with other existing fibres in practice. Moreover, these fibres have similar losses but different lengths and diameters, potentially leading to varying performance in gain enhancement, which will be discussed later. To test CSRS, the signal was fixed and the pump wavelength was tuned to confirm any increase in the conversion efficiency due to coupling to Raman effects.

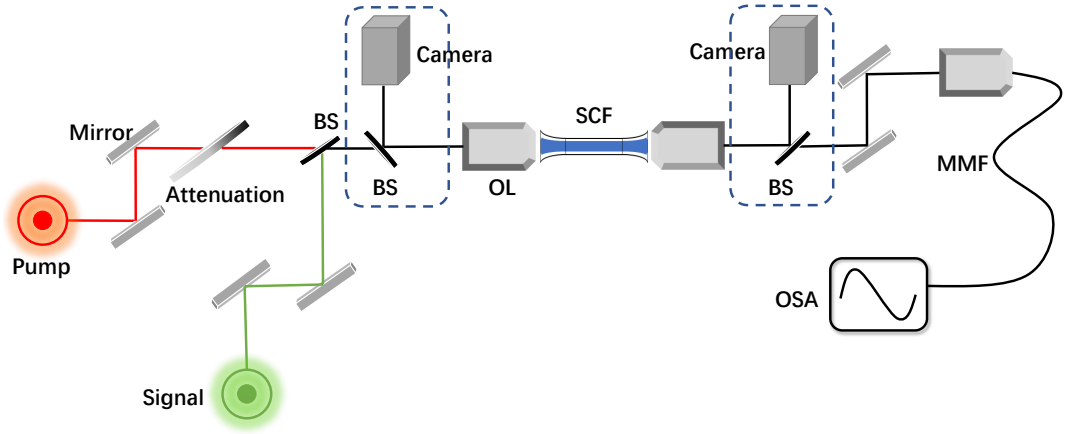

FIGURE 4.15: Experimental setup for CSRS in the mid-infrared band. BS, beam splitter; OL, optical lens; MMF, muti-mode fibre; OSA, optical spectrum analyzer.

4.3.3 Experimental verification

At the outset of the CSRS investigation, the underlying mechanism of this nonlinear phenomenon was theoretically analyzed. In the mid-infrared band CSRS measurement, IRS was firstly observed and experimentally verified using a CW light sources. Observing IRS in the telecom band is challenging due to the short fibre length used in those experiments, insufficient for accumulating Raman scattering. The pump output power when tuning the pump wavelength from 2169 nm to 2172 nm is presented in Figure 4.16 (a) with a fixed input pump power of 300 mW. When the pump wavelength approaches the Raman shift relative to the signal wavelength of 1950 nm, the output pump power increases, concurrently with a corresponding absorption in the signal output power, as displayed in Figure 4.16 (b). Conversely, when the pump wavelength is around 2140 nm, away from the Raman shift, there is no evident increase and decrease in the pump output power and the signal output power, as depicted in Figure 4.16 (c) and (d). The experimental confirmation of IRS first validates the CSRS theory, explaining a specific nonlinear contribution to compensating the pump power.

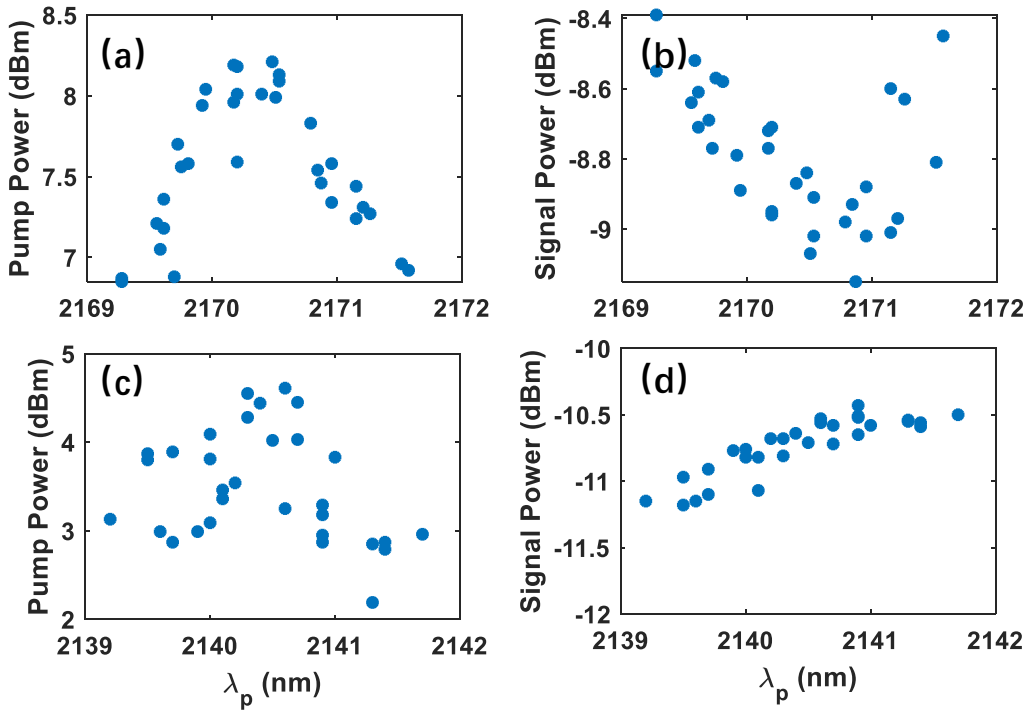

FIGURE 4.16: (a) Variation of pump output power and (b) signal output power with changing the pump wavelength around 2170 nm; (c) variation of pump output power and (d) signal power with changing the pump wavelength around 2140 nm, maintaining a fixed pump power of 300 mW for Fibre H.

The comparison of conversion efficiency between experimental data and simulation results for Fibre H under different pump powers is shown in Figure 4.17 (a). When the idler wavelength (λ_i) aligns with the peak Raman wavelength, the conversion efficiency experiences an increase, similar to what is observed in the telecom band, changing from ~ -54 dB up to ~ -47 dB and ~ -51 dB up to ~ -43 dB for coupled-in pump powers of 40 mW and 70 mW, respectively. The increase manifests as a distinct peak attributed to CSRS, with the experimental conversion efficiency almost consistent with simulation results. The possible reason for flatter trend in the experimental results is the lack of polarization control of pump and signal beams and the silicon quality difference. To delve into the impact of pump power on the conversion efficiency, Figure 4.17 (b) depicts the simulated results of CSRS and FWM as the pump power varies. In this simulation, the conversion efficiency of FWM was conducted with $f_R = 0$ to exclude the Raman effect. The experimental data (denoted by dots) closely mirrors the simulation results, behaving an upward trend with increasing pump power. This is due to the stronger nonlinear effects, including FWM and Raman scattering, introduced by higher pump powers. The conversion efficiency of FWM exhibits a similar trend to CSRS at lower pump power but maintains a linear increase with further ascending pump power. The noticeable differentiation between the conversion efficiency of CSRS and FWM is that CSRS exhibits a steeper gradient, which implies that CSRS could be enhanced significantly via increasing the pump

power coupled into the SCFs beyond 1 W. This suggest that the Raman scattering starts to dominate this nonlinear phenomenon at higher pump level. The enhancement of the conversion efficiency, as depicted in Figure 4.17 (c), maintains stable with low pump power but surges with further increases. The continuous increase in simulations indicates that higher pump power could achieve not only higher enhancement but also higher conversion efficiency. The notable difference between the conversion efficiency in the mid-infrared band and the telecom band results from the higher Raman enhancement due to the lower nonlinear absorption.

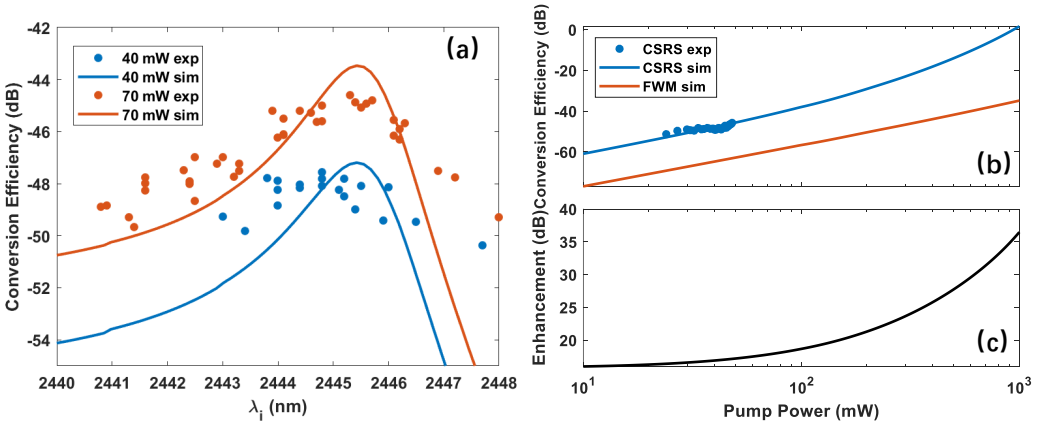

FIGURE 4.17: (a) Conversion efficiency as λ_i is tuned across Γ_R for Fibre H under different coupled-in pump power, 40 mW and 70 mW, as labeled in the legend. The experimental results are compared with simulations. (b) Conversion efficiency at the Raman peak with the increasing pump power under different conditions: FWM ($f_R = 0$) and CSRS ($f_R = 0.043$). (c) Enhancement of the conversion efficiency compared between CSRS and FWM.

Fundamentally, FWM, whose efficiency is highly dependent on the phase matching condition, serves as the bedrock of CSRS at low pump powers. The critical parameters affecting energy transfer amongst the pump, signal and idler include the core diameter and the propagation length. Experimental results for Fibre H and Fibre I are displayed in Figure 4.18 (a) together with simulation of GNLSE, demonstrating a consistent agreement between the data. The phase mismatch at 2170 nm for these two fibres, featuring different core diameters of 1976 nm and 1984 nm, leads to a deviation in the conversion efficiency from what is illustrated in Figure 4.14 (a). Specifically, the conversion efficiency decreases with an increase in the propagation length. To unearth the relationship between conversion efficiency, core diameter and propagation length, additional simulations were calculated and are illustrated in Figure 4.18 (b). The experimental maximum conversion efficiencies of -44 dB and -42 dB are marked by white squares. It is obvious that the conversion efficiency exhibits a linear increase with the propagation length when the core diameter is close to the optimized core diameter of $\sim$ 1900 nm. Conversely, the conversion efficiency varies periodically with length for non-optimum diameters, with the period shrinking rapidly as the core diameter increases, indicating a larger phase mismatch. The decrease in conversion

efficiency with an increasing core diameter is attributed to the reduction in light intensity of the guided light. Thus, these results shows that determining the appropriate length to achieve high conversion efficiency becomes essential, particularly when the core diameter deviates significantly from the optimal value.

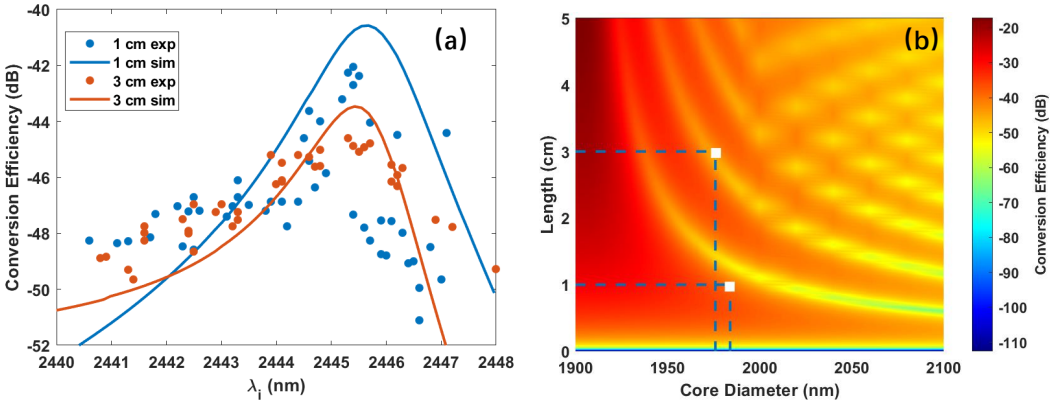

FIGURE 4.18: (a) Simulated and experimental results of conversion efficiency for Fibre H and Fibre I with the coupled-in pump power of 70 mW and the pump wavelength of 2170 nm. (b) Variation of conversion efficiency as functions of core diameter and propagation length, the pump is fixed at 2170 nm with the power of 70 mW, the signal is fixed at 1950 nm and the linear loss is 1 dB/cm.

New SCFs fabricated at KTH Royal institute of Technology demonstrate low linear loss and stability in tapering over lengths exceeding 6 cm. These characteristics are indicative of strong Coherent Stokes Raman Scattering (CSRS) behavior. Figure 4.19 (a) presents the experimental and simulation results for Fibre J at different coupled-in pump power, specifically 20 mW and 33 mW. The increase of the conversion efficiency at the Raman peak with the pump power maintains consistence to previous experiments. Despite a slightly larger phase mismatch for Fibre J compared to Fibre H and Fibre I, the conversion efficiency remains comparable to that of Fibre H at a relatively low pump power, arising from the smaller effective mode area. To explore the effect of the pump power on the conversion efficiency, the pump power was tuned in the experiments while maintaining a fixed pump wavelength at 2170 nm, aligning the idler wave with the Raman peak. These experimental results perfectly match with the simulation results, as displayed in Figure 4.19 (b). The conversion efficiency associated with FWM only ($f_R = 0$) was also calculated for comparison, and showed a linear trend with increasing pump power. The gradient of the CSRS curve matches that of FWM only when the pump power is small but becomes steeper when the power exceeds 100 mW due to the Raman enhancement. A decrease in the conversion efficiency as the pump power approaches 1 W is attributed to the appearance of higher-order Stokes/anti-Stokes wave. The enhancement of the conversion efficiency, as shown in Figure 4.19 (c), aligns with the trend of the conversion efficiency variation of CSRS, reaching a maximum enhancement of 55dB. This suggests that further

increase of the enhancement is still limited, even without accounting for nonlinear absorption, due to higher-order waves boosted with high pump power.

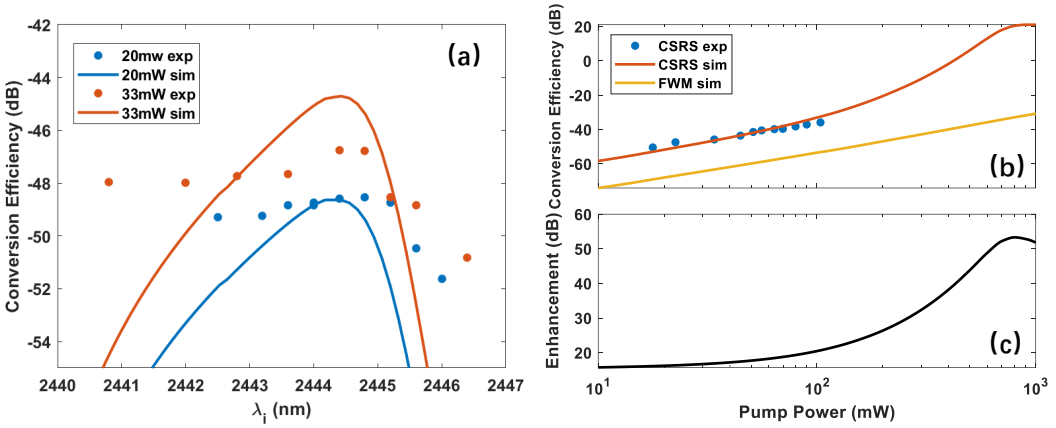

FIGURE 4.19: (a) Conversion efficiency as λ_i is tuned across Γ_R for Fibre H under different coupled-in pump power, 40 mW and 70 mW, as labeled in the legend. The experimental results are compared with simulations. (b) Conversion efficiency at the Raman peak with the increasing pump power under different conditions: FWM ($f_R = 0$) and CSRS ($f_R = 0.043$). (c) Enhancement of the conversion efficiency compared between CSRS and FWM.

In addition to the conversion efficiency, which stands as a pivotal criterion for assessing nonlinear efficiency, the idler output power poses another significant constraint for practical applications. Here, the simulation results for the Stokes output power under three distinct conditions, Raman scattering, FWM and CSRS, were calculated and illustrated in Figure 4.20 (a). The Stokes output power resulting from Raman scattering is minimal when the pump power is below 1 W, but it is expected to eventually increase beyond that available from FWM processes, following the overall trend observed. A notable distinction emerges when comparing the mid-infrared scenario to the telecom band. While the Stokes output power in the latter begins to decrease beyond a pump power of 200 mW, the former experiences continuous linear growth with increasing pump power due to the lack of the nonlinear absorption. In contrast, the Stokes output power for both FWM and CSRS exhibits a rapid surge at the beginning, followed by a sustained increase with pump power, but with different slopes. To quantitatively analyse the enhancement in the Stokes output power, the enhancement has been calculated and is displayed in Figure 4.20 (b). The enhancement initially spikes to 17 dB, then decelerates and ascends linearly to 37 dB with increasing pump power. Indeed, the trend of the curve suggests that the potential for a three-orders-of-magnitude enhancement could be further increased with higher pump power.

This section outlines the substantial enhancement of the conversion efficiency and Stokes output power achievable via the interaction between Raman scattering and FWM. This phenomenon has been experimentally validated in both the telecom and mid-infrared bands. Notably, the conversion efficiency observed under the phase

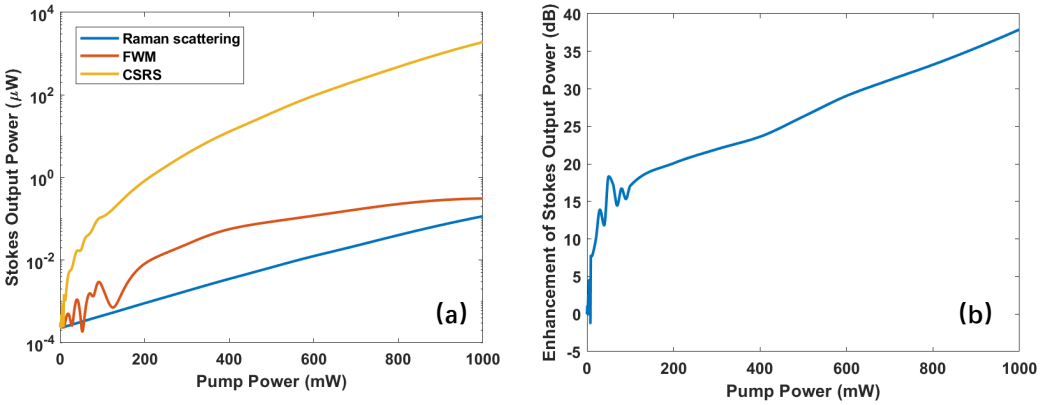

FIGURE 4.20: (a) Comparison of the normalized idler output power with the increasing pump power under different conditions: FWM, Raman scattering and CSRS for fibre A with pump at 2170 nm. (b) Enhancement of the Stokes output power as a function of pump power, which is the difference between the output power of CSRS and FWM in (a).

mismatch conditions surpasses traditional FWM conversion efficiency, with a wavelength conversion band that extends far beyond the previously reported FWM bandwidth [108], posing a challenge to conventional FWM observation. Crucially, the absence of stimulated Brillouin scattering (SBS) in the SCFs eliminates the requirement of SBS compensation schemes. This characteristic significantly simplifies the architectures required for parametric amplification when compared to silica fibres [114]. Moreover, the fibre tapering process demonstrated here is not limited to SCFs, that can also be applied to other semiconductor fibre platforms, including those with germanium dopants [115]. This opens up the possibility of exploiting Raman-enhanced wavelength conversion across an even broader wavelength range.

Chapter 5

Coherent Stokes Raman scattering in silicon planar waveguides

Although SCFs offer a degree of dispersion engineering, the imprecision in the fabrication process makes it challenging to exert the accurate control over the dispersion properties. This limitation results in a large phase mismatch, yielding a narrow FWM bandwidth and reduced conversion efficiency of CSRS. In contrast, planar waveguides have mature fabrication techniques, boasting high manufacturing accuracy that enables the superior control over dispersion engineering. This chapter is focused on CSRS based on silicon rib waveguides, aiming to amplify the idler output power and conversion efficiency at the Stokes wavelength. The comparison between the rib waveguide and SCFs is thoroughly investigated to delineate the advantages and disadvantages of these two platforms. The subsequent sections address the calculation of dispersion parameters with varying structural parameters for rib waveguides in the telecom and mid-infrared bands, which is essential for selecting a proper waveguide structure. Simulations of CSRS performance are given as a guide for upcoming experiments. Preliminary experiments were conducted, and the results are compared with simulations to affirm the feasibility of enhancing conversion efficiency and Stokes output power in rib waveguides. Lastly, the influencing factors are discussed to explore the stability of Raman enhancement on both the conversion efficiency and Stokes output power. This holistic exploration contributes to a comprehensive understanding of the potential and challenges associated with employing rib waveguides for CSRS applications. In this work, I was responsible for the simulations, waveguide design and polishing, major steup building and nonlinear experiments.

5.1 Comparison between SCFs and planar silicon waveguides

A comparison between SCFs and planar rib waveguides in terms of the structure, effective mode area, dispersion profile and nonlinear performance will be conducted in the telecom band. The longitudinal structure of SCFs, shown at the bottom of Figure 5.1 (a), is composed of down taper, waist and up taper. Taper sections are preserved to ensure efficient free space coupling, addressing the low coupling efficiency introduced by the micrometer-size core diameter. The critical parameter in designing the SCF to operate at the specific wavelength is the core diameter (D), annotated in the sketch of the cross section for the waist region at the top left corner of Figure 5.1 (a). The mode distribution is symmetrical due to the symmetric structure of fibres, which indicates that the polarization influence of injected light is limited. The variation of A_{eff} with D, shown at the top right corner in Figure 5.1 (a) shows that A_{eff} continuously grows with increasing D. The longitudinal waveguide design depicted at the bottom of Figure 5.1 (b) is similar as that of SCFs, where the straight section is sandwiched between two coupling regions (a down and up taper) to ensure good coupling into the few hundred nanometer-sized waveguides. The waveguide design is based on a silicon on insulator (SOI) platform with a silicon thickness of 500 nm, selected as the achievable propagation losses are typically much lower than in 220 nm platforms [116]. The waveguide can then be defined using standard photolithography and etching techniques to produce a rib structure, as illustrated in the top image of Figure 5.1 (a), where H is the thickness of the silicon layer on the top of the SOI wafer, h is the etch depth and W is the width. It is obvious that the mode in rib waveguides is polarisation-dependent, which introduces extra coupling loss. A_{eff} varying with the change of h and W, shown at right-up corner, indicates that A_{eff} increases with decreasing h and increasing W but is smaller than that of SCFs.

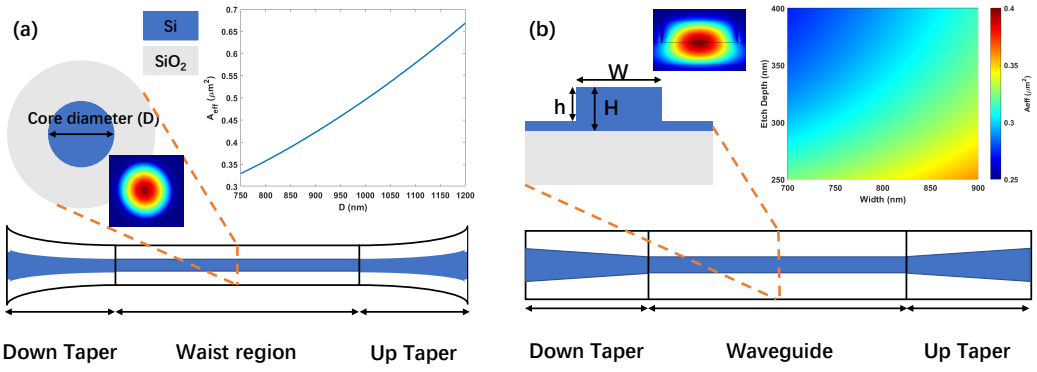

FIGURE 5.1: (a) Diagram of the SCF structure, cross section of the waist region was depicted at left-up corner with the mode distribution example, A_{eff} varying with the change of the core diameter is shown at the right-up corner. (b) Diagram of planar waveguide, cross section of the waveguide was depicted at left-up corner with the mode distribution example, A_{eff} varying with the change of the etch depth (h) and width (W) is shown at the right-up corner. Blue represents the silicon and gray represents silica as the legend shows.

To further explore the structural influence, the dispersion parameters of the SCF with a core diameter of 920 nm and the planar waveguide with h of 350 nm and W of 790 nm are calculated, as shown in Figure 5.2 (a). It is evident that β_2, symbolised by solid lines for these two structures, is both close to zero at 1545 nm, with values of -2.45×10^{-3} ps^2/m for the SCF and -2.49×10^{-3} ps^2/m for the planar waveguide, respectively. β_4, symbolised by dash lines at 1545 nm, has opposite signs, with values of -5.63×10^{-7} ps^4/m for the SCF and 3.53×10^{-7} ps^4/m for the planar waveguide. This indicates that these two structures both could meet the phase matching condition when pumping at 1545 nm, while the wavelength conversion bandwidth of the planar waveguide should be broader than that of the SCF according to Eq.(2.16). To verify the difference between the wavelength conversion bandwidths, the FWM conversion efficiencies pumping at 1545 nm with switching the signal wavelength are simulated by solving NLSE and shown in Figure 5.2 (b). In these simulations, the linear loss is assumed to be 1 dB/cm to be compatible with the universal value for SCFs and planar waveguides. The propagation length is 1 cm, the pump power is 100 mW and the signal power is 5 mW. It is clear that the 3 dB bandwidth, over 1000 nm of the planar waveguide, is wider than that of SCF, approximately 626 nm, which is consistent with the results of the difference in dispersion parameters. The conversion efficiency of planar waveguide is slightly larger than that of SCF owing to the smaller effective mode area, 0.31 μ^2m for the planar waveguide compared with that for the SCF, 0.44 μ^2m. The sharp peaks at the Raman shift wavelength are due to the interaction between the FWM and Raman, furthermore, the left side peak is CSRS and the right side one is CARS. The deviation of the conversion efficiency, about 4 dB, between CSRS and CARS originates from the inherently higher energy transfer efficiency at Stokes wavelength than that at the anti-Stokes wavelength, which is consistent with what is achieved in Chapter 3 3.3. During the fabrication of SCFs and planar rib waveguides, another significant difference is that the linear loss for SCFs is lower than that of rib waveguide overall, which could be identified in detail in Appendix A. This is owing to the larger effective mode area and the lack of scattering loss introduced by the etch steps in the rib waveguide fabrication.

SCFs are developed for low linear loss but achieving the precise control of the core diameter is challenging with existing tapering techniques. In contrast, planar waveguides, while having higher linear loss, compensate for this by allowing accurate structural control in two dimensions, including the etch depth and the width. Additionally, planar waveguides have a smaller A_{eff} and a wider FWM bandwidth. Consequently, planar waveguides are promising platforms for obtaining higher conversion efficiency, as indicated by the comparisons.

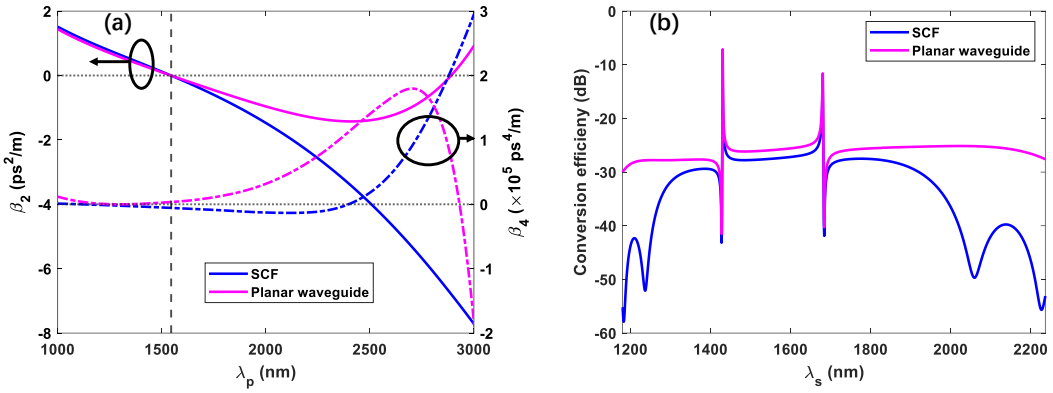

FIGURE 5.2: (a) β_2 denoted by the solid lines and β_4 denoted by the dash lines. (b) Conversion efficiencies as functions of the signal wavelength (λ_s) when pumping at 1545 nm, the signal power is 5 mW and the propagation length is 1 cm. Results are presented for the SCF and planar platforms, as labelled in the legends.

5.2 CSRS in the telecom band

5.2.1 Structural design and simulations for CSRS

In order to realise the phase-matching conditions for CSRS in the telecom band, the dispersion profile is firstly investigated for various waveguide dimensions (h and W values) for the chosen pump wavelength of 1545 nm, as shown in Figure 5.3 (a). Specifically, it is preferable to operate near the ZDW, depicted by the black dash line to obtain a broad FWM bandwidth. Figure 5.3 (a) shows that the zero dispersion condition can be achieved for different combinations of h and W, with larger widths simply corresponding to larger etch depths. Moreover, β_2 changes slowly along the width, but dramatically along the etch depth, which suggests that the dispersion profile is more sensitive to the critical dimension of waveguides. To further define the optimal structural parameters, the scattering loss ($\alpha_s l$) are simulated by calculated the scattering factor in COMSOL. Theoretical reason for the scattering loss is the roughness of the side wall formed during the etching process. The scattering loss is proportional to the loss factor that depends on the geometry and mode field-dependent quantity [117]:

$$\alpha_s l \propto \frac{\oint_C |E_k|^2 dl}{\iint E_k \times H_k^* dS'}, \tag{5.1}$$

where E_k and H_k is the electric and magnetic field, C is the perimeters of the air–silicon interfaces in the cross section. The larger the loss factor, the stronger the scattering loss. Scattering loss increases with increasing the etch depth but is relatively insensitive to the change of the width when the width changes from 670 nm to 900 nm

at a pump wavelength of 1545 nm. Combined with the variation of A_{eff}, depicted in Figure 5.3 (c), where A_{eff} has a similar trend with the SL, the smaller etch depth and width is better to achieve smaller A_{eff} and scattering loss. Beside A_{eff} and diffuse scattering loss, the critical factor is the nonlinear performance. To illustrate the influence of the different waveguide dimensions on the nonlinearity, Figure 5.3 (d) shows conversion efficiencies for three different combinations of h and W as a function of the signal wavelength. The simulations were conducted with a pump power of 100 mW and the signal power of 5 mW. The propagation length was set to 1 cm. CSRS and CARS efficiently boost in these structures. As seen in Figure 5.3 (d), the conversion efficiency for CSRS remains approximately stable for the different combinations of h and W. The bandwidth, defined as the signal wavelength range where the conversion efficiency drops by 3 dB from the maximum value at the centre of the curve, is largest for the etch depth of 350 nm. This is due to the difference in the values of β_2 and the corresponding fourth-order dispersion parameter β_4, which combine to minimise the total dispersion. As a result, a target structure with $h = 350$ nm and $W = 790$ nm was determined as a compromise between a small mode area to achieve a high mode intensity, but with the potential for low losses through a modest etch depth. This structure has dispersion values of $\beta_2 = -2.49\times10^{-3}$ ps^2/m and $\beta_4 = 3.53\times10^{-7}$ ps^4/m.

Following identification of the optimal structure, the influence of the structural parameters on the RE-FWM conversion efficiency was investigated to validate the design for the existing fabrication techniques. In these simulations, the system parameters are the same as those used for Figure 5.3 (d). Figure 5.4 (a) displays the conversion efficiency as a function of λ_s as the etch depth h is changed from 280 nm to 420 nm. As expected, the bandwidth is at a maximum when h is equal to the optimum value of 350 nm, but decreases quite sharply as h is increased or decreased away from this. Figure 5.4 (b) then shows the efficiency as the waveguide width W is changed from 670 nm to 900 nm. Again, the bandwidth is maximum for the designed width of 790 nm, but the rate of decrease of the bandwidth as the width is adjusted is less sharp than for the changing etch depth. In both cases it is clear that CSRS, marked by the black dash boxes, is strongly excited when the bandwidth of FWM overlaps with the Raman gain spectrum. Figure 5.4 (c) and (d) display the conversion efficiency as a function of h and W, which are extracted from Figure 5.4 (a) and (b), respectively. The reference conversion efficiency is set as -10 dB, as denoted by the dash lines in Figure 5.4 (c) and (d), which is around 4 dB less than the maximum conversion for the 100 mW pump. Based on this reference value, the fabrication tolerance of the etch depth h is 20 nm and of the width W is 47 nm, which are well within the attainable resolutions for existing photolithography technologies [118]. The smaller structural tolerance of h compared with that of W is consistent with the dispersion analysis, which further confirms that the nonlinear performance is more sensitive to the smallest dimension of planar waveguides.

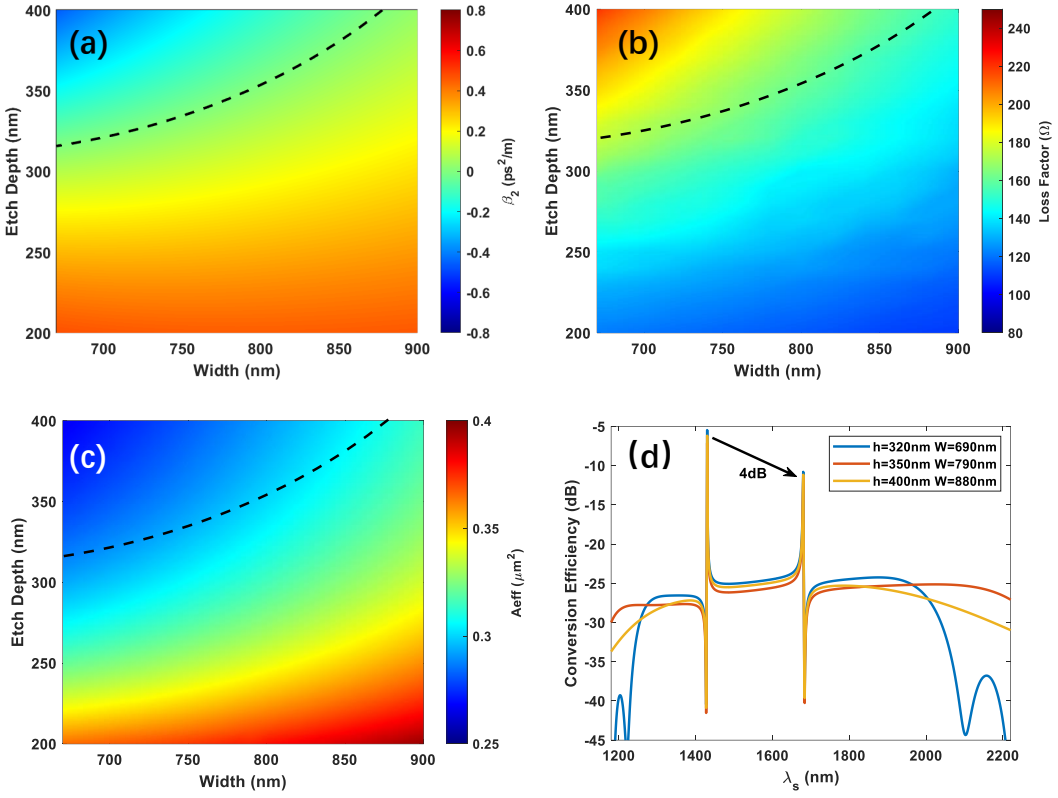

FIGURE 5.3: (a) β_2, (b) Scattering loss and (c) A_{eff} varying with etch depth and width. The black dash line represents β_2 is equal to zero. (d) Plot of conversion efficiency as a function of λ_s for waveguide designs with different combinations of h and W that have a GVD equal to zero at the 1545 nm pump wavelength (i.e., the dimensions are selected from the black dash line in (a). The simulations are conducted with a pump power of 100 mW, a signal power of 5 mW and a propagation length of 1 cm.

Having established the fabrication tolerances for this design, the performance of the RE-FWM by comparing the conversion efficiency and Stokes output power for the CSRS process is subsequently investigated. Figure 5.5 (a) plots a colour map of the conversion efficiency as functions of pump power and waveguide length, with the remaining parameters for the pump, signal and waveguide the same as used previously for Figure 5.4. From this result, as the pump power increases above $\sim$ 100 mW, the conversion efficiency saturates at a propagation length of $\sim$ 3 cm. This saturation can be attributed to the fact that for high pump powers the Stokes wave is sufficiently enhanced to transfer energy to the anti-Stokes wave, as well as to higher-order Stokes waves. As a result, the optimal pump power to achieve a maximum conversion efficiency of over 20 dB is only 170 mW , with a propagation length of 3 cm. Although this pump power is higher than those used in other studies of FWM [119][120], such powers are readily available within telecom systems and the advantage of our approach is that it only relies on a simple waveguide design, without the need for extremely low linear loss or ring resonator designs, to achieve an enhancement in the conversion efficiency of $\sim$ 50 dB.

Figure 5.5 (b) then shows a colour map of the achievable Stokes output power as

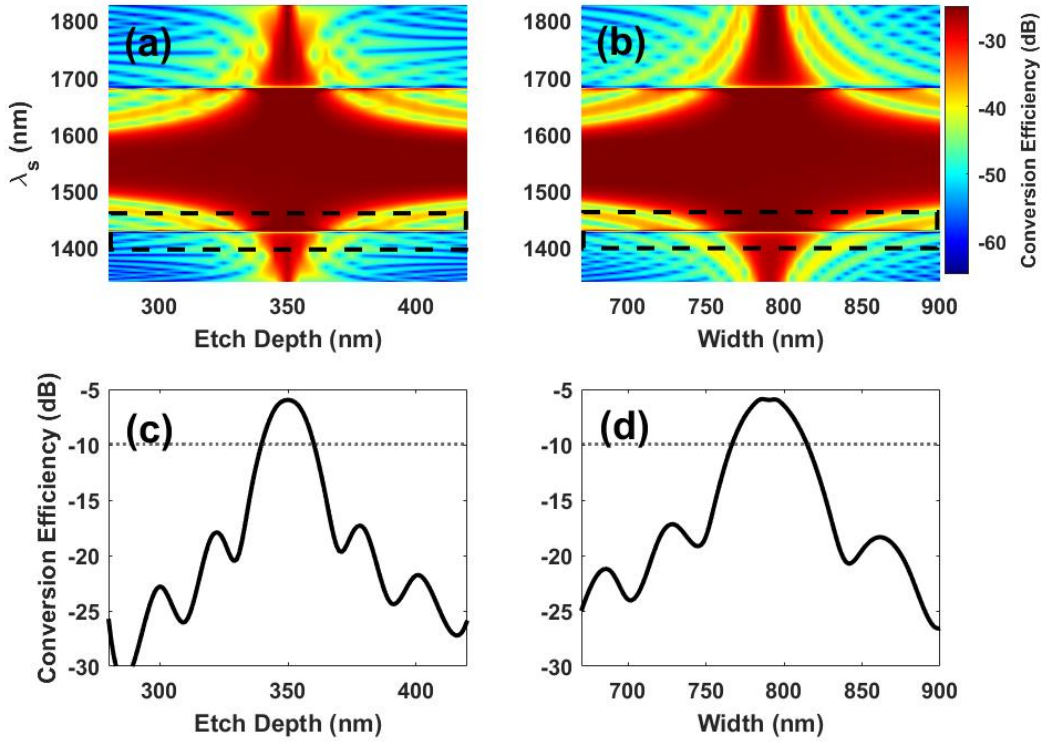

FIGURE 5.4: (a) Conversion efficiency as functions of h and λ_s. (b) Conversion efficiency as functions of W and λ_s. (c) and (d) show the conversion efficiencies of the CSRS processes, marked with black dash boxes in (a) and (b), respectively, where signal is tuned to the anti-Stokes wavelength of 1430 nm. In all cases the pump wavelength is 1545 nm with a power of 100 mW, the signal power is 5 mW and the propagation length is 1 cm.

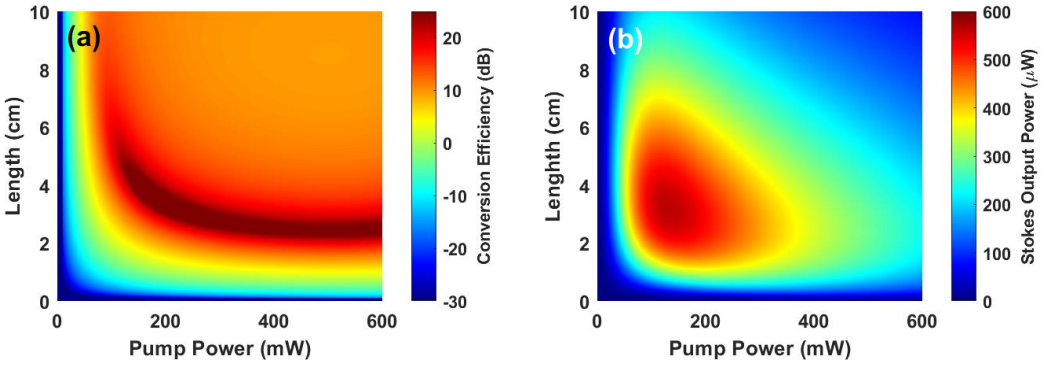

FIGURE 5.5: (a) Conversion efficiency and (b) Stokes output power as functions of the pump power and waveguide length when pumping at 1545 nm with a 5 mW signal beam positioned at 1430 nm. The waveguide width is 790 nm and the etch depth is 350 nm.

functions of pump power and waveguide length. In contrast to Figure 5.5 (a), this shows that the output idler power saturates for both increasing power and length, reaching a maximum of 560 μW for a 130 mW pump at a length of 3 cm. We attribute the saturation associated with increasing power both to the conversion of the first-order Stokes wave to higher-order waves as well as nonlinear absorption

associated with TPA and free-carrier effects. The saturation for increasing propagation length is primarily due to the linear loss, and the Stokes output power could be increased through further reduction of the losses. However, it is worth noting that for this design, the optimal propagation length to achieve the maximum conversion efficiency and the maximum Stokes output power is 3 cm so that a single waveguide could be used to achieve both. Moreover, it is quite remarkable that the potential Stokes power generated using the RE-FWM scheme is 7 dB larger than what has been generated by pure SRS alone using a waveguide of a comparable length but with the inclusion of a p-i-n structure to reduce the free-carrier absorption [121]. Significantly, if we reduce the losses to 0.3 dB/cm in our simulations, which corresponds to the lowest linear loss for planar waveguides in the telecom band at this time [122], we can achieve idler powers up to 1.47 mW for a pump power of only 80 mW and a length of 10 cm.

5.2.2 Experimental verification

5.2.2.1 Characterisation of rib waveguide

According to NLSE, linear loss and nonlinear loss are crucial parameters for predicting the nonlinear performance in simulations, especially in the telecom band. When a new platform is employed to observe nonlinear effects, characterising corresponding parameters, including linear loss and β_{TPA}, is essential to improve simulations and ensure accuracy. The variation of output power and spectrum of SPM for Rib A (details for waveguide applied in experiments are listed in Appendix A) under a pulse laser source were recorded to estimate β_{TPA} and linear loss. The pump wavelength is 1.54 μm with a pulse duration of 720 fs and a repetition rate of 47 MHz. The lifetime of free carriers introduced by TPA at the scale of such a waveguide is around several nanoseconds [123][124], much shorter than the relaxation time between two pulses, resulting in limited effects on the nonlinear performance. Hence, the free carrier lifetime is fixed at 10 ns in the following simulations.

The experimental setup is the same as Figure 3.2 shows. The total insertion loss measured in experiments for Rib A is 27 dB, including coupling loss and linear loss. For a specific linear loss, for example 2 dB/cm, the value of input coupling loss (ICL) is determined by the choice of β_{eff}, ensuring the simulated curve of the output power aligns with the experimental data, as shown in Figure 5.6 (a). In the experiment, the output power was recorded with the pump power varying from a few hundred micro-watts to tens of milli-watts. The output power increases linearly at low pump level, then the rate of increase decreases due to the presence of TPA, introducing nonlinear loss. The bend ratio serves as an effective criterion for selecting possible combinations of β_{TPA} and linear loss. The parameters for each combination that can

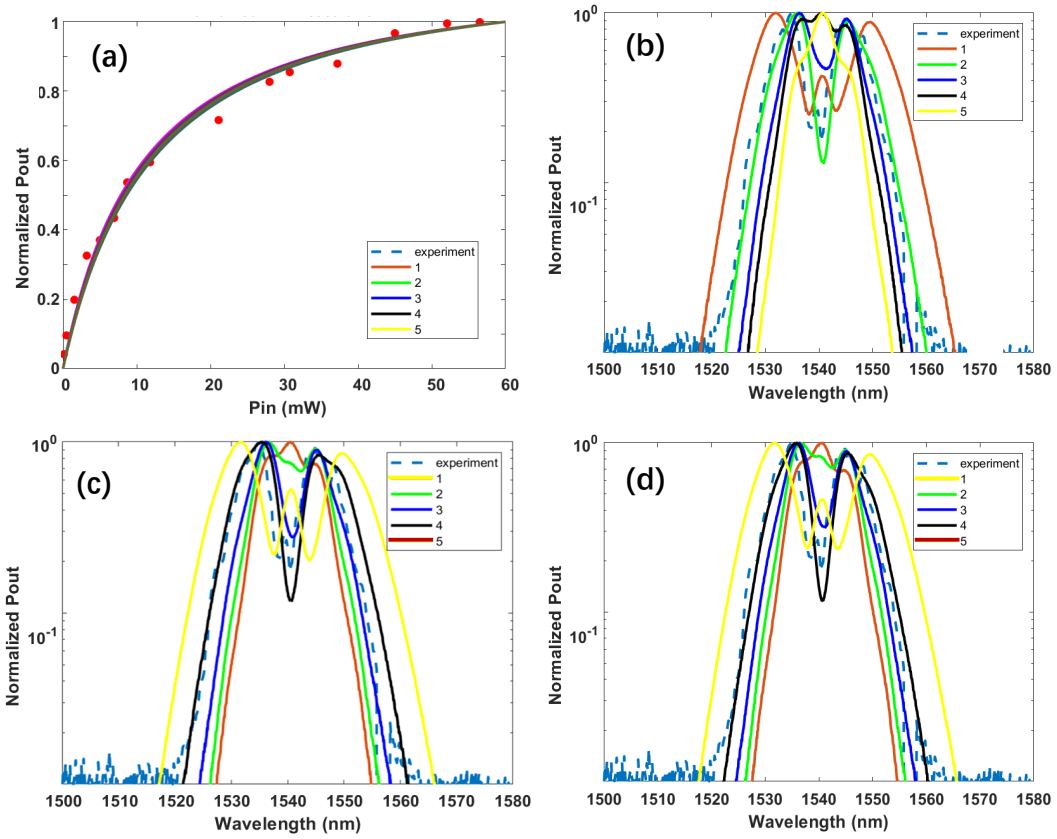

FIGURE 5.6: (a) Comparison of the output pump power between experimental data and simulation results under various conditions labeled in the legend corresponding to Table C.1 (details provided in Appendix C), where the average input power ranges from several hundred micro-watts to tens of milli-watts. (b)-(d) Spectrum of SPM for Rib A under different linear loss and β_{TPA} conditions labeled in the legend corresponding to Table C.1, Table C.2 and Table C.3, respectively with the average pump power of 60 mW. The pump wavelength is 1.54 μm with a pulse duration of 720 fs, and a repetition rate of 47 MHz. 1, 2,3, 4 and 5 correspond to the serial numbers in various tables.

match the output power curve are listed in Table C.1. Simulation results for these combinations perfectly match the experimental data. To distinguish differences between each combination, the spectrum of SPM with an average pump power of 60 mW, as presented in Figure 5.6 (b), was recorded to determine the value of β_{TPA}. Different values of β_{TPA} indicate various broadening of SPM spectra, the smaller the value, the wider the SPM spectrum. When β_{TPA} is equal to 7×10^{-12} m/W, the simulation result is consistent with the experimental data. For different values of linear loss, 3 dB/cm and 4 dB/cm, possible combinations of β_{TPA} and ICL are listed in Table C.2 and Table C.3, and the corresponding SPM spectra are depicted in Figure 5.6 (c) and (d). The overall trends for SPM broadening with different values of β_{TPA} are similar to Figure 5.6 (b), and the optimised value of β_{TPA} remains 7×10^{-12} m/W, the smaller β_{TPA}, the broader the SPM. It is significant to note that SPM broadening is affected only by β_{TPA}, while linear loss and coupling loss have a limited influence on

the spectrum evolution. The effective way to determine the value of β_{TPA} is through the measurement and comparison of SPM spectrum.

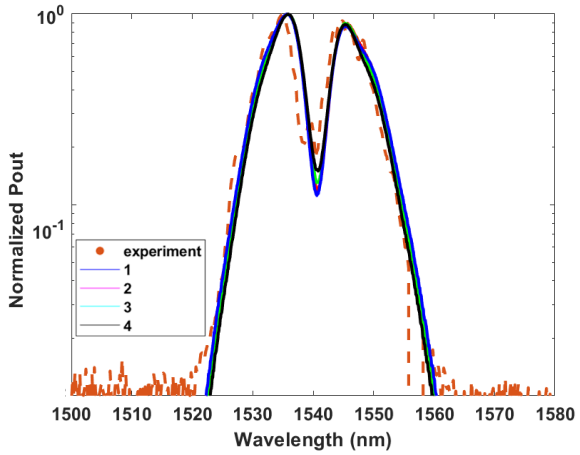

FIGURE 5.7: Spectrum of SPM for Rib A under different linear loss and coupling loss conditions labeled in the legend corresponding to Table C.4 with the average pump power of 60 mW. The pump wavelength is 1.54 μm with a pulse duration of 720 fs, and a repetition rate of 47 MHz. 1, 2, 3 and 4 correspond to the serial number in the table.

After determining the value of β_{TPA}, the linear loss with the corresponding coupling loss need to be determined. Therefore, different possible combination of linear loss and coupling loss are listed in Table C.4. The SPM spectra for different combinations are presented in Figure 5.7. The spectra for different combination overlapping with each other re-validate that linear loss and coupling have a limited influence on the broadening of SPM. According to the Fresnel reflection rule, the output coupling loss (OCL) should be around 3 dB, which helps to narrow the range of linear loss to $2 - 3$ dB.

To validate the effectiveness of the value of linear loss, $\beta_T PA$ and coupling loss, the trends of output power for waveguides with different lengths are measured and simulated. In this simulation, β_{TPA} is set to 7×10^{-12} m/W, ICL is equal to 18.5dB, and linear loss is 3 dB/cm. The results are shown in Figure 5.8, in which (a) and (b) are for Rib B with linear and log formats of the y axis to enlarge the difference, whilst (c) and (d) are for Rib C. This set of values can work very well, as the simulation results are well matched with the experimental data. In the following nonlinear simulations in the telecom band, these values will be applied to compare with the experimental data.

5.2.2.2 CSRS measurement

In the rib waveguide CSRS experiment, the same setup as that used for SCFs was employed, as illustrated in Figure 4.5. However, in this case, the SCFs were replaced by rib waveguide samples. The experimental conversion efficiency for Rib A and Rib D is depicted in Figure 5.9, where the pump wavelength is tuned around 1545 nm. The

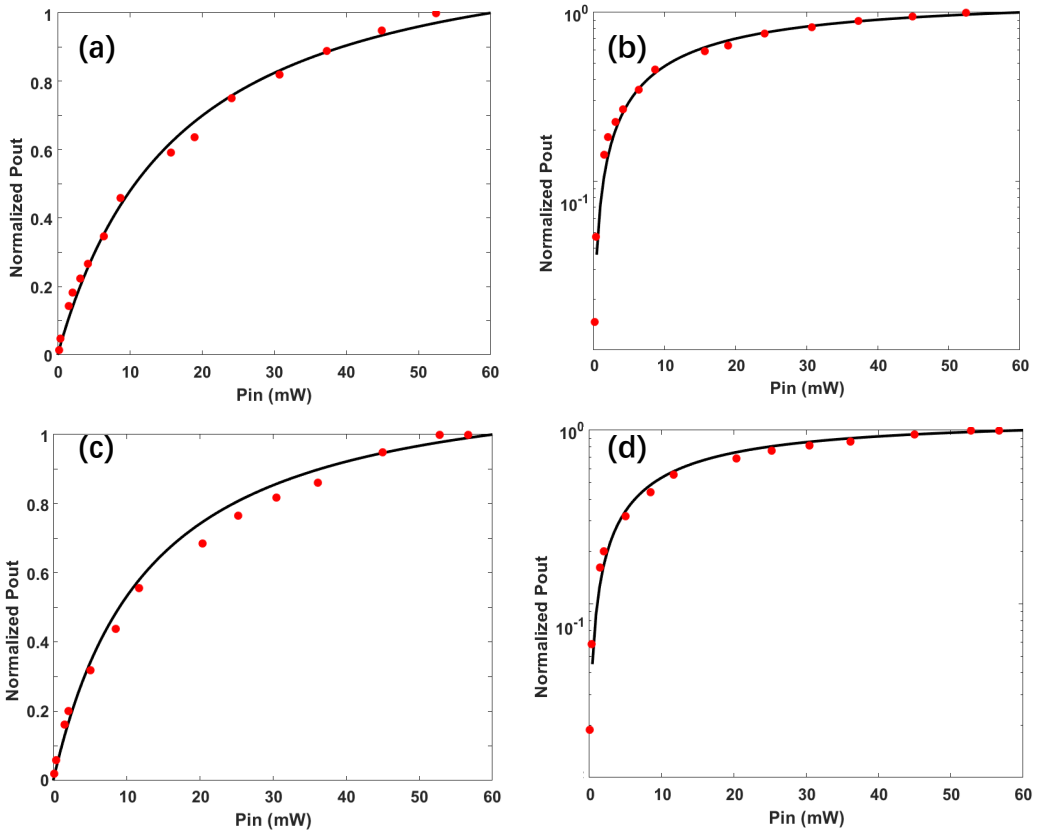

FIGURE 5.8: Comparison of the output pump power between experimental data and simulation results for Rib B (linear (a) and log (b) format of y axis) and Rib C (linear (c) and log (d) format of y axis), where the average input power ranges from several hundred micro-watts to tens of milli-watts. The pump wavelength is 1.54 μm with a pulse duration of 720 fs, and a repetition rate of 47 MHz.

coupled-in pump power is set at 12 mW, and the signal is fixed at 1432 nm with a coupled-in power of 70 μW. As the FWM generated idler wavelength (λ_i) approaches the peak Raman wavelength, the conversion efficiency for Rib A increases from ~ -42 dB up to ~ -37 dB, exhibiting a distinct peak at the Raman shift. A similar phenomenon was observed in Rib D, despite the variation in width and propagation length. To ensure an accurate enhancement of the conversion efficiency, simulations calculated by NLSE were conducted. In Rib A and Rib D, the conversion efficiencies at short wavelength side are ~ -47 dB and ~ -50 dB, respectively. Both show an increases of over ~ 10 dB, reaching ~ -37 dB with a pump power of only 12 mW.

To obtain higher conversion efficiency and explore the trends in enhancement, the idler output power and conversion efficiency were recorded while varying the coupled-in pump power, switching from hundred of micro-watts to ~ 20 mW. In the experiment, the pump wavelength was fixed at 1545 nm with the signal wavelength of 1432 nm. The experimental results shown in Figure 5.10 (a) and (b) reveal a linear increase in both idler output power and conversion efficiency with the pump power, ascending from -76 dB to -60 dB and -50 dB to -32 dB, respectively, when the pump

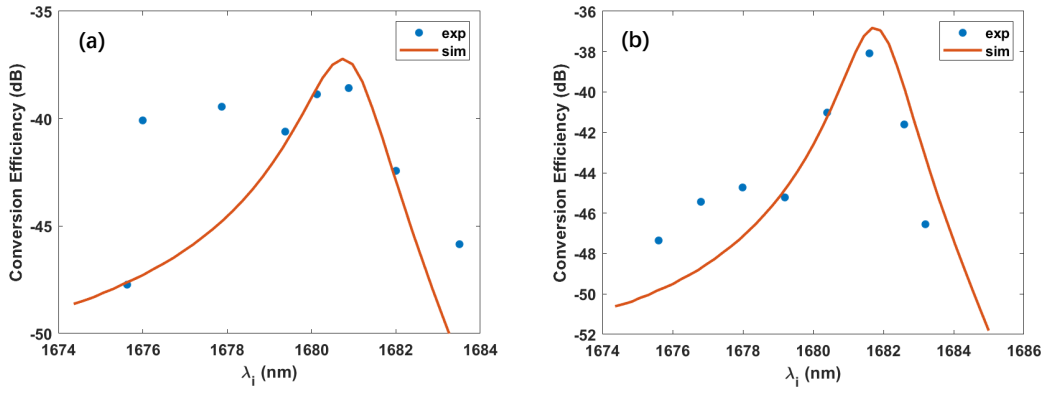

FIGURE 5.9: Conversion efficiency as λ_i is tuned across Γ_R for Rib A (a) and Rib D (b). The experimental results are compared with simulations of CSRS and FWM, as labeled in the legend. The pump wavelength is tuned around 1545 nm with a coupled-in power of 12 mW, while the signal is fixed at 1432 nm with a coupled-in power of 70 μW.

power is at a low level. These findings are consistent with the simulation results. Compared with existing fibre results, the conversion efficiency increases by 12 dB due to a better phase matching condition and a smaller effective mode area at the same pump power level. The maximum enhancement observed in the experiment is 15.5 dB for idler output power and 16 dB for conversion efficiency. However, when the pump power continues to increases to hundreds of milli-watts, the idler output power saturates and eventually decreases due to TPA and FCA in both CSRS and FWM. The differentiation of idler output power between CSRS and FWM, presented in Figure 5.10 (c), shows that with increasing pump power, the enhancement rises from 15 dB to $\sim$ 19 dB, proposing a plateau when the pump power reaches watts level. In contrast, the conversion efficiency exhibits a slightly different trend at high pump power level, where it shows a saturation pattern without an obvious decrease for both CSRS and FWM, as depicted in Figure 5.10 (b). The enhancement trend in conversion efficiency mirrors that of idler output power, increasing from 15 dB to $\sim$ 28 dB before starting to saturate. An interesting observation is that the enhancement of idler output power remains stable at 19 dB compared to the results in SCFs in the telecom band.

The maximum conversion efficiency observed in the experiment is up to -32 dB with a coupled in pump intensity of 70 GW/m^2, which is similar to the record of pure FWM in silicon waveguides but requires a smaller pump intensity by an order of magnitude [57][58]. This significant enhancement indicates that CSRS is a promising method to realize the high conversion efficiency and Stokes output power with the simplest structure.

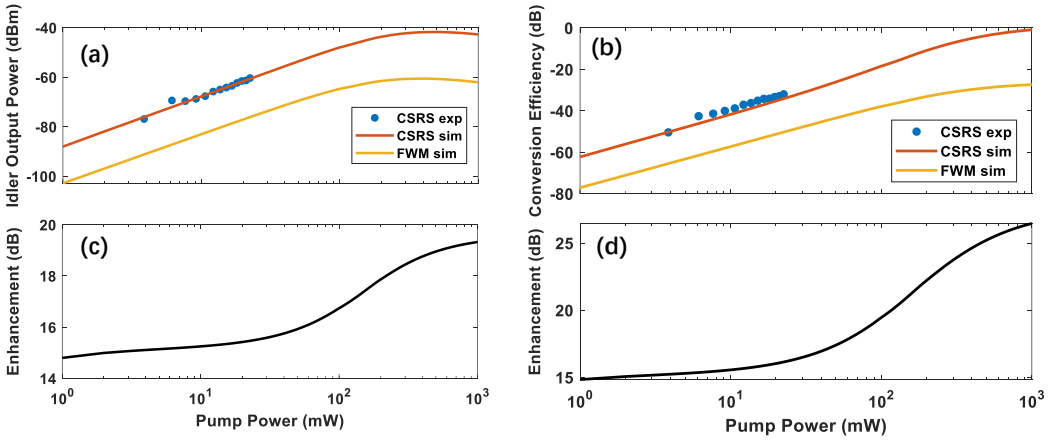

FIGURE 5.10: Trends of idler output power (a) and conversion efficiency (b) for CSRS and FWM for Rib A, as labeled in the legend, as a function of pump power. Enhancement of idler output power (c) and conversion efficiency (d), which is the difference between those of CSRS and FWM in (a) and (b), respectively. The pump wavelength is fixed at 1545 nm, the signal is fixed at 1432 nm with the coupled-in power of 70 μW.

5.3 CSRS in the mid-infrared band

As stated in the previous chapters, TPA and FCA, the main limitation of nonlinear performance in the telecom band, dramatically decrease when moving to longer wavelengths, even becoming negligible beyond 2.2 μm. CSRS based on the planar rib waveguide is also studied in the mid-infrared band to achieve a higher conversion efficiency and a larger Stokes output power, introducing a possible way to realize the light amplifiers and light sources on-chip in the mid-infrared band.

5.3.1 Structural design and CSRS simulation

In order to achieve phase-matching conditions for CSRS in the mid-infrared band, the dispersion profile for various waveguide dimensions, such as etch depth and width values, was firstly investigated, focusing on the chosen pump wavelength of 2170 nm, as presented in Figure 5.11 (a). Operating near the ZDW, depicted by the black dash line, is preferable to obtain a broad FWM bandwidth, ensuring overlap with the Raman gain peak. Figure 5.11 (a) demonstrates a trend similar to Figure 5.3, indicating that the zero dispersion condition can be achieved for different combinations of etch depth and width. Larger widths corresponds to larger etch depths. The variation rate is more gradual, with the range of the etch depth ranging just $\sim$ 50 nm when the width changes from 1400 nm to 1650 nm. Simultaneously, β_2 changes more slowly along the width, but more dramatically along the etch depth. This suggests that the dispersion profile is highly sensitive to the etch depth and less responsive to width variations. To further define optimal structural parameters, SL, calculated by Eq.(5.1), is shown in Figure 5.11 (b) to minimize side wall scattering loss. Scattering loss is slightly larger

on the left side with a smaller width and etch depth. In comparison, the variation of A_{eff}, depicted in Figure 5.11 (c), suggests that a smaller etch depth and width are preferable to achieve a smaller A_{eff}, which is on average twice larger than that in the telecom band. As a result, a compromise structure with $h = 250\,\text{nm}$ and $W = 1540\,\text{nm}$ was determined to balance a small mode area to achieve a high mode intensity while having the potential for low losses through a modest etch depth. The dispersion values for this structure are $\beta_2 = -2.77\times10^{-3}\ \text{ps}^2/\text{m}$ and $\beta_4 = 4.26\times10^{-7}\ \text{ps}^4/\text{m}$.

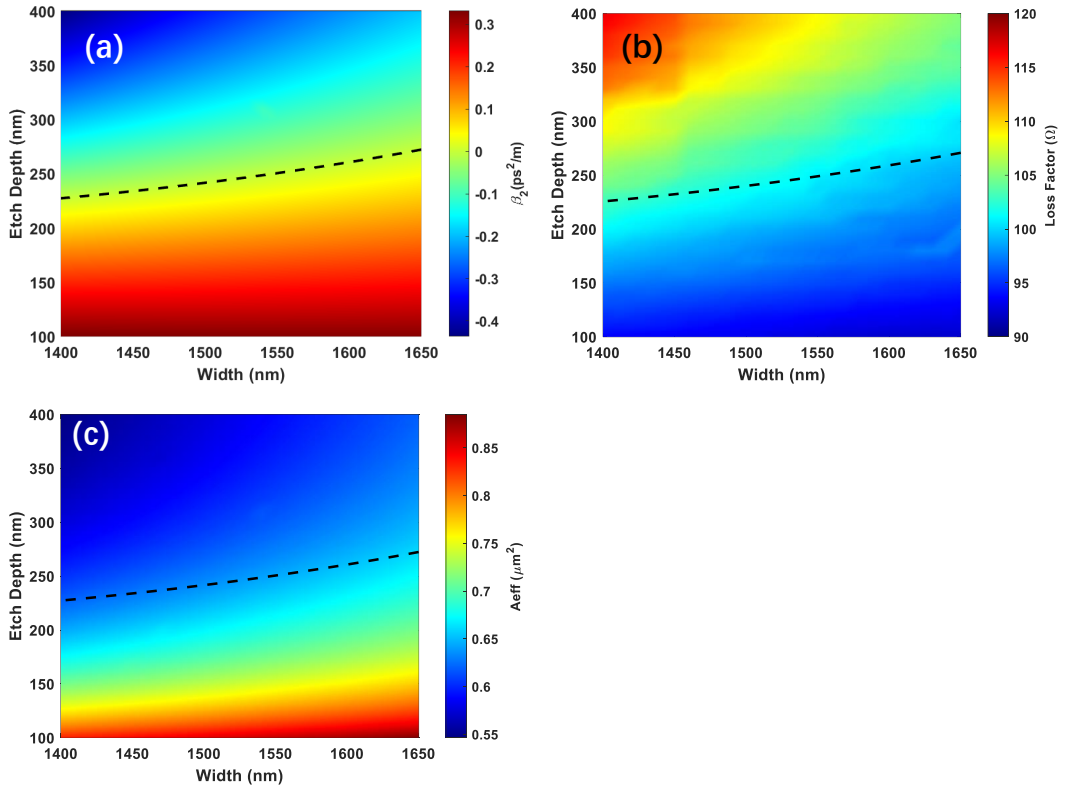

FIGURE 5.11: (a) β_2, (b) Scattering loss and (c) A_{eff} varying with etch depth and width at a wavelength of 2170 nm. The black dash line represents β_2 is equal to zero.

After determining the optimal structure, the influence of the structural parameters on CSRS conversion efficiency was investigated, thereby validating the design for the existing fabrication techniques. In these simulations, the pump is fixed at 2170 nm with the pump power of 100 mW, and the signal is set at 1950 nm with the power of 5 mW. The propagation length is 1 cm. Figure 5.12 (a) displays the conversion efficiency as a function of λ_s while varying the etch depth from 200 nm to 300 nm. As expected, the bandwidth is maximized when the etch depth equals the optimum value of 250 nm, but decreases sharply as the etch depth deviates from this value.
Figure 5.12 (b) shows the efficiency as the waveguide width is changed from 1400 nm to 1700 nm. Again, the bandwidth is maximum for the designed width of 1540 nm, but the decrease in bandwidth is less sharp than when adjusting the etch depth. In both cases, it is clear that CSRS, marked by the black dash boxes, is strongly excited when the bandwidth of FWM overlaps with the Raman gain spectrum. Figure 5.12 (c) and

(d) display the conversion efficiency as a function of etch depth and width, respectively, extracted from Figure 5.12 (a) and (b). The reference conversion efficiency is set at -20 dB, denoted by the dash lines in Figure 5.12 (c) and (d), around 4 dB less than the maximum conversion for the 100 mW pump. Based on this reference value, the fabrication tolerance for the etch depth is determined to be 30 nm and for the width to be 170 nm. These tolerances are larger than those in the telecom band for both dimensions, suggesting that the rib waveguide operating in the mid-infrared band is more robust in terms of the fabrication tolerances for observing strong CSRS.

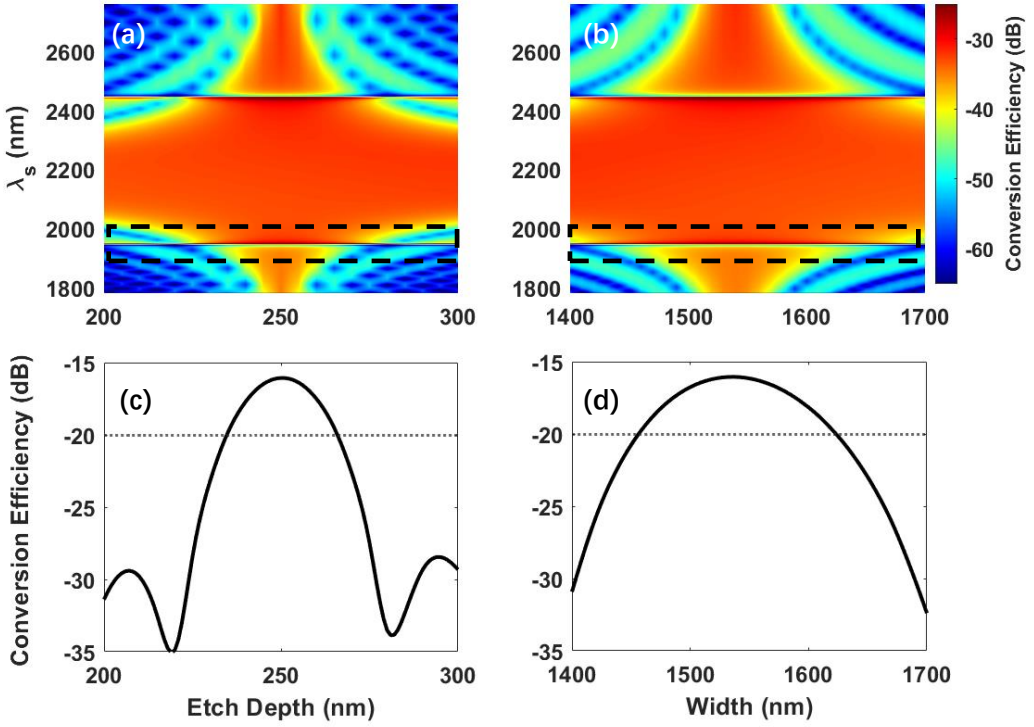

FIGURE 5.12: (a) Conversion efficiency as functions of h and λ_s. (b) Conversion efficiency as functions of W and λ_s. (c) and (d) show the conversion efficiencies of the CSRS processes, marked with black dash boxes in (a) and (b), respectively, where signal is tuned to the anti-Stokes wavelength of 1950 nm. In all cases the pump wavelength is 2170 nm with a power of 100 mW, the signal power is 5 mW and the propagation length is 1 cm.

To predict the maximum conversion efficiency and the Stokes output power that could be achieved in the mid-infrared band, the performance of CSRS is investigated by comparing the conversion efficiency and Stokes output power. Figure 5.13 (a) plots a colour map of the conversion efficiency as functions of pump power and waveguide length, with the remaining parameters for the pump, signal and waveguide identical as previously used in Figure 5.12. From this result, as the pump power increases beyond $\sim$ 600 mW, the conversion efficiency saturates at a propagation length of $\sim$ 0.7 cm. It then decreases and stabilizes at $\sim$ 10 dB. This decrease is attributed to the enhancement of Stokes wave at high pump power, leading to energy transfer to the anti-Stokes wave and higher-order Stokes waves.The optimal pump power for

achieving a maximum conversion efficiency of over 20 dB is found to be 260 mW, with a propagation length of ~ 3 cm. When the pump power is lower than 260 mW, the conversion efficiency remains stable along the propagation after reaching the maximum. The required pump power that is twice as large as that in the telecom band is due to the large A_{eff}, while the saturation length remains equivalent. Figure 5.13 (b) then displays a colour map of the achievable Stokes output power as functions of pump power and waveguide length. In contrast to Figure 5.5 (b), which exhibits an obvious maximum with limited pump power, this shows that the output idler power continuously increases with increasing pump power. However, there is saturation along the propagation length, attributed to the conversion of the first-order Stokes wave to higher-order waves and the linear loss. Further reduction of the losses could increase the saturation propagation length and Stokes output power. The pump power is capped at 1 W to avoid considerations of 3PA and its inducing TPA. Notably, for the mid-infrared band, the Stokes output power at the same level of pump power and propagation length is larger than that in the telecom band by a order of magnitude when the pump power reaches hundred of milli-watts as a result of the lack of nonlinear losses.

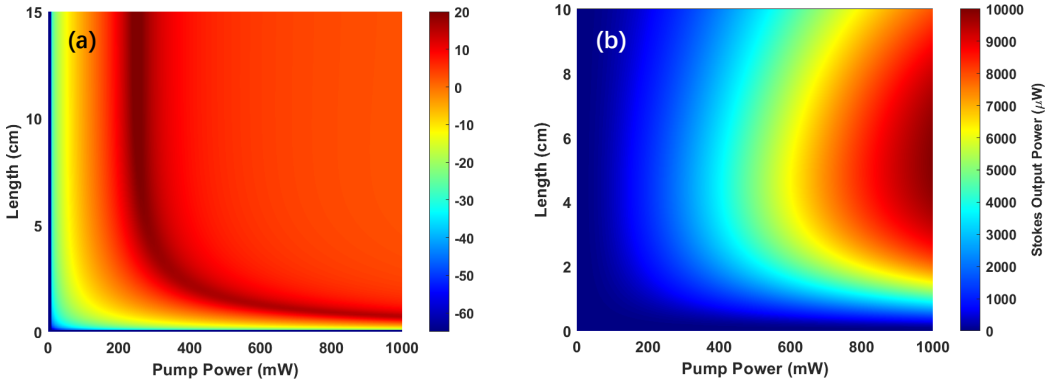

FIGURE 5.13: (a) Conversion efficiency and (b) Stokes output power as functions of the pump power and waveguide length when pumping at 2170 nm with a 5 mW signal beam positioned at 1950 nm. The waveguide width is 1540 nm and the etch depth is 250 nm.

5.3.2 Experimental verification

For the CSRS experiment in the mid-infrared, the same setup as that used for SCFs was utilised, as illustrated in Figure 4.15. Similar to the telecom band experiment, the SCFs were replaced by a rib waveguide sample. The experimental conversion efficiency for Rib E is depicted in Figure 5.14, where the pump wavelength is tuned around 2171 nm with a coupled-in pump power of 40 mW. The signal is fixed at 1950 nm with a coupled-in power of 350 μW. As λ_i approaches the peak Raman wavelength, the conversion efficiency increases from ~ -36 dB up to ~ -31 dB,

exhibiting a distinct peak at the Raman shift. The experimental results align with the simulation conducted by NLSE. The maximum conversion efficiency is equivalent to that observed in the telecom band, with double the pump power, owing to the halved A_{eff}. Here, the similar conversion efficiency in the telecom and mid-infrared bands is attributed to the low coupled pump power in the waveguide, which results in limited influence of nonlinear losses.

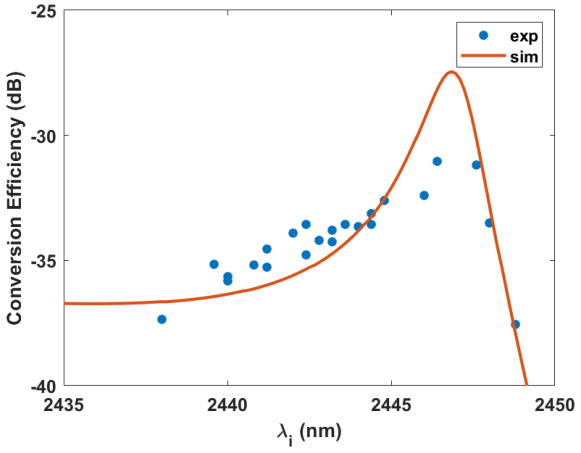

FIGURE 5.14: Conversion efficiency as λ_i is tuned across Γ_R for Rib E. The experimental results are compared with simulations of CSRS and FWM, as labeled in the legend. The pump wavelength is tuned around 2171 nm with a coupled-in power of 40 mW, while the signal is fixed at 1950 nm with a coupled-in power of 350 μW.

To obtain higher conversion efficiency and explore the trends in enhancement, the conversion efficiency and Stokes output power were recorded while varying the coupled-in pump power, switching from 30 mW to $\sim$ 45 mW. In the experiment, the pump wavelength was fixed at 2171 nm with the signal wavelength of 1950 nm. The experimental results shown in Figure 5.15 (a) and (c) display a linear increase in both conversion efficiency and Stokes output power with pump power, ascending from -40 dB to 30 dB and -70 dBm to -60 dBm, respectively. These findings are consistent with the simulation results. Whereas, for CSRS conversion efficiency with pump power exceeding 700 mW, the conversion efficiency slightly drops down. Compared with fibre results in the mid-infrared band, the conversion efficiency increases by 10 dB due to a better phase matching condition and a smaller effective mode area at the same pump power level. On the other hand, compared with the rib waveguide results in the telecom band, the conversion efficiency, as well as the idler output power, is equivalent.

The enhancement, shown in Figure 5.15 (b) and (d), has a similar trend as that in the telecom band, increasing gradually at low pump power levels. However, when the pump power continues to increases over 10 mW, the enhancement of Stokes output power start to decrease, resulted from the excitation of higher-order Stokes and anti-Stokes waves. Meanwhile, the enhancement of conversion efficiency continues to

increase due to the weakening of higher-order waves and the growth of the 1^{st}-order Stokes. The enhancement of conversion efficiency maximises at a pump power of 700 mW and then drop down as 1^{st}-order Stokes and ant-Stokes waves reach saturation and higher-order waves surge. The corresponding enhancement of Stokes output power increases again due to the increasing saturation power of 1^{st}-order Stokes waves induced by increasing the pump power. Compared with the enhancement of conversion efficiency and Stokes output power in the telecom band, the trend is unpredictable due to the lack of nonlinear losses and the appearance of higher-order Stokes and anti-Stokes waves.

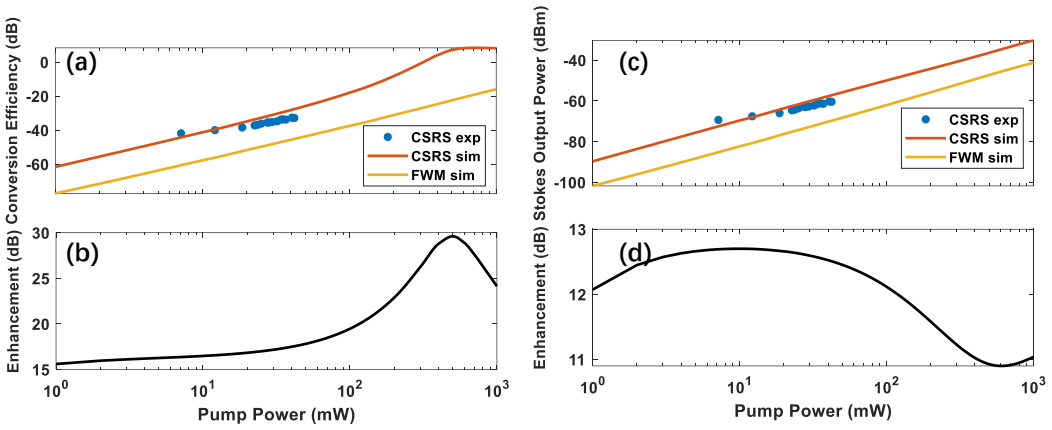

FIGURE 5.15: (a) Conversion efficiency and (c) Stokes output power for CSRS and FWM for Rib E, as labeled in the legend, as a function of pump power. Enhancement of conversion efficiency (b) and Stokes output power (d), which is the difference between those of CSRS and FWM in (a) and (c), respectively. The pump wavelength is fixed at 2171 nm, the signal is fixed at 1950 nm with the coupled-in power of 350 μW.

The conversion efficiency observed in the experiment is limited by the coupled in pump power and is only 2 dB larger than the previous results based on pure FWM in the silicon waveguide with the same light intensity [9]. This limitation is attributed to the low Raman efficiency at longer wavelengths, which is exacerbated by the larger effective mode area of the structure compared to that in the telecom band.

5.4 Exploration of the influencing factors for CSRS

The comparison of conversion efficiency and Stokes output power enhancement across different platforms and different wavelengths suggests that stability could be achieved in the telecom band. However, the trend appears irregular in the mid-infrared band for both platforms, possibly due to the absence of TPA and FCA. To further investigate the effects of potential influencing factors on the enhancement, corresponding simulations will be conducted and analysed using the control variable method. In this section, a variable control method was employed to study the impact of different parameters, which is a qualitative analysis not consistent with realistic

circumstances. Here, the conversion efficiency enhancement (CEE) and Stokes output power enhancement (PE) are defined as:

$$\begin{aligned} PE &= 10 \times log_{10} \frac{P_{Stokes-CSRS}}{P_{Stokes-FWM}}, \\ CEE &= 10 \times log_{10} \frac{P_{Stokes-CSRS}}{P_{anti-Stokes-CSRS}} - 10 \times log_{10} \frac{P_{Stokes-FWM}}{P_{anti-Stoks-FWM}} \\ &= PE + 10 \times log_{10} \frac{P_{anti-Stokes-FWM}}{P_{anti-Stokes-CSRS}}, \end{aligned} \tag{5.2}$$

where $P_{Stokes-FWM}$ and $P_{anti-Stokes-FWM}$ are calculated by setting $f_R = 0$. CEE and PE are represented by the blue line and red line, respectively, in the subsequent figures. The basic value for various parameters is listed in Table 5.1, which will be tuned individually for comparison.

Parameter description	Symbol	Value
Second-order dispersion parameter	β_2 (ps^2/m)	9.3×10^{-4}
Third-order dispersion parameter	β_3 (ps^3/m)	6.4×10^{-4}
Fourth-order dispersion parameter	β_4 (ps^4/m)	-6.2×10^{-7}
Effective mode area	A_{eff} (μm^2)	0.3
Nonlinear refractive index	n_2 (m^2/W)	6×10^{-18}
Raman fraction	f_R	0.043
TPA parameter	β_{TPA} m/W	10×10^{-12}
Pump power	P_p (mW)	1000
Signal power	P_s (mW)	2
Free carrier lifetime	τ (ns)	7.5
Propagation length	L (mm)	10
Linear loss	LL (dB/cm)	2
Pump wavelength	λ_p (nm)	1545

TABLE 5.1: The corresponding parameters of rib waveguide used in the nonlinear experiments.

First, the dispersion parameters that play an important role in FWM are explored, with results depicted in Figure 5.16. In this simulation, β_2, β_3 and β_4 are varied from -100 to $200\,ps^2/m$, -1×10^{-4} to $10 \times 10^{-4}\,ps^{-3}/m$ and -50×10^{-7} to $50 \times 10^{-7}\,ps^{-4}/m$. β_2 significantly influences both CEE and PE, as shown in Figure 5.16 (a). CEE oscillates around $25\,dB$, while PE fluctuates around $19\,dB$. Compared with the significant change of FWM conversion efficiency with various β_2, exceeding 30 dB, this variation range is relatively small, indicating that CEE and PE could maintain a relatively stable value under different β_2. As Figure 5.16 (b) shows, CEE and PE remain unchanged with variation in β_3, ~ 26 dB and ~ 16 dB, respectively, consistent with the corresponding results in Figure 5.16 (a). It indicates that β_3 has no effects on either CEE or PE, which is in accordance with the cancellation

of β_3 in the derivation of the phase mismatch function Equation 2.16. PE remains constant with changes in β_4, ~ 16 dB, while CEE slightly declines with increasing β_4 as shown in Figure 5.16 (c). The decrease in CEE is mainly due to the consideration of Raman gain at anti-Stokes waves being larger than the amplification of FWM that decrease as a result of the increasing phase mismatch with the rising β_4. Overall, among the dispersion parameters, β_2 is the primary factor influencing the enhancement of conversion efficiency and Stokes output power, but the change occurs within a narrow range, with β_4 serving as an auxiliary adjustment to CEE.

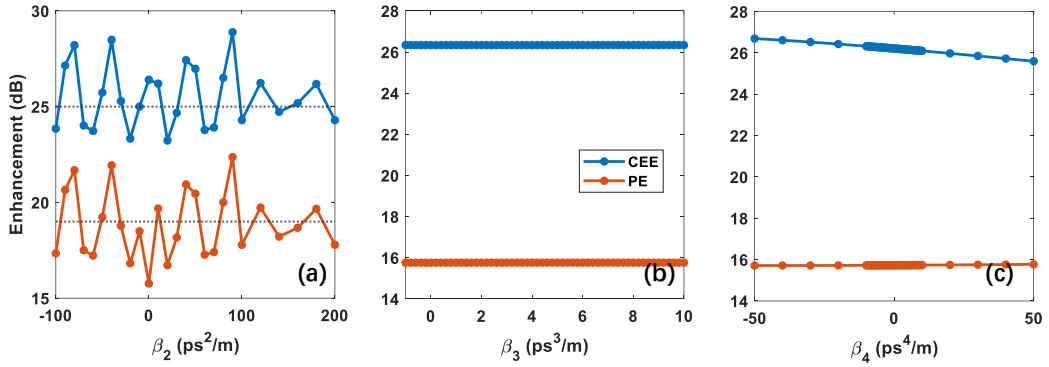

FIGURE 5.16: The influence of β_2 (a), β_3 (b) and β_4 (c) on CEE and PE, as labeled in the legend. In this simulation, $A_{eff} = 0.3\,\mu\text{m}^2$, $n_2 = 6 \times 10^{-18}\text{m}^2/\text{W}$, $f_R = 0.043$, $\beta_{TPA} = 10 \times 10^{-12}\text{m/W}$, the pump is 1545 nm with power of 1 W, the signal is 1432 nm with power of 2 mW, the free carrier life time is 7.5 ns, and the propagation length is 1 cm.

Next, the pump power will be discussed, which is crucial for boosting various nonlinear effects. CEE and PE varying with the rising pump power is depicted in Figure 5.17 (a). The variation with the pump power below 200 mW is dramatic, with CEE surging and PE declining initially. The slightly decrease in PE may because SRS dominating in CSRS, and the idler induced by FWM with a small pump power is weak, leading to a slightly higher enhancement. Once the FWM-induced idler becomes strong enough, and the parametric gain is much stronger than SRS in CSRS, PE stabilizes at ~ 16 dB. The significant increase in CEE is mainly due to the greater consumption of the signal at the anti-Stokes wavelength with the increasing pump power, as verified in the definition of CEE. CEE reaches a saturation point, around 27 dB, at a pump power of 1 W, then slightly decreases due to the appearance of higher-order waves. Conclusively, increasing pump power has limited influence on PE, firstly decreasing slightly, then remaining at 16 dB, while effectively increases CEE.

Besides the pump power, which obviously changes the light intensity for a specific structure, A_{eff} is an essential factor that should exhibit an inverse trend with increasing pump power. In Figure 5.17 (b), the increasing A_{eff} results in a minor increase in PE while leading to a significant drop in CEE from 27 dB to 21 dB, consistent with the variation range in Figure 5.17. The reduction of light intensity with the increase of A_{eff} results in the simultaneous decrease in the efficiency of FWM, IRS

and SRS, which could be offset in the calculation of PE but is exacerbated by the consideration of the anti-Stokes wave in the calculation of CEE.

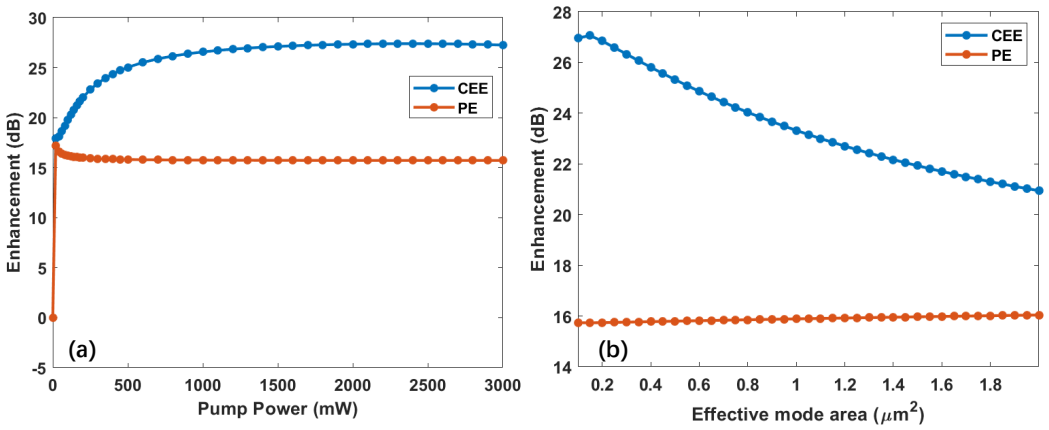

FIGURE 5.17: The influence of P_p (a) and A_{eff} (b) on CEE and PE, as labeled in the legend. In this simulation, $\beta_2 = 9.3 \times 10^{-4}\,\mathrm{ps}^2/\mathrm{m}$, $\beta_3 = 6.4 \times 10^{-4}\,\mathrm{ps}^3/\mathrm{m}$, $\beta_4 = -6.2 \times 10^{-7}\mathrm{ps}^4/\mathrm{m}$, $n_2 = 6 \times 10^{-18}\mathrm{m}^2/\mathrm{W}$, $f_R = 0.043$, $\beta_{TPA} = 10 \times 10^{-12}\mathrm{m/W}$, the pump is 1545 nm, the signal is 1432 nm with power of 2 mW, the free carrier life time is 7.5 ns, and the propagation length is 1 cm.

The nonlinear refractive index (n_2) is an essential parameter for estimating the nonlinear performance of materials, ranging from $2 \times 10^{-18}\mathrm{m}^2/\mathrm{W}$ to $8 \times 10^{-18}\mathrm{m}^2/\mathrm{W}$ in silicon, spanning from the telecom band to the mid-infrared band. To explore the influence of n_2, the value is adjusted within the possible range corresponding to silicon, even at the same pump wavelength. In Figure 5.18 (a), PE remains stable at about 16 dB but slightly drops with increasing n_2, while CEE has a significant rise from 16 dB to 32 dB and then exhibits a downward trend when n_2 is over $7.5 \times 10^{-18}\mathrm{m}^2/\mathrm{W}$. The stabilisation of PE is due to the saturation of SRS gain and the minor drop is attributed to the energy transfer to the higher-order waves in CSRS. The increase in CEE is mainly due to the consideration of anti-Stokes waves, which is consumed in CSRS and boosted in FWM. The subsequent decrease in CEE is due to the energy transfer back to anti-Stokes waves in CSRS with a large n_2.

To explore the influence of the signal power, it is tuned from nanowatts to watts to observe the variation of CEE and PE, as depicted in Figure 5.18 (b). PE and CEE exhibit a similar trend with increasing signal power, surging initially, then dropping down at a signal power of microwatt, and finally stabilising at 16 dB and 27 dB, respectively. However, when the signal power is comparable to the pump power, PE and CEE start to show opposite trends, and the signal cannot be treated as a weak signal, contrary to the conditions of CSRS. When the signal power is equivalent to the noise level, the main nonlinear effect at the Stokes wavelength is the spontaneous Raman scattering, and idler generated through FWM is negligible. This leads to the initial increase of CEE and PE. The following drop of CEE and PE is due to the power of idler generated by FWM starting to increase and excite SRS. When the signal power

is in the range between hundreds of microwatts and hundreds of milliwatts, the PE and CEE remain to be stable at 16 dB and 27 dB, respectively.

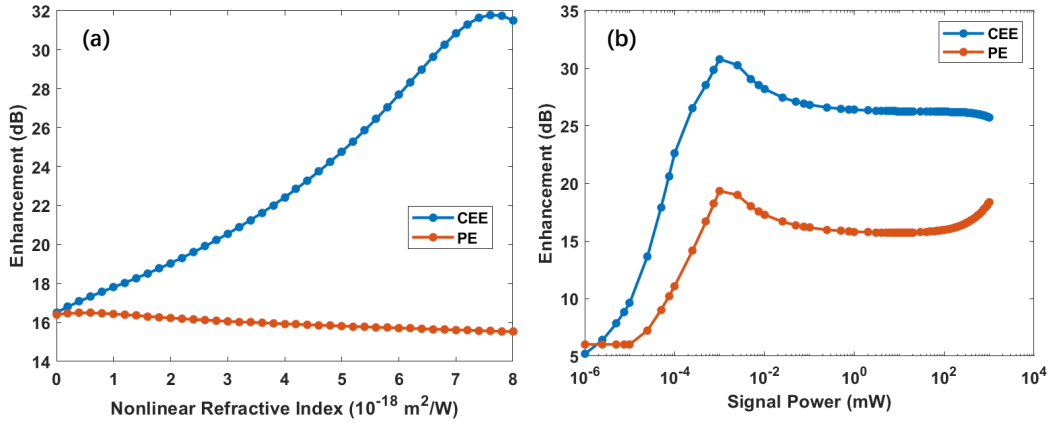

FIGURE 5.18: The influence of n_2 (a) and P_s (b) on CEE and PE, as labeled in the legend. In this simulation, $A_{eff} = 0.3\mu m^2$, $\beta_2 = 9.3 \times 10^{-4}\,ps^2/m$, $\beta_3 = 6.4 \times 10^{-4}\,ps^3/m$, $\beta_4 = -6.2 \times 10^{-7} ps^4/m$, $f_R = 0.043$, $\beta_{TPA} = 10 \times 10^{-12} m/W$, the pump is 1545 nm with the power of 1 W, the signal is 1432 nm, the free carrier life time is 7.5 ns, and the propagation length is 1 cm.

The Raman fraction (f_R) is a critical parameter for evaluating the Raman efficiency of materials, representing the fractional contribution of the delayed Raman response to the nonlinear polarisation. The value theoretically varies between 0 to 1, depending on the intrinsic characteristic of different materials. The variation of PE and CEE with the change of f_R is given in Figure 5.19 (a). In contrast to parameters in previous discussions, f_R has a dramatic effect on both CEE and PE. CEE reaches a maximum, 38 dB, when $f_R = 0.06$ due to the IRS consumption of the anti-Stokes waves with a relatively small Raman gain. It then drops down and stabilises when $f_R > 0.2$ due to the increase in the anti-Stokes waves as a result of strong Raman gain. CEE equals 27 dB when f_R is equal to the typical value of silicon, 0.043, consistent with other results. PE increases to the maximum, 29 dB, until $f_R = 0.4$, then drops down when $0.4 < f_R < 0.8$, finally increasing to 25 dB. The increase in PE is due to the stronger Raman gain with f_R, and the subsequent decrease arises from the energy transferring back to anti-Stokes waves. As Raman scattering is the origin of realizing the enhancement in CSRS, the Raman fraction determines exactly how much the enhancement could be obtained.

The TPA coefficient (β_{TPA}) is a critical parameter for silicon, which changes from $0 \times 10^{-12} m/W$ to $14 \times 10^{-12} m/W$, as it determines the nonlinear loss in the most studied wavelength bands, especially the telecom band. To explore the influence of β_{TPA}, the value is adjusted within the possible range corresponding to silicon, even at the same pump wavelength. In Figure 5.19 (b), PE remains stable at about 16 dB but slightly increases with the increasing β_{TPA}, while CEE has a significant rise from 8 dB to 32 dB and then a downward trend when β_{TPA} is over $5 \times 10^{-12} m/W$. The

stabilization of PE indicates that nonlinear absorption will have the same degradation in one process, no matter how many nonlinear effects are included. The initial increase in CEE may result from the significant IRS decrease of anti-Stokes waves, peaking at 5.5×10^{-12} m/W. The continuous decrease is due to the weakening of IRS and the relatively strong FWM and Raman gains.

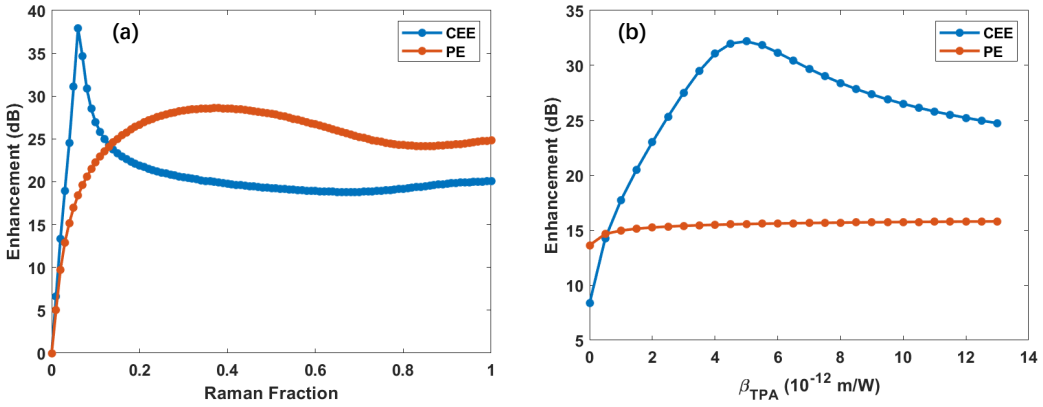

FIGURE 5.19: The influence of f_R (a) and β_{TPA} (b) on CEE and PE, as labeled in the legend. In this simulation, $A_{eff} = 0.3\mu m^2$, $\beta_2 = 9.3 \times 10^{-4}$ ps^2/m, $\beta_3 = 6.4 \times 10^{-4}$ ps^3/m, $\beta_4 = -6.2 \times 10^{-7}$ps^4/m, $n_2 = 6 \times 10^{-18}$m^2/W, the pump is 1545 nm with the power of 1 W, the signal is 1432 nm with the power of 2 mW, the free carrier life time is 7.5 ns, and the propagation length is 1 cm.

The free-carrier lifetime (τ) determines the strength of the FCA, typically ranging from a few nanoseconds to hundreds of nanoseconds depending on the silicon waveguide structure. To explore the influence of the free carrier lifetime, the value is adjusted within the possible range corresponding to silicon, and the result is depicted in Figure 5.20 (a). The trends of PE and CEE are similar to the those in Figure 5.19 (b) because the free carrier lifetime, along with β_{TPA}, contributes to the nonlinear loss. CEE achieves the maximum, 32 dB, when the free carrier lifetime is equal to 32 ns, and then drops to 20 dB and remains constant when the free carrier lifetime is longer. The influence of the free carrier lifetime on PE is limited, and PE remains stable at 16 dB.

The propagation length is another influencing factor as the phase matching condition changes along it, and the linear loss also accumulates, potentially affecting the conversion efficiency and Stokes output power. In Figure 5.20 (b), CEE reaches the maximum, 32 dB, at the length of 2.3 cm, then drop to 25 dB after further propagation and remains unchanged. The trend of CEE suggests an optimised propagation length at 20 mm, representing the maximum consumption on anti-Stokes waves.

Lastly, the linear loss (LL), which has a significant impact on the nonlinear process and the output power, will be discussed. The result is depicted in Figure 5.21. PE can be maintained with increasing linear loss, thanks to the uniform decrease in power in both CSRS and FWM. On the other hand, CEE experiences an obvious decline due to the weakening of IRS with increasing linear loss. This suggests that the output power

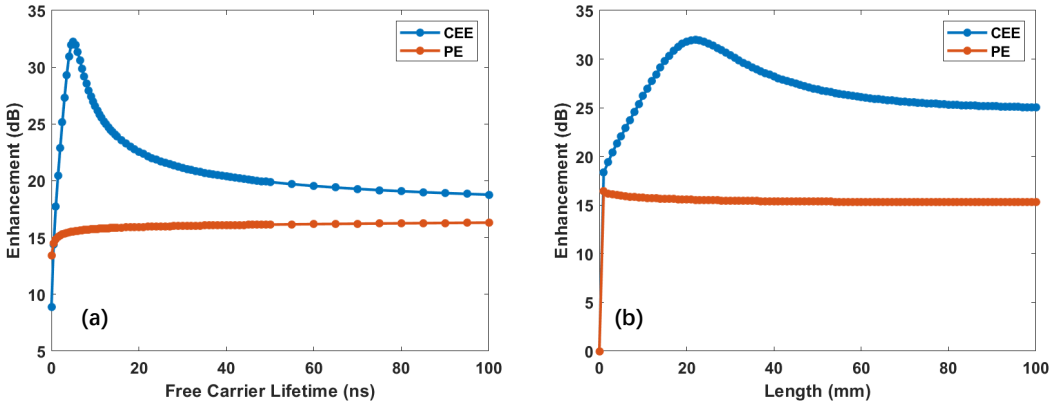

FIGURE 5.20: The influence of τ (a) and L (b) on CEE and PE, as labeled in the legend. In this simulation, $A_{eff} = 0.3\mu m^2$, $\beta_2 = 9.3 \times 10^{-4}\,ps^2/m$, $\beta_3 = 6.4 \times 10^{-4}\,ps^3/m$, $\beta_4 = -6.2 \times 10^{-7} ps^4/m$, $n_2 = 6 \times 10^{-18} m^2/W$, $f_R = 0.043$, $\beta_{TPA} = 10 \times 10^{-12} m/W$, the pump is 1545 nm with the power of 1 W, the signal is 1432 nm with the power of 2 mW.

can be amplified in a fixed level, but the conversion efficiency can be increased as much as possible when the linear loss is minimised. In summary, only β_2, P_s and f_R significantly influence PE, while CEE exhibits a more complex variation as it involves additional variables beyond PE.

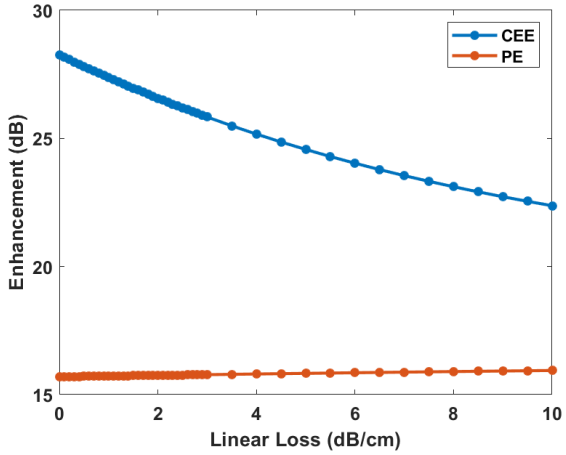

FIGURE 5.21: The influence of LL on CEE and PE, as labeled in the legend. In this simulation, $A_{eff} = 0.3\mu m^2$, $\beta_2 = 9.3 \times 10^{-4}\,ps^2/m$, $\beta_3 = 6.4 \times 10^{-4}\,ps^3/m$, $\beta_4 = -6.2 \times 10^{-7} ps^4/m$, $n_2 = 6 \times 10^{-18} m^2/W$, $f_R = 0.043$, $\beta_{TPA} = 10 \times 10^{-12} m/W$, the pump is 1545 nm with the power is 1 W, the signal is 1432 nm with the power of 2 mW, the free carrier life time is 7.5 ns.

This chapter investigates CSRS in rib waveguides in both telecom and mid-infrared band. The optimised structure design was determined based on the comparison between dispersion profiles, scattering loss and effective mode area. The experimental results surpassed those achieved in SCFs, primarily due to a smaller effective mode area and the fulfillment of phase matching conditions. However, the conversion

efficiency in the experiments is limited by the coupled-in pump power. In the future, coupling efficiency can be improved via optimising the experiment setup and introducing other couplers, such as grating coupler [125] or Y-type couplers [15].

Chapter 6

Slotted waveguides with flattened dispersion curve

The dispersion properties of the waveguides are essential for the Raman enhanced FWM in which the FWM is the foundation in this process. The gain spectrum of FWM could cover a wide wavelength range with a wide, flat and low dispersion property at specific pump wavelengths, which overlap multiple Raman shifts. This would be beneficial for facilitating Raman enhanced FWM and exciting higher-order Stokes waves. However, SCFs or rib waveguides dispersion property is far from optimal. In comparison, slotted waveguide structures exhibit a flat dispersion curve and the dispersion value is low enough to broaden the gain spectra of FWM [126][127]. In this section, the structure parameters of a SWG in the slot is demonstrated. Then the effects of different structure parameters on the dispersion profile is studied. The comparison of the conversion efficiency in two cases, FWM and Raman enhanced FWM, are given to verify whether the Raman enhanced FWM occurs in this structure. In this work, I was responsible for all simulations, waveguide design, polishing, and loss measurement.

6.1 Subwavelength grating design in slotted waveguides

Initially, the slot is empty, hence, the material refractive index of the slot n_m is equal to 1. If the side waveguide is far away from the core waveguide (Figure 6.1), the slotted structure has little influence on the dispersion properties. In this case, in order to effectively realize the influence of the side waveguide on the core waveguide, the width $slot_w$ of the slot section is close to 15 nm, and it is impossible to manufacture such a waveguide with the existing techniques. Through changing the material in the slot section, we found that $slot_w$ depends on the refractive index of the material in the slot. $slot_w$ could be extended up to $\sim$ 50 nm and $\sim$ 150 nm if SiO_2 ($n_m \sim 1.4$) and TiO_2

($n_m \sim 2.2$) would be applied. The larger the refractive index is, the wider $slot_w$ can be. However, deposition of different materials in the slot would be challenging as the slot is relatively narrow and there may be some voids near the corners. Also, chemical mechanical polishing (CMP) would be required to planarize the waveguide after the deposition. Therefore, a subwavelength grating (SWG) slot can be used as an alternative. In this circumstance, CMP would be avoided, and the slot refractive index could be controlled more accurately. The details of the structure are given in Figure 6.1. The slot divides the waveguide asymmetrically in two parts and the upper cladding is air. The left part is the side waveguide, and the right part is the core waveguide. The depth of the slot section is different from the core height, H, and a certain thickness of silicon is preserved with height, h. SWG is fabricated in the slot section, acting as a metamaterial with a proper refractive index. Here, the refractive index, n_m, is set to 2.2 in the following calculations to achieve a larger slot width for improved fabrication feasibility. The duty cycle and the period of the SWG obtained through Eq.(2.1) and Eq.(2.2), are about 0.35 and 300 nm, respectively. Besides the SWG in the slotted waveguide, other structure parameters are determined by comparing the dispersion properties with different designs in the following section.

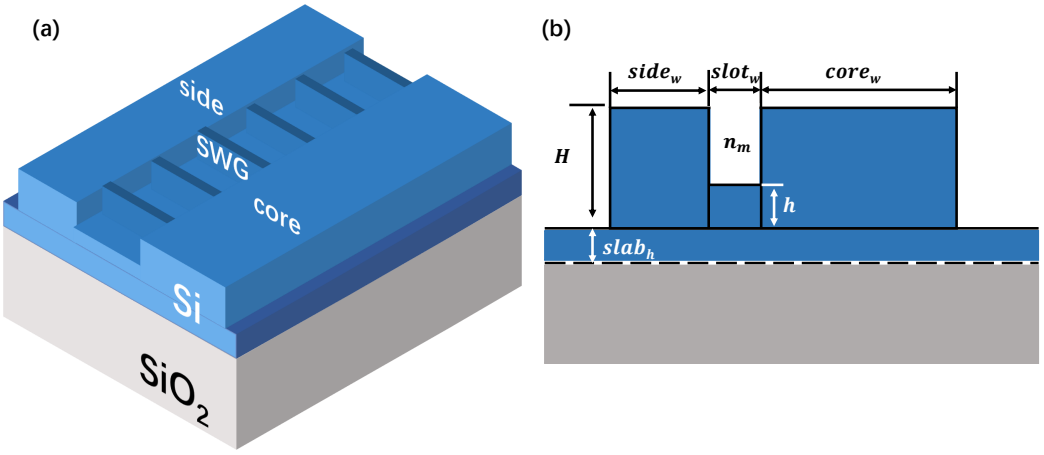

FIGURE 6.1: Structure diagram (a) and the cross-section diagram (b) of the slotted waveguide which is consist of a side waveguide and a core waveguide separated by the SWG.

The slotted waveguide with $core_w = 1500$ nm, $H = 300$ nm, $side_w = 600$ nm, $slot_w = 150$ nm, $slab_h = 200$ nm and $h = 50$ nm was taken as an example to analyse the light mode supported in such structures. The structural parameters especially the $core_w$ were chosen for the position of the ZDW based on the analysis in Chapter 5. When the wavelength is set at 2.2 μm that is comparable to the structure size and the desired wavelength for nonlinear phenomena, three different light mode with different n_{eff} existing in the slotted waveguide are selected to illustrate the electric filed distribution as Figure 6.2 shows. The light is tightly confined in the core waveguide with n_{eff} being 3.03, which is the same as normal circumstances in the

traditional rib waveguide depicted in Figure 6.2 (a). When n_{eff} is 2.88 close to the equivalent refractive index of the slot section, the electric field is more concentrated in the slot section compared with the core and side waveguides. The higher TE mode also appears as expected with n_{eff} of 2.75 in the slotted waveguide, as depicted in Figure 6.2 (c). The slotted waveguide performs as two independent rib waveguides as Figure 6.2 (d) shows when the operating wavelength is 1.8 μm, which is much smaller than the overall structural dimension and comparable to the size of the core waveguide or side waveguide. When the wavelength increases up to 3 μm, the fundamental light mode in the core waveguide experience a distortion shown in Figure 6.2 (e). The centre of the mode moves to the slot side, and the electric field is predicted in the slot section, which leads to n_{eff} to decrease to 2.79. It is obvious that the slotted waveguide works as a unit entity, and various sections effectively interact with each other at a wavelength beyond 2.2 μm, which is larger than the size of the overall structure. When the working wavelength is further increased to 4.5 μm, the light mode supported in the slotted waveguide is completely different from the previous cases, transforming into a slot mode in which light is majorly confined in the slot section and n_{eff} decrease to 2.36, close to n of equivalent material in the slot section. The analysis of light modes supported by the slotted waveguide indicates that appropriate structural size and operating wavelength can ensure that the slotted waveguide operates in the interference mode rather than the independent mode and the slot mode. Another significant characteristic of this structure is that the typical supported mode is the TE mode, which is influenced by the aspect ratio.

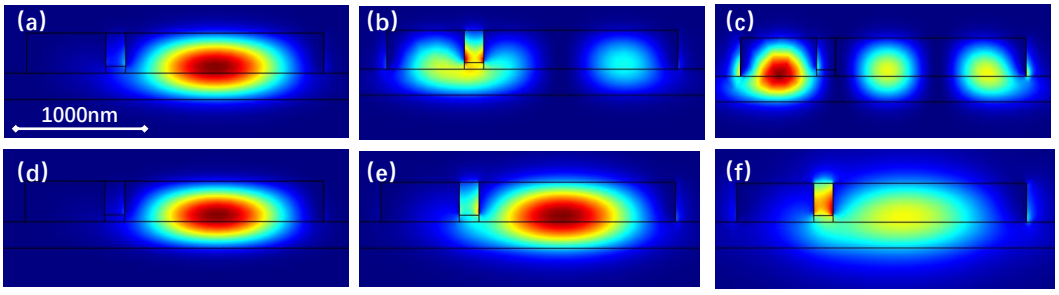

FIGURE 6.2: (a) Fundamental mode in the core waveguide at 1.3 μm, $n_{eff} = 3.29$; (b) Fundamental mode in the side waveguide at 1.3 μm, $n_{eff} = 3.23$; (c) higher mode in the core waveguide at 1.3 μm, $n_{eff} = 3.14$; (d) fundamental mode in the core waveguide at 2.5 μm, $n_{eff} = 2.88$; (e) fundamental mode in the side waveguide at 2.5 μm, $n_{eff} = 2.67$; (f) slot mode in the slotted waveguide at 3.8 μm, $n_{eff} = 2.47$.

6.2 Nonlinear performances for different structures

Before determining the slotted waveguide structure, different structure designs of slotted waveguides are compared in terms of the dispersion properties and the conversion efficiencies including or excluding the Raman response to find out the optimised structure to obtain a broader FWM spectrum. The distinction in dispersion

properties between the strip waveguide and the rib waveguide in the initial stage of my project motivated the comparison between different structure designs of slotted waveguides with and without the slab. The shallow depth of the slot is beneficial in fabrication, hence, the preserved silicon height (h) in the slot is also taken into consideration. Here, three structures are taken into considerations, structure 1 without the silicon slab beneath the waveguide and the preserved silicon in slot in the form of a SWG structure (Figure 6.3 (a)), structure 2 without the silicon slab but retaining silicon in slot in the form of a SWG structure (Figure 6.3 (b)), and structure 3 with the slab and the preserved silicon in the slot in the form of a SWG structure (Figure 6.3 (c)). For different structures, the geometrical parameters to achieve flat and low dispersion profiles are slightly different from each other. The comparison of the second-order dispersion profiles of different waveguides is given in Figure 6.4 (a). ZDWs are about 1.9 μm, 2 μm and 2 μm for structure 1, structure 2 and structure 3, respectively. It is obvious that values of β_4 are positive near ZDWs for these three structures, which means that β_2 that can be altered by adjusting the pump wavelength should be negative to minimize the phase mismatch. When pumping near the ZDWs with a negative β_2, the total linear phase mismatch (Δ_k) between pump (ω_p), signal (ω_s) and idler (ω_i) could be calculated by Eq.(2.16) which includes β_2 and β_4. Figure 6.4 (b) shows the comparison of Δk for different structures. The linear phase mismatch in structure 1 is slightly larger than that in the other two. However, it is still hard to distinguish between structure 2 and structure 3 which one has better nonlinear performance in the gain spectrum broadening according to the linear phase mismatch. Hence, the conversion efficiency spectrum is another important factor to further distinguish the performance differences of structures.

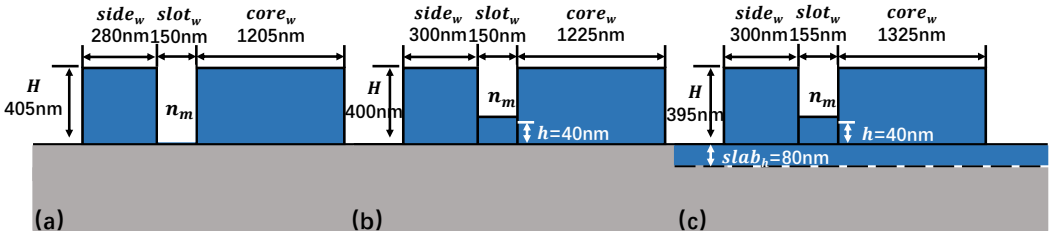

FIGURE 6.3: Cross sections of different slotted waveguide designs. Structure 1: slotted waveguide without a silicon slab beneath the waveguide and the preserved silicon in the slot; (b) Structure 2: slotted waveguide without a silicon slab beneath the waveguide but the preserved silicon in the slot; (c) Structure 3: slotted waveguide with a silicon slab beneath the waveguide and the preserved silicon in the slot.

Figure 6.5 illustrates the difference in the conversion efficiency between the three waveguides. The conversion efficiency without the Raman scattering is calculated for $f_R = 0$, while the conversion efficiency with the Raman scattering is calculated for $f_R = 0.043$. The pump power is 100 mW, the signal power is 1 mW and the propagation length is 1 cm. The pump wavelength is 1.9 μm, 2 μm, 2 μm, respectively for structure 1, structure 2 and structure 3. RE-FWM appears in all these three

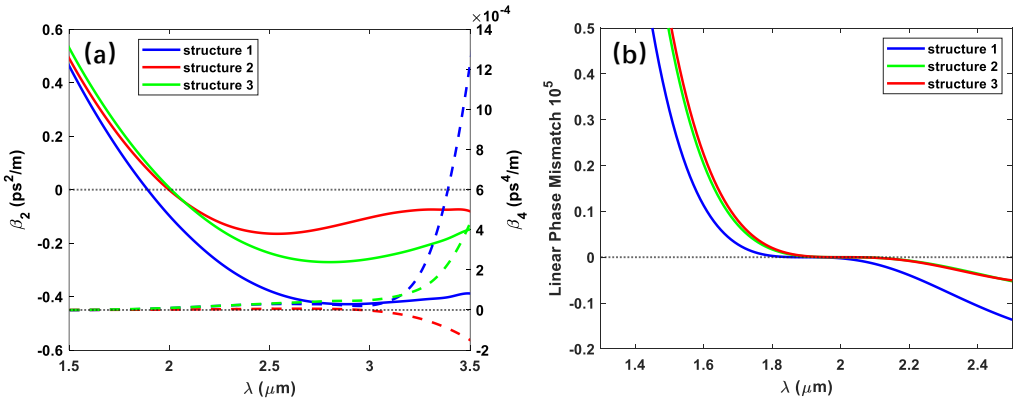

FIGURE 6.4: (a) Second-order (denoted by solid lines) and fourth-order (denoted by dash lines) dispersion parameters, β_2 and β_4, comparison. (b) Linear phase mismatch among structure 1, structure 2 and structure 3, when pumping at the ZDWs with negative β_2.

structures at the Raman shift including CARS and CSRS, and the enhancement is up to around 10 dB. The significant difference is the wavelength conversion band width for different structures. The wavelength conversion bandwidth in structure 1 is approximately from 1.6 μm to 2.3 μm, which is the narrowest. The wavelength conversion bandwidth in structure 2 is approximately from 1.7 μm to 2.5 μm, which is slightly larger than that of structure 1. For structure 3, the wavelength conversion bandwidth is up to around 3 μm, which is over three times that of the Raman shift. Through the comparison of gain spectra of the three structures, structure 3 is more promising to achieve a broad and flat wavelength conversion bandwidth, which could support higher-order Stokes generation with high-intensity pump injection.

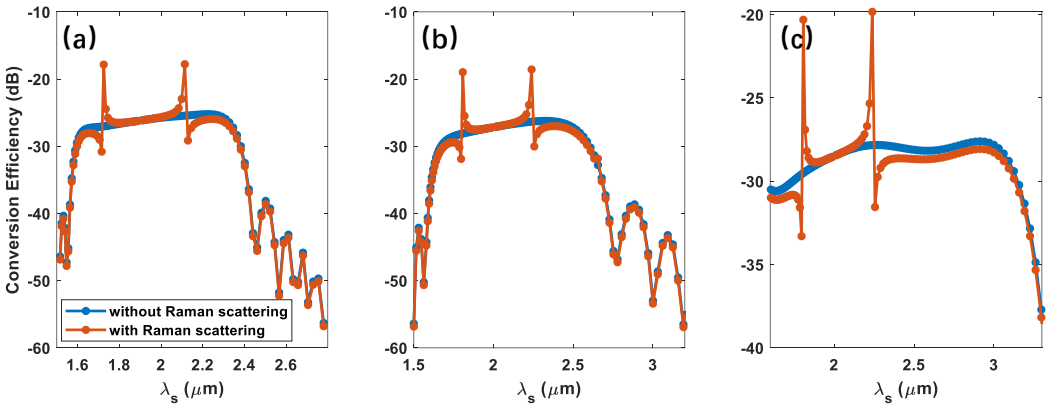

FIGURE 6.5: The conversion efficiency with and without the Raman scattering of (a) structure1; (b) structure 2; (c) structure 3, when pumping near ZDWs with negative β_2. The pump power is 100 mW the signal power is 1 mW and the propagation length is 1 cm

6.3 Effects of structure parameters on the dispersion curve

For the RE-FWM experiments, the available light sources with high pump power in our laboratories are around 1.54 μm and 2.17 μm as well as the corresponding signal light sources at anti-Stokes Raman wavelengths. As illustrated in the comparison of telecom band and mid-infrared band, nonlinear absorption is significantly smaller in the mid-infrared band than in the telecom band, which could even be ignored when the wavelength goes beyond 2 μm. Hence, in the following simulations, the ZDW needs to be adjusted to around 2.1 μm. According to the calculations of the dispersion profiles for structure 3, the structure parameters are selected as: the waveguide height $H = 395$ nm, the core waveguide width $core_w = 1325$ nm, the slot width $slot_w = 155$ nm, the side waveguide width $side_w = 300$ nm, the slab height $slab_h = 80$ nm, the preserved silicon step height $h = 40$ nm. In the following simulations, all the structure parameters are gradually tuned based on the above parameters, in which an adjusted parameter accompanies other fixed parameters at optimised values. Dispersion is simulated by the software COMSOL, and the calculation approach is the same as for the rib waveguides. The dispersion profile can be tailored by adjusting the structure parameters, $slab_h$, h, H, $side_w$, $slot_w$, $core_w$ as Figure 6.6 illustrates. Comparisons of the dispersion profiles among varying structure parameters are given and the optimised structure parameters will be presented at the end.

Firstly, the effect of the variation of waveguide height on the dispersion curve is given in Figure 6.6 (a). H is increased from 200 nm to 480 nm with the step of 20 nm. In the short wavelength, the change of H has little influence on the dispersion. However, the difference of the dispersion profile becomes obvious with the increase of the wavelength.When H is less than 320 nm, β_2 remains positive along the wavelength. The left ZDW occurs when H is larger than 360 nm and has a slightly blue shift with the increase of H. The left ZDW is almost around 2 μm and the position of the left ZDW is relatively insensitive to the change of H. In the middle of the dispersion profile, the slope initially becomes gentle when H increase from 200 nm to 400 nm, then becomes sharper again when H continues to increase, which means that it can produce flat and low dispersion when H is around 400 nm. The right ZDW occurs when H is larger than 360 nm, exhibiting a red shift with the increasing of H, which leads to the extension of the middle flat range but with a sharper slope.

Figure 6.6 (b) shows the variation of the dispersion curve with the increase of the core waveguide width, $core_w$, which is tuned from 600 nm to 1600 nm with a step of 200 nm. The change in dispersion distribution introduced by $core_w$ is much more obvious than the change in H, especially the trend on the left. When $core_w$ is smaller than 800 nm, β_2 is positive along the wavelength with the large slope. The left ZDW shifts towards the longer length from about 1.7 μm to about 2.25 μm with increasing

$core_w$ and the appropriate $core_w$ is between 1200 nm to 1400 nm for the fixing pump wavelength of 2.17 μm. The trend of the right ZDW is distinctive from the previous situations, which increase initially with the $core_w$ increasing to 1400 nm and then decrease with further increase of $core_w$. The middle part of the dispersion curve turns to be flat with the increase of $core_w$ and the dispersion value is getting closer to zero. In the range of $core_w$ mentioned above, from 1200 nm to 1400 nm, the dispersion curve is relatively flat, and the value is small enough. Hence, this range of $core_w$ could produce a flat and low dispersion property and a suitable ZDW.

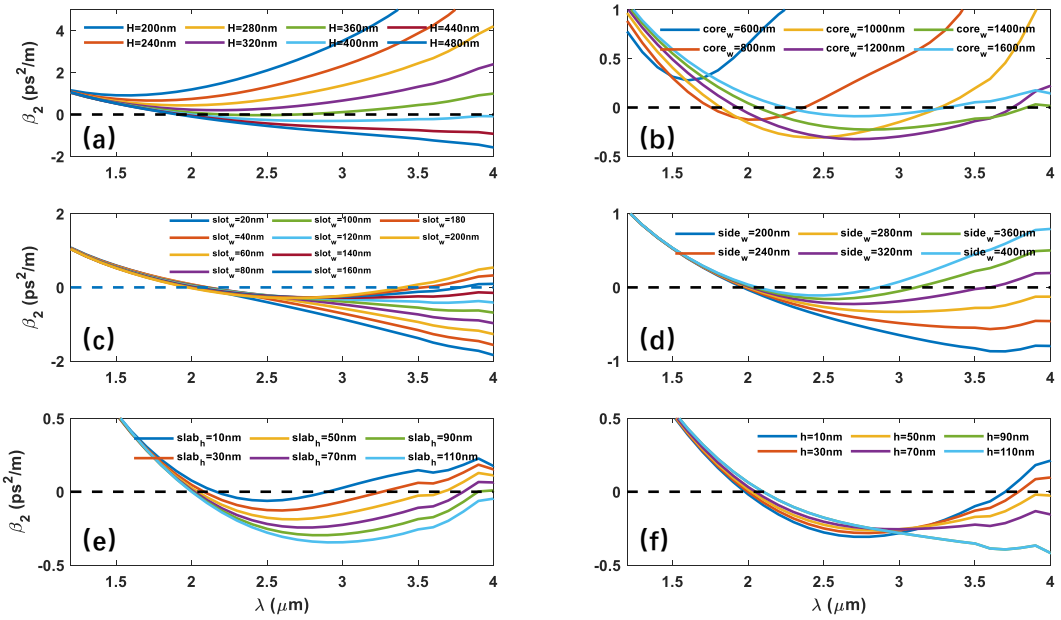

FIGURE 6.6: Comparison of the dispersion profiles with the changing (a) waveguide height, H; (b) core width, $core_w$; (c) slot width, $slot_w$; (d) side width, $side_w$; (e) slab height, $slab_h$; (f) preserved silicon step height, h.

The effect of the slot width, $slot_w$, on the dispersion curve is depicted in Figure 6.6 (c). $slot_w$ is adjusted from 20 nm to 200 nm with a step of 20 nm. The left side of the dispersion curve is maintained with the change of $slot_w$, especially the position of the left ZDW. On the other hand, the right ZDW has a blue shift with the increase of $slot_w$ and the larger $slot_w$ is, the smaller the variation scope between the ZDWs is. When the side waveguide is far away from the core waveguide, it has a limited influence on the dispersion property of the core waveguide. The slope of the middle section of the dispersion curve gets smaller with the increasing of $slot_w$ from about 20 nm to 120 nm and then becomes larger when $slot_w$ continues to be increased. Meanwhile, the flat middle section of the dispersion curve decreases.

The influence of the side waveguide width, $side_w$, on the dispersion curve is given in Figure 6.6 (d). $side_w$ is altered from 200 nm to 400 nm with a step of 40 nm. When $side_w$ is larger than 400 nm, there should be no ZDW according to the trend. As the side waveguide is comparable to the core waveguide, which is equivalent to the increase in $core_w$, the increasing $core_w$ leads to the disappearance of ZDW and positive β_2. This is

consistent with the trend seen in Figure 6.6 (b). The left ZDW is about 2 μm with a tiny red shift when $side_w$ increases. The slope of the middle part initially becomes smaller when $side_w$ increase from 200 nm to 280 nm, then it turns to be sharper again when $side_w$ keeps on increasing. The right ZDW has an obvious blue shift when $side_w$ grows.

Figure 6.6 (e) depicts the influence of the slab height, $slab_h$, on the dispersion curve. $slab_h$ changes from 10 nm to 110 nm with a step of 20 nm. At short wavelengths ($< 1.5\,\mu$m), the influence of different slab height on the dispersion curves could be ignored. The left ZDW gently shifts towards shorter wavelength from 2.2 μm to 2 μm with the increase of $slab_b$ around 2 μm. The significant transformation is the position of the right ZDW which has a significant red shift. The variation of the right ZDW is consistent with the change depicted in Figure 6.6 (a) since the increase of $slab_h$ is equivalent to the increase of H. The properly chosen $slab_h$ is dependent on the position of the left ZDW and the slop of the middle section of the dispersion curve.

Figure 6.6 (f) demonstrates the effect of the preserved silicon step height, h, on the dispersion profiles. h raises from 10 nm to 110 nm with a step of 20 nm. At shorter wavelength, there is no obvious variation happening due to the change of h. The influence on the left ZDW is insignificant but it still slightly moves to the longer wavelength with large h. The gradient of the middle part decreases when h increases from 10 nm to 70 nm, then it becomes steeper again with larger h. When h is comparable with H, the slot section has limited influence on the core waveguide that forms an ordinary rib waveguide with the side waveguide.

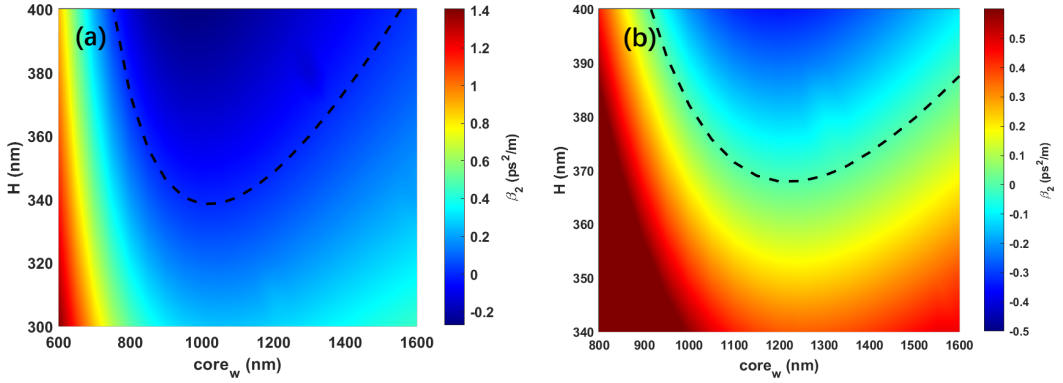

FIGURE 6.7: Comparison of β_2 with the variation of H and $core_w$ at the pump wavelength of 2.17 μm (a) and 3 mum. The dash lines represent β_2=0.

According to the analysis of these structural parameters, it is obvious that H and $core_w$ effectively influence the position of the left ZDW. With the designed pump wavelength of 2.17 μm, the dispersion comparison between different combinations of H and $core_w$ is presented in Figure 6.7 (a). As $core_w$ deviates by 1000 nm on both sides, H increases rapidly. Based on the exploration of the mode in the previous section, $core_w$ should be comparable to the pump wavelength. Thus, $core_w$ should be greater than 1000 nm to

minimize the influence of the slot section on the light mode. The wider the $core_w$, the tighter the mode confined in the core waveguide. Here, H is chosen to be 395 nm.

To achieve a wider FWM bandwidth, the dispersion comparison at a wavelength of 3 μm is depicted in Figure 6.7 (b). As illustrated in Figure 6.6, the dispersion value at 3 μm could serve as an evaluation criterion to select the proper structural parameters. β_2 should be negative, indicating that the right ZDW is farther from 2.17 μm. The zone above the dash line is the target region. Combined with the zero dispersion line in Figure 6.7 (a), $core_w$ is chosen as 1325 nm, where β_2 is negative to achieve the phase matching condition. The variation range of $core_w$ is approximately from 1300 nm to 1400 nm to maintain β_2 at 2.17 μm negative and as low as possible.

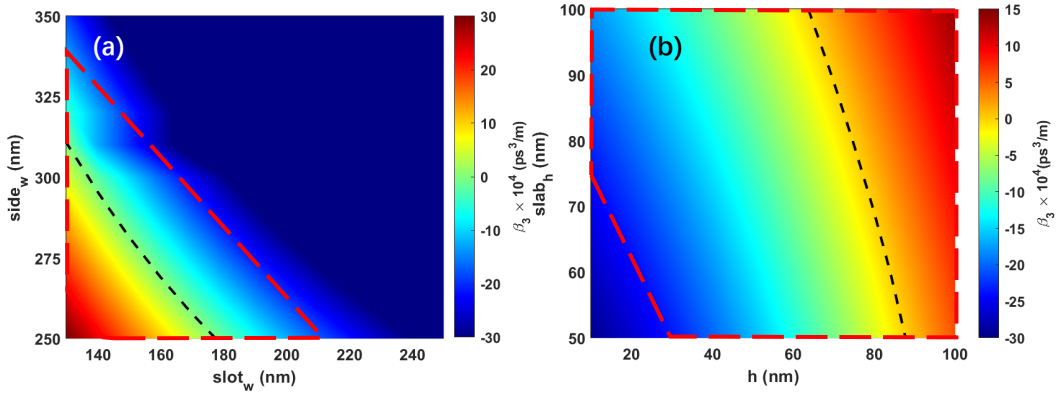

FIGURE 6.8: Comparison of β_3 as functions of $slot_w$ and $side_w$ (a) and as functions of $slab_h$ and h (b) at the wavelength of 3 μm. The dash lines represent β_3=0.

The change in $slot_w$ and $side_w$ does not significantly affect the position of the left ZDW but does alter the shape of the dispersion curve. This is due to the asymmetric structure of the slotted waveguides, where the side waveguides and slot section act as perturbations to the mode in the core waveguide. When H and $core_w$ are fixed at 395 nm and 1325 nm respectively, the variation of β_3 at the wavelength of 3 μm with changes in $slot_w$ and $side_w$ is shown in Figure 6.8 (a). The value of β_3, which can be treated as the derivative of β_2, should be controlled around 0 to extend the middle flat part of the dispersion curve and broaden the FWM bandwidth. The suitable region is marked by the red dashed box, where $slot_w$ ranges from $\sim$ 140 nm to $\sim$ 210 nm and $side_w$ ranges from $\sim$ 270 nm to $\sim$ 340 nm.

The changes in $slab_h$ and h primarily affect the shape of the dispersion curve rather than the position of the left ZDW due to their small variation range. To better estimate the suitable size range, H, $core_w$, $slot_w$, and $side_w$ are fixed at 395 nm, 1325 nm, 155 nm, and 300 nm, respectively. The change of β_3 at the wavelength of 3 μm with variations in $slab_h$ and h is depicted in Figure 6.8 (b). The value of β_3 should be controlled around zero to achieve a flat dispersion in a wide wavelength range. The suitable region for the choice of $slab_h$ and h is marked by the red dashed box, where β_3 remains

as small as possible. The variation range of $slab_w$ ranges from 75 nm to 100 nm, and that of h ranges from 30 nm to 100 nm.

All the details of one suitable structure parameters are concluded in Table 6.1 including the determined parameters and the corresponding variation range. The existing fabrication accuracy, with a scale of 5 nm [118], ensures the feasibility of structure tolerances such as $core_w$, $slot_w$, $side_w$, $slab_h$ and h. However, achieving a precise value for H without any tolerance remains a current challenge, pointing to ongoing manufacturing difficulties. The complex structure design for slotted waveguides may introducing serious sidewall scattering loss compared with the simple rib waveguide, which indicates the linear loss is possible higher. The mode simulation also suggests that the long wavelength is easily to excite the higher mode in slotted waveguides which need to be took into consideration in the future theoretical and experimental exploration.

Parameters	Determined size (nm)	Size range (nm)
H	395	395
$core_w$	1325	1300-1400
$slot_w$	155	140-210
$side_w$	300	270-340
$slab_h$	80	75-100
h	40	30-100

TABLE 6.1: The suitable structure parameters for the slotted waveguide.

6.4 Higher-order Stokes generation and supercontinuum generation

The original pursuit to obtain the flat and wide dispersion profiles is the higher-order Stokes waves generation in the mid-infrared band to explore a method to generate mid-infrared light sources. The principle for exciting the higher-order Stokes waves is the high pump power and the interaction between FWM and Raman scattering. To explore the nonlinear performance of slotted waveguide in the mid-infrared band, the RE-FWM is simulated in the optimized structure with parameters stated in Table 6.1. In this simulation, the pulse pump source is 2.17 μm with the time duration of 40 ps and the fixed peak power of 20 W, the CW signal is 1.95 μm with the power of 5 mW, the linear loss is assumed to be 0.2 dB/cm, the possible lowest value for rib waveguides with existing fabrication techniques [13]. The choice of the linear loss value is because the light is confined within the core waveguide, and here the influence of the SWG is not considered. The output power of various higher-order Stokes waves along the propagation length is shown in Figure 6.9 (a). It is obvious that 1^{st}, 2^{nd}, 3^{rd}, 4^{th}, 5^{th} and 6^{th}-order Stokes waves gradually increases and reaches

maximum within the propagation length of 2 cm. 1^{st}, 2^{nd} and 3^{rd}-order Stokes waves with the wavelengths of 2.44 μm, 2.8 μm and 3.28 μm, respectively, sustains a high level of power after further propagation, about hundreds micro watts, which is remarkable for the on-chip silicon waveguide without the ring resonators [67]. For 4^{th}, 5^{th}, 6^{th}-order Stokes waves with the corresponding wavelengths of 3.95 μm, 4.97 μm and 6.7 μm, they experience the periodic fluctuations along the propagation length, the higher the order, the shorter the period. The phase mismatch at the longer wavelengths is the main reason for such periodic fluctuations. 7^{th} and 8^{th}-order Stokes waves could be observed theoretically after the propagation length of 4 cm and 6 cm. But the light mode of the wavelength over 3.8 μm should be transformed into the slot mode during the propagation as analysed in the previous analysis of the light mode supported in the slotted waveguide. The absorption losses of SiO_2 ans Si at wavelengths over 4 μm and 8 μm are another limitation of higher-order Stokes waves. In this simulation, the absorption at longer wavelengths is not included, resulting in the appearance of strong higher-order Stokes waves beyond 8 μm. Hence, 1^{st}, 2^{nd} and 3^{rd}-order Stokes waves is the focus of this section even it is possible to generate higher-order Stokes waves at extremely longer wavelength theoretically. The evolution of the light spectrum is depicted in Figure 6.9 (b). The growth of the higher-order Stokes and anti-Stokes waves is consistent with that described in Figure 6.9 (a). The spectrum broadening of the higher-order Stokes waves is due to the fixed bandwidth of the Raman gain spectrum, about 10 GHz, in the simulation. The linewidth of Stokes waves is limited by the pump linewidth that could be adjusted by reducing pump pulse duration, which is beneficial to the supercontinuum generation around Stokes waves.

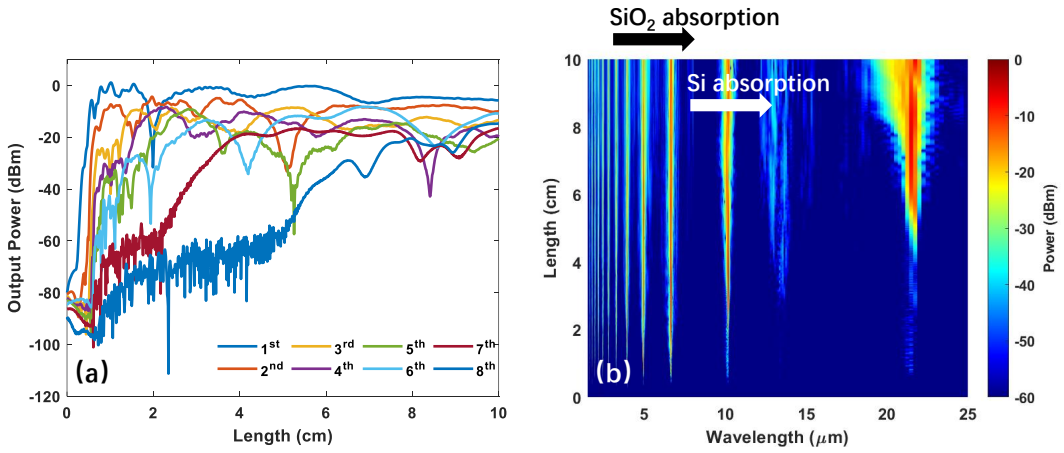

FIGURE 6.9: (a) Output power of various higher-order stokes along the propagation length, as labeled in the legend (b) Evolution of pulse spectrum. The pulse pump source is 2.17 μm with the time duration of 40 ps and the fixed peak power of 20 W, the CW signal is 1.95 μm with the power of 5 mW, the linear loss is assumed to be 0.2 dB/cm.

To investigate the supercontinuum generation in the slotted waveguide, the spectrum

is simulated with the same conditions as in Figure 6.9 but switching the pulse duration from 40 ps to 5 ps. As demonstrated in the Chapter 2, Raman scattering is a delayed nonlinear phenomenon of materials with the response time of 3 ps. The pulse duration should be larger than 3 ps to ensure the occurrence of the Raman scattering. Figure 6.10 (a) shows the output spectrum of the pump pulse propagating 10 cm with the assistance of CW signal light. The bandwidth of the supercontinuum generation is up to 6.5 μm, from 1.5 μm to 8 μm. The peak light intensity is just 4×10^{13} W/m^2, which is much smaller than record, 2.2×10^{15} W/m^2 in the literature [84], while the bandwidth is larger than [84], 4 μm covering wavelength from 2 μm to 6 μm. The evolution of the pulse spectrum shown in Figure 6.10 (b) indicates that the higher-order Stokes maintains the narrow linewidth within the propagation length of 2 cm, whereas higher Stokes wave starts to expend as a result of SPM when it propagates further, and forms supercontinuum generation at the propagation length of 4 cm. The supercontinuum spectrum keeps stable with the increase of the propagation length, therefore, the suitable device length should be at least 4 cm. A potential approach to mitigate the absorption loss of SiO_2 at wavelengths beyond 4, μm involves the removal of the SiO_2 substrate through SWG structure.

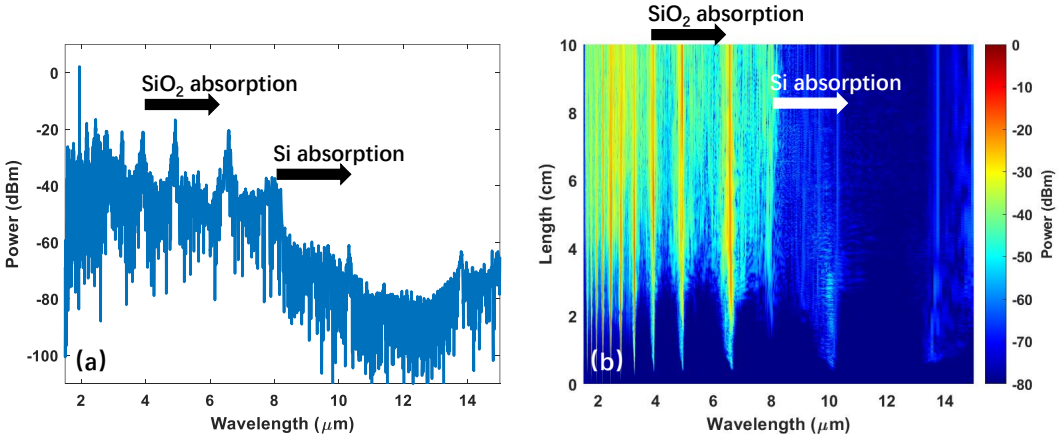

FIGURE 6.10: (a) Spectrum output power at a propagation length of 10 cm. (b) Evolution of pulse spectrum. The pulse pump source is 2.1 μm with the time duration of 5 ps and the fixed peak power of 20 W, the CW signal is 1.95 μm with the power of 5 mW, the linear loss is assumed to be 0.2 dB/cm.

6.5 Slotted waveguide testing

Samples were fabricated based on optimised structural parameters with step changes of structural parameters, $slot_w$, $slot_w$, $core_w$ and DC (duty cycle). As listed in Table 6.2 and Table 6.3, $slot_w$ varies from 240 nm to 140 nm with a step of 20 nm, $side_w$ varies from 320 nm to 280 nm with a step of 20 nm, $core_w$ varies from 1380 nm to 1300 nm with a step of 20 nm and the DC value are 0.36 to 0.34. The linear loss, averaged from two identical samples, is calculated by the cut-back method as stated in Chapter 2, and

the length difference of each testing sample is 2 mm. For different DC, the influence of the variation of $slot_w$ on the linear loss has similar trend. The linear loss becomes smaller with $slot_w$ of 240 nm, 200 nm and 140 nm. It reaches maximum, over 15 dB/cm, with $slot_w$ of 220 nm, while achieves minimum, 10 dB/cm, with $slot_w$ of 140 nm. This suggested that the suitable $slot_w$ is about 140 nm to minimise the linear loss. The influence of $side_w$ with DC of 0.36 shows that the minimum linear loss, 7 dB/cm, can be achieved when $slot_w$ is 300 nm. However, the change of $side_w$ with DC of 0.34 has limited influence on the linear loss that remains to be around 12 dB/cm. There is no obvious trend for the linear loss with the variation of $side_w$ due to the limited experimental data. The linear loss obtains the minimum, 10 dB/cm with $core_w$ of 1380,nm and DC of 0.34. Meanwhile, linear loss with different DC has a descent trend when $core_w$ change from 1360 nm to 1320 nm, and the minimum linear loss is obtained with $core_w$ of 1320 nm. The sample test results show that the linear loss of the optimised structure should be around 10 dB/cm. The high linear loss makes it difficult to observe nonlinear phenomena in experiments. The next goal is to improve the fabrication quality or structural design of slotted waveguides to reduce linear losses and thus enhance nonlinearity.

$slot_w$ **(nm)**	**linear loss (dB/cm)**	$side_w$ **(nm)**	**linear loss (dB/cm)**	$core_w$ **(nm)**	**linear loss (dB/cm)**
240	13	320	16	1360	24
220	17	300	7	1340	18
200	10	280	18	1320	11
160	13				
140	10				

TABLE 6.2: The linear loss of slotted waveguides with the DC of 0.36.

$slot_w$ **(nm)**	**linear loss (dB/cm)**	$side_w$ **(nm)**	**linear loss (dB/cm)**	$core_w$ **(nm)**	**linear loss (dB/cm)**
240	11	320	12	1380	10
220	15	300	13	1360	17
200	12	280	12	1340	19
160	15			1320	11
140	10			1300	17

TABLE 6.3: The linear loss of slotted waveguides with the DC of 0.34.

This chapter introduces slotted waveguides as an effective means to attain a flat and low dispersion profile, facilitating broadband FWM covering multi Raman shifts. The emergence of higher-order Stokes waves presents a promising avenue for developing light sources or achieving supercontinuum generation. However, initial fabrication attempts revealed challenges with the existing design. Simultaneously, the appearance of slot mode at longer wavelengths, as well as the absorption of SiO_2 and Si, inhibits

extension of wavelength band, promoting a reassessment of the structure and exploration of alternative materials.

Chapter 7

Waveguide fabrication

This chapter introduces the fabrication of silicon core fibres (SCFs), rib and slot planar waveguides applied in the experiments. The fabrication of SCFs is first demonstrated in detail, including the production of drawn fibres, tapering processes, and improvements in the fixation method. Then it comes to the fabrication of rib waveguides, containing the design of chips and the preparation for the testing. Finally, the design of slot waveguide chips and the preparation before testing are illustrated.

7.1 Fabrication and fixing method of SCFs

In Chapter 3, the Raman scattering, FWM and RE-FWM of SCF with different core diameters has been studied. The fabrication and fixation methods of low-loss SCFs will be explained in detail here to complement the overall research on such a silicon platform.

7.1.1 Fabrication of SCFs

SCFs used in our experiments was produced by the well-established molten core drawing (MCD) method in traditional silicon fibres. As Figure 7.1 shows, silicon rod is placed into the silica tube sealed at one end to form a preform [128]. A thin calcium oxide layer between silicon and silica acts as a diffusion barrier to prevent oxygen in silica cladding going into the silicon core. It also helps to reduce cracking and separation between core and cladding due to the thermal expansion, which facilitates the construction of smaller-sized SCFs. The whole sample is placed in a furnace set at a temperature above the melting point of silicon and the transition temperature of silica. During the drawing process, the silicon core melts into a liquid state and the silica cladding softens but maintains the core shape cylindrical. SCFs fabricated by

MCD method typically have the outer diameter of $\sim 125\,\mu$m with the core diameter of $\sim 15\,\mu$m as Figure 7.1 (c) shows. In addition, the MCD method ensures that considerable lengths of silica-core fibres on the order of kilometers can be manufactured. However, the polysilicon core with the grain size of hundreds micrometer to millimeter after cooling down introduces high linear losses, between $4-10\,$dB/cm [129]. On the other side, the core dimension of as-drawn fibres is quite large, which limits the observation of nonlinear phenomena. Therefore, tapering process is applied to produce low loss SCFs with small core dimension to meet the design requirement for realising nonlinear applications.

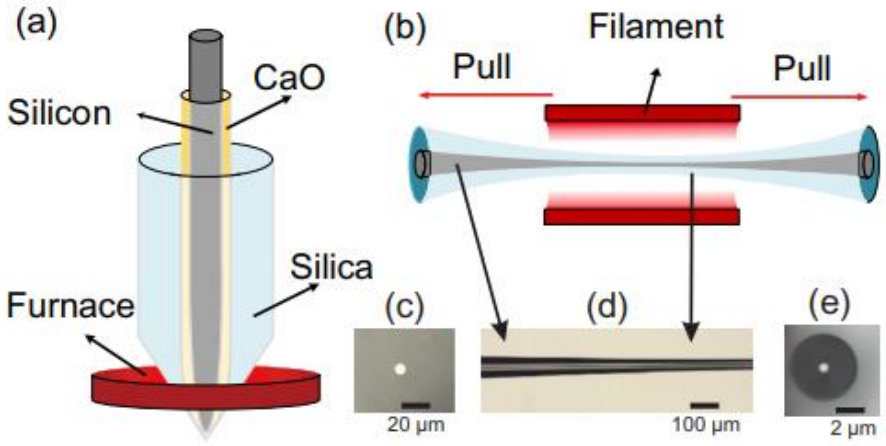

FIGURE 7.1: (a) Molten core drawing method of SCFs; (b) Tapering process of the drawing fibres; (c) facet of as-drawn fibres; (d) magnified view of the area, tapering section, indicated by arrows; (e) facet of tapering fibres. [6]

The tapering machine, VytranGPX300, as Figure 7.2 illustrates, is used for the tapering process of as-drawn fibres. Firstly, an as-drawn SCF is spliced with a single mode fibre using the same machine to save as-drawn fibres. Prior to splicing, it is essential to cut the single-mode optical fibre and as-drawn fibres using a fibre optic cleaver. This ensures that the end facets are smooth and clean, allowing for inspection under a microscope and ultimately enhancing the quality of the splicing process. The single mode fibre is fixed in the left holder on the left blocker, and the SCF is fixed in the right holder on the right blocker. The vacuum pump is on to maintain fibre stability during processing. The ends of single mode fibre and the as-drawn fibre could be aligned through adjusting the position of the left and right blockers which could be precisely tuned by the software. The implanted microscope can help to observe the alignment of fibres. The working temperature increased by the electronic-heating plates can be altered by changing the working power, which is usually set at around 50 W during splicing. This value would decrease due to filament aging, hence it should be tested and adjusted for every single fabrication round. The tension monitor would record the tension variation over time, and the tension increasing from 0 to $3-5\,$g means high quality splicing and smooth joints.

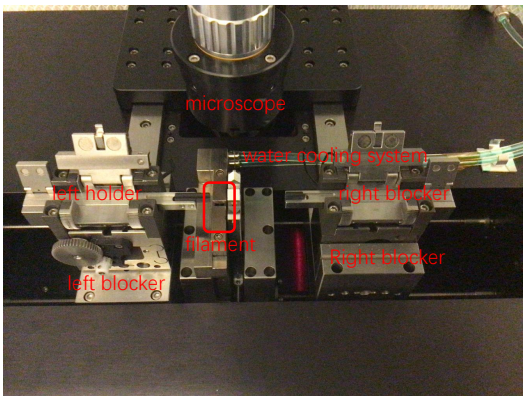

FIGURE 7.2: Instrument diagram of vytranGPX300

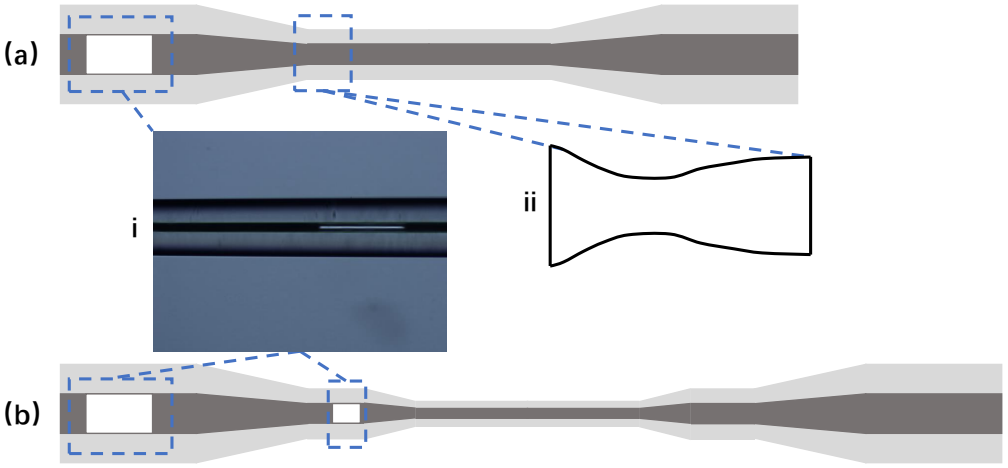

FIGURE 7.3: (a) Fibres after the first tapering step; (b) fibres after the second tapering step; (i) photograph of the vacuum section; (ii) trend near the end of the tapering section.

Then the fibre is ready to do tapering as Figure 7.1 (b) depicts. The core dimension of the designed tapered SCF operating in the wavelength range from 1 μm to 2 μm varies from 800 nm to 2000 nm, which means that the two-step tapering process is necessary to achieve the precise control of the core size and high quality of the silicon core. In the first tapering process, the section of the as-drawn fibre is placed in the filament with the single mode fibre placed in the left holder and the SCFs placed in the right holder. The position could be adjusted to make the filament near the joint between SCF and single mode fibre. The length of the tapering section is usually set to 3 mm and the length of the waist section depends on the design of the tapered SCFs. The filament is set to a suitable temperature with the corresponding power of about 60 W to melt the silicon core and soften the silica cladding. The left and right blockers move in opposite directions, pulling on both ends of the fibre. The tension monitor records the change in tension over time, as illustrated in Figure 7.4. Before starting tapering, the tension is stable at T_0. Subsequently, with a temperature increase, the fibre softens, leading to a sudden decrease in tension (T_1). Tension peaks as the down taper section is formed

(T_2), then falls to a plateau (T_3) as it remains in the waist-forming area. Occasionally, a tension peak (T_4) may occur during the up taper formation, followed by a final decrease after completing all processes. It is noteworthy that T_4 should be controlled under 30 g to avoid breakage. This machine can accurately control the tapering speed according to the input dimensions, which is superior to the control of the MCD method. The photographs of the tapering sections and the waist cross section are shown in Figure 7.1 (d) and (e). The overall top view is illustrated in Figure 7.3 (a). Due to thermal shrinkage, a vacuum region exists near the start of the tapering process as displayed in the inset (i) of Figure 7.3. An enlarged view of the end of the tapered section is shown in inset (ii) of Figure 7.3. It is obvious that the transitional part first becomes smaller, then grows up again and remains stable after that. The second tapering process should start at the uniform part after the shrinkage part. The second tapering process is similar to the first tapering process but it is conducted at a different temperature. The top view of a SCF after second tapering process is depicted in Figure 7.3 (b). There exist two vacuum regions on one side, which need to be removed before characterising the tapered SCF.

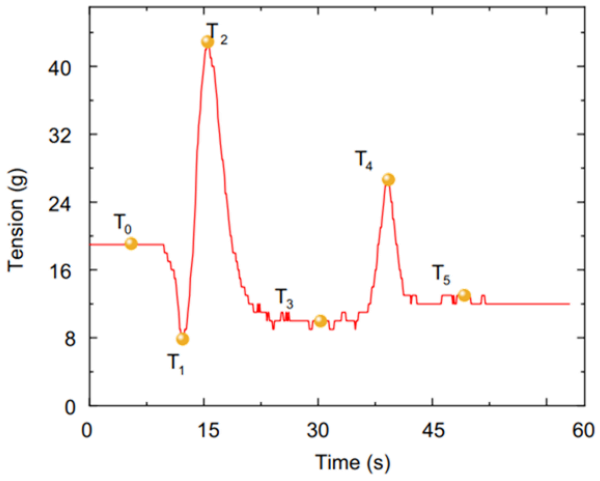

FIGURE 7.4: An typical example for tension variation as a function of time, T_0 to T_5 represents different situation during tapering. [26]

The classical recipe for the two-step tapering process is that the outer diameter usually changes from 125 μm to 49 μm in the first tapering step and the specific value for the second tapering step is altered according to the design target core diameter. The final core diameter is estimated by the following ratio relation:

$$D_{des} = D_{1st-end} \frac{D_{2nd-end}}{D_{2nd-ini}} \frac{1}{R_{clad/core}}. \tag{7.1}$$

In which, D_{des} is the design core diameter, $D_{1st-end}$ is the final outer diameter after the first tapering step, typically 49 μm, $D_{2nd-end}$ and $D_{2nd-ini}$ are the end and start values

of the outer diameter set in the recipe for the second tapering step, $R_{clad/core}$ is the ratio between the outer diameter and the core diameter, around 8.5 with a slight change from 8 to 9 during the tapering process. For example, set the value of the second tapering step from 80 μm to 27 μm to achieve a target core diameter of 1900 nm.

The key parameter for manufacturing the low loss tapered SCFs is the temperature of the filament that can be detected with tension detector in real-time. The smaller the tension is, the higher the temperature is. As shown in the previous section, there is a tension peak during the formation of the upper tapering section, and the larger the peak, the higher the actual temperature. The temperature is essential for the quality of the silicon crystal, as it affects the linear loss. The loss measurement through various fibres with different combinations of the temperature for two tapering steps are listed in Table 7.1. These values are averages obtained from more than two fibres, with an error margin of around 1 dB. Here, the first tapering step is to reduce the outer diameter from 125 μm to 49 μm and the second tapering step is to reduce the outer diameter from 49 μm to 16 μm. Through comparing the linear loss with different tensions of the first tapering step, it is clear that smaller linear loss could be achieved when the tension is varying from 40 g to 50 g. When changing the tension of the second tapering step with the fixed tension of the first tapering step (40 g) the minimum linear loss could be achieved with the tension of 34 g. Moreover, the tension of the second tapering step should be higher than that of the first tapering step, which can result in low linear loss.

The original SCFs were fabricated at Clemson University [130], with a cladding (125 μm) to core (14 μm) ratio of around 8.9. This ratio limited the stable tapering length to $\sim$ 3 cm. A extensive exploration of new SCFs from KTH Royal Institute of Technology revealed an increased cladding (117 μm) to core (5.3 μm) ratio of up to 22, allowing for stable tapering lengths exceeding 6 cm. In contrast to previous US fibres with a relatively high linear loss of $\sim$ 10 dB/cm, KTH fibres exhibited lower linear loss ranging from 1.3 to 2 dB/cm, further reduced to 0.2 dB/cm after tapering. Despite these advancements, the characterisation of KTH fibres is still limited, requiring additional efforts for comprehensive analysis in the future. KTH fibres holds significant potential for the practical application of SCFs due to the combination of low linear loss and extended length.

7.1.2 Fixing method of SCFs

Initially, a tapered SCF would be pulled into a capillary and then fixed with assistance of wax as Figure 7.5 (a) shows. The red rectangle represents the capillary and the SCF is located within the yellow rectangle. After fixing a SCF, the polishing process could produce a smooth and flat facet as shown on the right side of Figure 7.5 (a). It is straightforward to distinguish between the capillary (red circle), wax (filling in the

1^{st} step (g)	2^{nd} step (g)	loss (dB/cm)	1^{st} step (g)	2^{nd} step (g)	loss (dB/cm)
23	20	3.9	44	40	2
30	22	3.5	50	49	2
33	23	3.7	50	56	2
35	30	3	51	21	1.4
40	29	2.5	53	44	2.4
40	30	2.5	56	49	4.4
40	31	4	61	45	3
40	34	1.2	68	49	2.8
40	65	2.5			

TABLE 7.1: Various tension combinations of 1^{st} and 2^{nd} step and the corresponding measured linear loss

gap between capillary and SCF) and SCF (yellow circle), and this facet shows the whole structure of the sample. In previous experiments, the maximum pump power of the CW light source was only 80 mW, which limited the nonlinear efficiency that depends heavily on the light intensity. When the pump power exceeds 80 mW, the wax would melt, the end facet becomes dirty and the insertion loss surges. For SCFs with submicron dimensions(core diameter of $\sim$ 800 nm) that operate in the telecom band, the nonlinear effects could still be observed with such level of pump power due to the relatively smaller effective mode area, approximately 0.3 μm^2. However, the observation of nonlinear phenomena encounters challenges in the mid-infrared band as the corresponding core diameter increases to several micrometers.

A new method to fix the tapered SCFs was investigated, which effectively increases the maximum experimental pump power. A rectangular groove with the width of 125 μm and the etch depth of 125 μm was etched on a blank silicon chip into which the tapered SCF could be placed as depicted in Figure 7.5 (b). The length of the chip holder could be cut according to the the length of the tapered SCFs. Wax is still used to fill the grooves to hold the fibre in place. The position of the fibre can be adjusted so that the vacuum area is outside the chip holder. There is additional UV glue stuck to the cured wax at both ends of the fibre, which is crucial for the next polishing process. The UV glue has enough support to avoid fibre breakage. The same polishing process produces smooth and flat facets, saving time compared to the original fixing method. The final step to ensure that the fibre can handle the high power is to use acetone to clean the wax on the input coupling side. If the facet is not clean, the sample can be lightly polished by hand using the finest polishing pad. The facet of a prepared sample is shown on the right side of Figure 7.5. The fibre is fixed in the chip holder without any wax near the input coupling side. In the experiment, the fibre can withstand the maximum pump power of CW light source up to 600 mW and the maximum average power of femtosecond laser up to 100 mW.

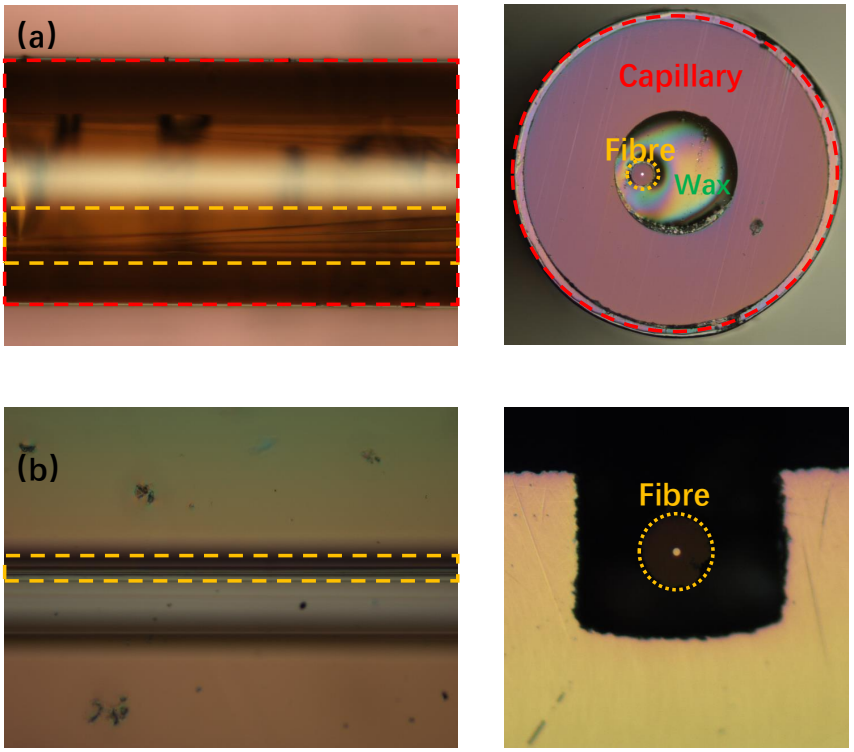

FIGURE 7.5: (a) Top view of the fibre fixed with the capillary on the right side; facet of the fibre in the capillary (b) Top view of the fibre fixed with the chip holder, facet of the fibre in the chip holder.

7.2 Fabrication of planar silicon waveguides

Chapter 5 and Chapter 6 study the nonlinear performance of rib and slot waveguides. Both silicon waveguides are planar waveguides, and their manufacturing process is completely different from the SCFs. In the following sections, the fabrication of planar waveguides will be explained in detail as a supplement to the waveguide research.

7.2.1 Fabrication of rib waveguides

All the parameters of the optimised rib waveguids are given in Chapter 5. To explore influences of different dispersion conditions, the simple method is to change the width of rib waveguides. The width parameters of waveguides operating at 1545 nm and 2170 nm are listed in Table 7.2, changing from 740 nm to 840 nm and from 1490 nm to 1590 nm with the step of 25 nm, respectively. The next step is to draw the layout design for lithography that is necessary before the fabrication. Considering the existing experimental conditions, free space coupling is adopted as the main approach to couple pump wave and signal wave into the waveguides. The cross section of rib waveguides to be tested is too small to couple the light and measure the output light

directly for its low coupling efficiency. Tapered waveguides are adopted as coupling waveguides at the input and output ports of the test sample. The structure of the tapered waveguide is depicted in Figure 7.6, in which w_1 is the width of the input port of the tapering section, w_2 is the width of the output port of the tapering section and L_T is the length of the tapering section. w_1 is traditionally set to 10 μm and w_2 keeps the same value as the rib waveguides. To reduce the loss introduced by the tapered waveguide, the length of the tapered waveguide is as long as possible for small mode distortion, and its length is 1mm normally. Through the simulation of the tapering section with L_T of 1 mm, w_1 of 10 μm and 740 nm by Lumerical, the coupling loss is negligible during the light propagation which suggests that such tapering sections work well in such design. Since there is only one etching step for the rib waveguide, the etching depth remains consistent for the complete waveguide design, including the remaining polished section, the upward tapered section, the rib waveguide for nonlinearity, the downward tapered section, and the remaining polished section as shown in Figure 7.7 (a). In order to test propagation losses and ensure that the input/output ports of different lengths are aligned for the next step of the polishing process, the bend waveguides are required on the chip. Here, the bend radius is 50 μm. The loss is calculated by FDTD and is about 0.0013 dB/90° bend for TE_0 mode.

Operation wavelength	**1545 (nm)**	**2170 (nm)**
Waveguide width	740	1490
	765	1515
	790	1540
	815	1565
	840	1590

TABLE 7.2: Waveguide width values for different operation wavelengths

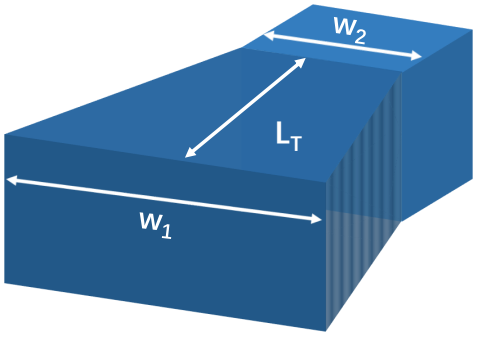

FIGURE 7.6: Tapering waveguides at the input and output port.

In the first fabrication round, the lithography for the 500 nm SOI wafer was carried out by electron beam (E-Beam), and rib waveguides were fabricated by chemical etching. The layout design for the rib waveguides is shown in Figure 7.7 (a). The cut-back method for the measurement of the propagation loss is demonstrated in Chapter 2.

Here, five different lengths are designed to test the propagation loss with the length difference of 2 mm. Another rib waveguide without any bends is designed to test the Raman enhanced FWM in the rib waveguide, which is set at the top of each section with different waveguide widths. The lengths of rib waveguides are designed to be 1 cm, 1.5 cm and 2 cm to explore the influence of the propagation length on the nonlinearity. On the chip, the parameter label is essential to distinguish the change of parameters, which is set above the left arm of the shortest waveguide for testing the propagation loss. The metrology box is necessary for the etch depth measurement. For rib waveguides, there is only one etch step during the fabrication, and the corresponding metrology box is set at the bottom of the chip. The chip label is beneficial to distinguish between chips with different structures, which is set near the left top corner in all chips. The fabricated chips need to be diced and polished. The polish marks are aligned at the beginning and the end of the waveguide. The resist layer used for lithography is washed away and photoresist (S1813) is deposited as a protective layer for dicing. After dicing, the protective layer is preserved for polishing. Two polishing methods are applied to these chips. For the first polishing method, mechanical polishing, sandpapers with different roughness are applied to polishing chips. For a waveguide with the height of 500 nm, the finest sandpaper mesh 200 nm is relatively rough, which results in an input coupling loss of about -18 dB at the input facet. Hence, the second polishing method, chemical-mechanical polishing, is tried to improve the polishing quality, reducing the coupling loss. Here Al_2O_3 particles with the size of 9 μm and 1 μm mixing with deionised (DI) water are used for the coarse lapping. Then, SF1 polishing fluid is mixed with DI water to remove the grain boundaries formed by interlaced noncrystalline particles on the rough surface to make the surface smooth. However, due to the lapping machine problem, the facets remain rough, which introduces the same level of coupling losses as the previous polishing method.

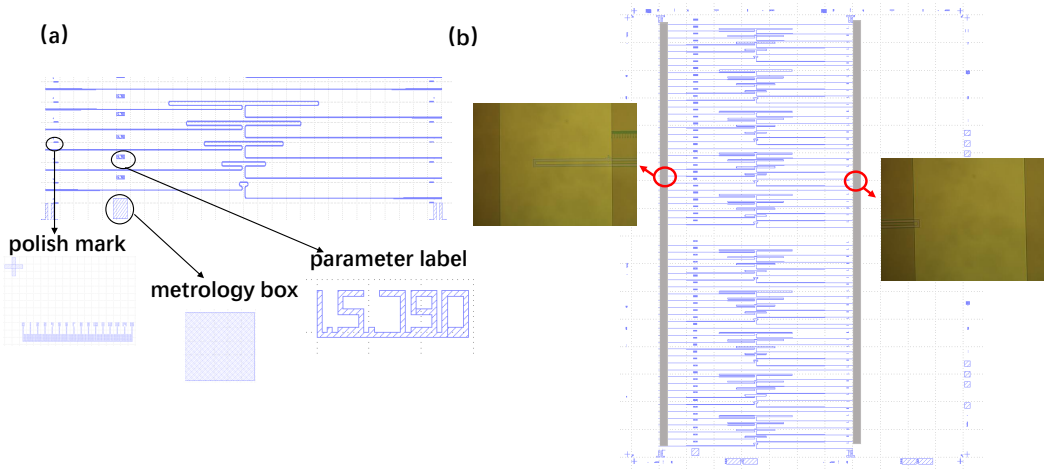

FIGURE 7.7: (a) Layout examples for rib waveguides; (b) second etch steps for the deep etch to improve coupling efficiency, photographs at two sides showing the real exposure position after the lithography.

The high coupling loss introduced by the polishing limits the nonlinear performance in rib waveguides, therefore, the deep etching was adopted instead of the polishing process. In the second fabrication round, the layout design is depicted in Figure 7.7 (b), the significant difference from the previous design is the grey zone representing the deep etching region. Photographs of the deep etching region on the left and right sides of the waveguide after lithography are shown in the inset of Figure 7.7 (b) to show the true location of the deep etching. As the etch depth of rib waveguides, 350 nm, is different from that of the deep etching, 104 μm, including the top silicon layer of 500 nm, BOX of 3 μm and the substrate of 100 μm, alignment marks are necessary for two etching processes. Since the thickness of resist layer is chosen to be 1.3 μm, the thickest in the existing techniques, E-Beam was no longer suitable for the lithography. DUV scanner is an alternative to do the lithography, which could operate on the thick resist layer. The first etch step for the waveguide etching is the same as in the first fabrication round and the second etch step for the deep etching is done by the plasma etching. Unfortunately, the resist layer was completely etched away during the etching process. Consequently, a silica hard mask is deposited on top of the wafer to protect the silicon waveguide structure, and then the HF fluid is used to rinse away the silica left after the lithography is completed. However, microscopic examination revealed that the waveguide structure had been damaged during the second etching step for deep etch manufacturing process, and subsequent experimental testing showed that none of the waveguides were functional. A future consideration is to explore suitable fabrication processes to perform high-quality deep etching, such as refining the etching recipe or switching the etching method, preserving the intact waveguide during fabrication. Another promising approach to reduce coupling losses is to design special couplers such as grating coupler [125], Y-type coupler[15], at the input ports.

7.2.2 Fabrication of slot waveguides

The critical size for the slot waveguide is below 200 nm which challenges the resolution of DUV scanner, therefore, E-Beam is a more suitable method to perform lithography of slot waveguides. The layout designs for slot waveguides are similar to those for the rib waveguides and an example is given in Figure 7.8. Since complex structures may introduce higher linear losses, only the middle part of the slot waveguide between the two bends is retained for measuring linear losses using the cut-back method. The complete waveguide structure includes remaining polished section, the upward tapered section, the rib waveguide for coupling, the slot waveguide, the rib waveguide for coupling, the downward tapered section, and the remaining polish section. The length of these waveguides is consistent with the design of rib waveguides with a length of 1 cm. The main difference is that SWGs (Figure 7.8) in the slot waveguides require one more etching step compared to the first round of

fabrication process for rib waveguides. Hence, there are two metrology boxes at the bottom of the chip measuring different etch depths. Meanwhile, the alignment marks for E-Beam at four corners of the chip are essential for the alignment between two etch steps. Other labels and marks are the same as that shown in Figure 7.7. The structural parameters of the slot waveguide is set of discrete values for the error caused by fabrication, which is already given in Table 7.3. Apart from the parameters mentioned above, the duty cycle is slightly changed from 0.34 to 0.36 to adjust the effective refractive index of the SWG.

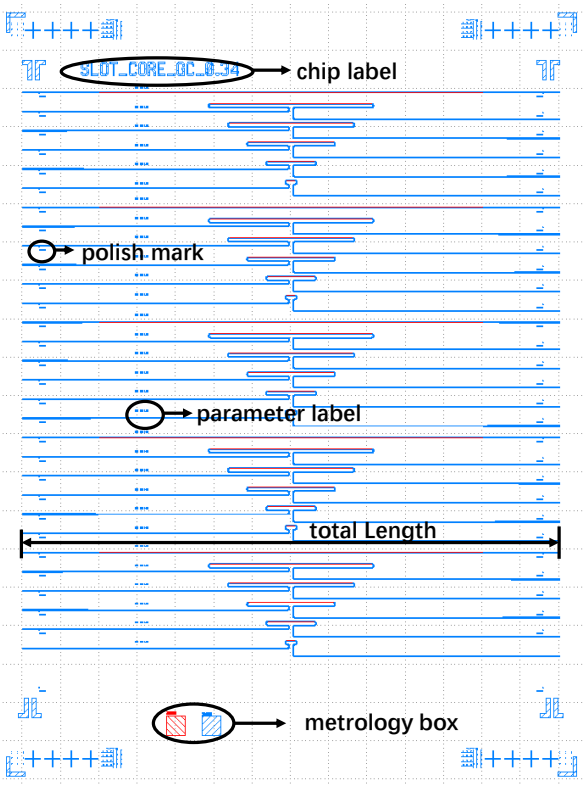

FIGURE 7.8: Layout examples for slot waveguides.

As mentioned in the layout design, coupling between the rib and slot waveguides is another essential part in the overall design as Figure 7.9 (a) shows. Figure 7.9 (a) depicts the transition region from the rib waveguide to the slot waveguide. The slot waveguide is inserted between rib waveguides which act as a coupling waveguide to testing the propagation loss. The coupling efficiency between the rib waveguide and the slot waveguide could be controlled through altering the width of the rib waveguide, w_c. In the following simulations, the mode profile is calculated by varFDTD. Initially, w_c is the same as the slot waveguide and the mode coupling is given in Figure 7.10 (a). The x axis is centered on the midpoint of w_c, and the y axis represents the normalized light intensity. Results for rib waveguides and slot waveguides are denoted by purple and blue, respectively. There is a slight mode mismatch between modes in rib waveguides and slot waveguides, and the coupling efficiency of mode coupling can be improved by adjusting w_c. The parameter sweeps

of w_c is utilised to check the mode profile with different w_c. The optimised mode coupling is shown Figure 7.10 (b), in which the mode in the rib waveguide is consistent perfectly with that in the slot waveguide. Due to the variation of structural parameters (illustrated by Figure 7.9 (b)), the optimised w_c for different structural parameters of slot waveguide needs to be simulated, and the results are given in Table 7.3. This coupling method is a preliminary plan aimed at reducing the coupling loss between the rib waveguide and slotted waveguide. However, for future advancements, more sophisticated coupling techniques such as tapered coupling waveguides or other shapes facilitating adiabatic coupling between different modal cross-sections could be considered to further minimize mode coupling loss.

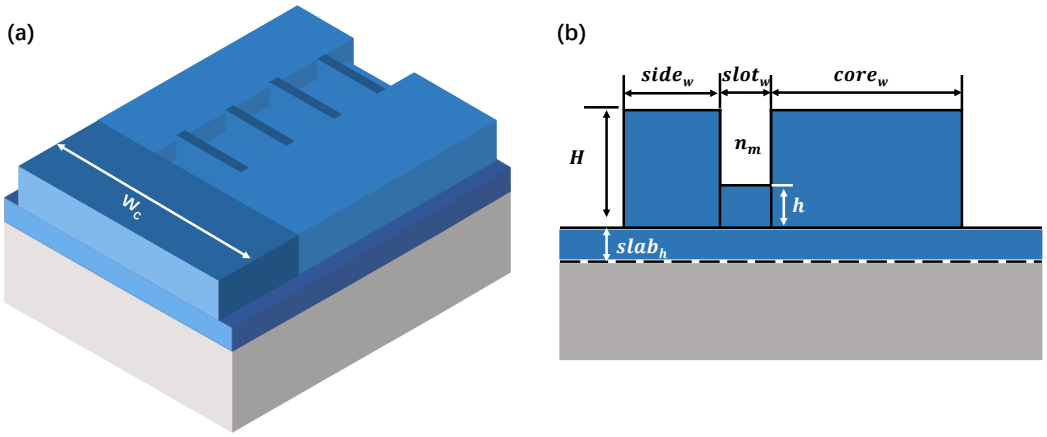

FIGURE 7.9: (a) Coupling waveguides before slot waveguides. (b) Cross-section of the slot waveguide which is consist of a side waveguide and a core waveguide separated by the SWG.

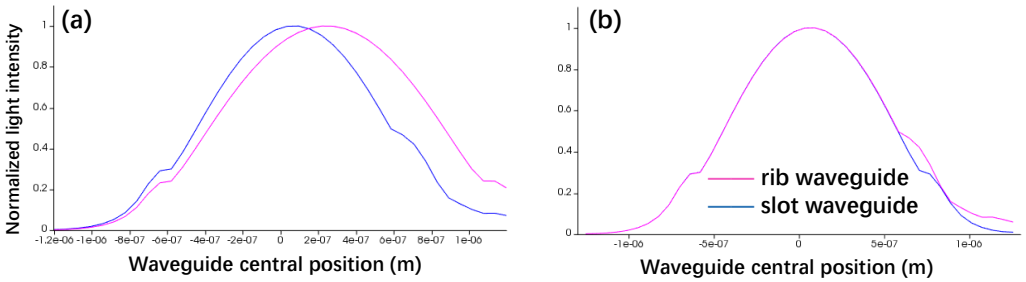

FIGURE 7.10: Mode coupling between the rib waveguide and the slot waveguide, x axis centered on the midpoint of w_c and y represents the electric field distribution, (a) mode mismatch condition when the width of the rib waveguide is the same as the slot waveguide; (b) mode match condition when the width of the rib waveguide is optimised.

After the fabrication, the same chip preparation was performed as for the first round of the rib waveguides, by cutting and polishing before testing. The results of the linear loss measurement is shown in Chapter 6, which is severely limited the nonlinear performance in the experiments. Future development should focus on enhancing

core$_w$ (nm)	w_c **(nm)**	**slot$_w$ (nm)**	w_c **(nm)**	**side$_w$ (nm)**	w_c **(nm)**
1300	1560	140	1624	320	1592
1320	1576	160	1624	300	1608
1340	1608	200	1592	280	1576
1360	1624	220	1592		
1380	1640	240	1592		

TABLE 7.3: Optimised w_c for different structural parameters of slot waveguides.

waveguide design to minimize linear loss. This could involve adjusting the structure design in the slot or exploring material changes.

Chapter 8

Conclusions

8.1 Summary

During my PhD study, the primary focus has been to comprehend silicon nonlinear optics and the fundamental theory of waveguides. This central theme of the study revolves around nonlinear wavelength conversion in silicon, particularly through Raman scattering and FWM. CSRS based on SCFs and planar waveguides has been a key area of in this wok. The experimental validation, including sample fabrication, characterisation and nonlinear measurements, provides robust support to the theoretical simulations and guide further developments in this field.

The thorough learning of fundamental concepts in nonlinear optics, encompassing phenomena such as Raman scattering, IRS, FWM, CARS and CSRS, provided a comprehensive foundation for my PhD study. Employing simulations based on NLSE, which includes the incorporation of delayed Raman effects, allowed me to discern the intricate interplay of dispersion, loss and nonlinearities in the propagation of light. The Raman results obtained in SCFs within both the telecom band and mid-infrared band marked a significant milestone, demonstrating effective Raman amplification in this platform. The net Raman probe gain reached 1.2 dB and 4 dB in the telecom band and mid-infrared band, respectively. Additionally, simulations for cascaded Raman in SCFs were conducted under picosecond pulsed pump conditions to optimise structural parameters, predict maximum gain, and anticipate the evolution of higher-order Stokes waves. In the investigation of FWM in SCFs in the mid-infrared band, the observation of CARS, with a conversion efficiency of -18 dB, surpassing the pure FWM conversion efficiency by 14 dB, inspired the exploration of CSRS in SCFs. This exploration aimed to achieve higher conversion efficiency via the interaction between Raman scattering and FWM.

The optimisation of SCF was conducted based on dispersion profiles, and subsequent simulations for CSRS was performed to predict the nonlinear performance, providing

guidance for practical experiments. Experimental results confirmed the existence of CSRS, aligning well with the simulation results. The comparison of conversion efficiency around the Raman shift, with and without Raman scattering, indicated that Raman scattering effectively increased conversion efficiency when the idler was generated at the Stokes wavelength with a small seed signal at the anti-Stokes wavelength. Simulations also explored the gain variation associated with pump power, suggesting that higher gains could be obtained by increasing the pump power. Power comparisons of pump, signal and idler under different conditions (CSRS, FWM, Raman scattering) were calculated. The trends of pump, signal and idler revealed a dominant nonlinear phenomenon in this process. The evolution of the three waves along the propagation distance indicated that periodic changes in the enhancement of the Stokes waves. In the experiment, the maximum conversion efficiency in the telecom band was -44 dB with an enhancement of 15 dB. Simulation results suggested an optimised propagation distance of 6.5 mm to achieve higher gain with existing SCF parameters. In the mid-infrared band, the maximum conversion efficiency was -43 dB with an enhancement of 17 dB. Simulation results indicated the need for optimised core diameter and length to achieve higher conversion efficiency in this band. The experimental results confirmed the enhancement of Raman scattering on FWM, but this enhancement was constrained by the coupled-in pump power and the precision in controlling over core diameters. A novel approach for fixing SCFs was employed to augment the coupled-in pump power, successfully increasing it by an order of magnitude. In an effort to improve tapering accuracy, the recipe for the tapering process has been refined. But the results is far from expectations, primarily due to the limitations in machine accuracy.

The fabrication accuracy limitation in SCFs prompts transition to planar waveguides, which provide precise control over etch depth and width. This platform demonstrated excellent dispersion engineering capability, meeting expectations for satisfying phase matching conditions. To achieve broadband FWM wavelength conversion overlapping with the Raman gain peak, dispersion profiles of rib waveguides were calculated to determine optimised structural parameters, assisted with comparisons between A_{eff} and SL. Two waveguides were selected for further study: one with an etch depth of 350 nm and width of 790 nm, and another with an etch depth of 250 nm and width of 1540 nm. These structures were chosen for their suitable position of ZDWs around available pump wavelengths in the laboratory, specifically 1545 nm and 2170 nm. CSRS simulations were then performed in the telecom and mid-infrared bands to predict nonlinear performance. Simulations indicate that conversion efficiency exceeding 0 dB is achievable with the proper CW pump power, and the Stokes output power reaches hundreds of micro-watts and several milli-watts in the telecom and mid-infrared band, respectively. In experiments, the maximum conversion efficiency reached ~ 30 dB with input pump power of only 20 mW and 40 mW in the telecom and mid-infrared bands. The primary challenge in this

experiment lies in the high coupling loss, restricting the coupled-in pump power. Various coupling methods, including tapered lens fibre and optical lens, have been utilised to improve the coupling efficiency. However, the effectiveness of these methods is hampered by the inferior facet quality resulting from polishing. Despite the introduction of deep etch, the fabrication process proved unsuccessful. As an final attempt, cleaving on the old chips was employed, albeit at the expense of sacrificing waveguides fabricated for linear loss testing. Through the comparison between the enhancement of conversion efficiency and Stokes output power in different bandwidths and platforms, the stabilisation and unpredictability of the enhancement variation motivated the exploration of influencing factors for Raman enhancement in CSRS. The comparison between CEE and PE under various conditions revealed that β_2, P_s and f_R significantly influence PE in the traditional waveguide environment.

To optimise the dispersion properties for higher-order Stokes wave generation to longer wavelengths, slotted waveguides are considered, aiming to produce a flat and low dispersion profile. The comparisons of dispersion profiles with different structure parameters, including slab height slab_h, core waveguide height H, core width core_w, slot width slot_w, preserved silicon step height h, side width side_w, are provided. The optimised structure parameters are summarised as follows: $\text{slab}_h = 80\,\text{nm}$ (variation range: 70 nm-90 nm), $H = 395\,\text{nm}$, $\text{core}_w = 1325\,\text{nm}$ (variation range: 1300 nm-1380 nm), $\text{slot}_w = 155\,\text{nm}$ (variation range: 140 nm-240 nm), $h = 80\,\text{nm}$ (variation range: 70 nm-90 nm), $\text{side}_w = 300\,\text{nm}$ (variation range: 270 nm-320 nm). With these optimised parameters, the cascaded Raman process assisted by CSRS, CARS and FWM could be obtained using a pulse pump. Specifically, the 7^{th} Stokes wave excited within the propagation length of $2\,cm$ in this process. The high fabrication accuracy indicated a potential for failure, necessitating adjustment to the structure design.

Towards the end, preparations for the waveguide fabrication are outlined for both SCFs and planar waveguides. For SCFs, the fabrication involves a tapering process applied to as-drawn fibres. Typically, a two-step tapering process is employed to achieve sub-micron core diameters. Meanwhile, replacing the poly silicon core with a single crystal silicon core results in extremely low linear loss, about 0.2 dB/cm. The fixing method for SCFs is improved to support higher pump power, facilitating the observation of nonlinearity in the mid-infrared band with CW laser sources. Regarding planar waveguides, detailed design considerations for input light coupling and the coupling between rib waveguides and slotted waveguides are explained. The mask design, including layout arrangement and label explanations, is illustrated to provide insight into the sample appearance. Challenges related to coupling efficiency are addresses, and the possible method is implemented in the second fabrication round.

8.2 Future development

This work successfully showcased nonlinearity in SCFs and planar waveguides, the initial experiment confirmed theoretical prediction, validating simulations. However, challenges emerged during sample fabrication and nonlinear measurements, necessitate a concerted effort to overcome these hurdles.

In the case of SCFs, limitations were encountered in Raman amplification in the telecom band due to the initial fixing method, which constrained the couple-in pump power to ~ 50 mW. A new fixing method was introduced to accommodate higher pump power to overcome this limitation, aiming for improved results. In addition, the linear loss for submicron SCFs in the telecom band exceeded 1 dB, surpassing the average value in the mid-infrared band due to the smaller core size. Refinement of the tapering recipe could mitigate the linear loss. Alternatively, employing KTH fibres instead of US fibres might be explored. However, the characterisation of nonlinear parameters for KTH fibres remains incomplete from the telecom to mid-infrared band. Simultaneously, achieving high quality submicron SCFs with tapering lengths over 2 cm pose a significant limitation for Raman scattering, accumulating along the length. While Raman amplification in the mid-infrared band has achieved a record up to now, future plans involve investigating cascaded Raman, serving as the Raman laser, with the picosecond laser sources. Ensuring low linear loss and propagation length with existing KTH fibres and tapering techniques is possible. However, unexpected limitations appears in experiments, hindering the generation of higher-order Stokes waves. The possible reason for the decrease in 1^{st} Stokes wave in the mid-infrared band is strong TPA, surpassing levels reported in the literature due to the extra tension from different materials in cladding and core. Further experiments are required to explore this phenomenon.

Concerning CSRS in SCFs, whether in the telecom or mid-infrared band, achieving precise control over the core diameter presents a barrier in meeting the phase matching condition with existing tapering techniques. Machine setting inaccuracies introduce a theoretical error of 100 nm, preventing the fabrication of an optimised structure compared to the required fabrication accuracy of 30 nm in the telecom band and 100 nm in the mid-infrared band. Additionally, non-uniformity along the original untapped fibres and the instability of the tapering machine contribute to this challenge. The estimated core diameter is calculated under the assumption that the ratio between cladding and core remains fixed. Nevertheless, this ratio fluctuates during the tapering process due to factors such as temperature and tapering speed, leading to an error bar of the core size. Currently, polishing the recipe after each tapering round is the primary method to approach the optimised core size. However, new tapering process is under exploration to achieve high precision control over core dimensions and ensure long lengths with high quality in the future. Another serious

issue is the low coupled-in pump power, a major limitation for obtaining high conversion efficiency and Stokes output power. The existing experimental setup could be optimised by introducing another objective lens on the input coupling side to adjust the mode profile, reducing input coupling loss. The highest input power achieved is $\sim 600\,\mathrm{mW}$ with the existing fixing method. In the future, new fixing method could be explored to withstand more pump power and observe stronger nonlinear effects.

Moving on to CSRS observed in rib waveguides, both in the telecom band and mid-infrared band, these are constrained by the coupled-in pump power. In contrast to SCFs, limited by the fixing method, the main challenging here is the substantial coupling loss. The second fabrication round, involving deep etching, encountered failure during the etching process, leading to the destruction of the silicon layer and waveguide structures. The recipe for deep etching needs development for future success. An alternative approach is to explore a new coupling design, such as grating couplers or other special types of couplers. Another noteworthy challenge is the high linear loss during the characterisation of planar waveguides. This high linear loss may be attributed to the roughness of the sidewall. In addition to improving the etching operation, an in-depth investigation into the influence of the etch depth and width is necessary to achieve an effective reduction in linear loss in the future. The experimental setup could also be adjusted to increase coupling efficiency, for example, by utilising aspheric lenses instead of spherical lenses.

Finally, the investigation of slotted waveguides represents another promising direction. However, the high linear loss has forbidden the observation of any nonlinear effects. This significant linear loss could potentially be attributed to SWGs, difficult in achieving perfect fabrication and cleaning and introducing extra loss. During testing, a higher-order light mode was easily excited and difficult to transfer to the fundamental mode by adjusting the coupling. The design of the slotted waveguide requires careful checking and refinement. The slot section might benefit from exploring alternative methods to realise separation between core and side waveguides. Conducting nonlinear measurements in a slotted waveguide with low linear loss holds promise for achieving supercontinuum generation.

Appendix A

List of samples and the relating parameters

Waveguide No.	h**(nm)**	W **(μm)**	L **(mm)**	β_2 **(ps^2/m)**	A_{eff} **(μm^2)**	α_l **(dB/cm)**
Rib A	350	840	15	0.32	0.063	$\sim$ 3 (at 1545 nm)
Rib B	350	840	10	0.32	0.063	$\sim$ 3 (at 1545 nm)
Rib C	350	840	20	0.32	0.063	$\sim$ 3 (at 1545 nm)
Rib D	350	815	20	0.3	0.031	$\sim$ 3 (at 1545 nm)
Rib E	250	1490	20	0.63	-0.024	$\sim$ 2 (at 2171 nm)

TABLE A.1: The corresponding parameters of rib waveguide used in the nonlinear experiments.

$\lambda\,(\mu m)$	n	$n_2\,(m^2/W)$	$\beta_{TPA}\,(m/W)$
1.432	3.489	4.2×10^{-18}	11.7×10^{-12}
1.5	3.482	5×10^{-18}	10.8×10^{-12}
1.545	3.478	5.5×10^{-18}	10×10^{-12}
1.992	3.453	7.6^{-18}	1.9×10^{-12}
2.17	3.447	6.4×10^{-18}	0.15×10^{-12}

TABLE A.2: Linear and nonlinear parameters for silicon at different wavelength. [22]

Appendix B

MATLAB code for NLSE

Code	Description
Resolution in the time and frequency domain	
tic;	Time record
Ntime=256*1024;	Number of time points
Tmax=1000;	Maximum time window
dT=2*Tmax/(Ntime);	Time resolution
TT=[-Ntime/2:(Ntime/2)-1]*dT;	Time window
FF=[-Ntime/2:(Ntime/2)-1]./(2*Tmax);	Frequency window
Fmax=max(FF);	Maximum Frequency window
dF=FF(2)-FF(1);	Frequency resolution
Constants and material parameters	
c=2.997924580e-4; $\%m/ps$	Speed of light
n2=4.196e-18; $\%m^2/W$	Nonlinear refractive index
Aeff=0.372e-12; $\%m^2$	Effective mode area
beta2=1.1040; $\%ps^2/m$	2nd order dispersion parameter
beta3=-4.0962e-5; $\%ps^3/m$	3rd order dispersion parameter
beta4=6e-7; $\%ps^4/m$	4th order dispersion parameter
lam=1.432e-6; $\%m$	Pump wavelength
k0=2*pi/lam; $\%1/m$	Wave vector
beta_TPA=11.772e-12; $\%m/W$	TPA coefficient
gamma=k0*n2/Aeff+i*beta_TPA/2/Aeff;	Nonlinear coefficient
sigma=1.45e-21; $\%m^2$	FCA cross section
kc=1.35e-27; $\%m^3$	FCA coefficient
mu=2*kc*k0/sigma;	Free carrier dispersion
tau=7.5e3; $\%ps$	free carrier lifetime
h=6.626068*1e-34; $\%m^2kg/s$	Planck constant

Waveguide parameters	
L=3e-2; %m	Crystal length
Alpha_l=2e2; %dB/m	Propagation loss
LdB=Alpha_l*L; %dB	
Lss=10^(LdB/10);	Loss in other units
alpha_l=log(Lss)/L;	
Parameters of pump source	
Tpp=100e3; %ps	Full width at half height (FWHM) of pump source
T0p=Tpp/1.665;	Width at 1/e
P0p=1000e-3; %W	Pump peak power
%E0=sqrt(P0)*sech(TT/T0);	Sech-shaped pulse
E0p=sqrt(P0p)*exp(-1/2*(TT/T0p).^2); %$sqrt(W)$	Gussian -shaped pump function
Tps=20;	Full width at half height of signal source
T0s=Tps/1.665;	
P0s=0;	signal peak power
deltf=15.45; %THz	Difference between the signal and the pump
phi_0=2*pi*deltf*TT;	Phase difference
E0s=sqrt(P0s)*exp(-1/2*(TT/T0s)^2) *exp(i*phi_0);	Signal function
E0=E0p +E0s;	Superposition of pump and signal
Ephoton=h*(FF + c/lam)*1e24; %pJ	Photon energy
Ef0=fftshift(ifft(fftshift(E0)))*2*Tmax+ sqrt(Ephoton*dF*A).* exp(i*pi*(2*rand(size(FF))-1));	Adding noise, A could be adjusted according to the real noise level
E0=fftshift(fft(fftshift(Ef0/2/Tmax)));	Fourier transform
Draw spectrum in time and frequency domain	
figure(1)	Draw figure 1
subplot(2,1,1);	Draw the top figure
plot(TT,abs(E0),^2);	Draw the light intensity in time domain
axis([-Tmax Tmax 0 inf])	Set the ranges of axis
title('z = 0 m');	
xlabel('Time (ps)')	
ylabel('Intensity (W/m ^)')	
Ef0 = fftshift(fft(fftshift(E0)));	
subplot(2,1,2);	
plot(FF,abs(Ef0).^2)	
xlabel('Frequency (THz)')	

ylabel('Spectrum (a.u.)')	
drawnow;	
Dispersive operators	
phi2=1/2*i*(2*pi*FF).^2*beta2;	2nd order
phi3=1/6*i*(2*pi*FF).^3*beta3;	3rd order
phi4=1/24*i*(2*pi*FF).^4*beta4;	4th order
Raman operators	
T1=10.3e-3; %*ps*	τ_1
T2=3.0315; %*ps*	τ_2
% gR=2.9e-10;	Raman gain
hR=zeros(1,Ntime);	Raman response function zeroed
hR(x1+1:end)=(T1^2+T2^2)/(T1*T2^2)	Raman response function
*exp(-TT(x1+1:end)/T2)	
.*sin(TT(x1+1:end)/T1);	
hRf=fftshift(fft(fftshift(hR)));	Fourier transform
HR=fftshift(fft(fftshift(hR)))*dT;	Fourier transform
% fR=gR*(0.105*pi)/(n2*k0*15.5*2*pi);	Fractional contribution of Raman response
fR=0.043;	
chi1111=HR;	
Propagation segment	
z=0;	
Lz=L;	
E1=E0;	
a1=1e-3;	Set the segment of the length
Nplots=(Lz-z)/a1+1;	
Nplots=round(Nplots);	
a=a1;	
b=2;	
pik=[0:a1:Lz];	
Create matrix and vectors for storage	
Eout=zeros(Nplots,Ntime);	
Eout(1,:)=E0;	
width=zeros(Nplots,1);	
width(1)=fwhm(TT, abs(E0),^2);	
energy=zeros(Nplots,1);	
energy(1)=sum(abs(E0).^2)*dT;	
disp(['Ein='num2str(energy(1))'pJ'])	

```
Nc=zeros(size(TT));
```

Main loop of the code

```
while z<Lz,                                  Set the limitation of the loop
drawnow
E1til=fftshift(ifft(fftshift(E1)));
dz=5e-4;                                     For fixed step propagation
z=z+dz;
if z>=a                                      Set the condition for drawing figures
Eout(b:)=E1;
width(b)=fwhm(TT,abs(E1).^2);
energy(b)=sum(abs(E1).^2)*dT;
figure(1)
subplot(2,1,1);                              Draw the top figure
plot(TT,abs(E1).^2);                         Draw the light intensity in time domain
axis([-Tmax Tmax 0 inf])                     Set the ranges of axis
title(['z =',num2str(z),'m,E'num2str(energy(b1))]);
xlabel('Time (ps)')
ylabel('Power (W)')
subplot(2,1,2);
plot(FF,abs(Ef0).^2)
xlabel('Frequency (THz)')
ylabel('Spectrum (a.u.)')
a=a+1;
b=b+1;
end
GVD=exp((phi2+phi3+phi4)*dz);                dispersion step
E1til=E1til.*GVD;
E1=fftshift(fft(fftshift(E1til)));
conv0=(fft(fftshift(abs(E1).^2))) .*fft-     Raman step solved by Runge-Kutta
shift(chi1111);                              method
int0=(1-fR)*abs(E1).^2+fR*fftshift(ifft((conv0)));
v1=E1-1/2*gamma/w0*dz*gradient(E1.*int0,TT);
conv1=fft(fftshift(abs(v1).^2)).*fftshift(chi1111);
int1=(1-fR)*abs(v1).^2+fR*fftshift(ifft((conv1)));
v=E1+i*gamma*dz*v1.*(int1-int0)-
gamma/w0*dz*gradient(v1.*int1,TT);
E1=v.*exp(i*dz*gamma*int0);
%Nc=zeros(size(TT));                         Free carrier step for pulse pump
%for ii=1:length(TT)-2
%Nc(ii+2)=(beta_TPA/(2*h*v0)*abs(E1(ii+1)).^4/Aeff^2
*1e-24-Nc(ii+1)/tau)*2*dT+Nc(ii);
```

%end	
Nc=beta_TPA/(2*h*v0)*mean(abs(E1))^4 /Aeff^2*1e-24*tau;	Free carrier step for CW light
E1=E1.*exp(-sigma/2*(1+i*mu).*Nc*dz);	
loss=exp(-0.5*alpha_l*dz);	Linear loss step
E1=E1.*loss;	
end	The end of the loop
Results	
Eout(Nplots,:)=E1;	
width(Nplots)=fwhm(TT,abs(E1).^2);	
energy(Nplots)=sum(abs(E1).^2).*dT;	
disp(['Eout='num2str(energy(Nplots))'pJ'])	
toc	Calculation time
Efp=fftmeshshift(abs(ifft(Eout.')).^2).';	Output pump power in frequency domain
Ef_windows=exp(-1/2*((FF-deltf)/2).^6);	Signal frequency window
Ef_outs=fftshift(ifft(ffshift(E1))).*Ef_windows;	
E_outs=fftshift(fft(fftshift(Ef_outs)));	Output specturm in signal frequency
Ef_windowp=exp(-1/2*((FF)/2).^6);	Pump frequency domain
Ef_outp=fftshift(ifft(ffshift(E1))).*Ef_windowp;	
E_outp=fftshift(fft(fftshift(Ef_outp)));	Out put spectrum in pump frequency

TABLE B.1: MATLAB code for NLSE.

Code	**Description**
function f=fftmeshshift(g);	Name the function and the variable
% f=fftmeshshift(g)	carriers out a columnwise fftshift on a matrix g
m=size(g,1);	
a=g(1:m/2,:);	
b=g(m/2+1,:);	
f=[b;a];	

TABLE B.2: Fourier transform code

Code	Description
function f=fwhm(TT,A);	Name the function and the variable; TT is the x grid and A is the profile whose width is to be measured
h=(max(A)-min(A))/2;	
A=A-h;	
is2=min(find(A>0));	Find the left edge of the pulse
is1=is2-1;	
if1=max(find(A>0));	Find the right edge of the pulse
if2=if1+1;	
if(if2>length(A))|(is2>length(A))	Conditions to determine whether A is an
|(is1<1)|(if1<1)	invalid matrix
f=nan;	output results
else	
xs=(A(is1)*TT(is2)-	
A(is2)*TT(is1))/(A(is1)-A(is2));	
xf=(A(if1)*TT(if2)-	
A(if2)*TT(if1))/(A(if1)-A(if2));	
f=xf-xs;	f is the FWHM of a pulse
end	

TABLE B.3: FWHM calculation code

Appendix C

Parameters for characterizing rib waveguide

No.	Linear loss (dB/cm)	ICL (dB)	β_{TPA} ($\times 10^{-12}$ m/W)
1	2	18	5
2	2	19.5	7
3	2	20.5	9
4	2	21.5	11
5	2	22.5	13

TABLE C.1: Parameters for choosing the proper β_{TPA} with the linear loss of 2 dB/cm.

No.	Linear loss (dB/cm)	ICL (dB)	β_{TPA} ($\times 10^{-12}$ m/W)
1	3	21	13
2	3	20.5	11
3	3	19.5	9
4	3	18.5	7
5	3	17.5	5

TABLE C.2: Parameters for choosing the proper β_{TPA} with the linear loss of 3 dB/cm.

No.	Linear loss (dB/cm)	ICL (dB)	β_{TPA} ($\times 10^{-12}$ m/W)
1	4	20.5	13
2	4	20	11
3	4	19	9
4	4	18.5	7
5	4	17	5

TABLE C.3: Parameters for choosing the proper β_{TPA} with the linear loss of 4 dB/cm.

No.	Linear loss (dB/cm)	ICL (dB)	β_{TPA} ($\times 10^{-12}$ m/W)	OCL (dB)
1	1	20	7	5.5
2	2	20	7	4.5
3	3	19	7	4
4	4	18.5	7	2.5

TABLE C.4: Parameters for choosing the proper $\beta_T PA$ and linear loss.

References

[1] Ricardo Claps, Dimitri Dimitropoulos, Varun Raghunathan, Y Han, and B Jalali. Observation of stimulated Raman amplification in silicon waveguides. *Optics Express*, 11(15):1731–1739, 2003.

[2] Haisheng Rong, Richard Jones, Ansheng Liu, Oded Cohen, Dani Hak, Alexander Fang, and Mario Paniccia. A continuous-wave Raman silicon laser. *Nature*, 433(7027):725–728, 2005.

[3] Varun Raghunathan, David Borlaug, Robert R Rice, and Bahram Jalali. Demonstration of a mid-infrared silicon Raman amplifier. *Optics Express*, 15(22):14355–14362, 2007.

[4] DR Solli, P Koonath, and B Jalali. Inverse Raman scattering in silicon: a free-carrier enhanced effect. *Physical Review A*, 79(5):053853, 2009.

[5] Mark A Foster, Amy C Turner, Jay E Sharping, Bradley S Schmidt, Michal Lipson, and Alexander L Gaeta. Broad-band optical parametric gain on a silicon photonic chip. *Nature*, 441(7096):960–963, 2006.

[6] Dong Wu, Li Shen, Haonan Ren, Meng Huang, Cosimo Lacava, Joseph Campling, Shiyu Sun, Thomas W Hawkins, Ursula J Gibson, Periklis Petropoulos, et al. Four-wave mixing-based wavelength conversion and parametric amplification in submicron silicon core fibers. *IEEE Journal of Selected Topics in Quantum Electronics*, 27(2):4300111, 2020.

[7] Xiaoping Liu, Richard M Osgood Jr, Yurii A Vlasov, and William MJ Green. Mid-infrared optical parametric amplifier using silicon nanophotonic waveguides. *Nature Photonics*, 4(8):557–560, 2010.

[8] Sanja Zlatanovic, Jung S Park, Slaven Moro, Jose M Chavez Boggio, Ivan B Divliansky, Nikola Alic, Shayan Mookherjea, and Stojan Radic. Mid-infrared wavelength conversion in silicon waveguides using ultracompact telecom-band-derived pump source. *Nature Photonics*, 4(8):561–564, 2010.

[9] Ryan KW Lau, Michaël Ménard, Yoshitomo Okawachi, Mark A Foster, Amy C Turner-Foster, Reza Salem, Michal Lipson, and Alexander L Gaeta.

Continuous-wave mid-infrared frequency conversion in silicon nanowaveguides. *Optics Letters*, 36(7):1263–1265, 2011.

[10] Lianghong Yin, Qiang Lin, and Govind P Agrawal. Soliton fission and supercontinuum generation in silicon waveguides. *Optics Letters*, 32(4):391–393, 2007.

[11] Jassem Safioui, François Leo, Bart Kuyken, Simon-Pierre Gorza, Shankar Kumar Selvaraja, Roel Baets, Philippe Emplit, Gunther Roelkens, and Serge Massar. Supercontinuum generation in hydrogenated amorphous silicon waveguides at telecommunication wavelengths. *Optics Express*, 22(3):3089–3097, 2014.

[12] L Shen, N Healy, L Xu, HY Cheng, TD Day, JHV Price, JV Badding, and AC Peacock. Four-wave mixing and octave-spanning supercontinuum generation in a small core hydrogenated amorphous silicon fiber pumped in the mid-infrared. *Optics Letters*, 39(19):5721–5724, 2014.

[13] Austin G Griffith, Ryan KW Lau, Jaime Cardenas, Yoshitomo Okawachi, Aseema Mohanty, Romy Fain, Yoon Ho Daniel Lee, Mengjie Yu, Christopher T Phare, Carl B Poitras, et al. Silicon-chip mid-infrared frequency comb generation. *Nature Communications*, 6(1):6299, 2015.

[14] Rai Kou, Taiki Hatakeyama, Jason Horng, Ji-Hun Kang, Yuan Wang, Xiang Zhang, and Feng Wang. Mid-IR broadband supercontinuum generation from a suspended silicon waveguide. *Optics Letters*, 43(6):1387–1390, 2018.

[15] Nima Nader, Abijith Kowligy, Jeff Chiles, Eric J Stanton, Henry Timmers, Alexander J Lind, Flavio C Cruz, Daniel MB Lesko, Kimberly A Briggman, Sae Woo Nam, et al. Infrared frequency comb generation and spectroscopy with suspended silicon nanophotonic waveguides. *Optica*, 6(10):1269–1276, 2019.

[16] Thibaut Sylvestre, Hervé Maillotte, Eric Lantz, and P Tchofo Dinda. Raman-assisted parametric frequency conversion in a normally dispersive single-mode fiber. *Optics Letters*, 24(22):1561–1563, 1999.

[17] R Claps, V Raghunathan, D Dimitropoulos, and B Jalali. Anti-stokes Raman conversion in silicon waveguides. *Optics Express*, 11(22):2862–2872, 2003.

[18] Xianwen Liu, Changzheng Sun, Bing Xiong, Lai Wang, Jian Wang, Yanjun Han, Zhibiao Hao, Hongtao Li, Yi Luo, Jianchang Yan, et al. Integrated high-Q crystalline AIN microresonators for broadband Kerr and Raman frequency combs. *ACS Photonics*, 5(5):1943–1950, 2018.

[19] Hojoong Jung, Zheng Gong, Xianwen Liu, Xiang Guo, Chang-ling Zou, and Hong X Tang. Stokes and anti-Stokes Raman scatterings from frequency comb lines in poly-crystalline aluminum nitride microring resonators. *Optics Express*, 27(16):22246–22253, 2019.

[20] Grégory Moille, Xiyuan Lu, Jordan Stone, Daron Westly, and Kartik Srinivasan. Fourier synthesis dispersion engineering of photonic crystal microrings for broadband frequency combs. *Communications Physics*, 6(1):144, 2023.

[21] Alexander L Gaeta, Michal Lipson, and Tobias J Kippenberg. Photonic-chip-based frequency combs. *Nature Photonics*, 13(3):158–169, 2019.

[22] Lin Zhang, Anuradha M Agarwal, Lionel C Kimerling, and Jurgen Michel. Nonlinear Group IV photonics based on silicon and germanium: from near-infrared to mid-infrared. *Nanophotonics*, 3(4-5):247–268, 2014.

[23] Alan D Bristow, Nir Rotenberg, and Henry M Van Driel. Two-photon absorption and Kerr coefficients of silicon for 850–2200nm. *Applied Physics Letters*, 90(19):191104, 2007.

[24] Robert W Boyd, Alexander L Gaeta, and Enno Giese. Nonlinear optics. In *Springer Handbook of Atomic, Molecular, and Optical Physics*, pages 1097–1110. Springer, 2008.

[25] Ricardo Claps, Dimitri Dimitropoulos, Yan Han, and Bahram Jalali. Observation of Raman emission in silicon waveguides at 1.54 μm. *Optics Express*, 10(22):1305–1313, 2002.

[26] Dong Wu. *Tapered silicon core fibres for optical parametric amplification and wavelength conversion in the telecom band*. PhD thesis, University of Southampton, 2022.

[27] RA Soref and JP Lorenzo. Single-crystal silicon: a new material for 1.3 and 1.6 μm integrated-optical components. *Electronics Letters*, 21(21):953–954, 1985.

[28] Graham T Reed, William Robert Headley, and CE Jason Png. Silicon photonics: the early years. In *Optoelectronic Integration on Silicon II*, volume 5730, pages 1–18. SPIE, 2005.

[29] Andrew Rickman. The commercialization of silicon photonics. *Nature Photonics*, 8(8):579–582, 2014.

[30] Ansheng Liu, Ling Liao, Doron Rubin, Hat Nguyen, Berkehan Ciftcioglu, Yoel Chetrit, Nahum Izhaky, and Mario Paniccia. High-speed optical modulation based on carrier depletion in a silicon waveguide. *Optics Express*, 15(2):660–668, 2007.

[31] David J Thomson, Frederic Y Gardes, Jean-Marc Fedeli, Sanja Zlatanovic, Youfang Hu, Bill Ping Piu Kuo, Evgeny Myslivets, Nikola Alic, Stojan Radic, Goran Z Mashanovich, et al. 50-Gb/s silicon optical modulator. *IEEE Photonics Technology Letters*, 24(4):234–236, 2011.

[32] Wei Cao, David Hagan, David J Thomson, Milos Nedeljkovic, Callum G Littlejohns, Andy Knights, Shaif-Ul Alam, Junjia Wang, Frederic Gardes, Weiwei Zhang, et al. High-speed silicon modulators for the 2 μm wavelength band. *Optica*, 5(9):1055–1062, 2018.

[33] Ya-Qing Bie, Gabriele Grosso, Mikkel Heuck, Marco M Furchi, Yuan Cao, Jiabao Zheng, Darius Bunandar, Efren Navarro-Moratalla, Lin Zhou, Dmitri K Efetov, et al. A MoTe2-based light-emitting diode and photodetector for silicon photonic integrated circuits. *Nature Nanotechnology*, 12(12):1124–1129, 2017.

[34] Lorenzo Pavesi, Luca Dal Negro, Ca Mazzoleni, G Franzo, and d F Priolo. Optical gain in silicon nanocrystals. *Nature*, 408(6811):440–444, 2000.

[35] Ernesto Ciaramella, Franco Curti, and Stefano Trillo. All-optical signal reshaping by means of four-wave mixing in optical fibers. *IEEE Photonics Technology Letters*, 13(2):142–144, 2001.

[36] Jeffrey O White and Amnon Yariv. Real-time image processing via four-wave mixing in a photorefractive medium. *Applied Physics Letters*, 37(1):5–7, 1980.

[37] Rodney S Tucker and Kerry Hinton. Energy consumption and energy density in optical and electronic signal processing. *IEEE Photonics Journal*, 3(5):821–833, 2011.

[38] Sergey A Babin, Dmitriy V Churkin, Arsen E Ismagulov, Sergey I Kablukov, and Evgeny V Podivilov. Four-wave-mixing-induced turbulent spectral broadening in a long Raman fiber laser. *J. Opt. Soc. Am. B*, 24(8):1729–1738, 2007.

[39] Zhican Zhou, Xiangpeng Ou, Yuetong Fang, Emad Alkhazraji, Renjing Xu, Yating Wan, and John E Bowers. Prospects and applications of on-chip lasers. *Elight*, 3(1):1, 2023.

[40] Dalziel J Wilson, Katharina Schneider, Simon Hönl, Miles Anderson, Yannick Baumgartner, Lukas Czornomaz, Tobias J Kippenberg, and Paul Seidler. Integrated gallium phosphide nonlinear photonics. *Nature Photonics*, 14(1):57–62, 2020.

[41] Xianwen Liu, Alexander W Bruch, Juanjuan Lu, Zheng Gong, Joshua B Surya, Liang Zhang, Junxi Wang, Jianchang Yan, and Hong X Tang. Beyond 100 THz-spanning ultraviolet frequency combs in a non-centrosymmetric crystalline waveguide. *Nature communications*, 10(1):2971, 2019.

[42] Minhao Pu, Luisa Ottaviano, Elizaveta Semenova, and Kresten Yvind. Efficient frequency comb generation in AlGaAs-on-insulator. *Optica*, 3(8):823–826, 2016.

[43] Laura C Sinclair, J-D Deschênes, Lindsay Sonderhouse, William C Swann, Isaac H Khader, Esther Baumann, Nathan R Newbury, and Ian Coddington.

Invited article: A compact optically coherent fiber frequency comb. *Review of Scientific Instruments*, 86(8):081301, 2015.

[44] Yunhong Ding, Davide Bacco, Kjeld Dalgaard, Xinlun Cai, Xiaoqi Zhou, Karsten Rottwitt, and Leif Katsuo Oxenløwe. High-dimensional quantum key distribution based on multicore fiber using silicon photonic integrated circuits. *NPJ Quantum Information*, 3(1):25, 2017.

[45] Elnaz Nazemi, Srivatsa Aithal, Walid M Hassen, Eric H Frost, and Jan J Dubowski. GaAs/AlGaAs heterostructure based photonic biosensor for rapid detection of Escherichia coli in phosphate buffered saline solution. *Sensors and Actuators B: Chemical*, 207:556–562, 2015.

[46] Ping Lu, Nageswara Lalam, Mudabbir Badar, Bo Liu, Benjamin T Chorpening, Michael P Buric, and Paul R Ohodnicki. Distributed optical fiber sensing: Review and perspective. *Applied Physics Reviews*, 6(4):041302, 2019.

[47] Alexander M Saeboe, Alexey Yu Nikiforov, Reyhaneh Toufanian, Joshua C Kays, Margaret Chern, J Paolo Casas, Keyi Han, Andrei Piryatinski, Dennis Jones, and Allison M Dennis. Extending the near-infrared emission range of indium phosphide quantum dots for multiplexed in vivo imaging. *Nano letters*, 21(7):3271–3279, 2021.

[48] Yicong Wu, Yuxin Leng, Jiefeng Xi, and Xingde Li. Scanning all-fiber-optic endomicroscopy system for 3D nonlinear optical imaging of biological tissues. *Optics Express*, 17(10):7907–7915, 2009.

[49] Katsuya Nagayama, M Kakui, M Matsui, Tatsuhiko Saitoh, and Y Chigusa. Ultra-low-loss (0.1484 dB/km) pure silica core fibre and extension of transmission distance. *Electronics Letters*, 38(20):1, 2002.

[50] Govind P Agrawal. Nonlinear fiber optics. In *Nonlinear Science at the Dawn of the 21st Century*, pages 195–211. Springer, 2000.

[51] Kaustubh Vyas, Daniel HG Espinosa, Daniel Hutama, Shubhendra Kumar Jain, Rania Mahjoub, Ehsan Mobini, Kashif M Awan, Jeff Lundeen, and Ksenia Dolgaleva. Group III-V semiconductors as promising nonlinear integrated photonic platforms. *Advances in Physics: X*, 7(1):2097020, 2022.

[52] Eric J Stanton, Jeff Chiles, Nima Nader, Galan Moody, Nicolas Volet, Lin Chang, John E Bowers, Sae Woo Nam, and Richard P Mirin. Efficient second harmonic generation in nanophotonic GaAs-on-insulator waveguides. *Optics Express*, 28(7):9521–9532, 2020.

[53] Katharina Schneider, Pol Welter, Yannick Baumgartner, Herwig Hahn, Lukas Czornomaz, and Paul Seidler. Gallium phosphide-on-silicon dioxide photonic devices. *Journal of Lightwave Technology*, 36(14):2994–3002, 2018.

[54] Minhao Pu, Hao Hu, Luisa Ottaviano, Elizaveta Semenova, Dragana Vukovic, Leif Katsuo Oxenløwe, and Kresten Yvind. Ultra-Efficient and broadband nonlinear AlGaAs-on-insulator chip for low-power optical signal processing. *Laser & Photonics Reviews*, 12(12):1800111, 2018.

[55] JP Donnelly, HQ Le, EA Swanson, SH Groves, A Darwish, and EP Ippen. Nondegenerate four-wave mixing wavelength conversion in low-loss passive InGaAsP-InP quantum-well waveguides. *IEEE Photonics Technology Letters*, 8(5):623–625, 1996.

[56] Utsav D Dave, Bart Kuyken, François Leo, Simon-Pierre Gorza, Sylvain Combrie, Alfredo De Rossi, Fabrice Raineri, and Gunther Roelkens. Nonlinear properties of dispersion engineered InGaP photonic wire waveguides in the telecommunication wavelength range. *Optics Express*, 23(4):4650–4657, 2015.

[57] Hiroshi Fukuda, Koji Yamada, Tetsufumi Shoji, Mitsutoshi Takahashi, Tai Tsuchizawa, Toshifumi Watanabe, Jun-ichi Takahashi, and Sei-ichi Itabashi. Four-wave mixing in silicon wire waveguides. *Optics Express*, 13(12):4629–4637, 2005.

[58] Mark A Foster, Amy C Turner, Reza Salem, Michal Lipson, and Alexander L Gaeta. Broad-band continuous-wave parametric wavelength conversion in silicon nanowaveguides. *Optics Express*, 15(20):12949–12958, 2007.

[59] Hon Ki Tsang, Chak Sham Wong, Tak Keung Liang, IE Day, SW Roberts, Arnold Harpin, John Drake, and Mehdi Asghari. Optical dispersion, two-photon absorption and self-phase modulation in silicon waveguides at 1.5 μ m wavelength. *Applied Physics Letters*, 80(3):416–418, 2002.

[60] Martijn JR Heck, Jared F Bauters, Michael L Davenport, Jonathan K Doylend, Siddharth Jain, Géza Kurczveil, Sudharsanan Srinivasan, Yongbo Tang, and John E Bowers. Hybrid silicon photonic integrated circuit technology. *IEEE Journal of Selected Topics in Quantum Electronics*, 19(4):6100117, 2012.

[61] Tin Komljenovic, Michael Davenport, Jared Hulme, Alan Y Liu, Christos T Santis, Alexander Spott, Sudharsanan Srinivasan, Eric J Stanton, Chong Zhang, and John E Bowers. Heterogeneous silicon photonic integrated circuits. *Journal of Lightwave Technology*, 34(1):20–35, 2015.

[62] Di Liang and John E Bowers. Recent progress in lasers on silicon. *Nature Photonics*, 4(8):511–517, 2010.

[63] H Ml Pask. The design and operation of solid-state Raman lasers. *Progress in Quantum Electronics*, 27(1):3–56, 2003.

[64] Richard L Espinola, Jerry I Dadap, Richard M Osgood, Sharee J McNab, and Yurii A Vlasov. Raman amplification in ultrasmall silicon-on-insulator wire waveguides. *Optics Express*, 12(16):3713–3718, 2004.

[65] Qianfan Xu, Vilson R Almeida, and Michal Lipson. Time-resolved study of Raman gain in highly confined silicon-on-insulator waveguides. *Optics Express*, 12(19):4437–4442, 2004.

[66] Ansheng Liu, Haisheng Rong, Mario Paniccia, Oded Cohen, and Dani Hak. Net optical gain in a low loss silicon-on-insulator waveguide by stimulated Raman scattering. *Optics Express*, 12(18):4261–4268, 2004.

[67] Haisheng Rong, Shengbo Xu, Oded Cohen, Omri Raday, Mindy Lee, Vanessa Sih, and Mario Paniccia. A cascaded silicon Raman laser. *Nature Photonics*, 2(3):170–174, 2008.

[68] Vittorio MN Passaro and Francesco De Leonardis. Investigation of SOI Raman lasers for mid-infrared gas sensing. *Sensors*, 9(10):7814–7836, 2009.

[69] Francesco De Leonardis, Benedetto Troia, Richard A Soref, and Vittorio MN Passaro. Investigation of germanium Raman lasers for the mid-infrared. *Optics Express*, 23(13):17237–17254, 2015.

[70] Zhao Li, Fengbo Han, Zhipeng Dong, Qingyang Du, and Zhengqian Luo. On-chip mid-IR octave-tunable Raman soliton laser. *Optics Express*, 30(14):25356–25365, 2022.

[71] Aihu Zheng, Qibing Sun, Leiran Wang, Mulong Liu, Chao Zeng, Guoxi Wang, Lingxuan Zhang, Weichen Fan, Wei Zhao, and Wenfu Zhang. Impact of third-order dispersion and three-photon absorption on mid-infrared time magnification via four-wave mixing in Si 0.8 Ge 0.2 waveguides. *Applied Optics*, 59(4):1187–1192, 2020.

[72] WJ Jones and BP Stoicheff. Inverse Raman spectra: induced absorption at optical frequencies. *Physical Review Letters*, 13(22):657, 1964.

[73] L Schneebeli, K Kieu, E Merzlyak, JM Hales, A DeSimone, JW Perry, Robert A Norwood, and N Peyghambarian. Measurement of the Raman gain coefficient via inverse Raman scattering. *J. Opt. Soc. Am. B*, 30(11):2930–2939, 2013.

[74] K Kieu, L Schneebeli, E Merzlyak, JM Hales, A DeSimone, JW Perry, RA Norwood, and N Peyghambarian. All-optical switching based on inverse Raman scattering in liquid-core optical fibers. *Optics Letters*, 37(5):942–944, 2012.

[75] Boyuan Jin, Jinhui Yuan, Chongxiu Yu, Xinzhu Sang, Qiang Wu, Feng Li, Kuiru Wang, Binbin Yan, Gerald Farrell, and Ping Kong Alexander Wai. Tunable

fractional-order photonic differentiator based on the inverse Raman scattering in a silicon microring resonator. *Optics Express*, 23(9):11141–11151, 2015.

[76] Yanmei Cao, Libin Zhang, Yonghao Fei, Xun Lei, and Shaowu Chen. Effect of frequency chirp on supercontinuum generation in silicon waveguides with two zero-dispersion wavelengths. *Optics Communications*, 334:190–195, 2015.

[77] Jun Rong Ong, Ranjeet Kumar, Ryan Aguinaldo, and Shayan Mookherjea. Efficient CW four-wave mixing in silicon-on-insulator micro-rings with active carrier removal. *IEEE Photonics Technology Letters*, 25(17):1699–1702, 2013.

[78] Minghui Yang, Yuhao Guo, Jing Wang, Zhaohong Han, Kazumi Wada, Lionel C Kimerling, Anuradha M Agarwal, Jurgen Michel, Guifang Li, and Lin Zhang. Mid-IR supercontinuum generated in low-dispersion Ge-on-Si waveguides pumped by sub-ps pulses. *Optics Express*, 25(14):16116–16122, 2017.

[79] Jinhui Yuan, Zhe Kang, Feng Li, Xianting Zhang, Xinzhu Sang, Qiang Wu, Binbin Yan, Kuiru Wang, Xian Zhou, Kangping Zhong, et al. Mid-infrared octave-spanning supercontinuum and frequency comb generation in a suspended germanium-membrane ridge waveguide. *Journal of Lightwave Technology*, 35(14):2994–3002, 2017.

[80] Jintao Lai, Jinhui Yuan, Yujun Cheng, Chao Mei, Xian Zhou, Qiang Wu, Binbin Yan, Kuiru Wang, Keping Long, Chongxiu Yu, et al. Dispersion-engineered T-type germanium waveguide for mid-infrared supercontinuum and frequency comb generations in all-normal dispersion region. *OSA Continuum*, 3(9):2320–2331, 2020.

[81] Jason J Ackert, David J Thomson, Li Shen, Anna C Peacock, Paul E Jessop, Graham T Reed, Goran Z Mashanovich, and Andrew P Knights. High-speed detection at two micrometres with monolithic silicon photodiodes. *Nature Photonics*, 9(6):393–396, 2015.

[82] Nima Nader, Daniel L Maser, Flavio C Cruz, Abijith Kowligy, Henry Timmers, Jeff Chiles, Connor Fredrick, Daron A Westly, Sae Woo Nam, Richard P Mirin, et al. Versatile silicon-waveguide supercontinuum for coherent mid-infrared spectroscopy. *APL Photonics*, 3(3):036102, 2018.

[83] Mengjie Yu, Yoshitomo Okawachi, Austin G Griffith, Nathalie Picqué, Michal Lipson, and Alexander L Gaeta. Silicon-chip-based mid-infrared dual-comb spectroscopy. *Nature Communications*, 9(1):1869, 2018.

[84] Neetesh Singh, Darren D Hudson, Yi Yu, Christian Grillet, Stuart D Jackson, Alvaro Casas-Bedoya, Andrew Read, Petar Atanackovic, Steven G Duvall, Stefano Palomba, et al. Midinfrared supercontinuum generation from 2 to 6 μm in a silicon nanowire. *Optica*, 2(9):797–802, 2015.

[85] Guang S He and Song H Liu. *Advanced nonlinear optics*. World Scientific, 2018.

[86] EA Golovchenko, Pavel V Mamyshev, Alexei N Pilipetskii, and EM Dianov. Mutual influence of the parametric effects and stimulated Raman scattering in optical fibers. *IEEE Journal of Quantum Electronics*, 26(10):1815–1820, 1990.

[87] Zhaolu Wang, Hongjun Liu, Nan Huang, Qibing Sun, and Xuefeng Li. Mid-infrared Raman amplification and wavelength conversion in dispersion engineered silicon-on-sapphire waveguides. *Journal of Optics*, 16(1):015206, 2013.

[88] William M Tolles, Joseph W Nibler, JR McDonald, and Albert B Harvey. A review of the theory and application of coherent anti-stokes Raman spectroscopy (CARS). *Applied Spectroscopy*, 31(4):253–271, 1977.

[89] Günther Roelkens, Dries Van Thourhout, and Roel Baets. High efficiency silicon-on-insulator grating coupler based on a poly-silicon overlay. *Optics Express*, 14(24):11622–11630, 2006.

[90] Dirk Taillaert, Peter Bienstman, and Roel Baets. Compact efficient broadband grating coupler for silicon-on-insulator waveguides. *Optics Letters*, 29(23):2749–2751, 2004.

[91] S Rytov. Electromagnetic properties of a finely stratified medium. *Soviet Physics JEPT*, 2:466–475, 1956.

[92] Robert Halir, Przemek J Bock, Pavel Cheben, Alejandro Ortega-Moñux, Carlos Alonso-Ramos, Jens H Schmid, Jean Lapointe, Dan-Xia Xu, J Gonzalo Wangüemert-Pérez, Íñigo Molina-Fernández, et al. Waveguide sub-wavelength structures: a review of principles and applications. *Laser & Photonics Reviews*, 9(1):25–49, 2015.

[93] Ryan KW Lau, Michael RE Lamont, Yoshitomo Okawachi, and Alexander L Gaeta. Effects of multiphoton absorption on parametric comb generation in silicon microresonators. *Optics Letters*, 40(12):2778–2781, 2015.

[94] Mulong Liu, Leiran Wang, Qibing Sun, Siqi Li, Zhiqiang Ge, Zhizhou Lu, Weiqiang Wang, Guoxi Wang, Wenfu Zhang, Xiaohong Hu, et al. Influences of multiphoton absorption and free-carrier effects on frequency-comb generation in normal dispersion silicon microresonators. *Photonics Research*, 6(4):238–243, 2018.

[95] Tak-Keung Liang and Hon K Tsang. Role of free carriers from two-photon absorption in Raman amplification in silicon-on-insulator waveguides. *Applied Physics Letters*, 84(15):2745–2747, 2004.

[96] Z Yusoff, JH Lee, W Belardi, TM Monro, PC Teh, and DJ Richardson. Raman effects in a highly nonlinear holey fiber: amplification and modulation. *Optics Letters*, 27(6):424–426, 2002.

[97] Anna C Peacock and Noel Healy. Nonlinear optics in tapered silicon fibres. In *Nonlinear Optics and Applications VI*, volume 8434, pages 149–156. SPIE, 2012.

[98] Sijing Liang, Saurabh Jain, Lin Xu, Kyle RH Bottrill, Natsupa Taengnoi, Massimiliano Guasoni, Peng Zhang, Mengben Xiao, Qiongyue Kang, Yongmin Jung, et al. High gain, low noise, spectral-gain-controlled, broadband lumped fiber Raman amplifier. *Journal of Lightwave Technology*, 39(5):1458–1463, 2021.

[99] Sho Kasumie, Fuchuan Lei, Jonathan M Ward, Xuefeng Jiang, Lan Yang, and Síle Nic Chormaic. Raman laser switching induced by cascaded light scattering. *Laser & Photonics Reviews*, 13(10):1900138, 2019.

[100] Uğur Teğin and Bülend Ortaç. Cascaded Raman scattering based high power octave-spanning supercontinuum generation in graded-index multimode fibers. *Scientific Reports*, 8(1):12470, 2018.

[101] Haonan Ren, Ozan Aktas, Yohann Franz, Antoine FJ Runge, Thomas Hawkins, John Ballato, Ursula J Gibson, and Anna C Peacock. Tapered silicon core fibers with nano-spikes for optical coupling via spliced silica fibers. *Optics Express*, 25(20):24157–24163, 2017.

[102] M Kudinova, G Bouwmans, O Vanvincq, R Habert, S Plus, R Bernard, K Baudelle, A Cassez, B Chazallon, M Marinova, et al. Two-step manufacturing of hundreds of meter-long silicon micrometer-size core optical fibers with less than 0.2 dB/cm background losses. *APL Photonics*, 6(2), 2021.

[103] Tonglei Cheng, Xiaojie Xue, Weiqing Gao, Takenobu Suzuki, and Yasutake Ohishi. The second-order Raman Stokes stronger than the first-order Raman Stokes due to inverse Raman scattering in a single mode tellurite fiber. *IEEE Journal of Quantum Electronics*, 53(4):6800504, 2017.

[104] Shaul Pearl, Nir Rotenberg, and Henry M van Driel. Three photon absorption in silicon for 2300–3300nm. *Applied Physics Letters*, 93(13), 2008.

[105] Zhenhong Wang, Bin Zhang, Jun Liu, Yufeng Song, and Han Zhang. Recent developments in mid-infrared fiber lasers: Status and challenges. *Optics & Laser Technology*, 132:106497, 2020.

[106] Kaiheng Zou, Kai Pang, Hao Song, Jintao Fan, Zhe Zhao, Haoqian Song, Runzhou Zhang, Huibin Zhou, Amir Minoofar, Cong Liu, et al. High-capacity free-space optical communications using wavelength-and mode-division-multiplexing in the mid-infrared region. *Nature Communications*, 13(1):7662, 2022.

[107] Philip J Davis and Ivan Polonsky. 25. Numerical Interpolation, Differentiation, and Integration. In *Numerical Interpolation Differentiation and Integration*, 1972.

[108] Dong Wu, Than S Saini, Shiyu Sun, Meng Huang, Qiang Fu, Thomas W Hawkins, John Ballato, and Anna C Peacock. Broadband, tunable wavelength conversion using tapered silicon fibers extending up to 2.4 μm. *APL Photonics*, 8(10):106105, 2023.

[109] Dong Wu, Li Shen, Haonan Ren, Joseph Campling, Thomas W Hawkins, John Ballato, Ursula J Gibson, and Anna C Peacock. Net optical parametric gain in a submicron silicon core fiber pumped in the telecom band. *APL Photonics*, 4(8):086102, 2019.

[110] Meng Huang, Shiyu Sun, Dong Wu, Haonan Ren, Li Shen, Thomas W Hawkins, John Ballato, Ursula J Gibson, and Anna C Peacock. Continuous-wave Raman amplification in silicon core fibers pumped in the telecom band. *APL Photonics*, 6(9):096105, 2021.

[111] Meng Huang, Shiyu Sun, Than S Saini, Qiang Fu, Lin Xu, Dong Wu, Haonan Ren, Li Shen, Thomas W Hawkins, John Ballato, et al. Raman amplification at 2.2 μm in silicon core fibers with prospects for extended mid-infrared source generation. *Light: Science & Applications*, 12(1):209, 2023.

[112] Andrzej Gajda, Lars Zimmermann, Mahmoud Jazayerifar, Georg Winzer, Hui Tian, Robert Elschner, Thomas Richter, Colja Schubert, Bernd Tillack, and Klaus Petermann. Highly efficient CW parametric conversion at 1550 nm in SOI waveguides by reverse biased pin junction. *Optics Express*, 20(12):13100–13107, 2012.

[113] Nathalie Vermeulen, JE Sipe, and Hugo Thienpont. Quasi-phase-matched cavity-enhanced Raman converter based on a silicon nanowire ring. *IEEE Photonics Technology Letters*, 22(24):1796–1798, 2010.

[114] Vladimir Gordienko, ÁD Szabó, MFC Stephens, Victor Vassiliev, CB Gaur, and NJ Doran. Limits of broadband fiber optic parametric devices due to stimulated Brillouin scattering. *Optical Fiber Technology*, 66:102646, 2021.

[115] David A Coucheron, Michael Fokine, Nilesh Patil, Dag Werner Breiby, Ole Tore Buset, Noel Healy, Anna C Peacock, Thomas Hawkins, Max Jones, John Ballato, et al. Laser recrystallization and inscription of compositional microstructures in crystalline SiGe-core fibres. *Nature Communications*, 7(1):13265, 2016.

[116] AG Rickman, GT Reed, and Fereydoon Namavar. Silicon-on-insulator optical rib waveguide loss and mode characteristics. *Journal of Lightwave Technology*, 12(10):1771–1776, 1994.

[117] Eric Numkam Fokoua, Seyed Abokhamis Mousavi, Gregory T Jasion, David J Richardson, and Francesco Poletti. Loss in hollow-core optical fibers:

mechanisms, scaling rules, and limits. *Advances in Optics and Photonics*, 15(1):1–85, 2023.

[118] Sameer Saharan, Bhuvnesh Yadav, Aseem Grover, and Shivam Saini. Fabrication methods for Bio-MEMS. In *Advances in MEMS and Microfluidic Systems*, pages 210–227. IGI Global, 2023.

[119] Mingfei Ding, Ming Zhang, Shihan Hong, Yi Zhao, Long Zhang, Yi Wang, Haitao Chen, Zejie Yu, Shiming Gao, and Daoxin Dai. High-efficiency four-wave mixing in low-loss silicon photonic spiral waveguides beyond the singlemode regime. *Optics Express*, 30(10):16362–16373, 2022.

[120] Jianxun Hong, Kenta Rokumyo, Jiawei Mao, Alisa Bannaron, Hiromu Sato, and Shiyoshi Yokoyama. Efficient four-wave mixing wavelength conversion in a hybrid silicon slot and polymer microring resonator. *Optics Express*, 30(25):45499–45507, 2022.

[121] Mohammad Ahmadi, Jacques Lefebvre, Wei Shi, and Sophie LaRochelle. Non-reciprocal sub-micron waveguide Raman amplifiers, towards loss-less silicon photonics. *IEEE Journal of Selected Topics in Quantum Electronics*, 29(1: Nonlinear Integrated Photonics):1–8, 2022.

[122] Shawn Yohanes Siew, Bo Li, Feng Gao, Hai Yang Zheng, Wenle Zhang, Pengfei Guo, Shawn Wu Xie, Apu Song, Bin Dong, Lian Wee Luo, et al. Review of silicon photonics technology and platform development. *Journal of Lightwave Technology*, 39(13):4374–4389, 2021.

[123] D Dimitropoulos, R Jhaveri, R Claps, JCS Woo, and B Jalali. Lifetime of photogenerated carriers in silicon-on-insulator rib waveguides. *Applied Physics Letters*, 86(7), 2005.

[124] NM Wright, DJ Thomson, KL Litvinenko, WR Headley, AJ Smith, AP Knights, JHB Deane, FY Gardes, GZ Mashanovich, R Gwilliam, et al. Free carrier lifetime modification for silicon waveguide based devices. *Optics Express*, 16(24):19779–19784, 2008.

[125] Robert Halir, Pavel Cheben, Siegfried Janz, Dan-Xia Xu, Íñigo Molina-Fernández, and Juan G Wangüemert-Pérez. Waveguide grating coupler with subwavelength microstructures. *Optics Letters*, 34(9):1408–1410, 2009.

[126] Bart Kuyken, Xiaoping Liu, Richard M Osgood, Roel Baets, Günther Roelkens, and William MJ Green. Mid-infrared to telecom-band supercontinuum generation in highly nonlinear silicon-on-insulator wire waveguides. *Optics Express*, 19(21):20172–20181, 2011.

[127] Amy C Turner-Foster, Mark A Foster, Jacob S Levy, Carl B Poitras, Reza Salem, Alexander L Gaeta, and Michal Lipson. Ultrashort free-carrier lifetime in low-loss silicon nanowaveguides. *Optics Express*, 18(4):3582–3591, 2010.

[128] J Ballato, T Hawkins, P Foy, R Stolen, B Kokuoz, M Ellison, C McMillen, J Reppert, AM Rao, M Daw, et al. Silicon optical fiber. *Optics Express*, 16(23):18675–18683, 2008.

[129] Erlend F Nordstrand, Andrew N Dibbs, Andreas J Eraker, and Ursula J Gibson. Alkaline oxide interface modifiers for silicon fiber production. *Optical Materials Express*, 3(5):651–657, 2013.

[130] Ursula J Gibson, Lei Wei, and John Ballato. Semiconductor core fibres: materials science in a bottle. *Nature Communications*, 12(1):3990, 2021.

List of publications

C.1 Journal

1. ***ShiyuSun***, Meng Huang, Dong Wu, Li Shen, Haonan Ren, Thomas W. Hawkins, John Ballato, Ursula J. Gibson, Goran Z. Mashanovich, and Anna C. Peacock. "Raman enhanced four-wave mixing in silicon core fibers." Optics Letters 47, no. 7 (2022): 1626-1629.

2. ***ShiyuSun***, Mashanovich G Z, Peacock A C. "Design of integrated silicon waveguides for Raman-enhanced four-wave mixing in the telecom band." Optics Express 32, no. 6 (2024): 8715-8722.

3. Meng Huang, ***ShiyuSun***, Than S. Saini, Qiang Fu, Lin Xu, Dong Wu, Haonan Ren et al. "Raman amplification at 2.2 μm in silicon core fibers with prospects for extended mid-infrared source generation." Light: Science & Applications 12, no. 1 (2023): 209.

4. Meng Huang, ***ShiyuSun***, Dong Wu, Haonan Ren, Li Shen, Thomas W. Hawkins, John Ballato, Ursula J. Gibson, and Anna C. Peacock. "Continuous-wave Raman amplification in silicon core fibers pumped in the telecom band." APL Photonics 6, no. 9 (2021).

5. Meng Huang, ***ShiyuSun***, Than Saini, Qiang Fu, Lin Xu, Dong Wu, HAONAN REN et al. "Mid-infrared Raman Amplification in Silicon Core Fiber." (2023).

6. Li Shen, Meng Huang, ***ShiyuSun***, Dong Wu, Zhiwei Yan, Haonan Ren, and Anna C. Peacock. "Toward in-fiber nonlinear silicon photonics." APL Photonics 8, no. 5 (2023).

7. Dong Wu, Li Shen, Haonan Ren, Meng Huang, Cosimo Lacava, Joseph Campling, ***ShiyuSun*** et al. "Four-wave mixing-based wavelength conversion and parametric amplification in submicron silicon core fibers." IEEE Journal of Selected Topics in Quantum Electronics 27, no. 2 (2020): 1-11.

C.2 Conference Papers

1. ***ShiyuSun***, Meng Huang, Dong Wu, Li Shen, Haonan Ren, Thomas W. Hawkins, John Ballato, Ursula J. Gibson, Goran Z. Mashanovich, and Anna C. Peacock. "Raman enhanced four-wave mixing in silicon core fibers." 2021 IEEE Photonics Conference (IPC). IEEE, p. 1-2 (2021)

2. ***ShiyuSun***, Meng Huang, Dong Wu, Li Shen, Thomas W. Hawkins, John Ballato, Ursula J. Gibson, Goran Z. Mashanovich, and Anna C. Peacock. "Role of Phase-matching on Raman-enhanced FWM in Silicon Core Fibers." In CLEO: QELS_Fundamental Science, pp. FTh2A-7. Optica Publishing Group, 2022.

3. Meng Huang, ***ShiyuSun***, Than S. Saini, Qiang Fu, Lin Xu, Dong Wu, Haonan Ren et al. "Mid-infrared Spontaneous and Stimulated Raman Scattering in a Silicon Core Fiber." Research Square (2023).

4. Dong Wu, Than S. Saini, ***ShiyuSun***, Li Shen, Meng Huang, Thomas Hawkins, John Ballato, and A. C. Peacock. "Broadband MIR wavelength conversion in a tapered silicon core fiber." In 2023 Conference on Lasers and Electro-Optics Europe & European Quantum Electronics Conference (CLEO/Europe-EQEC), pp. 1-1. IEEE, 2023.

5. Meng Huang, Haonan Ren, Li Shen, Dong Wu, ***ShiyuSun***, Thomas W. Hawkins, John Ballato, Ursula J. Gibson, and Anna C. Peacock. "Stimulated Raman Scattering in a Tapered Submicron Silicon Core Fiber." In CLEO: Science and Innovations, pp. STh5A-3. Optica Publishing Group, 2021.